Université de Bourgogne

Faculté des Sciences

Laboratoire Interdisciplinaire Carnot de Bourgogne

Département Nanosciences

Fabrication and characterization of Thermo-Plasmonic routers for Telecom Applications

Thèse présentée à l'Université de Bourgogne pour obtenir
le grade de Docteur (Mention Physique)

par

Karim HASSAN

Soutenue le 12 Juillet 2013 devant la commission d'examen composée de:

Bozhevolnyi	S. I.	Professeur, Univ. South. Denmark	Rapporteur
Bachelot	R.	Professeur, Univ. Tech. Troyes	Rapporteur
Dagens	B.	Directeur de Recherche, Univ. Paris Sud	Examinateur
Finot	C.	Professeur, Univ. Bourgogne	Examinateur
Dereux	A.	Professeur, Univ. Bourgogne	Co-directeur de thèse
Weeber	J.-C.	Professeur, Univ. Bourgogne	Directeur de thèse

To Vanessa.

A la fin il n'en restera qu'un!

— **Denis Brognard** [**Koh Lanta**]

Remerciements

Durant ces trois dernières années, j'ai eu l'opportunité d'évoluer aussi bien dans ma vie professionnelle que personnelle, et ceci grâce à de nombreuses personnes qui m'ont données du temps, des idées, de la force et parfois même leur confiance. Il est évident que la période de la thèse est tout à fait propice à ce genre d'évolution, à l'interface entre fin d'étude et début de carrière, où l'on doit à la fois apprendre et découvrir, mais sans un cadre de travail approprié, tout pourrait être plus dur. L'équipe d'Optique Submicronique et NanoCapteur du Laboratoire Interdisciplinaire Carnot de Bourgogne remplit parfaitement ce rôle, les portes de chaque chercheur y sont toujours ouvertes (c'est un leurre chez Eric F.). Aussi je remercie Gérard, Alexandre, Laurent et Juan pour leur expertise scientifique, technique, et sportive, avec des discussions tant chaleureuses que prolifiques. Je pense également au trio d'Eric B. F. et L. qui m'ont soutenus pour divers projets comme l'enseignement ou les barbecues d'équipes (dans le pure respect des règles de sécurité). Merci à Elly pour son soutien indéfectible.
Il est difficile d'avoir un mot ou son antonyme pour chacun et chacune de mes collègues doctorants, post-doctorants, et autres laborantins, mais je dirai merci à Simon sa "Grandeur", Thomas et David pour leur "Finesse", Antonin pour son "Illettrisme", Johan et Jérémie pour leur "Multiplicité", Thibault, Flo, et Nono pour leur "Superficialité", Michael for his wisdom, Mingxia, Fillimon, Padmnabh, Ece, Christian, Serkan, Stéphane, Marie, Pauline, Pierre, Sébastien, Rémi, Delphine et Jean pour leur présence. J'ai souvent du faire appel aux services du département de mécanique et d'électronique qui ont toujours su répondre à mes attentes, un savoir faire à ne pas négliger, merci à Brice en particulier.
Enfin, tout ce travail n'aurait pas été possible sans un encadrement aussi efficace. C'est pourquoi je remercie Alain Dereux, qui m'a donné envie dès la troisième année de Licence de poursuivre dans cette voie de par sa motivation débordante qui transparaissait lors de ces enseignements, cachée pour certains derrière un tableau noir plein d'équations, mais bien visible pour ceux qui savaient l'écouter. Mes derniers mots sont dédiés à Jean-Claude Weeber, qui a été bien plus qu'un professeur pour moi, le mot "juste" pourrait être défini par cet homme par qui j'ai eu la chance de rejoindre la Science.

Contents

General Introduction

This thesis work has been conducted in the framework of the European Project "Platon". The project Platon aims at the realization of the first Tb/s optical routing chip using plasmonic structures for optical interconnects inside wide electronic systems such as backplanes and blade servers. The fabrication and experimental characterization of standalone hybrid polymer-metal plasmonic 2×2 routing elements activated by thermo-optical effects represent a central objective of this project prior to an on-chip integration. The actual interconnects systems, purely based on electronics in most cases, have been optimized year after year to anticipate the needs in term of data processing (bandwidth and operation speed), following the growth of the virtual contents to be manipulated, provided by numerical networks and supercomputers. However, these side systems suffer from the same trend than every electronic system defined by the RC-delay when the components density is increased at its physical limits [1]. Optical interconnects have been propelled as the next technology to be developed in order to circumvent the microelectronic issues with a reduced power consumption and footprint. Among all the innovations required to replace electronic links by optical links, various devices have to be developed and next combined to create completely monolithic optical chips. The needs start from the simple transmission lines corresponding to optical waveguides, to more complex active components [2]. In this context, plasmonic can be viewed as a disruptive approach proposing new interconnect solutions relying on the specific properties of electromagnetic modes supported by metal-dielectric interfaces [3]. The intrinsic nature of plasmonic structures opens the possibility to create original devices allowing the simultaneous transmission of both electric and optical signals along a same material support [4, 5]. Recently, a specific kind of plasmonic waveguides known as Dielectric Loaded Surface Plasmon Polariton Waveguide (DLSPPW) has been suggested and demonstrated. These waveguides are comprised of dielectric ridges lying on a metal film and are able to confine electromagnetic fields at sub-micron dimensions at telecom wavelengths. One of the main interest of DLSPPWs is that the optical properties of the dielectric load can be engineered to match practical applications. For example, in the framework or this thesis, the thermo-optic coefficient of the dielectric load is the parameter of key interest. Indeed, in this work we specifically target the development of thermo-optical plasmonic devices from the design to the optical characterization. The

manuscript is divided into two parts. The first part is comprised of two chapters.

The very first chapter aims at giving an overview of the context of this work. After a brief review of the plasmonic waveguiding configurations reported so far, we focus on the polymer-metal DLSPP Waveguides that will be of primary interest all along this work. We present the state of the art in terms of modeling fabrication and characterization of these waveguides. The second chapter is dedicated to a deeper description of the physical properties of DLSPPWs. These properties will be discussed on the basis of the results of numerical tools and experimental characterization methods that will be operated in all the following of the manuscript. We describe the so-called Leakage Radiation Microscopy (LRM) at telecom wavelengths. This technique is particularly well-suited for the observation of leaky modes but is also subject to limitations that will be analyzed in details.

The second part of the manuscript is divided into three chapters all devoted to the discussion of the performances of thermally activated DLSPPW-based routers or switches. In the third chapter of the manuscript, we consider evanescently coupled plasmonic resonators that are activated by flowing a current through the metal film. The properties of these plasmonic resonators are analyzed on the basis of LRM images recorded at different temperatures. Although well-suited to demonstrate thermal-control of plasmonic resonators, LRM can only hardly be used to investigate the dynamic of the thermal response of the devices under consideration. Beyond Joule heating of the thermo-plasmonic devices, we first detail in the fourth chapter that photo-thermal heating is an approach of practical interest for the development of power effective routers. We also demonstrates, that photons in the context of photo-thermal activation can be replaced by plasmons, opening the way towards "all-plasmonic" components. In order to circumvent the LRM limitations in term of acquisition speed, we first show an original fiber-to-fiber characterization method. With this approach, a moderate response time in the range of several microseconds are measured and emphasizes the need for an improvement of the DLSPPW router designs. Such an improvement is specifically addressed in the fifth chapter with the description of an original configuration for DLSPPW relying on a dihedral geometry. These Dihedron waveguides are obtained by adding a vertical metal wall to a standard DLSPPW. In the basis of numerical modeling, we show that Dihedron DLSPPWs are of interest to minimize the footprint of DLSPPW components and to improve the thermo-optical response time of these devices. Finally, we demonstrate that these Dihedrons waveguides can be operated to achieve polarization conversion over short propagating distances.

PART I

State of art and introducing work

First Part Overview

This first part is comprised of two chapters describing the context of this thesis. We first give a brief overview of the topic of plasmonic waveguiding. Next we focus onto plasmonic components based on Dielectric Loaded Surface Plasmon Polariton Waveguides (DLSPPWs) that existed before the beginning of the thesis. This specific kind of plasmonic waveguide has been found of interest for the design of both passive and active components. The second chapter describes the physical properties of the DLSPPWs including new results extracted from momentum-space spectroscopy. These two chapters are necessary prior to a good understanding of the second part specifically dedicated to the study of thermally tuned DLSPPW components.

CHAPTER 1

Context

In this chapter, we propose an overview of the context of this work. During the last decade, there has been a tremendous amount of works dedicated to plasmonic waveguides. Plasmonic waveguides can be viewed as a disruptive approach for light waveguiding compared to standard refractive index based components. Plasmonic waveguides of all kind rely on the propagation of different plasmon modes along a metallic structure. The presence of such metallic structures offers the unique opportunity to investigate new physical effects based on the fact that the metal does not only play the role of waveguide core but can also be used for other purpose such as current flowing or strong light absorption at specific frequencies. The FP7 European Project Platon (2010-2013) in the context of which the results of this thesis have been obtained relies on this approach. In Platon, the metal structures support the plasmon mode but are also used as a heating electrodes. Prior to the review of plasmonic waveguiding structures reported in the literature so far, we give first a very brief description of the Platon project.

Platon is the first project which aims at realizing an optical routing architecture on chip, by combining Silicon photonics and Plasmonics as shown Figure 1.1. The final motherboard combines several features to obtain a complete 2×2 or 4×4 Tb/s hybrid router. Multiplexers will be used at the input of the chip, this is mandatory for using Wavelength Division Multiplexing (WDM) signals (optical data coming from multiple wavelength channels). Silicon-On-Insulator (SOI) photonic waveguides are used for low loss transmission across the chip. A plasmonic matrix for thermo-optical switching and routing operations based on Dielectric Loaded Surface Plasmon Polariton Waveguides (DLSPPWs) is implemented, and driven by electronic circuits. This kind of routers features compactness and very low power consumption. The complete platform is expected to be advantageous compared to the existing telecom optical routing devices in term of footprint and power consumption thanks to the plasmonic structures, all without suffering of high losses thanks to the hybridization between SOI and DLSPPWs.

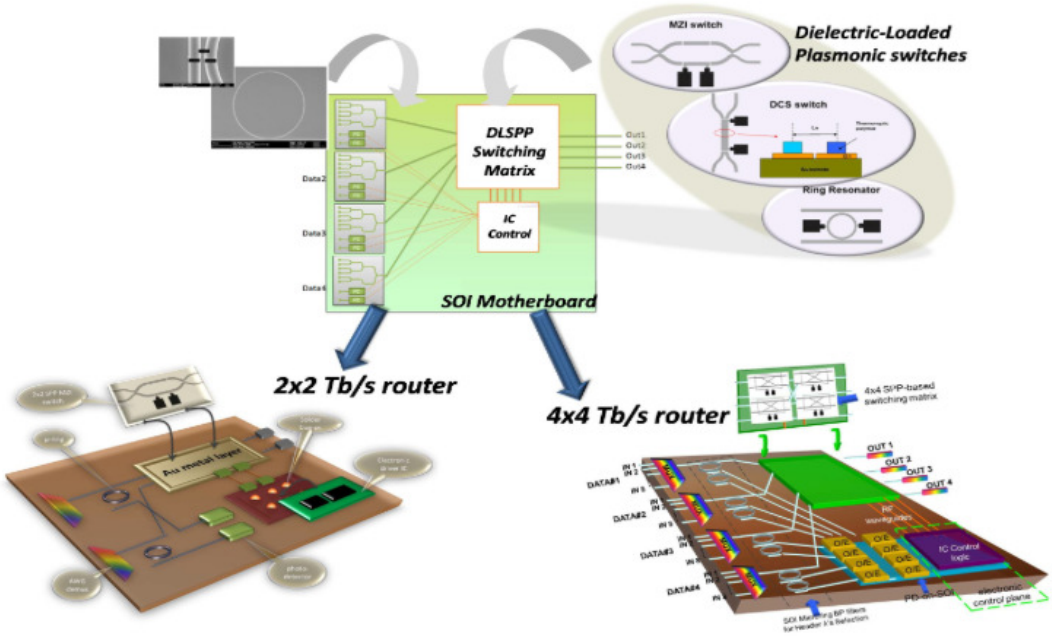

Figure 1.1: Platon project routing architecture.

The six European partners of this project are:

* Centre for Research and Technology Hellas / Informatics and Telematics Institute - CERTH/ITI (Greece)
* Fraunhofer-Gesellschaft zur Foerderung der Angewandten Forschung e.V. - Institut fuer Zuverlassigkeit und Mikrointegration - IZM (Germany)
* Syddansk Universitet - SDU (Denmark)
* Université de Bourgogne - UB (France)
* Institute of Communication and Computer Systems/National Technical University of Athens - ICCS/NTUA (Greece)
* Gesellschaft fuer Angewandte Mikro- und Optoelektronik mit beschrankter Haftung - AMO GmBH (Germany)

Coordinated by the Dr. Nikos Pleros from CERTH/ITI (Greece), all these groups worked jointly to realize this hybrid architecture.

The objectives of this project are numerous, but the efforts have been distributed on all the consortium partners. As far as this PhD work was concerned, the efforts have been principally focused on the plasmonic elements fabrication tasks and characterization of

standalone components. Their integration on the final chip was achieved by L. Markey also at UB.

1.1 Motivation: Carrying optical data on chip

Nowadays, the exchange of information needs to handle large amounts of data as fast as possible. The standard solution for telecommunication is placed in the C-band frequency/wavelength range, determined by the extreme efficiency of the low loss silica optical fibers [6, 7] network traveling all around the world with $\simeq 1\mathrm{dB/km}$ propagation losses. On the other side, information is not yet generated optically but electrically on chips and then converted to optical signal away from the chips. With the well known limitations of electrical interconnects in term of bandwidth due to the RC-latency [1], the possibilities of extremely large bandwidth offered by optical devices operating at high speed suggested a fast hybridization of the two domains. The challenges for the next decade are to create new technologies that will be first, compatible with the existing telecommunication network and second, compatible with the electronic machines that generate the data.

The need for optical interconnects platforms appears critical to link physically different data carriers network and high power computers and data servers which require to share informations continuously inside them [8]. Because the integrated optic domain is wide, optical fiber waveguides, and optical integrated circuits fields have been clearly identified as two different domains, even if they are really conceptually close to each other [2]. Moreover, the recent concept of cloud computing shows the motivations to make the computing tasks remote from the users even for the public audience. This orientates the future needs into extremely wide data carriers nowadays supported by fiber optics, and consequently improvements of the optical interconnect devices in term of footprint and power consumption [9].

Silicon-On-Insulator (SOI) waveguides have been proved to be one of the best solutions for carrying data on chip [10–14]. Such a waveguide supports low loss photonic modes (at least relatively to the size of a chip), with a diffraction limited light confinement $\simeq \lambda/2$ into the core of the waveguide (extremely important for high density integration), λ being the free space optical wavelength. SOI technology becomes the most promising way to integrate optical components with electronics on chip for two reasons. First the technological requirements in term of manufacturing and resolution have been already over-developed by the electronic industries for decades, and second the cost compared to the processing of III-V materials such as lithium niobate ($LiNbO_3$), Gallium arsenide ($GaAs$) ..., is really low thanks to the microelectronic economy. All the work performed previously in term of design of integrated optic waveguides made of III-V materials is still valid [15].

On the other hand, besides all the advantages offered by the Silicon photonics waveguides in term of confinement, loss, and compatibility with SOI interface, creating completely monolithic photonic systems can not be resolved by using only passive components. Many optical components need to be developed to realize an "all-optical"

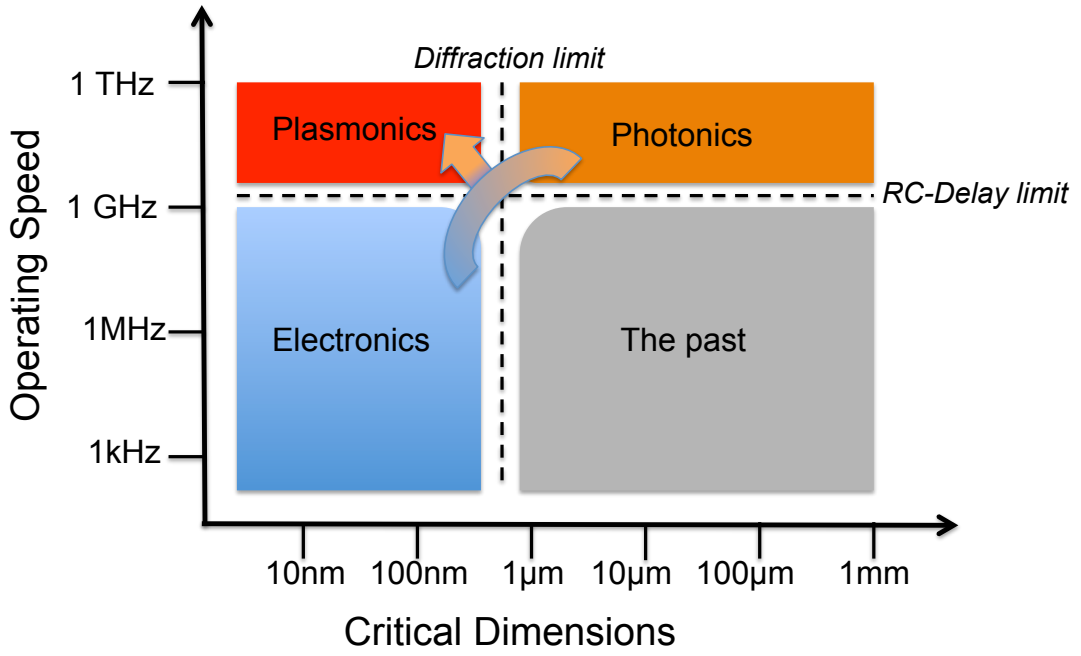

Figure 1.2: Technological boundaries (Inspired from [4]).

on-chip system. The new optical components have to be competitive with the microelectronics ones, and also in a first step compatible with them since the transition between the two technologies can not be performed before full photonic data processing becomes a mature technology.

Far away from the invention of revolutionary optical components, such as transistors that revolutionized the microelectronics, recent works on the Surface Plasmon Polaritons (SPPs) field [4, 5], reveal several passive and active structures compatible with the telecommunication requirements, in particular waveguides similar to Silicon photonic ones. The today popular Figure 1.2 broadly define Plasmonics relatively to Photonics and Electronics in term of dimensions and operating speed. From this point of view, Plasmonics appear to be a technological solution that will not be limited in term of bandwidth like Electronics, and also not limited in term of minimum size like Photonics. As we will discuss later, Plasmonic components are still at an early stage of development and a lot of compromises need to be dealt with before approaching the expected high performances. Recently, many projects aim at building a bridge between Electronics and Photonics using the duality of Plasmonics properties. Their main common idea is to take benefit on the mandatory presence of a metal (layer, wire, particles), that could be linked to electronic drivers, on top of what the enhancement of the electromagnetic field can be used to propagate or manipulate an optical signal. A short reminder of

different plasmonic components proposed so far is presented in the next section prior to the development of the active plasmonic components studied in this thesis.

1.2 Surface Plasmon Polariton Waveguides

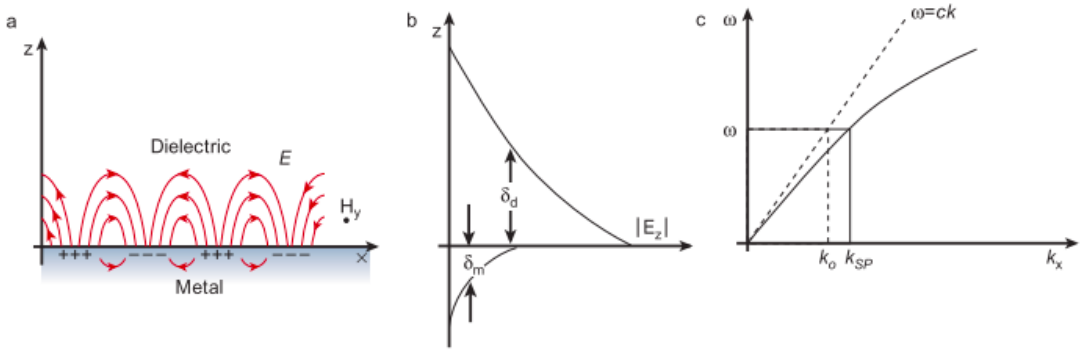

Figure 1.3: Surface plasmon basics (a) schematic view of the Surface Plasmon-Polariton coupling, (b) Field intensity on both metal-dielectric domains, (c) Dispersion relation. Reprinted by permission from Macmillan Publishers Ltd: Nature [16], copyright 2003.

The Figure 1.3 shows a schematic view of the physical nature of Surface Plasmon Polaritons supported by a planar interface. SPPs waves are electromagnetic waves existing at the interface separating a metal from a dielectric. The dielectric functions of the metal and the dielectric feature real parts of opposite signs. Free electrons of the metal can be excited collectively (i. e. all with the same polarization) forming a plasmon that can be coupled to photons at the interface with the dielectric, this coupling is called polariton [17]. The Figure 1.3 (a) shows the resulting Surface Plasmon Polariton wave, exponentially decaying perpendicular to the metal-dielectric interface [3], with a low penetration of the field inside the metal as depicted in Figure 1.3 (b). From the electromagnetic matching conditions at the interface, such a surface mode can be show to verify the following dispersion relation:

$$\varepsilon_1 k_z^{(2)} + \varepsilon_2 k_z^{(1)} = 0 \tag{1.1}$$

where $k_z^{(i)}$ and ε_i (i=1,2) represent the wave vector and the permittivities of the metal and the dielectric media respectively, which can be formulated explicitly as:

$$k_x = k_o \sqrt{\frac{\varepsilon_1 \varepsilon_2}{\varepsilon_1 + \varepsilon_2}} = k_{SPP}, \tag{1.2}$$

where k_{SPP} and $k_o = \frac{2\pi}{\lambda_o}$ are respectively the parallel component of the wave vector of the SPP mode and the module of the incident wave vector. This dispersion relation is plotted schematically on Figure 1.3(c), where we can see a momentum mismatch between the light line and the SPP dispersion curve at any frequency ω. The dielectric

function of the metal ε_2 is complex, so is k_{SPP}. The propagation length referring to the exponential damping of the SPP mode is then defined using it imaginary part as

$$L_{SPP} = \frac{1}{2\mathrm{Im}(k_{SPP})} = \frac{c}{\omega}\left(\frac{\varepsilon_2' + \varepsilon_1}{\varepsilon_2'\varepsilon_1}\right)^{\frac{3}{2}} \frac{(\varepsilon_2')^2}{\varepsilon_2''} \tag{1.3}$$

with the complex dielectric function of the metal $\varepsilon_2 = \varepsilon_2' + i\varepsilon_2''$.

One can note that L_{SPP} is proportional to the ratio $\frac{(\varepsilon_2')^2}{\varepsilon_2''}$, consequently for $\varepsilon_2' >> \varepsilon_2''$, several metals are of great interest at telecom wavelengths such as Gold ($\varepsilon_{\lambda=1550nm} = -131.7 + i12.6$) or Silver ($\varepsilon_{\lambda=1550nm} = -86.6 + i8.7$), the latter leading to hundreds of microns propagation length.

The enhancement of the field provided by such an interface mode is also of great interest since the field is naturally "confined" on both media which means that SPPs could be exploited at a sub-wavelength level, i. e. using nano-scale metal structures [16, 18]. The field enhancement can be either localized [19] (for example around a metallic nano-particle [20]) or delocalized (for example SPP waves propagating along thin metallic films [21]). In this second option, many configurations have been proposed to carry an optical signal. The recent report of *Han and Bozhevolnyi* [22] gives an interesting overview of the different possibilities existing for guiding radiation with SPPs that have been developed so far. From this quite exhaustive list, some configurations appear to be suitable for carrying data on chip at telecom wavelengths, in particular the three dimensional SPP waveguide using a dielectric ridge deposited onto a metal film and denoted after as DLSPPWs. Such a waveguide relies on index contrast effect that induces a lateral confinement of the SPP modes similar to standard photonic waveguides [23]. The underlying reasons for the choice of this particular plasmonic waveguide as a building block for active components in our project are detailed in the following sections.

1.2.1 2D Surface Plasmon Polariton waveguides

Starting from the general case of the metal-dielectric surface plasmons described above, many options exist to transform the planar SPP waves into guided SPP waves. Several important steps need to be expanded to show the way of thinking that converged to the 3D plasmonic waveguides chosen in our project.

Multi-Interface SPPs

As the electromagnetic field of an interface SPP is already shaped in one direction, the first approach proposed to guide SPP waves has been to combine two SPP interfaces placed in close proximity. This new three layers system could be a thin metal layer surrounded by dielectric or a thin dielectric layer surrounded by metals [24–27], respectively insulator-metal-insulator (IMI) and metal-insulator-metal (MIM) systems. Those two configurations, shown in Figure 1.4, offer many interesting characteristics by taking advantage of a third media to modify the physical constants of the original single

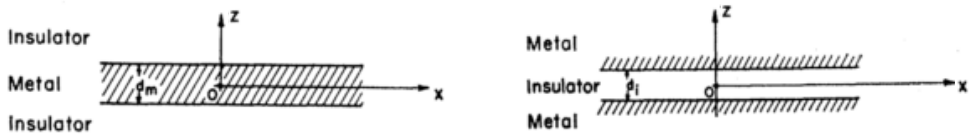

Figure 1.4: Schematic view of insulator-metal-insulator (IMI) (a) and metal-insulator-metal (MIM) (b). Reprinted figure with permission from [24]. Copyright 1969 by the American Physical Society.

interface modes (phase and attenuation constants).

Insulator-Metal-Insulator

Such a configuration supports different modes denoted SPP film modes, the film being the metal layer. This system could be represented for example by a metal film ($\varepsilon_2 = \varepsilon_m$) of thickness d_m, deposited onto a dielectric substrate (ε_1), glass or Silicon, then the superstrate third layer could be either air or any other dielectric (ε_3). The dispersion relation becomes:

$$\begin{aligned}(\varepsilon_2 k_z^{(1)} + \varepsilon_1 k_z^{(2)})(\varepsilon_3 k_z^{(2)} + \varepsilon_2 k_z^{(3)}) + \\ (\varepsilon_2 k_z^{(1)} - \varepsilon_1 k_z^{(2)})(\varepsilon_3 k_z^{(2)} - \varepsilon_2 k_z^{(3)}) \exp -(2k_z^{(2)} d_m) = 0\end{aligned} \tag{1.4}$$

If the metal layer is thick, i. e. typically more than 100 nm at telecom wavelengths, the SPP modes on each metal-dielectric interfaces do not interact with each other. For smaller thicknesses, the dispersion relation is verified for two kind of modes called symmetric and asymmetric modes, referring to the symmetry of the electric field distribution perpendicular to the interfaces, as shown Figure 1.5.

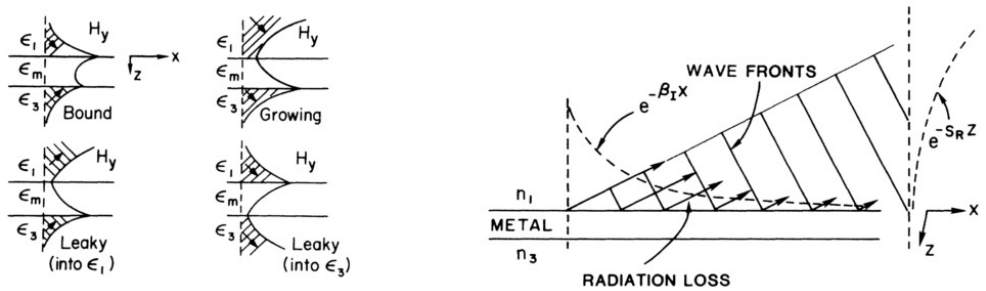

Figure 1.5: Schematic view of an asymmetric ($\varepsilon_1 \neq \varepsilon_3$) insulator-metal-insulator (IMI) field mode profiles and related radiation loss for leaky modes. Reprinted figure with permission from [25]. Copyright 1986 by the American Physical Society.

Radiative (leaky) and non-radiative solutions can be distinguished, depending on how the wave front is tilted and how the field intensity decays or grows in the dielectric medium. One can note that the coherent leakage of such SPP modes could be detected through the substrate, providing a powerful far-field imaging method that will be described later. Usually, when the system is not symmetric with respect to the metal layer (i. e. $\varepsilon_1 \neq \varepsilon_3$), the solutions are called Short-Range SPP modes [25], whereas for identical dielectric media ($\varepsilon_1 = \varepsilon_3$), the solutions are known as Long-Range SPP modes [28, 29], referring to their extended propagation length. Among the short range mode, the symmetric mode is peaked at the interface with the lowest refractive index medium and has the largest propagation constant.

Metal-Insulator-Metal

For the MIM case, one particular mode has to be highlighted, the Gap SPP mode [30], that exists whatever the thickness d_i of a dielectric sandwiched between two identical metals (see Figure 1.4). Such a mode possesses a very high confinement and has been used as basic concept for plasmonic slot waveguides structures.

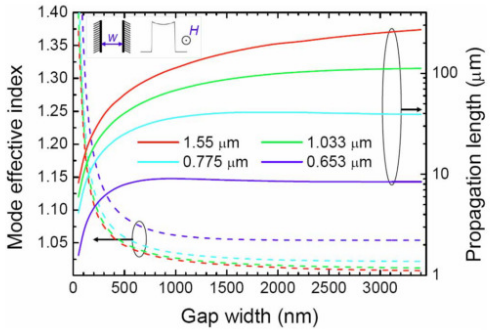

Figure 1.6: Gap SPP mode properties as a function of the dielectric thickness (Reprinted with permission from [31]).

Figure 1.6 shows the effect of the dielectric thickness (here air) on the effective index and propagation length of a Gap SPP mode. As the gap between the two metals is reduced, the effective index increases and the propagation length decreases, but without cutoff. This particularity could be of great interest since the spacial extent of such a mode can reach deep sub-wavelength confinement ($\sim \lambda/15$) at the expense however of short propagation length in the range of 1 μm. At telecom wavelengths, 100 μm propagation length can be reached with $\lambda/2$ confinement.

Summary

Triple layer systems are of interest to manipulate the evanescent field decay of the plasmon modes. Confinement and propagation length of both IMI and MIM modes are inevitably linked, but can be precisely controlled compared to the single interface SPP modes, specifically by using the appropriate layer thickness. However those two

primary systems do not offer any lateral confinement (along the out of plane y direction in Figure 1.4). Nevertheless, IMI and MIM are the two basic configurations that are further used for the design of plasmonic waveguides featuring a lateral confinement, as will be discussed in the next section.

1.2.2 3D Surface Plasmon Polariton waveguides with lateral confinement

By modifying partially the geometry of IMIs and MIMs configurations, many 3D waveguiding structures have been highlighted, from nano-wires for IMIs [32, 33], to channel SPPs for MIMs [34]. We review in the following some of the 3D plasmonic waveguides proposed so far.

Metal stripe waveguides

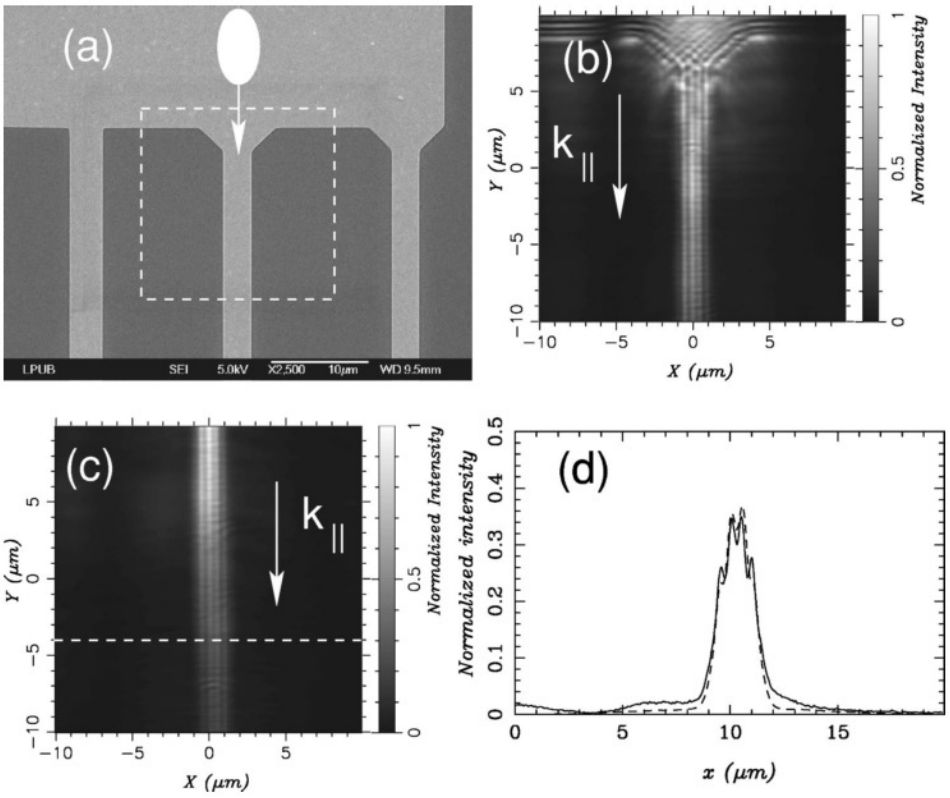

Figure 1.7: (a) SEM view of metal Stripes plasmonic waveguides, (b-c) PSTM images of metal stripes waveguides, (d) Intensity measured along a metal stripe cross section. Reprinted figure with permission from [35]. Copyright 2003 by the American Physical Society.

Given that the electromagnetic field of SPP waves is bounded to the metal layer(s), reducing the extended thin metallic film of IMIs to a finite width stripe would obviously

enforce a lateral confinement. This approach has motivated several works that predicted LR-SPP modes for metal stripes either embedded in an uniform dielectric medium [36] or SR-SPP supported by a substrate with a refractive index larger than the superstrate's one [37]. The first observation of metal stripe waveguides has been performed onto glass substrates [38, 39], leading to a small propagation length of the SPP because of the difference of index between the air superstrate and the glass substrate.

Using Scanning Photon Tunneling Microscopy (PSTM) Figure 1.7 (b) and (c), the effect of the width of the metal stripe on the SPP mode has been investigated [35]. The coupling to the SPP mode has been realized by the Attenuated Total Reflexion (ATR) method, also known as Kretschmann-Reather configuration [3]. This excitation method will be used in chapter 4.

As metal stripes SPP modes can lead to tens of micrometers propagation length [38], such plasmonic waveguides have been proposed as a possible basic elements for integrated optic circuitry [40]. Nevertheless, because of the small effective index of such symmetric SPP modes, metal stripes waveguides cannot exhibit strong lateral confinement, thus an efficient coupling with a rectangular photonic waveguide could be quite challenging.

V-groove shape

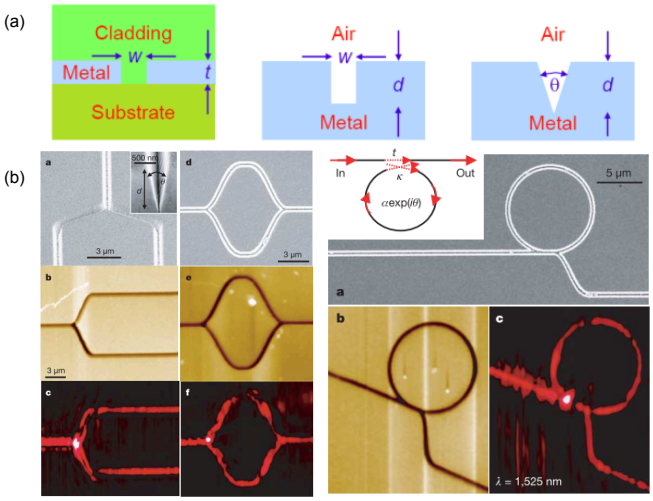

Figure 1.8: (a) Three CPP components designs, (b) V-groove components. Adapted with permission from [31] and reprinted by permission from Macmillan Publishers Ltd: Nature [41], copyright 2006.

The Figure 1.8 (a) shows different waveguide structures based on the MIM configuration [31], the third one being known as V-groove waveguide, using the particular anisotropy of the shape of the groove to confine the SPP inside the dielectric non-uniform gap. This shape had been introduced earlier as Channel polaritons [34].

This configuration has been mainly investigated because it combines several important

features for integrated optics. In fact, V-groove provides a great confinement ratio ($\lambda/5$) coupled to relatively good propagation length (tens of microns), with small bending losses and mono-mode operation [41]. Thus, many passive optical components have been demonstrated using V-groove waveguides (Mach-Zehnders, ring resonators) as shown in the Figure 1.8 demonstrating the practical interest of such a configuration for optical interconnects. However, this configuration is far from being cost effective as it is implemented into several micrometers thick films and features a very short wedge not feasible by UV lithography but by focused ion beam milling. Moreover, only passive components relying on this configuration have been reported up to now.

3D slot waveguides

Derived from the MIM configuration, slots waveguides using Gap SPP modes have been so far proposed.

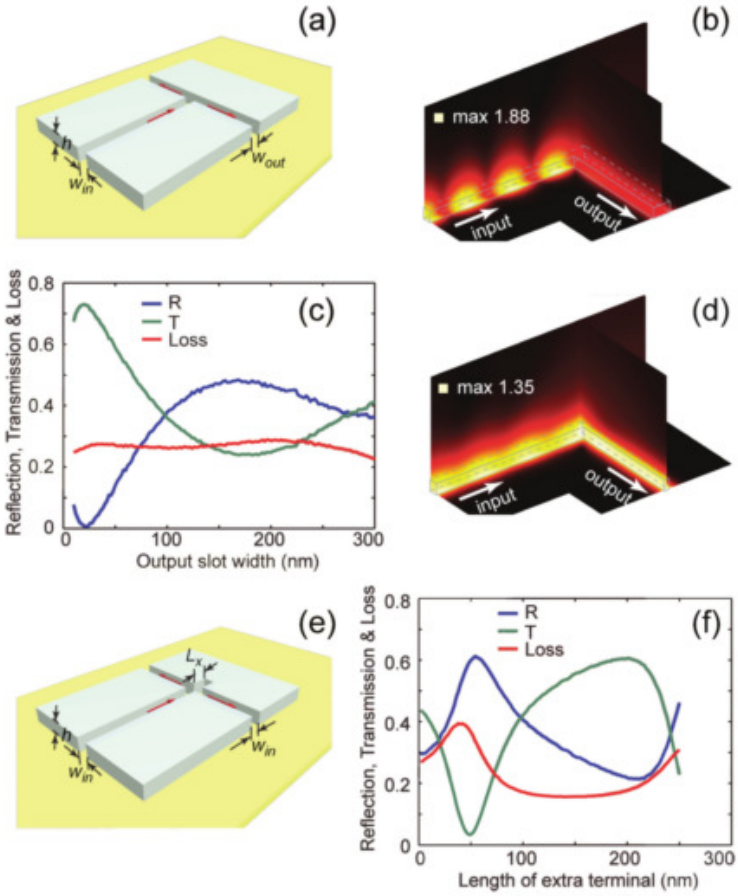

Figure 1.9: (a) and (e) Slot waveguide schematic views, (b) and (d) Respective field map representations, (c) and (f) Corresponding reflection and transmission curves. Reprinted with permission from [42].

MIM systems provide a high confinement without cutoff [24] that is used in the case of slot waveguides. This concept is first to use the dielectric gap as the waveguide itself instead of modifying the three layers shape as it was done for V-groove waveguides [43]. The out-of-plane confinement is achieved by surrounding this system with homogeneous dielectric [44].

Figure 1.9 shows a schematic view of this kind of waveguide together with typical computed transmission curves for a right angle device [42]. The overall concept is of great interest since the cross section of the waveguide is just slightly smaller than SOI strip waveguides ($w \times t = 100 \times 80$ nm), thus an efficient coupling between the two technologies has been recently achieved [45], in a fully CMOS-compatible process. Nevertheless, only passive waveguiding structures have been reported until now.

Dielectric Loaded Surface Plasmon Polariton Waveguides

This configuration is of primary interest in this work. Based on the well-understood conventional integrated optics [6, 7, 23], a new 3D waveguide configuration has been proposed, relying on a core refractive index larger than the superstrate index and denoted hereafter as Dielectric Loaded Surface Plasmon Polariton Waveguide (DLSPPW) [46].

A typical waveguide is depicted in Figure 1.10. The waveguiding structure is comprised of a dielectric ridge deposited onto an optically opaque metal layer. The mode propagating inside the dielectric ridge is optically separated by the substrate by metal

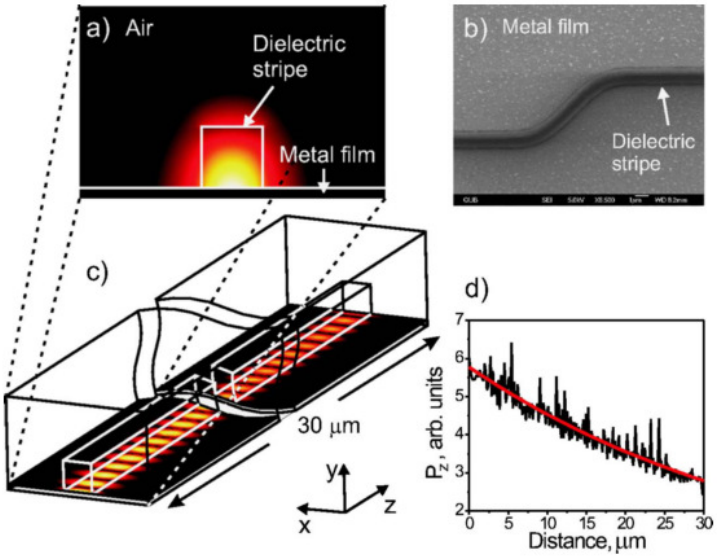

Figure 1.10: DLSPPW waveguide concept (a) Electric field map, (b) SEM image, (c) 3D schematic view, (d) Exponential decay representation. Reprinted with permission from [47]. Copyright 2007 , American Institute of Physics.

layer with a thickness around $\simeq 100\text{nm}$, allowing the use of material for the dielectric ridge with a refractive index smaller than the refractive index of the substrate on which the metal is deposited. Although the lateral confinement is based on the index contrast resulting from the difference of dielectric-metal and the air-metal SPP mode, the DLSPPW mode is vertically confined due to its plasmonic nature, and therefore suffers ohmic losses. Typical parameters at telecom wavelengths of almost $L_{SPP} = 45\mu\text{m}$ decay length and 500nm to 600nm square cross section for mono-mode operation have been demonstrated [47, 48]. Such a configuration offers many features compatible with an hybridization with SOI (cross-section and free choice of the substrate), and the possibilities to introduce active properties as we will see in the following section.

Summary

Many other plasmonic waveguide structures have been also reported, such as metallic nano-particles chains [49, 50], or metal wedges [51]. But in all cases, the critical issue is to find a good compromise between confinement and losses. This general trend of the plasmonic waveguiding topic has been considered following two approaches. Many works aimed at finding special waveguide shapes to provide the best propagation length possible, in general at the expense of confinement (for example with IMIs $L_{SPP} \nearrow$, $k'_{SPP} \searrow$). On the other hand, the SPP waves can feature very high effective index, so many works have been directed to reach the highest confinement possible of these electromagnetic waves (for example with MIMs $k'_{SPP} \nearrow$, $L_{SPP} \searrow$). Those two separated ways of thinking clearly show that whatever the approach for SPP waveguiding is, one has to deal with the compromise between field confinement and propagation losses and possibly with other constraint such as efficient connection of the SPP waveguide to other optical devices. In this respect, the DLSPPW configuration has been chosen because it appears to be a good compromise between confinement and loss, and the shape (cross-section) of the waveguide being close to the ones of typical SOI strip waveguide [52], it is expected that merging both technologies would be easier than for most of other possible plasmonic guiding structures. A more detailed overview on the passive and active components based on DLSPPWs is given below.

1.3 DLSPPW-based components

1.3.1 Passive telecom components based on DLSPPWs

DLSPPWs have been first demonstrated by *Steinberger et al.* using SiO_2 stripes on gold films, including bend structures [46] and then by *Reinhardt et al* where dielectric waveguide and Y-splitter fabricated by two-photon polymerization have been shown [53]. These early first steps have been extensively studied during the following years, leading to numerous optimizations obtained by various calculations and experiments.

DLSPPW optimization by simulation

In 2007, a complete and accurate modelisation of the DLSPPW configuration has been performed by *Holmgaard and Bozhevolnyi* [48] using Effective-Index Method

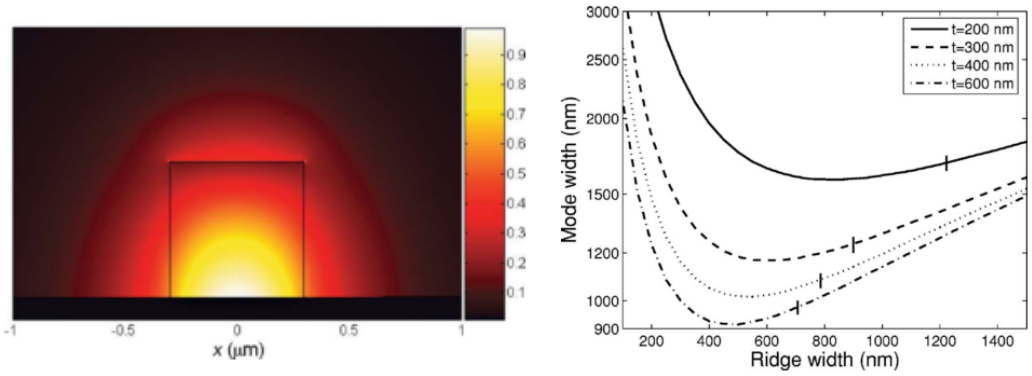

Figure 1.11: Lateral confinement of a DLSPPW mode (a) Electrical field map distribution, (b) Mode width in function of the dielectric ridge width. Reprinted figure with permission from [48]. Copyright 2007 by the American Physical Society.

(EIM). This approach gives a good starting point to fabricate single mode DLSPPW based components at telecom wavelength. In particular, the lateral confinement of the DLSPPW mode as a function of the geometric parameters of the dielectric ridge has been fully established (see Figure 1.11 field map (a) and mode width calculations (b)). A second numerical work has been performed the same year by *Krasavin and Zayats* using a full three-dimensional Finite Element Method (FEM) modeling [47]. They demonstrate the feasibility of using DLSPP waveguide for efficient telecom passive components, such as directional couplers, bend waveguides and Y-splitters.

Maturation of DLSPPW-based components

After their first experimental demonstration in 2006, *Steinberger et al.* continued to develop dielectric stripes plasmonic waveguides using SiO_2 [54], based on *Krasavin and Zayats* simulations [47]. Even if this work has been performed outside of the C-Band, i. e. at $\lambda = 800nm$, this is the first experimental work that extracts *in situ* the performances of DLSPPW-based components. Transmission as a function of a radius of curvature for bend DLSPPWs and coupling length of directional couplers have been extracted from the experimental images. Practically, the authors used both near field microscopy (Photon Scanning Tunneling Microscope) and Leakage Radiation Microscopy (LRM), taking advantage of the intrinsic losses of the devices to collect images of modal propagation through the thin metal film. This second technique will be developed further in the chapter 2. Figure 1.12 displays some of the experimental work performed by *Steinberger et al.* for a DLSPPW directional coupler made of SiO_2.

Momentum-space observations

A similar work by *Massenot et al.* introduced two novelties by using Polymer (polymethylmethacrylate) (PMMA)) instead of SiO_2 and also by observing the conjugated plane of a DLSPPW mode [55], obtained by imaging the back focal plane of a LRM

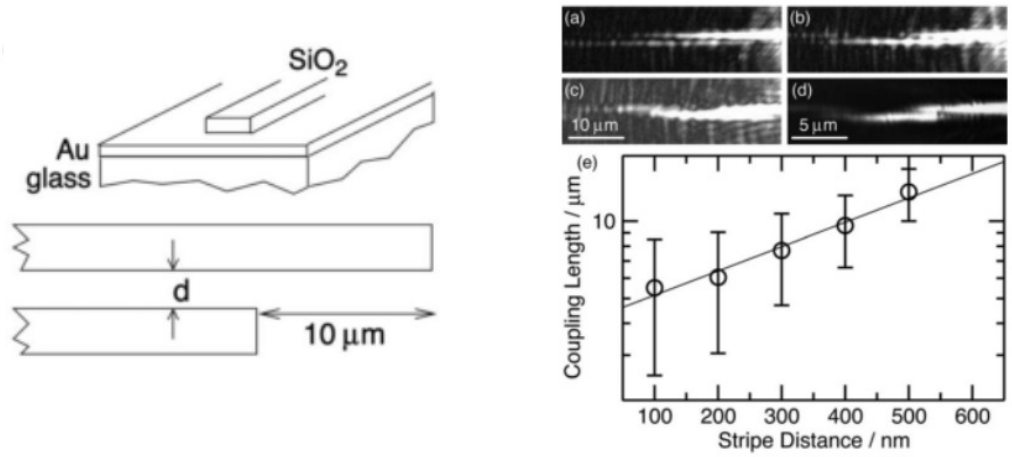

Figure 1.12: (a) Schematic view of a DLSPPW made of SiO_2 and DLSPPW directional coupler observation (b) by near field spectroscopy and Leakage Radiation Microscopy, (c) Coupling length in function of the gap d. Reprinted with permission from [54]. Copyright 2007, American Institute of Physics.

setup, as introduced a year before by *Drezet et al.* [56].

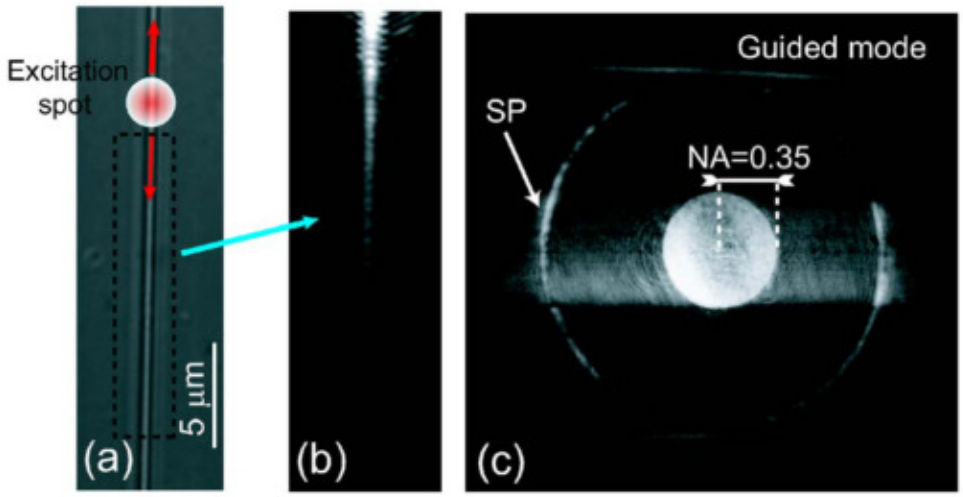

Figure 1.13: k-space visualization of a DLSPPW loaded with PMMA (a) Optical image, (b) LRM direct plane image, (c) LRM Fourier plane image. Reprinted with permission from [55]. Copyright 2007, American Institute of Physics.

The Fourier plane images allowed to extract directly both real part and imaginary part of the mode effective index, as shown on Figure 1.13 (b) and (c), where both direct plane and Fourier plane are displayed respectively. This method will be detailed

in chapter 2.

S-bend and Splitters made of Polymer

Experimental results on DLSPPW made of polymer at telecom wavelength have been reported in 2008 [57, 58]. The results confirmed the good confinement of the mode for the geometry previously investigated numerically [47, 48] and quite low propagation losses even in the case of S-bend structures and splitters [59].

Improving the excitation of DLSPPWs have been reported using triangular tappers to increase the coupling efficiency to the guided mode [58]. An efficient excitation of the DLSPPWs is highly desirable as it determines the quality of the experimental images. In addition, the reduction of coupling losses for true data-com component testing is mandatory since the SPP modes are more lossy when compared to the standard integrated optic components.

Wavelength filter based on DLSPPWs

Three kinds of filtering components based on the DLSPPW have been reported by *Holmgaard et al.*, the Waveguide Ring Resonator (WRR) [60, 61], the in-line Bragg Grating [62] and the Directional Couplers [63, 64] (detailed in chapter 2). These components work as wavelength filters, as illustrated in Figure 1.14 for the case of WRRs.

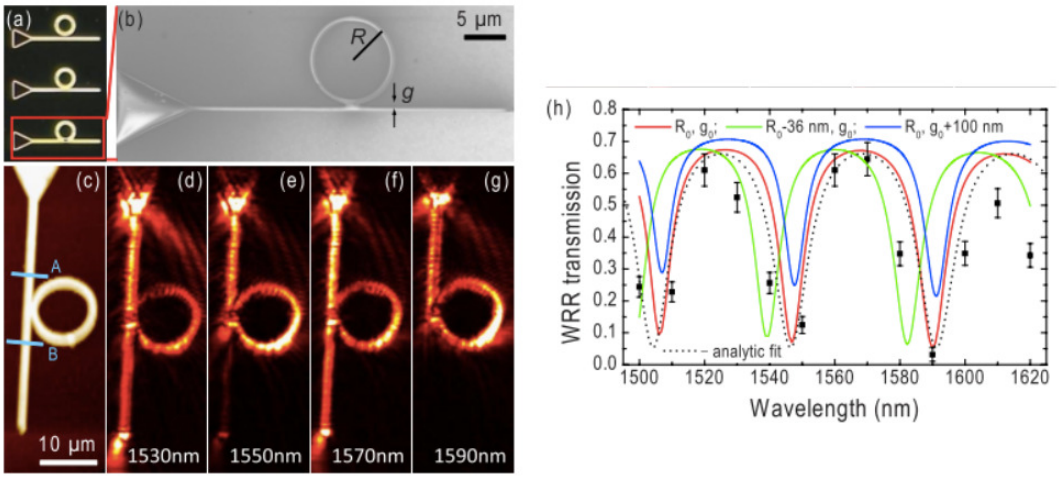

Figure 1.14: First DLSPPW ring resonator made of PMMA (a) SEM image and near field spectroscopy images at different wavelength, (b) Filtering efficiency for different geometrical parameters. Reprinted with permission from [62]. Copyright 2009, American Institute of Physics.

WRR filters rely on the resonance of the ring resonator evanescently coupled to the straight bus waveguide. Depending on the wavelength, the field after a round trip within the resonator can be either in phase or out-of-phase with respect to the field of the waveguide. This structure will be extensively discussed in chapter 3, with work a

dedicated on geometrical optimizations for thermo-optical filtering.

Alternatively, Micro-disk resonators have been proposed [65] by means of vectorial 3D-FEM simulations. The conclusions highlight high quality factors compared to WRR filter of same footprint, in particular for small radii.

DLSPPW integration

Finally, important results for the integration of the DLSPPW components using PMMA as loading material into SOI circuitry have been reported.

First, even if the confinement of a DLSPPW mode supported by a thin metal layer is imposed by the lateral width of the dielectric ridges, it has been demonstrated that this thin metal film must have a minimum width to prevent leakage of the DLSPPW mode into the substrate. A typical value of $w_{\min} = 1.75\mu m$ has been estimated for a dielectric square cross-section of $600\ nm$ according to *Grandidier et al.* [66]. It is worth to note that such a cutoff width has a direct impact onto the footprint of the DLSPPWs components, possible solutions for minimizing this footprint will be given in the chapter 5 through the introduction of a new design.

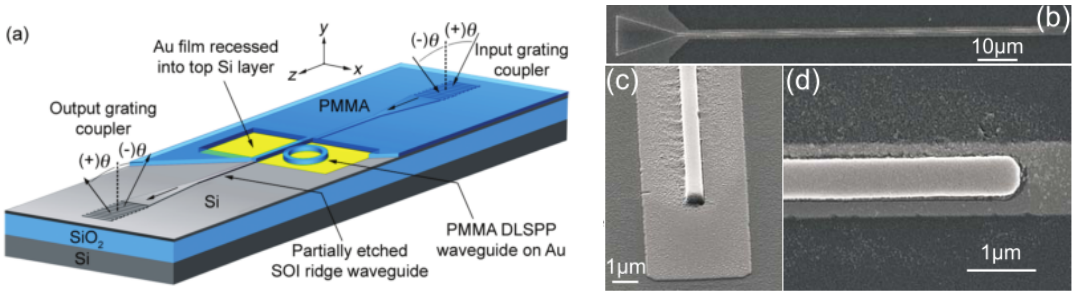

Figure 1.15: (a) DLSPPW to Silicon waveguides (Reprinted with permission from [67]. Copyright 2010 American Chemical Society), (b) DLSPPW on a finite width metal strip (Reprinted with permission from [66]. Copyright 2010, American Institute of Physics).

Second, the coupling between DLSPPW and Silicon photonics waveguides has been demonstrated by the group of *Atwater* [67] in 2010. This work demonstrates an efficient coupling of approximately $1dB$ loss per SOI-DLSPPW interface. The characterization of a DLSPPW WRR structure coupled to Silicon waveguides has also been reported, showing the practical interest of the SOI-to-Plasmonic hybridization, at the early stage of this thesis.

Other noticeable results

- Various computation methods such as the differential method [68], and a density of state based mode solver [69] have been applied to DLSPPWs.
- 3D-FEM (Finite Elements Method) [70] has applied to curved DLSPP waveguides and has shown that the displacement of the field outside of the waveguide for small radius induces bending losses in addition to the intrinsic losses.
- Achieving an efficient excitation to DLSPPW structures using Fiber-to-Fiber

coupling has been shown, also known as end-fire coupling [71–73]. An other Fiber-to-Fiber coupling method using dielectric grating couplers will be demonstrated chapter 4, making possible the telecom characterization of standalone DLSPPW components and the measure of dynamic thermal process.

1.3.2 Active telecom components based on DLSPPWs

It has been established that DLSPPWs are suitable for the design of passive components at the telecom wavelengths. Several numerical tools have been adapted/developed to predict precisely the expected performances of such DLSPPW-based devices. In this direction, only a few active components have been fabricated and studied experimentally.

The term of active component is used in the following to denote a component which is controlled by an external signal whatever the physical nature of this signal (electrical, optical, ...).

DLSPPW components with gain medium

Following their previous model based on FEM, *Krasavin and Zayats* proposed a solution to reduce the intrinsic Ohmic losses of a DLSPPW mode using active material as the loading material (i. e. replacing the dielectric ridge with a material that provides an optical gain) [74, 75]. This early work not only shows a good way to compensate the losses, but it also proposes to take advantage of the active media to modulate a DLSPPW mode. Indeed, if an active media is used for one of the two arms of a MZI structure, it gives the possibility to induce a change of the refractive index by illuminating the active arm. The phase difference between the two arms can be controlled, which modulates the output signal optically.

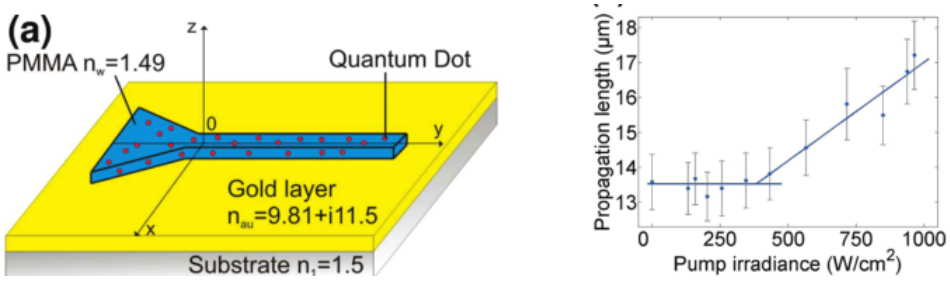

Figure 1.16: (a) Schematic view of Q-dots doped DLSPPW, (b) Propagation length in function of the pump power (Adapted from [76]).

Obtaining gain media can be achieved by doping the dielectric ridges with any optical emitters, such as quantum dots [76–80]. DLSPPWs made of PMMA doped with quantum dots show a loss compensation around 30% at telecom wavelength, as shown in Figure 1.16. This experimental result has been confirmed on the basis of numerical modeling relying on a density of state mode solver.

Thermo-optic DLSPPW components

This last topic is of key interest for this thesis since the routing function of the Platon chip architecture is based on the thermo-optic control of DLSPPW structures.

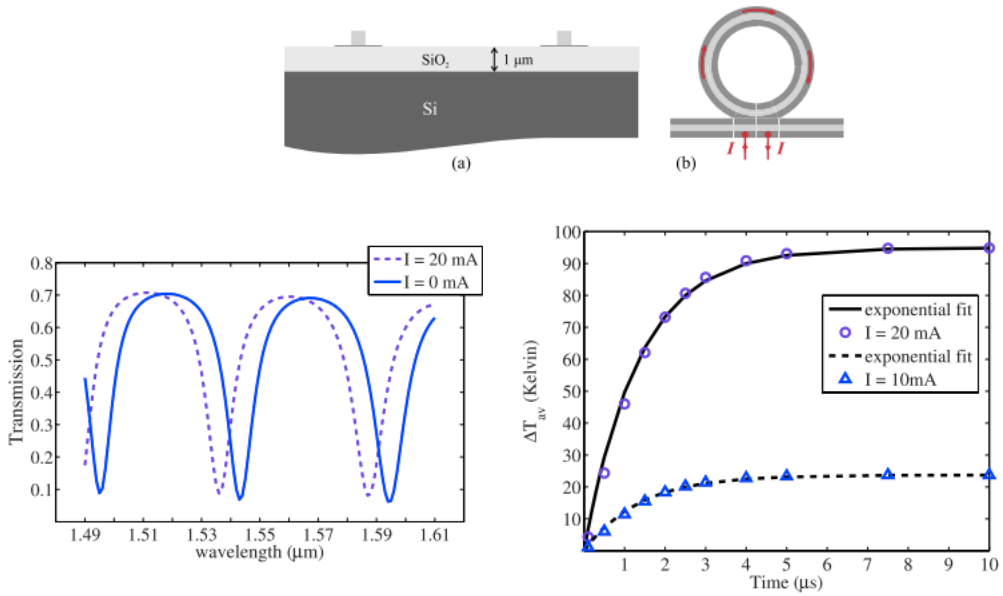

Figure 1.17: (a) Schematic view of a PMMA loaded SPP WRR, (b) Transmission curve for two temperature states, (c) Time response of a thermally-tuned DLSPPW filter. Reprinted with permission from [81]. Copyright 2009, American Institute of Physics.

Based on the wavelength selective DLSPPW ring resonator introduced earlier [60], 3D FEM calculations show that such a filter could be activated thermo-optically, provided that the geometry of the resonator has been optimized [81]. An electric current flowing through the metal stripe (fig. 1.17(a)), can shift the resonance peak of the DLSPPW filter(fig. 1.17(b)). This phase shift is caused by the Joule heating of the metal which rises the temperature of the overlying polymer. The Thermo-Optical Coefficient (TOC) determines the amplitude of the shift for a given temperature increase. In the example of fig. 1.17(c), the TOC $\frac{\partial n}{\partial T} = -1.0^{-4}\ K^{-1}$ of PMMA polymer is moderate. The temperature change induces a modification of the optical index on the polymer, leading to a change of the effective index of the mode propagating on the WRR, with a time response expected close to $1\mu s$ (fig. 1.17(c)).

Using PMMA as loading material, the first thermo-optically driven DLSPPW devices have been demonstrated experimentally by *Gosciniak et al.* in 2010 [82]. By using the end-fire coupling shown earlier, thermo-optical tuning of Mach-Zehnders (fig. 1.18), WRRs and Directional Couplers featuring 20% modulation depth was achieved. Those results

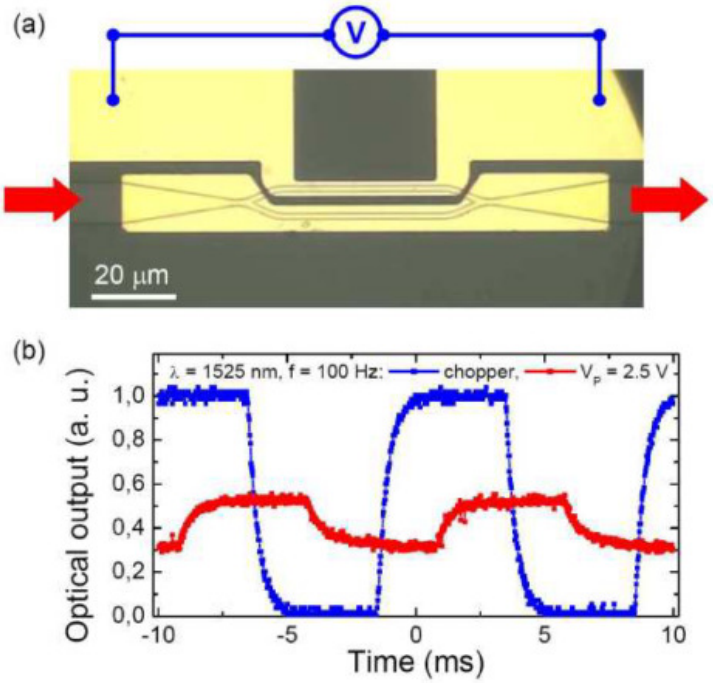

Figure 1.18: (a) PMMA DLSPPW MZI optical image. (b) Corresponding thermo-optical modulation generated electrically (Adapted with permission from [82]).

confirm that thermo-optic DLSPPW components work, nevertheless some optimizations of design could clearly improve the performances as proposed for the WRR [81]. Those optimizations require fine manufacturing process to obtain mono-mode waveguides and sub-micron gap control for WRR. It was finally suggested that other materials could be used to improve the performances (higher TOC polymers...).

1.4 Conclusion

In summary, starting from the basic properties of 2D IMI and MIM SPP waveguides, we have described the properties of the main SPP waveguides featuring a good compromise between field confinement and losses. In this context, DLSPPW-based structures play an important role as they fulfill many requirements needed to design efficient thermo-optical active components. In particular, DLSPPWs support guided mode with a sub-micron field confinement compatible with typical SOI waveguides cross-sections. In addition, DLSPPW modes feature reasonable propagation distances of several tenth of microns at telecom frequencies. By using the know-how on DLSPPW established for passive components, we address in this thesis the implementation of thermo-optically controlled routers for high bit rate transmission. In this respect, the work and the results discussed hereafter contribute to make plasmonic more practical for datacom applications.

CHAPTER 2

Advanced analysis of passive DLSPPWs

Since 2006, DLSPPW based passive components have been well developed, and the performances at the telecom wavelengths optimized [47, 48, 58, 83]. Both numerical and experimental tools have evolved sufficiently to predict and then verify over a short period of time the physical properties of such components. In particular, the advent of Electron Beam Lithography (EBL) used to shape the polymer ridges of DLSPPWs [46, 83], provides a good flexibility in term of fabrication for fast prototyping. Moreover, standard near field microscopy initially used to investigate such confined fields [84], is nowadays well complemented by the so called Leakage Radiation Microscopy (LRM) method, that is well suited to visualize propagation of DLSPPW modes [54, 58, 83], and to extract their effective index through a wave-vector distribution imaging [83, 85–87].

This chapter gives more insight into the physical properties of passive DLSPPW structures that will be used all along this thesis work. We will first remind the properties of a single mode DLSPPW and expose briefly the fabrication and characterization process based on EBL and LRM, techniques used for the study of both passive DLSPPW components in this chapter and then for thermo-optical routers in chapter 3 and chapter 4. An advanced analysis of two basic DLSPPW components (linear coupler and bent waveguide) by means of momentum space spectroscopy images, i. e. by recording the back focal plane on the LRM setup is then discussed. This analysis will demonstrate the added value of the Fourier plane imaging and also its limitations. The understanding of the passive DLSPPW properties exposed in this chapter are necessary prior to the presentation of the thermo-optical DLSPPW-based components detailed on the second part.

2.1 Physical properties of DLSPPWs

A schematic view of a DLSPPW is shown in Figure 2.1 (a). A dielectric ridge, in general a polymer, is fabricated onto a thin metal film. For an almost square cross section of around $w \times t = 600 \times 500$ nm, the structure support a quasi-TM mode at telecom wavelengths. This mode is well confined into the dielectric, as shown in Figure 2.1 (b). This confinement is due to the contrast of effective index between SPP mode supported

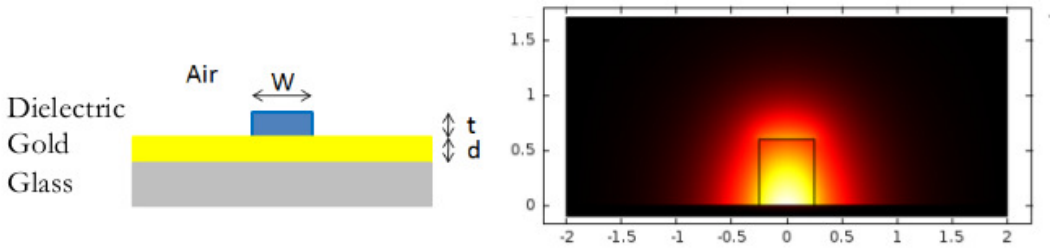

Figure 2.1: (a) Schematic view of a basic PMMA DLSPPW cross section of a width w=600 nm and thickness t=500 nm onto a 60 nm thick gold film. (b) Corresponding Electric field map of the DLSPPW mode at λ=1550 nm ($n_{PMMA} = 1.489$, $n_{Au} = 0.55+i11.5$, $n_{substrate} = 1.5$).

by the metal/dielectric interface and the metal/air interface. A DLSPPW mode can be defined by a complex effective index N_{eff} such as:

$$N_{eff} = \frac{\beta'}{k_o} + i\frac{\beta''}{k_o} = n'_{eff} + in''_{eff} \tag{2.1}$$

where the real part β' refers to the phase constant of the mode, and the imaginary part β'' refers to the attenuation constant related to the propagation length by $L_{spp} = \frac{1}{2\beta''}$.

Several methods exist to calculate exactly or approximately this complex index values:

- Differential method [88]
- Green function method
- Effective Index Method (EIM) [89]
- Finite Element Method (FEM)...

The Differential method and Green function method returns exact solutions of the Maxwell's equations but are more time consuming compared to EIM and FEM. However, the approximate methods give sufficiently accurate results for DLSPPWs, as documented in the ref. [48, 74, 81].

A mode solver based on FEM would find instantly the possible modes supported by a DLSPPW, depending on the geometric parameters (and also providing an educated guess of effective index), as shown in Figure 2.1 (b), where we obtain n_{eff}=1.260 and L_{SPP}=41.6 µm using the commercial FEM mode solver COMSOL. Finding the effective index using the Differential method is not immediate, and requires in two steps:

- Calculation of the reflectivity spectra using plane waves gives n_{eff},
- Calculation of the propagation length L_{SPP} using a Gaussian beam illumination.

This method being based on a plane-wave expansion of the electromagnetic field, it is well adapted to investigate the optical properties of gratings. In our case, the non-periodic DLSPPW is approached using a so-called "supercell" with a period sufficiently large to prevent significant coupling between two adjacent waveguides. We typically used a period of about 6 µm.

Differential method applied to DLSPPWs

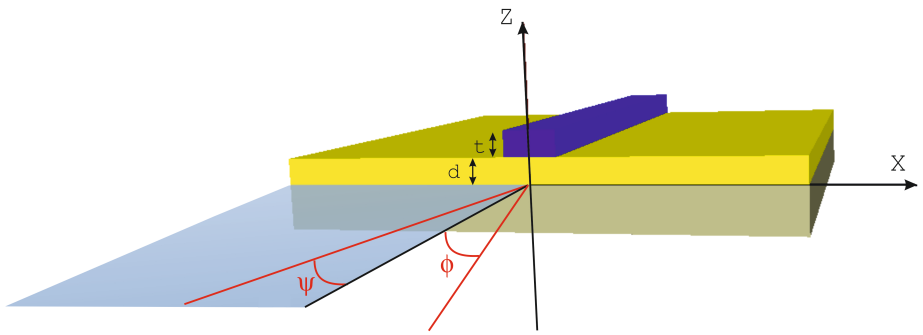

Figure 2.2: 3D Schematic view of the DLSPPW configuration used for the reflectivity calculation

Reflectivity spectra: A polymer ridge of width w, height t is illuminated by a TM plane wave under an incident angle ϕ (Fig. 2.2). By sweeping the incident angle ϕ, the reflectivity spectra of such a configuration is recorded, showing a local minimum related to the coupling between the incident plane wave and the DLSPPW modes, as for the well known Attenuated Total Reflection method for basic SPP waves [3].

The excitation angle of the DLSPPW mode θ_{SPP} is then related to the real part of the effective index by:

$$n'_{eff} k_o = \beta' = n_1 k_o \sin\theta_{SPP} \tag{2.2}$$

where n_1 is the index of the substrate.

The Figure 2.3 depicts an example of reflectivity spectra of a DLSPPW with the geometric parameters w=600 nm, t=500 nm and d=60 nm. We found $n'_{eff} = 1.5 * \sin(57.36) = 1.263$, which is in good agreement with the result obtained by FEM. For the thermo-optic components studied on the second part of this thesis, the routing functionalities will be obtained by a change of this phase constant provided by dielectric ridges sensitive to the temperature changes (through by their Thermo-Optical Coefficient (TOC)).

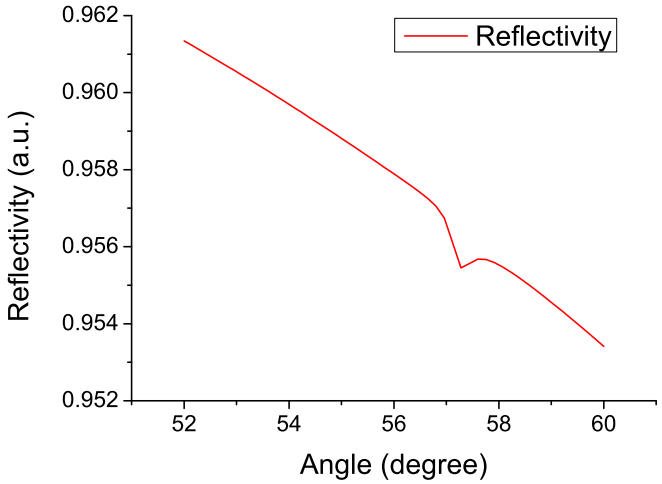

Figure 2.3: Reflectivity spectra of a DLSPPW at λ=1550 nm obtained with the differential method for the DLSPPW shown in Figure 2.2

Damping distance: A two dimensional Gaussian beam is illuminating locally the DLSPPW structure at an average angle of incidence corresponding to the dip of the reflectivity spectrum shown in Figure 2.3. Then we can extract the intensity profile of the mode along the direction of propagation Figure 2.4 (a). This profile can be fit using an exponential law to obtain the propagation length, as shown Figure 2.4 (b).

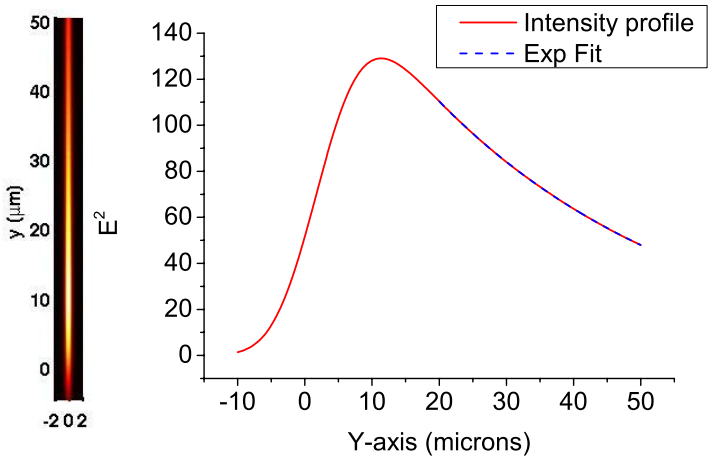

Figure 2.4: Intensity map (a) and profile (b) of a DLSPPW obtained by Differential method

One can note that the fitting has to be performed away from the incident Gaussian beam to avoid any impact of the Gaussian beam shape on the decay calculation. We found L_{SPP}=38.9 µm, which is in good agreement with the results obtained by the commercial FEM mode solver. Both numerical tools will be used further for the calculation of various DLSPPW modes, in particular for enhanced DLSPPW properties provided by a metallic shield at the end of this chapter.

Experimentally, the evaluation of both real and imaginary part of N_{eff} is the first action to be led since it can confirm that the fabricated geometry is in agreement with the modeling. A procedure for the evaluation of these basic parameters is described in details in the following section.

2.2 Experimental background

2.2.1 DLSPPW fabrication

To fabricate the DLSPPW components considered in this work, two standard microfabrication approaches are available in our laboratory. By using photo-sensitive or electro-sensitive polymers, dielectric structures can be modeled on top of a metallic film by means of respectively UV lithography or EBL. In both cases, a known amount of energy per surface is needed to cross-link or brake polymer chains. UV lithography is preferred for industrial production since a single design can be repeated many times by a single illumination process (and some chemical, thermal pre/post treatments). But this method requires the use of physical masks where the pattern are fixed (direct or inverted patterns depending on the positive or negative resin). EBL is more accurate very versatile in term of design, but at the expense of time consuming lithography processes not acceptable at an industrial production stage. One can note that some polymers allow both UV lithography and EBL processing.

The waveguides considered in this chapter have been fabricated using EBL performed with a Scanning Electron Microscope (SEM) JEOL 6500F coupled to a lithography software RAITH (Elphy Quantum). A Poly(methylémethacrylate) (PMMA) is deposited by spin-coating onto a typically 65nm-thick gold film thermally evaporated on a glass substrate. Then the dielectric ridges are defined by exposing the polymer to electrons (Fig. 2.5(a)). The subsequent amount of resin is removed by a developer solution of 2/5 MIBK/Isopropanol. The resulting passive DLSPPW structures are depicted schematically in Figs. 2.5 (b) to (d). The thickness of all DLSPPWs fabricated in this study is fixed at t=560 nm and the width at $w = 600$ nm. For such dimensions, the DLSPPW structures shown in Fig. 2.5 are single-mode at telecom wavelength. Scanning electron micrograph of the DLSPPWs structures are shown in Fig. 2.5 (e) to (g).

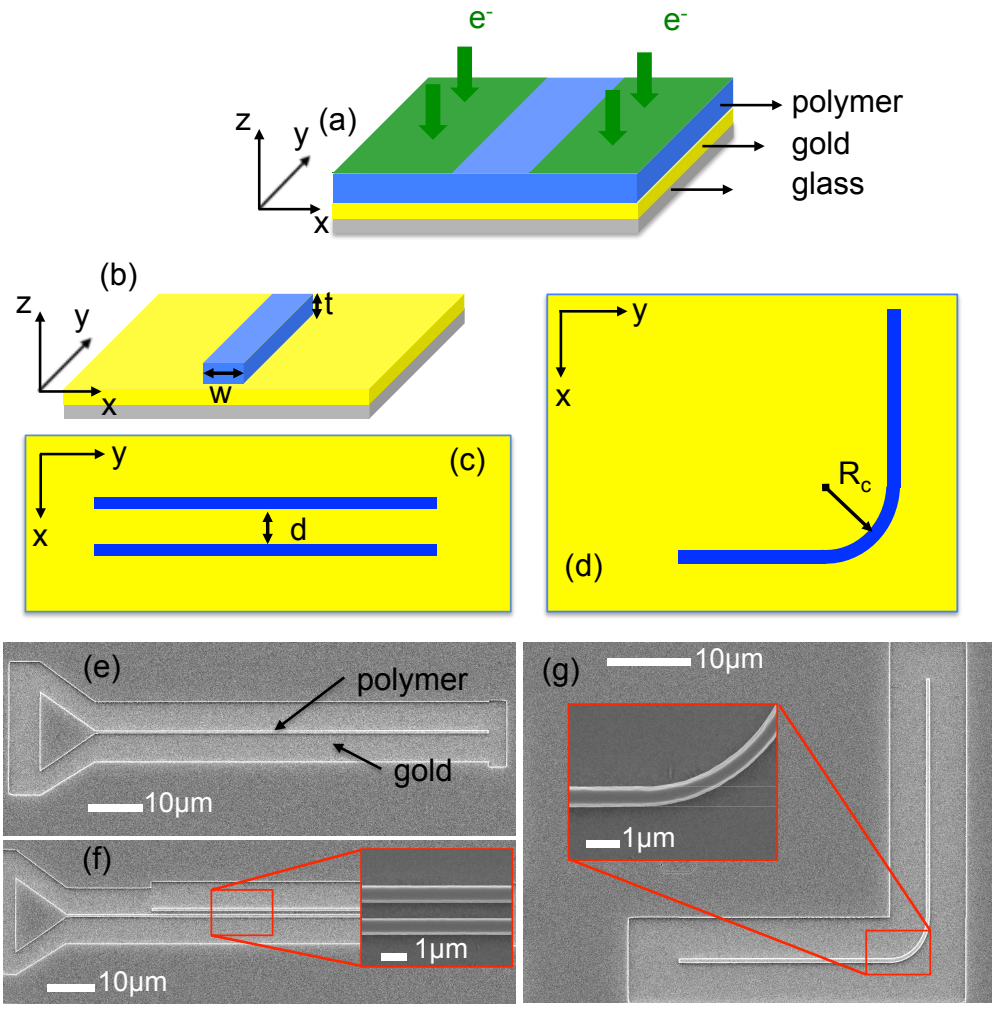

Figure 2.5: (a) Electron Beam exposure (b) Schematic view of a basic DLSPPW with a width w of 600 nm and thickness t=560 nm. (c) Schematic view of two coupled waveguides separated by a gap d. (d) Schematic view of a waveguide with a curved section with a bend radius R_c. (e), (f) and (g) are scanning electron micrographs of typical devices corresponding to the configurations (b), (c), and (d), respectively.

2.2.2 Characterization setup

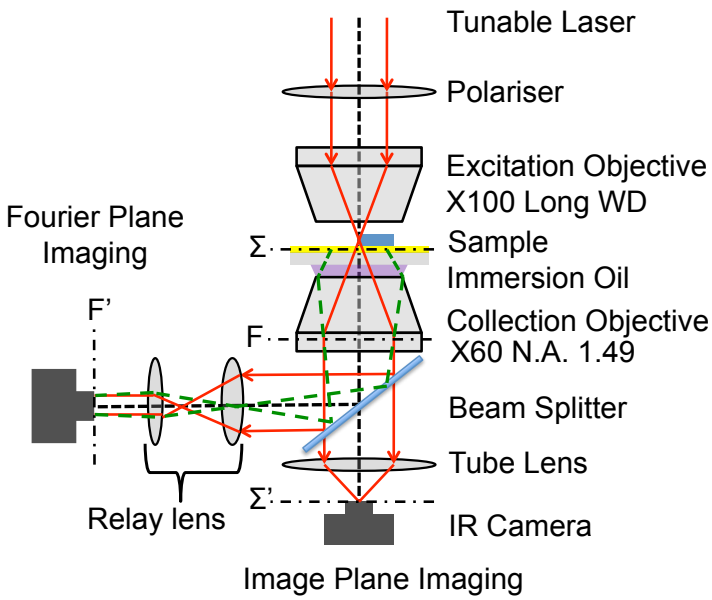

Figure 2.6: Schematic of the leakage radiation microscope used in this study. Launching of the plasmon mode in the waveguides is obtained by focusing a laser operating at λ=1510 nm with a long working distance objective. Surface plasmon leakages are collected by an oil immersion objective and are imaged on two cameras placed at the conjugated image (field) plane and Fourier (aperture) plane, respectively.

Optical characterization is performed by using a home-made leakage radiation microscope (LRM). The principle of this method is only recalled here, more details can be found in the review by Drezet *et al.*[90]. The schematic view of our experimental set-up is illustrated in Fig. 2.6. An incident tunable laser beam (fixed at λ=1510 nm hereafter) is focused by a 100 × microscope objective on the extremity of a DLSPP waveguide. The sharp discontinuity defined by the polymer structure acts a local scatterer and produces a spread of wave-vectors, some of which resonant with the surface plasmon modes supported by the geometry. By controlling the incident polarization parallel to the longitudinal axis of the waveguide [91], the DLSPPW mode can thus be readily excited. Leakage radiation microscopy (LRM) provides a far-field imaging technique to directly visualize surface plasmon propagation and investigate its fundamental properties [92, 93]. This method relies on the collection of radiation losses occurring in the waveguide during propagation. These losses are emitted in the substrate at an angle phase-matched with the in-plane wave-vector of the SPP mode. In our LRM, the plasmon radiation losses are collected by an oil-immersion objective with a numerical aperture (N.A.) of 1.49. A tube lens focuses the leakages in an image plane (IP) conjugated with the object plane where an InGaAs infrared camera is recording the two-dimensional intensity distribution.

Images recorded at this plane provide direct information about the propagation of the surface plasmon mode developing in the DLSPPW. To complete the analysis, we have also used the Fourier transforming property of the objective lens to access the wave-vector distribution of the emitted light. The angular distribution of the rays radiated in the substrate and collected by the objective lens is transformed to a lateral distribution at the objective back focal plane. Quantitative measurement of the complex surface plasmon wave-vector, or equivalently its complex effective index, consists at measuring the radial distance of the rays with respect to the optical axis. Access to momentum space was done by inserting a beam splitter in the optical path and a set of Fourier transforming relay lens. The lenses are forming an image conjugated with back focal plane of the objective. This Fourier plane (FP) contains the two-dimensional wave-vector distribution of the leakage radiation and momentum-space spectroscopy can thus be readily performed.

2.2.3 Calibrating leakage radiation images

Figures 2.7 (a) and (b) show images of the leakage radiation intensity of a single-mode DLSPPW recorded in the conjugated image and Fourier planes, respectively. The plasmon mode is launched at the bottom of the structure and propagates to the top of the image with an exponentially decaying intensity. The image of Fig. 2.7(b) is a direct measurement of the wave-vector content of the intensity distribution shown in Fig. 2.7(a). For both FP and IP images, a calibration was performed prior to any data extraction. For calibrating IP images, we used the known waveguide length as a calibration standard. With the system magnification one pixel represents $\simeq$0.6 µm. For FP images, the N.A. of the objective was used to calibrate k_x and k_y axes. The largest ring in Fig. 2.7(b) represents the N.A.=1.49 specified by the manufacturer. The central disk is the numerical aperture of the $\times$100 excitation objective at N.A.=0.52. One pixel provides a ΔN.A. $\simeq$ 0.012 on the FP images.

The propagation length L_{SPP} of the DLSPPW mode supported along this straight waveguide presented in Fig. 2.7 can be directly extracted from direct-space image by fitting an exponential decay of the intensity along the waveguide $I = I_0 \exp(-y/L_{SPP})$. Here a L_{SPP}=42.2 µm is determined from the fit to the experimental data illustrated in Fig. 2.7(c). Experimentally, the FP image displayed in Fig. 2.7(b) contains more information than a direct space image since the real part and imaginary part of the effective index can be directly measured. The signature of the mode is represented by a single line at a constant $n_{eff}=k_y/k_o$=1.262$\pm$0.006. The intensity measured along k_y/k_o at k_x=0 is related to the surface plasmon through the following formula [77]: $I(k_x,k_y) \propto |\widetilde{H}_0(k_x)|^2/[(k_y-\beta')^2+(1/2L_{spp})^2]$. $\widetilde{H}_0(k_x)$ is the k_x-Fourier transform of the guided magnetic field at the objective focal point. The imaginary part of the effective index is also estimated precisely through a Lorentzian fit. The width Δn_{eff} of the β'/k_o line is a measure of the losses experienced by the plasmon mode and is thus inversely proportional to its propagation length L_{spp} [3]. We obtain from the FP image a L_{spp}=43.3 µm in fairly good agreement with L_{spp}=42.2 µm measured from the

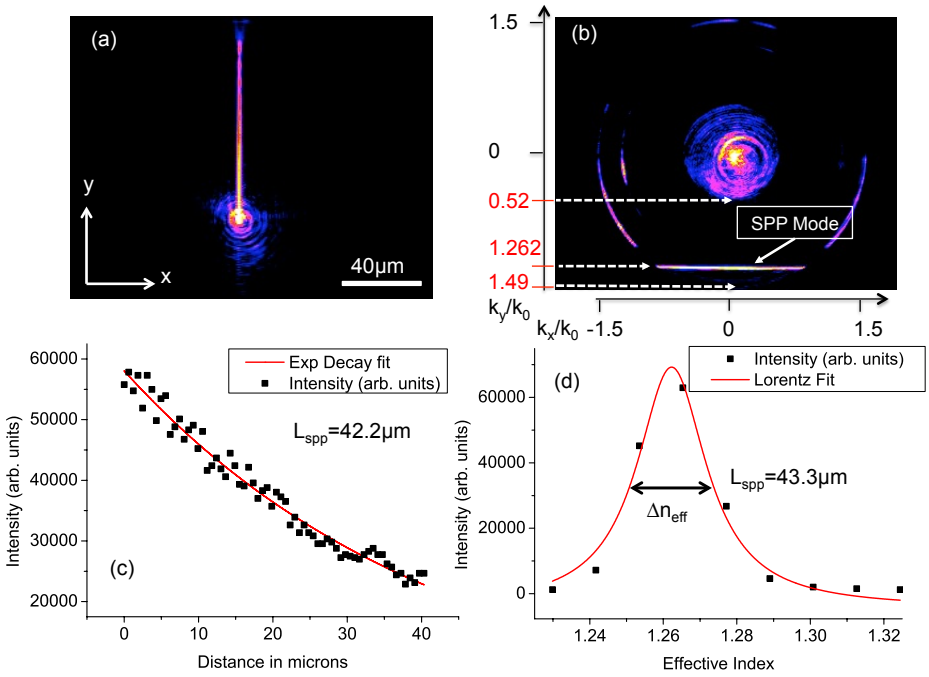

Figure 2.7: (a) Intensity distribution recorded at the image plane of a surface plasmon mode propagating along a straight DLSPPW. The excitation spot is readily visible at the lower portion of the waveguide. (b) Corresponding wave-vector distribution. The central disk represents the numerical aperture of the illumination objective (0.52). The DLSPP mode is recognized as a bright line at constant k_y/k_x (arrow). (c) Exponential fit of the experimental decaying plasmon intensity along the waveguide leading to a L_{spp}=42.2 µm. (d) Lorentzian fit of the FP plasmon mode signature centered at β'/k_o=1.262. The full with at half maximum Δn_{eff} is inversely proportional to L_{spp}.

direct-space analysis.

Summary

The fabrication process and characterization tools have been described. The direct and reciprocal space imaging system offered by the LRM setup have been calibrated. Once calibrated, the LRM set-up allows us to extract quantitative informations about the DLSPPW modes. We consider now the LRM study (in the direct and reciprocal space) of linear directional and bend waveguides in order to demonstrate the interest but also the limits of leakage radiation microscopy for waveguiding structures characterization.

2.3 Momentum-space spectroscopy of linear couplers

2.3.1 Experimental measurements

The first component we consider is a directional coupler comprised of two interacting straight DSLPPWs [54, 63, 69, 74], separated by an edge-to-edge distance d varying from

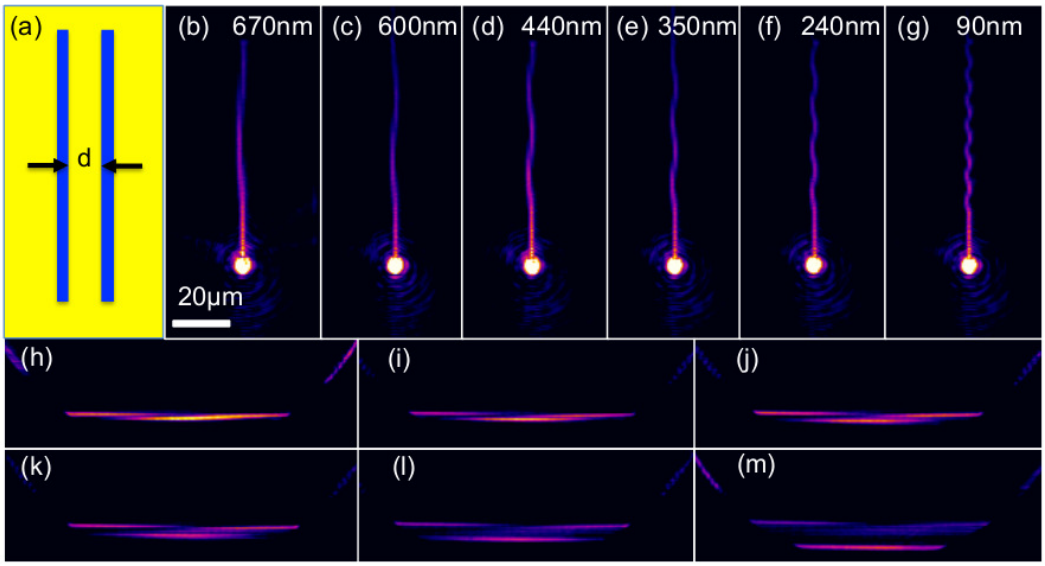

Figure 2.8: (a) Schematic of a linear DLSPPW coupler. (b) to (g) are direct-space images of the intensity distribution in linear DLSPPW couplers with edge-to-edge distance d equals to 670 nm, 600 nm, 440 nm, 350 nm, 240 nm and 90 nm respectively. (h) to (m) are the corresponding wave-vector distributions unambiguously demonstrating the degeneracy lift of the coupled waveguides for small values of d.

670 nm to 90 nm (see Fig. 2.8(a)). This elementary configuration is well-known from coupled-mode theory [94]. When the gap distance d is reduced, the degenerate modes propagating in the uncoupled waveguides hybridize and split into a symmetric and an antisymmetric modes. Each mode possesses its own propagation constant, β'_s and β'_{as} respectively, critically depending on d. A beating of these two modes can be observed in leakage radiation microscopy [63, 69] where a mode propagating in one waveguide can be totally transferred to the second after a coupling distance L_c [64]. Figures 2.8(b)-(g) qualitatively show the evolution of the beating pattern and the coupling distance L_c for decreasing separation distances d. More interesting is the corresponding wave-vector distributions depicted in the series of the FP images in Figs. 2.8(h) to (m). When the DLSPPWs are weakly coupled (d=670 nm), the Fourier content of Fig. 2.8(h) strongly resembles that of a single DLSPP mode in Fig. 2.7(b). When d is reduced, a clear splitting of the modes is observed indicative of a strong interaction between the waveguides. The parity of the modes with respect to the z-axes and passing through the center of the waveguide can be readily determined from Fig. 2.8(m). The asymmetric mode has an odd parity with two maxima centered on each side of k_y/k_o axis.

Figure 2.9 illustrates the benefit of performing the momentum-space spectroscopy described here. Figures 2.9(a) and (b) are the leakage radiation images recorded at the conjugated Fourier plane and image plane for a linear coupler with d=440 nm, respectively. The effective indices of the symmetric n^s_{eff} and antisymmetric n^{as}_{eff} modes

are evaluated by Lorentzian fits of crosscuts of the momentum distribution along the k_y/k_o axis marked by the circles in Fig. 2.9(a). n_{eff}^{as} was evaluated at two different wave-vector positions with respect to the k_y/k_o axis, labeled as n_{eff}^{as} and $n_{eff}^{as'}$. The fits to the data are represented in Figs. 2.9(c) and (d) for the antisymmetric mode leading to $n_{eff}^{as} \simeq n_{eff}^{as'}$=1.260±0.006. The effective index of the symmetric mode is measured at n_{eff}^{s}=1.310±0.006 (Fig. 2.9(e)). The coupling length L_c can now be evaluated using the following relation [64]

$$L_c = \frac{\pi}{|\beta'_s - \beta'_{as}|}, \tag{2.3}$$

where $\beta'_s = k_o \times n_{eff}^{s}$ and $\beta'_{as} = k_o \times n_{eff}^{as}$. Then

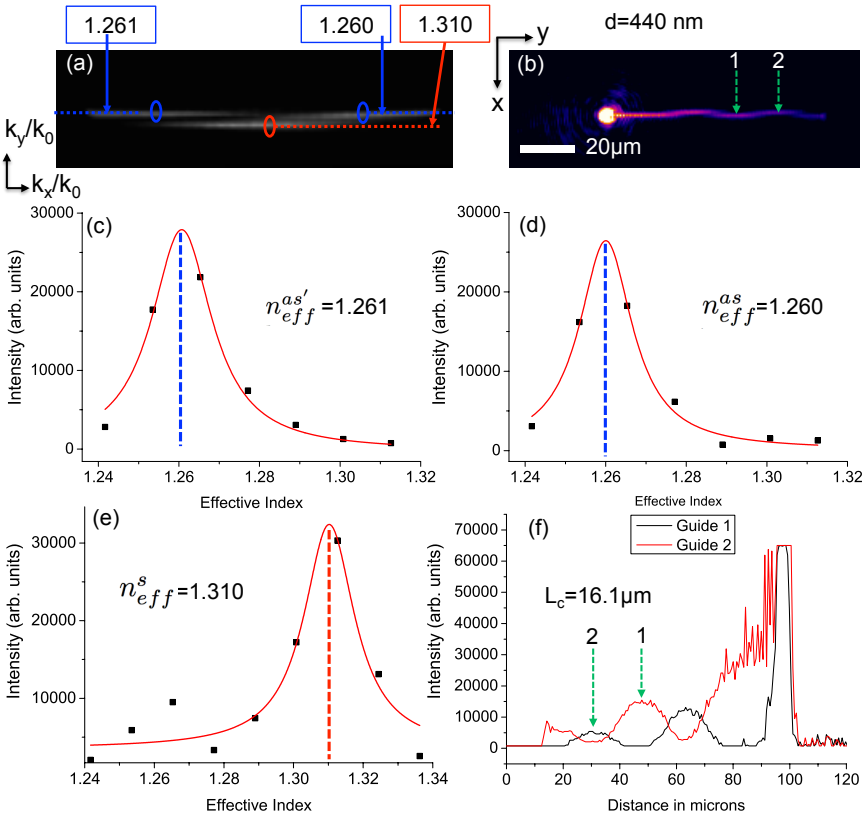

Figure 2.9: (a) and (b) are the respective leakage radiation Fourier and image planes obtained from a linear DLSPPW coupler with d=440 nm. (c) and (d) are Lorentzian fits of the asymmetric mode at the location marked by the circle in (a). (e) is a Lorentzian fit of the symmetric mode. (f) Longitudinal intensity cross sections taken along the two coupled waveguides in (b) showing the energy transfer from one DLSPPW to the other defining the coupling length L_c.

$$L_c = \frac{\lambda_0}{2|n_{eff}^{s} - n_{eff}^{as}|} = 15.2\mu m. \tag{2.4}$$

This procedure was repeated for the different DLSPPW separation distances d. The extracted values of the split modes and coupling length L_c are reported in Table 2.3.1. L_c was estimated taking into account an average value of n_{eff}^{as} and $n_{eff}^{as'}$. For comparison purposes, L_c was also determined by analyzing the beating pattern recorded in the image plane (Fig. 2.9(b)). A longitudinal cross-section of the leakage intensity taken along each DLSPPWs is shown in Fig. 2.9(f) for d=440 nm. The transfer of the mode between the two waveguides is obtained after L_c ~16 µm. Within our pixel resolution, this value compares well with the L_c determined by the analysis of the degeneracy lift of the effective indices by Eq. 2.4. The advantage of a momentum-space spectroscopy is that, unlike near-field measurement [54, 64], the effective indices can be directly measured and mode symmetry visualized [83, 91]. On the contrary, L_c inferred from direct plane analysis only provides the difference between the two propagation constants $|\beta'_s - \beta'_{as}|$ without discriminating the symmetric mode from the antisymmetric one.

Table 2.1: Measured values of the effective indices of the asymmetric and symmetric modes and estimated coupling length L_c for linear DLSPPW couplers with different edge-to-edge separation d. L_c values were estimated independently by momentum-space spectroscopy and direct-plane analysis.

d [nm]	n_{eff}^{as}	$n_{eff}^{as'}$	n_{eff}^{s}	L_c [µm](FP)	L_c [µm](IP)
090	1.230	1.234	1.403	4.4	4.3
240	1.241	1.244	1.343	7.5	7.7
350	1.252	1.254	1.316	12.0	11.8
440	1.260	1.261	1.310	15.2	16.1
600	1.262	1.263	1.299	20.6	21.1
670	1.271	1.271	1.294	32.8	31.4

2.3.2 Comparison with Finite Element Method

To confirm these experimental results, we numerically simulated linear DLSPPW coupler with the commercial FEM mode solver COMSOL. The optical index of the PMMA waveguide is $n_{PMMA} = 1.535$ and that of the gold substrate is $n_{gold} = 0.536 + i9.5681$ at λ=1510 nm [95]. The transversal electric field distribution of the asymmetric and symmetric mode shown Figs. 2.10 (a) and (b) for d=400 nm. Figure 2.10 (c) provides a comparison of the evolution of the degeneracy lift with separation distance d. The measured data quantitatively reproduces the response of the simulated device.

With this first example of directional coupler, we have shown the interest of LRM to extract useful information about DLSPPW structures. However, LRM characterizations are also subject to limitation that are discussed in detail in the next section.

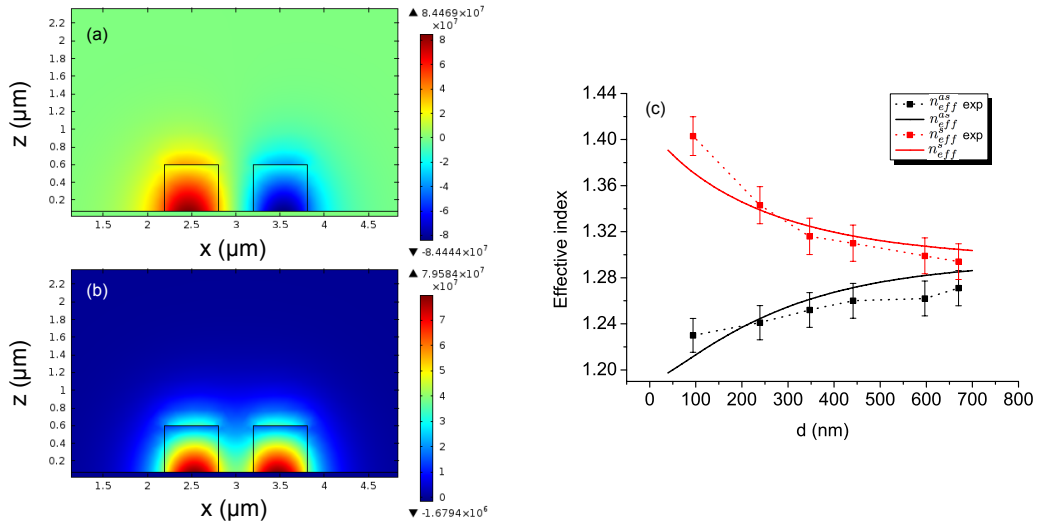

Figure 2.10: (a) and (b) are the electric field profiles of the asymmetric and symmetric modes propagating in two coupled DLSPPWs separated by a d=400 nm. (c) Comparison between the experimental splitting of the modes and the calculated values for various coupling distance d.

2.4 Momentum-space spectroscopy of curved DLSPPWs

2.4.1 Experimental images

In this section, we investigate the momentum distribution of another well-known basic routing element: 90° curved waveguide. This DLSPPW structure has been extensively studied by various groups and the effect of bend radius on the overall losses is well understood [70, 74, 96–98]. By performing momentum-space spectroscopy of the supported mode, we visualize and analyze the wave-vector content of the bend section for this routing device. We demonstrate the limitations of momentum-space spectroscopy to extract modal properties of this elementary building block. The curved DLSPPW is composed of two L=30 μm long straight waveguides with w=600 nm. These two input and output waveguides are linked by a circular 90° bend waveguide of radius R_c. Bent DLSPPWs with R_c ranging from 5 μm to 19 μm were fabricated. The leakage intensity distribution image of a R_c=19 μm curved waveguide is shown Fig. 2.11(a). The corresponding wave-vector distribution is depicted in Fig 2.11(b). The two straight lines at k_x and k_y constant are related to the mode propagating along the y and x-oriented waveguides, respectively. The line at k_x=constant is the input waveguide. This Fourier plane shows additional signatures such as the illumination wave-vector span (central disk) and planar plasmon modes supported by the Au/air or Au/PMMA taper interfaces. Of particular interest here is the Fourier signature of the bent section of the waveguide visible as an arc of circle linking the two modes.

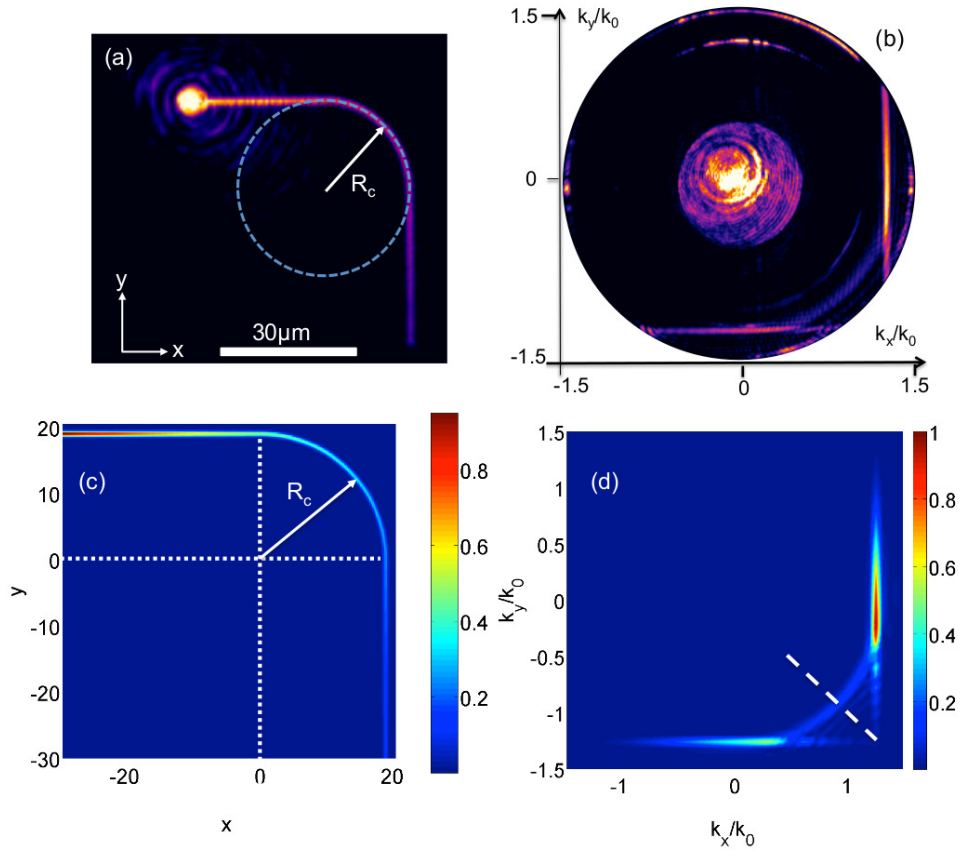

Figure 2.11: (a) and (b) Leakage radiation image of a bent waveguide with R_c=19 µm and its corresponding wave-vector distribution, respectively. The Fourier content of the curved section is appearing as an arc linking the two k_x and k_y lines. (c) and (d) Computed intensity of the mode propagating in the routing element and its corresponding wave-vector distribution, respectively.

2.4.2 Fourier plane model

Instead of full numerical simulations, we propose in the following a very simple analytical model that explains the main features of the measured Fourier plane images. To this aim, we approximate the mode that propagates in the bend structure by a gaussian profile with a finite propagation length. The characteristics of the gaussian profile was defined by the experimental data obtained from a straight waveguide; namely n_{eff}=1.262 and L_{SPP}=42.2 µm. The mode width was fixed at w_0=500 nm according to the analysis of *Holmgaard and Bozhevolnyi* [48].

The magnetic field is written as follow:

- input straight guide ($-L < x < 0$, $y > 0$)

$$H_y(x,y) = H_o \exp\left[\frac{-(y-R_c)^2}{w_0^2}\right] \exp[ik_{SPP}x]\,, \tag{2.5}$$
$$= H_o \exp\left[\frac{-(y-R_c)^2}{w_0^2}\right] \exp[in_{eff}k_o x] \exp[-x/2L_{SPP}]\,,$$

- circular portion ($x > 0$, $y > 0$)

$$H_r(r,\theta) = H_o \exp[-L/2L_{SPP}] \exp\left[\frac{-(r-R_c)^2}{w_0^2}\right] \exp[ik_b R_c \theta]\,, \tag{2.6}$$

  where $r = \sqrt{x^2+y^2}$, $\theta = \arctan(x/y)$ and k_b is the complex wave-vector of the mode in the curved section.

- output straight guide ($x > 0$, $-L < y < 0$)

$$H_x(x,y) = H_o \exp\left[\frac{-(x-R_c)^2}{w_0^2}\right] \exp[-L/2L_{SPP}] \tag{2.7}$$
$$\times\ \exp[-R_c\pi/4L_{SPP}] \exp[in_{eff}k_o y] \exp[-y/2L_{SPP}]\,.$$

The momentum representation $\tilde{H}(k_x,k_y)$ was obtained by a Fourier transform

$$\tilde{H}(k_x,k_y) = \int_{-L}^{R_c+3\times w_0} \int_{-L}^{R_c+3\times w_0} H(x,y) \exp\left[-i(k_x x + k_y y)\right] dxdy. \tag{2.8}$$

where the integration window is truncated to limit the calculation on the mode extension. Outside this area, the mode profile vanishes so that its contribution to the Fourier transform is negligibly small.

To simulate the curved DLSPPW, we maintained the propagation constant in the curved section equal to that of the straight waveguides ($k_b = \beta$). This assumption remains valid for $R_c > R_l$ where R_l is the limiting radius where bend losses can be neglected. R_l have been recently numerically estimated for DLSPPW [70] confirming an analytical expression historically used for standard optical waveguides [96]

$$R_l > \frac{24\pi^2|w_3|^3}{\lambda^2}. \tag{2.9}$$

Here w_3 corresponds to the length over which the field outside of the waveguide decays by $1/e$. With $w_3 \simeq w_0$, $R_l \simeq 13$ µm. When the radius is below R_l, bending loss are induced by a radial displacement of the mode profile with respect to the waveguide axis [70]. This displacement pushes the field outside the waveguide leading to a lower phase velocity and a modification of the effective index [2].

Considering curvature loss as an additional exponential decay is a good approximation

to quantify the total loss induced by the bend and estimate the transmission of the 90° waveguide. However, this approximation is not representative of real shape of the field along the bend and consequently cannot be used to model Fourier images of the kind displayed in Fig 2.11 (b). Note that a transformation optics method for curved optical waveguides [99] has been very recently adapted for the calculation of the bending losses in the case of highly confined photonic and plasmonic waveguides [100]. Such an approach could be used to improve our model.

For $R_c > R_l \simeq 13$ µm, we show that the propagation and momentum-space representations simulated with these basic assumptions (Figs. 2.11 (c) and (d)) reproduce the experimental observations of Figs. 2.11 (a) and (b). We compare the profile of the calculated Fourier transform (Fig. 2.11 (d)) to the experimental wave-vector distribution (Fig. 2.11 (b)) by extracting momentum profiles at different radial coordinates indicated in Fig. 2.12 (a) for R_c=19 µm. Figures 2.12 (b), (c) and (d) show the calculated and experimental wave-vector distributions taken along the k_x and k_y axis and at -π/4, respectively. The position and width of the calculated wave-vector profiles are in very good agreement with the measured data validating thus our preliminary assumptions. Some extra signatures are visible on the experimental cuts: a peak at 1.49 in Fig. 2.12 (b) corresponds to the numerical aperture of the collection objective, and the contribution of the surface plasmon excited in the nearby gold film is visible at 1.08 in Fig. 2.12 (d). Noticeable also is the presence of Gibbs oscillations revealed by this momentum-space spectroscopy (arrows Figs. 2.12 (b) and (c)) . The origin of these oscillations in reciprocal space is discussed below.

2.4.3 Analytical development

In order to achieve analytical expressions and propose a simple physical understanding of the measured Fourier images, we simplified further the model. We consider each part of the waveguide (straight and bend) independently from each others. The straight parts are approximatively 30 µm long, a length smaller than the longitudinal decay of the supported mode (L_{SPP}=42 µm). If we consider only the field in the input straight waveguide along the x coordinate, the Fourier transform of the magnetic field written in Eq. 2.5 reads

$$\tilde{H}_y(k_x) = H_o \int_{-L}^{0} \exp[i\beta - k_x x)]\, dx\,, \tag{2.10}$$

where we neglected the y-gaussian profile for the sake of clarity but this could be easily considered. Then the intensity in the Fourier plane along k_x direction writes

$$|\tilde{H}_y(k_x)|^2 = |H_o|^2 \frac{1 - 2e^{-\beta'' L}\cos((\beta' - k_x)L) + e^{-2\beta'' L}}{(\beta' - k_x)^2 + \beta''^2} \tag{2.11}$$

If $L \to \infty$ then $|\tilde{H}_y(k_x)|^2 \to 1/[(\beta' - k_x)^2 + \beta''^2]$ and follows a Lorentzian profile, as expected. If the straight part length L is small in comparison to L_{SPP}, the resulting

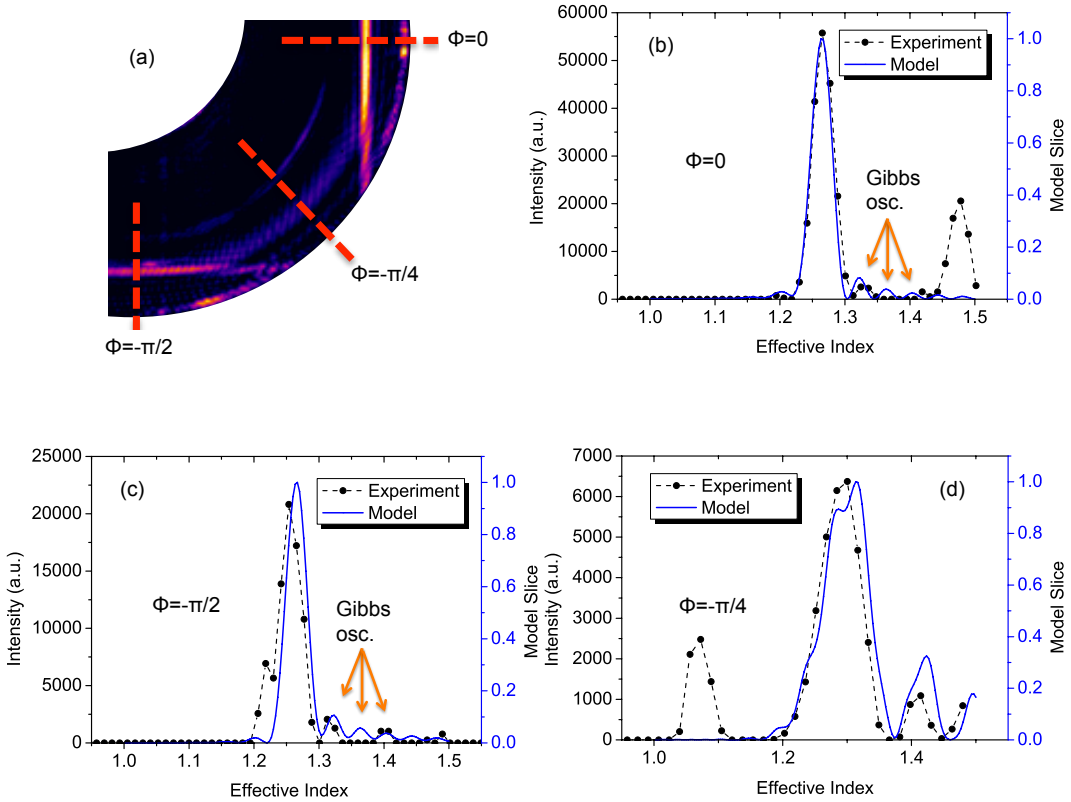

Figure 2.12: (a) Experimental momentum-space image of a $R_c = 19$ µm bend waveguide. The dashed lines indicate the position of the momentum profile in the following graphs. (b) (c) and (d) show the comparison of the calculated and experimental wave-vector distributions along the k_x, k_y and -π/4 axis, respectively.

Fourier transform is not simply defined by a Lorentzian function. Because of the finite integration limit, extra oscillations are becoming visible (Gibbs oscillations) as illustrated in Figs. 2.12 (b) and (c). For long waveguides (as in Fig. 2.7 (a) where $L > L_{SPP}$), no oscillation of the wave-vector distribution is observed. Figure 2.13 shows the impact of the integration boundaries L on the momentum space representation of a single straight waveguide for a fixed propagation length of 40 µm. There is a perfect agreement between the numerically calculated Fourier transform and its analytical solution given by Eq. 2.11. For integration boundaries greater than the propagation length the two calculations match with a Lorentz function generally used.

Since the momentum space representation of a straight waveguide can be expressed for any integration boundaries, we now look for the expression of a curved waveguide alone. On Fig. 2.12 (d), the $-\pi/4$ profile shows the experimental momentum space of a 90° curved waveguide linked by an input and an output waveguide. We approximate in the

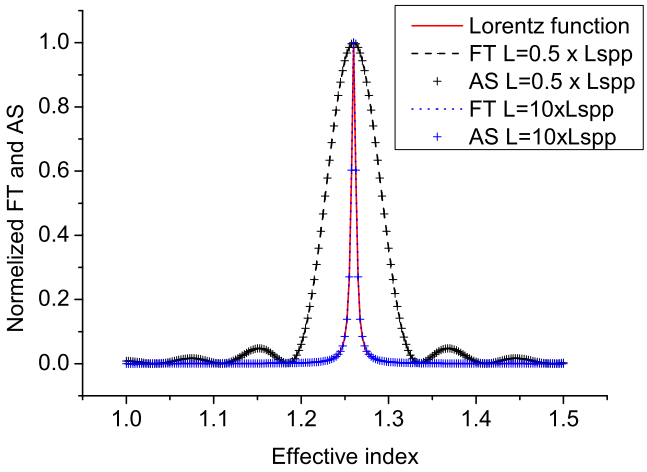

Figure 2.13: Effect of the DLSPPW length on Fourier plane calculations. Dashed lines: calculated Fourier plane (FT) cross section for $L = 0.5 \times L_{spp}$ and $L = 10 \times L_{spp}$. Crosses: analytical solutions (AS) calculated from Eq. 2.11 with the same integration boundaries. Red solid line: calculated Lorentzian profile of the wave-vector distribution of a plasmon mode with a propagation length of 40 µm. When $L < L_{spp}$ Gibbs oscillations and widening of the wave-vector content occur..

following a solution considering a fully symmetric configuration consisting of a lossless circular waveguide. Losses are omitted to maintain the radial symmetry valid between [0;2π]. The Fourier transform in a 360° bend can be expressed in polar coordinates as

$$\tilde{H}(k_r,\phi) = \int_0^{\infty}\int_0^{2\pi} H_r(r,\theta)e^{-2i\pi k_r r\cos(\theta-\phi)} r\,dr d\theta. \tag{2.12}$$

$H_r(r,\theta)$ is given by Eq. 2.6. Since this function is periodic with respect to θ between [0;2π], we can expand $H_r(r,\theta)$ in a Fourier series:

$$H_r(r,\theta) = \sum_{n=-\infty}^{+\infty} H_n(r)e^{in\theta}, \tag{2.13}$$

where the n^{th} harmonic is

$$\begin{aligned} H_n(r) &= \frac{1}{2\pi}\int_{-\pi}^{\pi} H_r(r,\theta)e^{-in\theta}d\theta \\ &= \exp\left[\frac{-(r-R_c)}{w_0^2}\right]\mathrm{sinc}(k_b R_c\pi - n\pi). \end{aligned} \tag{2.14}$$

The Fourier transform of the field (Eq. 2.12) can now be written as follow

$$\tilde{H}_n(k_r,\phi) = \sum_{n=-\infty}^{+\infty} (-i)^n e^{i\phi n} 2\pi \int_0^{\infty} r H_n(r) J_n(2\pi k_r r) dr, \tag{2.15}$$

$$\tilde{H}_n(k_r,\phi) = \sum_{n=-\infty}^{+\infty} h_n f_n(k_r,\phi), \tag{2.16}$$

with

$$h_n = \mathrm{sinc}(k_b R_c \pi - n\pi), \tag{2.17}$$

and

$$f_n(k_r,\phi) = (-i)^n e^{i\phi n} 2\pi \int_0^{\infty} r \ \exp\left[\frac{-(r-R_c)}{w_0^2}\right] J_n(2\pi k_r r) dr.$$

$J_n(2\pi k_r r)$ is the Bessel function of the first kind of n^{th} order. Further simplification can be achieved by extracting the main n^{th} harmonic h_n of the series. It is deduced from Eq. 2.17 and is such that:

$$k_b R_c \pi - n\pi = 0 \Leftrightarrow n = k_b R_c. \tag{2.18}$$

Therefore the Fourier series is dominated by the harmonic integer that is the closest to the product $k_b R_c$.

Figure 2.14 illustrates a comparison between the experimental data extracted from momentum-space spectroscopy, the Fourier calculations derived from Eq. 2.8 already used in Figure 2.12, and the analytical approximation discussed above. The experimental Fourier planes of Figs. 2.14 (a) to (d) only show the region of interest for four different radii. The corresponding wave-vector profiles extracted and calculated at $-\pi/4$ (dashed lines in figure 2.11(d)) are plotted in the graphs of Figs. 2.14 (e) to (h). For radius $R_c > R_l$, the Fourier calculations and the analytical solutions are in good agreement with the experimental data. For large radii the signature of the bend in momentum space is defined only by the phase difference $k_b(2\pi R_c) = n2\pi$. This corresponds to resonance condition of a ring resonator.

Experimentally, the periodic condition on θ is not verified since the structure considered is formed by an arc of circle. Nonetheless, using the $n = 100^{\text{th}}$ order of the Bessel function in Eq. 2.15 for R_c=19 µm and the 68^{th} order for R_c=13 µm the experimental data and the calculated Fourier transform can be well reproduced (Figs. 2.14 (e) and (f)).

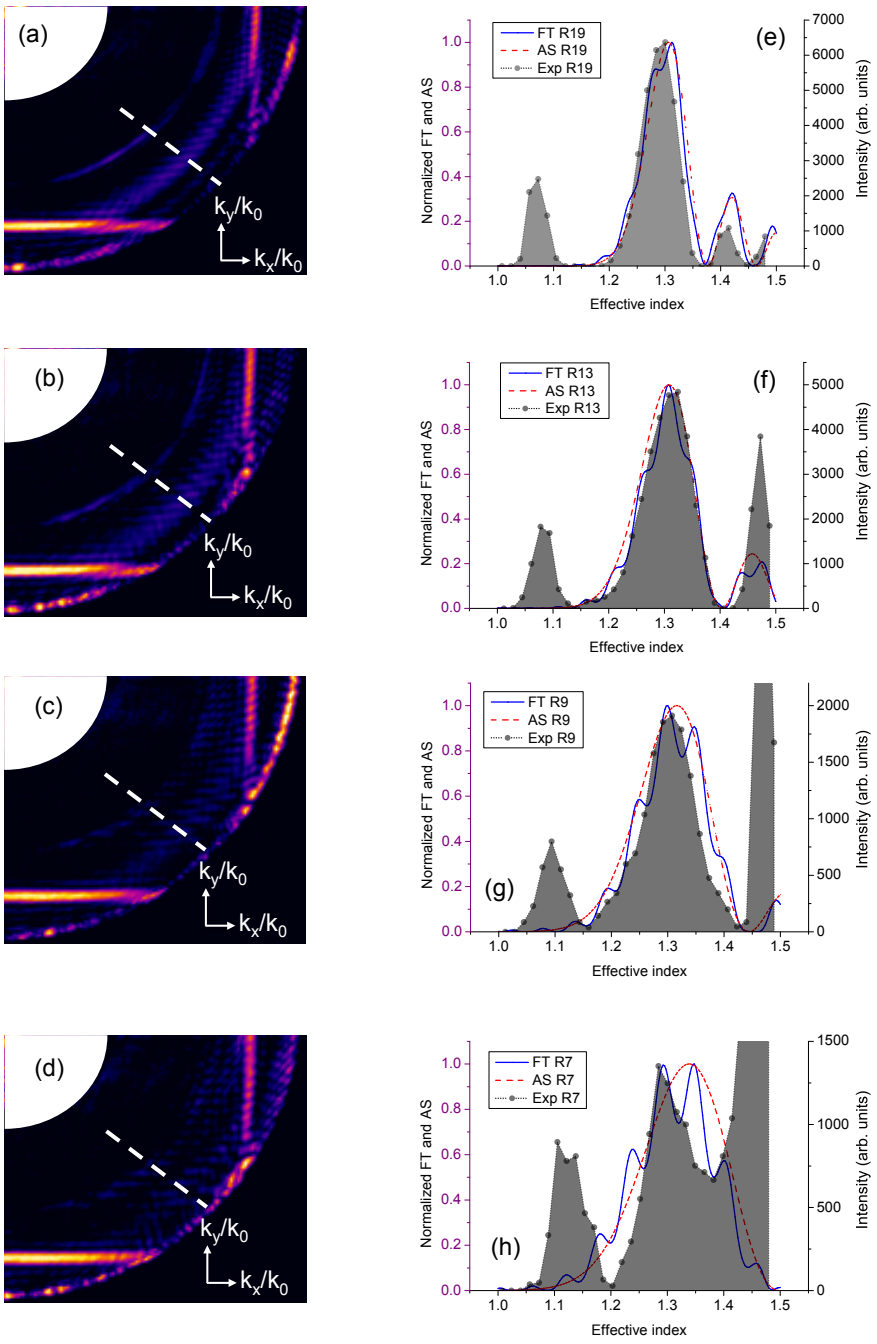

Figure 2.14: (a-d) Selected region of interest of the experimental momentum-space images for curved waveguides with R_c=19 µm, 13 µm, 9 µm, and 7 µm, respectively. (e) to (h) Experimental profiles (shaded areas) of the wave-vector distribution taken along the dashed line in (a) to (d). The solid blue lines are the calculated profiles using Eq. 2.8 already reported in Fig. 2.12. The red dashed lines show the analytical solutions obtained with the n^{th} order rendering the best agreement with the data. n=100, 68, 43, and 37, respectively.

For radius $R_c < R_l$, the calculated profiles deduced from Eq. 2.8 and from the $n = 47^{th}$ and $n = 37^{th}$ orders for R_c=9 µm and R_c=7 µm, respectively are deviating from the experimental cross-cuts (Figs. 2.14 (g) and (h)). This disagreement is expected since none of the two models (Fourier transform and analytical approximation) take in account bending losses.

Summary

By using dual-plane leakage radiation microscopy we have fully quantified the key parameters characterizing two important dielectric-loaded surface plasmon polariton routing devices: linear couplers and 90° curved waveguides. We unambiguously demonstrated the added-value of performing momentum-space spectroscopy. The degeneracy lift for strongly coupled waveguides and the symmetry of the split modes can be directly visualized and quantified. The wave-vector distribution associated to the curved section of the waveguide was also readily observed. We developed a numerical and an analytical analysis to understand the experimental momentum distribution. We found that for large radii (vanishing bending loss), we can link the plasmon signature in Fourier space with the geometrical and modal properties of the bend structure. The radial dependence of the wave-vector distribution is governed by the phase difference $k_b(2\pi R_c)$. For smaller radii of curvature the bend loss needs to be accounted for by developing an approach including realistic field shape.

2.5 Conclusion

In summary, after a short review of the physical properties of the DLSPP waveguides of interest in this work, we have detailed the fabrication and characterization tools that will be operated in all the following of this manuscript. In particular, we have investigated carefully the interest but also the limitations of radiation leakage microscopy in the context of DLSPPW components characterization. To that aim, we have considered in detail two configurations, a linear directional coupler and a 90° bent DLSPPW waveguide. By performing a momentum-space analysis of directional coupler we have shown the added value of LRM approach compared to other imaging techniques such as near-field optical microscopy for example. Indeed, by using LRM, not only the direct space image of the structure can be obtained but also the Fourier space intensity distribution from which key information such as the effective index or the waveguided modes parity can be extracted. However, by considering 90° bent DLSPPW, we have shown that LRM is also subject to limitations. For instance, LRM cannot be used to extract directly bend losses using either direct plane or Fourier plane imaging. This limitation occurs from the fact that both field confinement of the DLSPPW mode and its losses (propagation and bend) in the bent region contribute simultaneously to the wave-vector intensity distribution. Hence, separating each contribution turns out to be difficult at least when the radius of curvature of the DLSPPW is sufficient for bent losses to be significant. With these limitations in mind, we operate LRM in the next chapters for the analysis of thermo-optically controlled DLSPPW-based routers.

PART II

Control Of Thermo-Optical DLSPPWs functionalities

Second Part Purpose

The challenges for dynamically controlled plasmonic devices have been introduced in chapter 1. In the context of optical interconnects, DLSPPWs have been chosen to bring new functionalities compatible with the best chip-scaled data carriers, the SOI waveguides. Following the experimental and numerical study of elementary passive DLSPPW components in chapter 2, the second part of this thesis is dedicated to the experimental characterization of thermo-optical components. The chapter 3 will be dedicated to electrically controlled DLSPPW-based thermo-optical filters and routers. The evaluation of the performances of standalone DLSPPW components is of primary interest prior to their integration on-chip, and the limitations of LRM for such studies will be discussed. Beyond the electrical control of active DLSPPW systems, we show in chapter 4 how to exploit SPPs to create all-plasmonic active components. In this case, the thermo-optical operation is achieved by light absorption related to the excitation of either localized surface plasmon of metallic nano-particles or traveling thin film SPP modes. While DLSPPW characterization still relies on LRM in chapter 3, we will detail in chapter 4 a new test set-up allowing us to perform fiber-to-fiber studies of standalone DLSPPW based devices.

CHAPTER 3

Electrical control of DLSPPWs components

Taking advantage of high Thermo-Optical Coefficients of polymers, thermo-optical control of DLSPPW devices implemented onto a metal strip have been reported [82]. In this case the metal stripe simultaneously plays the role of waveguide core and heating electrode, a situation that is expected to be optimum in the context of thermo-optically controlled devices. However, prior to the implement of such a concept, the performances of DLSPPW-based systems need to be first evaluated and second optimized.

To that aim, we first propose an experimental characterization of DLSPPW RaceTrack Resonators (RTRs). This component is a variant of WRRs introduced in chapter 1 [60, 62, 67]. WRRs are expected to be suitable for spectral filtering, through a fine adjustment of their geometric parameters (radius, gap) [81, 82]. However, WRRs feature relatively low extinction ratio due to their weak coupling with the bus waveguide. On the contrary, the RTR configuration which feature an elongated shape is expected to improve this coupling owning to a better control of the interaction distance between the bus waveguide and the resonator. In this study, we will investigate in details thermo-optical performances addressed electrically.

Beyond thermo-optical filtering, we show in the second part of this chapter that RTRs can be implemented as thermo-optical routers by crossing at 90° two RTRs, this configuration will be denoted hereafter as X-Add-Drop routers [101]. The quantitative efficiency of such a routing device is again evaluated by LRM imaging and then compared to FEM calculations.

Next LRM is also used to investigate the performances of an other promising DLSPPW routing configuration, the Dual-Mode Interferometer (DMI). The DMI configuration relies on the interference of two co-propagating modes with different effective index. In essence a DMI is not different from a directional coupler with the advantage that the DMI configuration does not requires to control critical dimension such as separation gaps and hence providing a greater fabrication tolerance than evanescent coupling-based configuration. The thermo-optical performances of DMIs will be compared to FEM calculations and the limitations of the LRM method for the purpose of dynamic telecom

devices will be highlighted.

3.1 Thermo-optical control of DLSPPW filters: RaceTrack Resonators

This first section reports on the geometrical optimization of RTRs to improve the extinction ratio to a level of practical interest in devices such as optical filters. By extracting the experimental transmission spectra at telecom wavelengths (from 1500 nm to 1600 nm) for various structures, we analyze the performances with the help of a model of lossy resonator coupled to a lossy waveguide. For approximatively 250 nm gaps separating the RTR and the bus waveguide, resonators are shown to be always under-coupled for sub-micron interaction lengths. Adjusting the structural parameters of the RTR allows to identify the optimum critical coupling condition that leads to much larger extinction ratios than those of WRRs. Finally, the static (DC) Joule heating of the metal film supporting the RTR will be used to increase the temperature of the loading material. When the loading material features a thermo-optical coefficient around $\frac{\partial n}{\partial T} = -1.0^{-4}\ K^{-1}$, a blue shift of the RTR resonance wavelength larger than 4 nm is observed for a typical increase of the temperature below 80 K.

3.1.1 Experimental images

The resonators studied in this work are depicted in Figure 3.1 (a). A bus waveguide

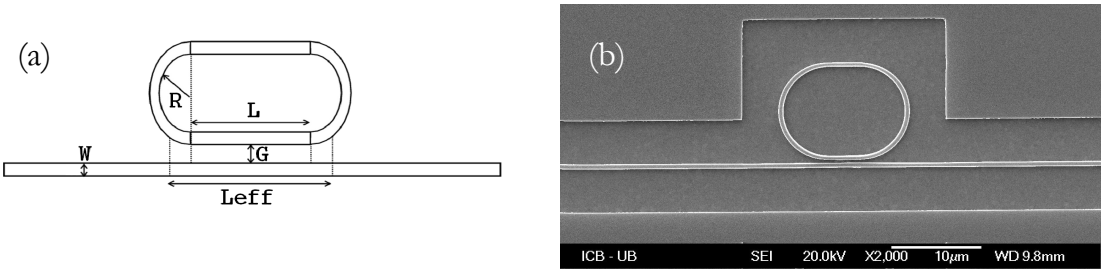

Figure 3.1: (a) Schematic view of a racetrack shaped resonator. Three structural parameters are used to define the geometry of the resonator, the separation gap G, the interaction length L and the radius R. (b) Scanning electron microscope image of a typical DLSPPW resonator made of PMMA lying on a thin gold film.

with a rectangular cross-section of $W \times H$ is coupled to a racetrack resonator. The RTR-bus waveguide system is characterized by three main parameters: the radius R of the RTR, the gap G separating the bus from the RTR and the straight interaction length L. If L is set to zero, the RTR reduces to a ring resonator. For sufficiently large radius R, the straight length L is different from the interaction length L_{eff} along which the bus waveguide exchanges energy with the resonator. Figure 3.1 (b) shows a scanning electron image of the a typical RTR fabricated by EBL, following the fabrication process described in chapter 2. For the purpose of thermo-optical heating presented in the following, the underlying gold film width has been limited to 3 mm (and still 65 nm-thick). Then the DLSPPW bus and resonator waveguides are displaying a nearly square cross-section ($W = 560$ nm and $H = 570$ nm), and support a DLSPPW mode with a

real effective index of refraction ranging from 1.2 to 1.3. The optical characterization of RTRs is performed by means of LRM [21, 55, 92]. The principle of this method has been previously detailed in chapter 2 (Fig. 2.6), only the direct space images will be used to extract the performances in the following.

Figure 3.2 shows a typical radiation leakage image of a RTR when excited at resonance so that the incident DLSPP mode traveling from the right to the left is efficiently filtered by the resonator. The waveguide coupled to the RTR is basically a plasmonic notch filter whose spectrum can be obtained directly from the LRM direct space images. By integrating the intensity collected within the rectangular areas located on each side of the resonator as displayed in Fig. 3.2, the ratio of transmitted over incoming power can be evaluated at the wavelength of interest. Sweeping the incident frequency over the tunable range of the laser results in a transmission spectrum of the filter. This experimental approach relies on the fact that the DLSPP modes losses are not only due to the intrinsic ohmic damping but also to these radiation leakages exploited in by the measurement method. Thus, the propagation length of these modes could be increased and the performances of the resonators could likely be improved by minimizing these radiation leakages. However, for the experimental conditions considered here (frequency range, gold thickness = 65±5 nm), the radiation leakage channel provides a rather low contribution to the total losses. Indeed, by making the gold film optically thick (around 100 nm at λ=1550nm), we computed that the damping distance of the DLSPPW mode is increased by only 14% compared to the experimental situation. This means that the results discussed in the next section are not significantly impacted by the order of magnitude of the radiation leakages and can safely be interpreted as optimum performances of the RTRs.

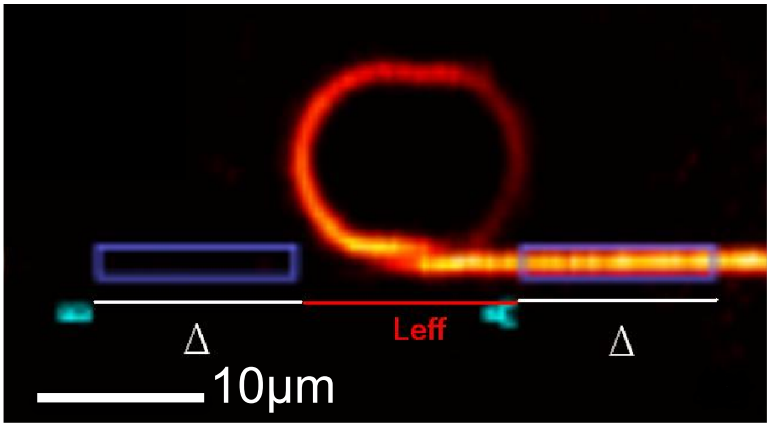

Figure 3.2: Typical radiation leakage image in the case of a resonant resonator (λ =1512 nm). The input and output signals at a given wavelength are obtained by integrating the pixel values of the radiation leakage image within the perimeters shown on each side of the resonator.

3.1.2 Lossy resonator model

The quantitative analysis of the plasmonic RTRs properties is conveniently performed by modeling the transmission through a lossy bus waveguide coupled to a lossy resonator. The theory of evanescently coupled ring resonators has been long established [94, 102] and has been extensively used to investigate dielectric resonators. In such situations, the equations describing the resonators are often simplified owing to their rather weak losses and corresponding high quality factor [103]. In order to provide the reader with a self-consistent description of the plasmonic resonators, we briefly recall this formalism in the case of lossy waveguides. To that aim, we refer to the approach described in reference [104]. The RTR spectra can be analyzed on the basis of mainly two quantities α and t. From a physical point of view, when a field amplitude normalized to unity enters the resonator, α is the light field amplitude after a round-trip in the resonator. Thus α^2 is power loss factor accounting for any loss channels including, propagation losses, bend losses or scattering losses. A non-lossy resonator is of course characterized by $\alpha = 1$. As already noted by several authors [60, 67], in the case of plasmonic resonator, it is convenient to note the coefficient α as $\alpha = \alpha_b \times \alpha_{prpg}$ where α_b refers to pure bend losses and $\alpha_{prpg} = \exp\left[-k''_{spp}(2\pi R + 2L)\right]$ describes the propagations losses along the perimeter of the resonator, with k''_{spp} being the damping constant of the plasmonic mode. Under the assumption of the absence of any loss within this coupling region, the second important coefficient t represents the amplitude of the light field within the bus waveguide at the output of the coupling region when a field amplitude normalized to unity entered this said region. We emphasize that this definition of t does not imply that the losses are neglected over the coupling region but simply that the losses are not introduced in the definition of t. In other words, t describes the evanescent energy transfer from the bus waveguide to the resonator but not the propagation losses along this coupling length. Taking into account the damping of the plasmonic mode and the integration of the intensity over the input and output regions of interest on the radiation leakage microscopy images, the power transmission in our situation is given by [104]:

$$T = e^{-2\,k''_{spp}(\Delta + L_{eff})}\left(\frac{\alpha^2 + t^2 - 2\,\alpha\,t\,\cos(\phi + \phi_c)}{1 + \alpha^2\,t^2 - 2\,\alpha\,t\,\cos(\phi + \phi_c)}\right) \tag{3.1}$$

where ϕ is the phase accumulated during a round trip along the resonator, n_{eff} the effective index of the plasmonic mode and ϕ_c an extra phase term accounting for the interaction of the resonator with the bus waveguide. The resonator is resonant when:

$$\phi + \phi_c = \frac{2\pi n_{eff}(\lambda)(2\pi\,R + 2L)}{\lambda} + \phi_c = 2\pi m \tag{3.2}$$

where m is an integer. In this situation the power transmission reduces to:

$$T = e^{-2k''_{spp}(\Delta + L_{eff})}\frac{(\alpha - t)^2}{(1 - \alpha\,t)^2} \tag{3.3}$$

From equation (3.1), it is a simple matter to extract the extinction ratio $ER = \frac{T_{max}}{T_{min}}$:

$$ER = \left[\frac{(\alpha + t)}{(\alpha - t)}\frac{(1 - \alpha t)}{(1 + \alpha t)}\right]^2, \tag{3.4}$$

The ER may become very large at resonance if the critical coupling condition $\alpha = t$ is verified [94]. The quality factor of a resonance centered around the wavelength λ_m is defined as:

$$Q = \frac{\lambda_m}{\Delta\lambda_{FWHM}} \tag{3.5}$$

where $\Delta\lambda_{FWHM}$ denotes the full spectral range at $T_{HM} = \frac{T_{max}+T_{min}}{2}$. Starting from the resonance contition, the range $\Delta\lambda_{FWHM}$ for a resonance of order m is given by:

$$\Delta\lambda_{FWHM} = \frac{\lambda_m \ \lambda_m^{HM}(\phi + \phi_c)_{HM}}{\pi(2\pi R + 2L) \ N_g(\lambda_m)} \tag{3.6}$$

where $(\phi+\phi_c)_{HM}$ is the phase at wavelength λ_m^{HM} defined by $T(\lambda_m^{HM}) = T_{HM}$. Evaluated at λ_m, the function N_g is the so-called group index of refraction given by $N_g(\lambda_m) = n_{eff}(\lambda_m)+\lambda_m\frac{\partial n_{eff}}{\partial\lambda}$. The phase coefficient $(\phi+\phi_c)_{HM}$ is directly related to the coefficients α and t through the relation:

$$\cos(\phi + \phi_c)_{HM} = \frac{T_{HM}(1 + \alpha^2\ t^2) - \alpha^2 - t^2}{2\alpha\ t(T_{HM} - 1)} \tag{3.7}$$

which can be also written after some algebra as:

$$(\phi + \phi_c)_{HM} = \arccos\frac{2\alpha\ t}{1 + \alpha^2\ t^2} \tag{3.8}$$

Using this last equation and assuming $\lambda_m \simeq \lambda_m^{HM}$, the quality factor is then given by:

$$Q \simeq \frac{\pi N_g(\lambda_m)P}{\lambda_m}\left(\arccos\frac{2\alpha t}{1 + \alpha^2 t^2}\right)^{-1}. \tag{3.9}$$

Thus, knowing α and t, the properties of practical interest (Extinction ratio and quality factor) of the RTRs can be extracted from equations (3.4) and (3.9). Note that, in the case of the lossy RTRs considered here, equation (3.9) should not be oversimplified as it is usually done when considering dielectric resonators. Indeed, it will appear later that the condition $\alpha\ t \simeq 1$ is never verified for plasmonic RTRs so that the usual simplification of the expression of quality factor should not be used when dealing with plasmonic resonators [105].

3.1.3 Structural parameters optimization

As already introduced earlier, a bus waveguide coupled to a racetrack resonator is characterized by mainly three structural parameters: the interaction length L, the resonator radius R and the separation gap G (see Fig.3.1). From a practical point of view, when working with DLSPPWs, the gap between the bus waveguide and the resonator can only be hardly varied in a controlled way at the scale of a few tenth of nanometers. For this reason, the separation gap is fixed to $G = 240 \pm 40$nm for all the samples considered in the following. This value corresponds to the lowest resolution limit that could be achieved by deep UV lithography (wavelength 250 nm), a processing method that can be applied to many polymers DLSPPWs. We focus now onto RTRs with different radii and interaction lengths. In order to define starting points for the optimization of the radius, it is worth to refer first to the numerical simulations of Ref. [81]. Although the configurations considered in this work are DLSPPW ring resonators rather than racetrack resonators, the numerical results discussed in this reference are still very useful for a RTRs that are not too strongly elongated. When propagating along a bent waveguide, a plasmonic mode loses energy mostly due to propagation losses (ohmic losses+radiation leakages) and bend losses. The minimization of propagation losses along a ring resonator can be achieved by reducing the radius R however at the cost of an increase of bend losses. On the basis of a Finite-Element-Method, Tsilipakos *et al* have shown that a good compromise between propagation losses and bend losses is obtained for DLSPPW ring resonators with $R = 5\mu m$. Starting from this value, RTRs with radius around $5\mu m$ have been fabricated and characterized. Figure 3.3 shows the spectra of RTR with $L = 2\mu m$, and increasing radius of $R = 4.5, 6.5$ and $7.5\mu m$. The value of L chosen for this experiment is just an initial reasonable guess that does not necessarily ensure optimum extinction ratio for the RTR. The transmission spectrum of the RTR with $R = 4.5\mu m$ exhibits two resonances over the spectral range of interest whereas three are visible for $R = 6.5\mu m$ and $R = 7.5\mu m$. From equation (3.3) it is clear that increasing the radius R reduces the Free Spectral Range (FSR) between two resonances in agreement with the experimental results where the FSR is found to be 50 nm, 36 nm and 32nm for $R = 4.5\mu m$, $6.5\mu m$ and $7.5\mu m$ respectively. In addition, increasing the radius in the range reported here already changes the resonances by several orders of magnitude, thereby illustrating that the spectral position of these resonances does not follow a monotonous trend when R is varied.

The characteristic values of α and t for the plasmonic RTRs with varying radius are obtained by fitting the experimental power transmission spectra with the lossy resonator model previously described. The fitting is performed with the Levenberg-Marquardt method using α, t and ϕ_c as adjustable parameters. The rather short perimeters of the studied RTR lead to spectra featuring large FSR. The dispersion of coefficients α and t necessarily impacts the shape and the ER of the transmission dips observed over the full spectral range of interest. It has been admitted so far [60, 67] that the dispersion of α and t could be included in the power transmission model simply by

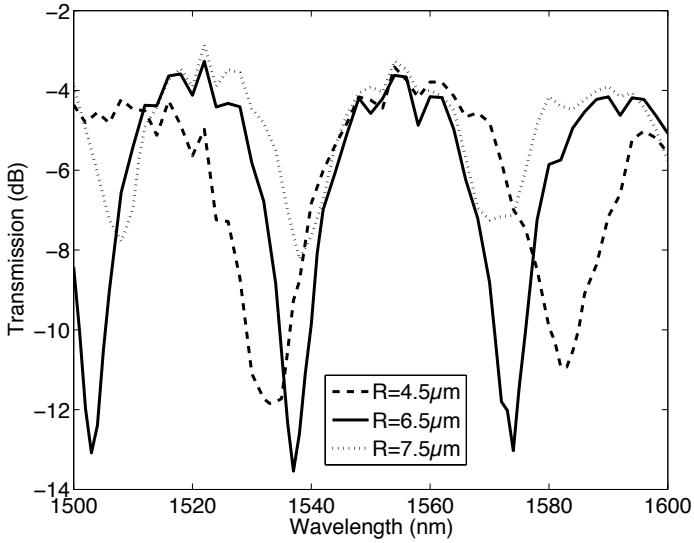

Figure 3.3: Power transmission spectra of resonators with different radius R The separation gap ($G = 240 \pm 40$nm) and the interaction length ($L = 2.0\mu m$) are fixed.

considering the dispersion of the complex effective index of straight DLSPPW modes. However, this assumption could fail when considering, as in the case reported here, spectral range as large as 100 nm. For example, for α, the dispersion of the damping constant of the DLSPPW mode account for the dispersion of α_{prpg} but does not help for the possible dispersion of α_b. For this reason, we find more appropriate to restrict the fitting to the spectral range of a single resonance of the experimental transmission spectrum. In this way, the resulting values of α and t are determined for a given resonance rather than assumed to be valid for the whole spectrum. Figure 3.4(a) shows a typical result of the multidimensional fit procedure applied to the central resonance of a RTR resonator with $R = 6.5\mu m$. Note that although we restrict the fitting procedure to a single resonance, the dispersion of the complex effective index of the DLSPPW mode is taken into account in the computations. The phase constant of the DLSPPW is given by the real effective index of a straight DLSPPW computed by using the differential method [55, 83] (Fig. 3.4(b)) whereas the dispersion of the damping constant is obtained from $k''_{SPP} = \frac{1}{2L_{SPP}}$ where L_{SPP} is the the damping distance measured along straight DLSPPWs and displayed in Fig. 3.4(c). The values of α and t obtained for the central resonance of RTRs of three different radii R are given in Table (3.1). The extinction ratio and quality factor computed from these values of α and t are also given along with the experimental values for ER and Q directly extracted from the spectra.

A maximum value of α (meaning a less lossy resonator) is found for the intermediate radius $R = 6.5\ \mu m$. A lower value of α is related to larger bend losses (α_b) for $R = 4.5\ \mu m$ while it is due to larger propagation losses (α_{prpg}) for $R = 7.5\ \mu m$. In agreement with

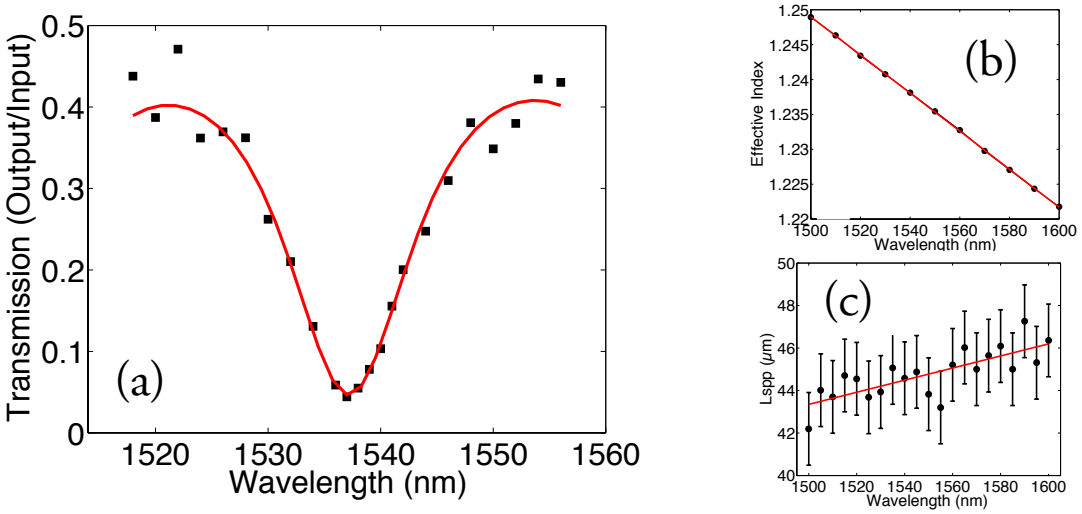

Figure 3.4: (a) Results of the fitting procedure applied to the central resonance of the spectrum corresponding to $R = 6.5\mu m$ displayed in Fig. 3.3. (b) Computation of the dispersion of the real effective index of a straight PMMA DLSPPWs. (c) Experimentally measured dispersion of the damping distance of the plasmon mode along straight PMMA DLSPP waveguides.

Table 3.1: Characterization of the central resonance of the spectra recorded for increasing radius resonators (see Fig. 3.3).

R	t	α	α_{prpg}	α_b	Bend Losses	Q|Q_{exp}	ER|ER_{exp}
μm			dB	dB	$dB.rad^{-1}$		dB
4.5	0.59	0.34	-1.6	-3.0	-0.49	91|85	8|8
6.5	0.61	0.40	-2.2	-1.7	-0.28	136|122	9|10
7.5	0.72	0.34	-2.5	-2.2	-0.35	155|135	5|5

the theoretical results of reference [81], a trade-off between bend and propagation losses is found for resonators featuring a radius around 6 μm. For this intermediate radius, t being significantly larger than α suggests that this resonator is weakly coupled. This weak coupling leads to a moderate extinction ratio around 10 dB. The loaded quality factor $Q = 130$ predicted by the model (Equation 3.9) is in good agreement with the experimental value $Q_{exp} = 122$. The observed weak coupling suggests that better extinction ratios should be obtained provided that the interaction length is increased. In order to test this hypothesis, resonators with a fixed radius of $R = 5.8\mu m$ and increasing interaction length have been fabricated. The separation gap is in the same range as before. The spectra obtained for these RTRs are displayed in figure 3.5. The RTR perimeter increasing when L increases, both the FSR and the spectral positions

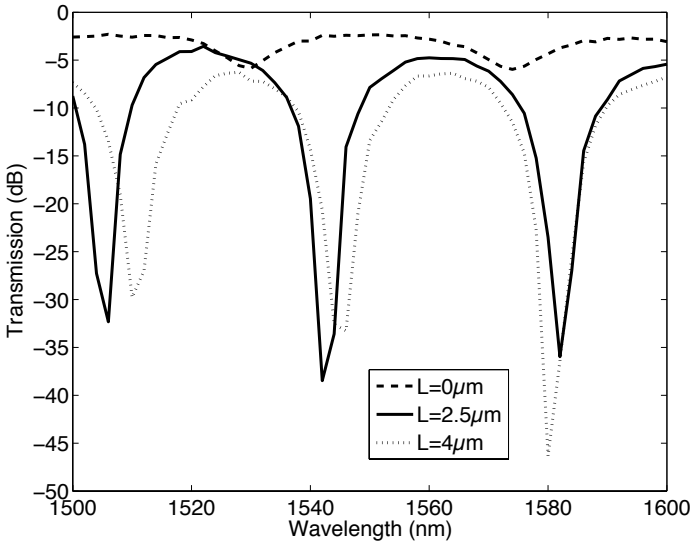

Figure 3.5: Power transmission spectra of resonators with increasing interaction lengths L. The separation gap ($G = 240 \pm 40$nm) and the radius ($R = 5.8\mu m$) are fixed.

of the resonances are affected by the value of L. However, it is clear that changing the interaction length changes mainly the extinction ratio. The interest of plasmonic racetrack shaped resonators is then unambiguously demonstrated by these results where a roughly 25 dB improvement of the extinction ratio is obtained by increasing L from 0 (ring resonators) to 4μm. The coefficients α and t for these resonators are given in table 3.2.

Table 3.2: Characterization of the central resonance of the spectra recorded for R=5.8μm resonators when the interaction length L is increased (see Fig. 3.5).

L	t	α	α_{prpg}	α_b	Bend Losses	Q|Q_{exp}	ER|ER_{exp}
μm			dB	dB	$dB.rad^{-1}$	dB	dB
0	0.82	0.41	-1.8	-2.0	-0.32	132|128	3|3
2.5	0.40	0.38	-2.0	-2.2	-0.35	107|123	28|17
4	0.34	0.33	-2.2	-2.7	-0.42	108|88	32|27
4.5	0.25	0.27	-2.2	-3.4	-0.54	104|101	26|26

For $L = 0\mu m$, the resonator is clearly weakly coupled. When increasing L, the value of t decreases due to the improved coupling from the bus waveguide to the resonator. As expected, the power loss factor decreases with increasing L in such a way that the critical coupling condition ($\alpha = t$) is obtained for L around 2.5 μm. For such an interaction

length, the loaded quality factor is around Q =110. When increasing the interaction length, we still observe a quasi critical coupling for $L = 4\mu m$ and $L = 4.5\mu m$, but the losses become unavoidably larger (smaller α) than in the case $L = 2.5\mu m$: this regime of larger L leads to extra propagation losses (due to the larger resonator's perimeter) that are compensated by the energy transfer through the enlarged coupling length. By examining the values of the bend losses obtained when varying L for the fixed radius of the experiments, we find the unexpected behavior that the observed bend losses increase with L. This result shows that the equation $\alpha = \alpha_{prpg} \times \alpha_b$ where α_{prpg} is the propagation loss factor for a straight DLSPPW is rather inaccurate. It is likely that the damping constant of the DLSPPW mode of the curved waveguide is significantly different from that of a straight waveguide. Therefore, the assessment of the contribution of the bend losses to the total losses is certainly more subtle than implicitly assumed using standard models. Note that this finding is consistent with the results obtained by momentum-space spectroscopy on bend DLSPPWs performed in chapter 2, where for small radii the reciprocal space images could not been related to an analytical model that does not include the transverse modal field shape.

3.1.4 Thermo-optical response of racetracks resonators

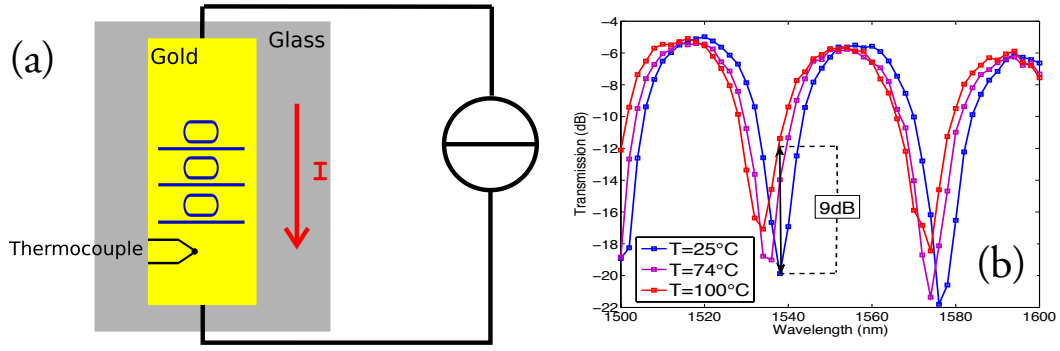

Figure 3.6: (a) Schematic view of the experimental set-up used for the thermo-optics DC characterization of the resonators. (b) Change of the transmission spectra of the resonator with $R = 5.8\mu m$, $L = 2.5\mu m$ and $G = 240 \pm 40nm$ as a function of the temperature.

First results of thermo-optical low frequency modulation of DLSPPW ring resonators ($L = 0$) have recently been reported [82]. The results of the previous section show that a RTR with a radius $R = 5.8\mu m$ and an interaction length of $L = 2.5\mu m$ is a good compromise in terms of quality factor and extinction ratio and clearly provides a significant improvement relatively to the figures achievable by using simple ring resonators ($L = 0$). Therefore, this paragraph addresses the thermo-optical performances of these optimized RTR. As shown schematically in Fig. 3.6(a), the RTRs are heated by flowing an electrical current through the 3 mm-wide gold strip on which the plasmonic resonators are implemented.

A micro-thermocouple is thermally connected to the metal film by means of a droplet of thermal grease. By calibrating the response of thermo-couple on a hot plate of controlled temperature, the temperature of the gold film corresponding to a given current intensity has been estimated. Figure 3.6(b) shows the spectra of the RTR recorded for different current intensities corresponding to three different temperatures. Let us note that these temperatures correspond to the data provided by the thermo-couple and are only indicative of the average temperature of the waveguide. At room temperature, the central resonance is peaked at 1538 nm whereas for T around 373 K, the resonance is blue-shifted by about 4.5 ± 0.5 nm. This blue shift corresponds to an increase of the transmitted power level by about 9 dB. The change of the transmitted level is illustrated in Figure 3.7. In the cold state, the RTR is resonant when the wavelength in

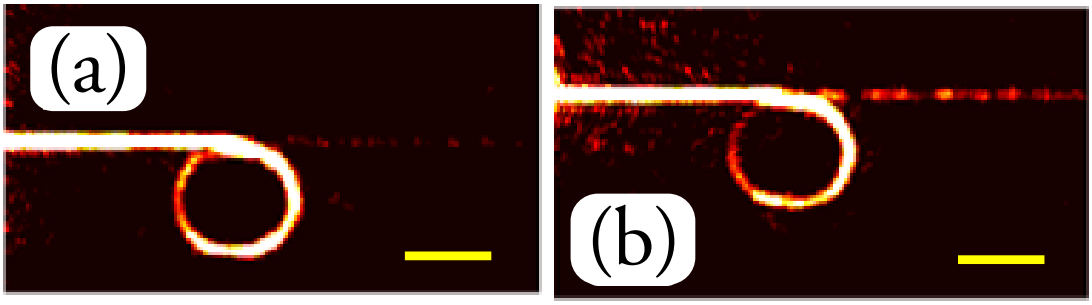

Figure 3.7: (a) Radiation leakage image recorded at $\lambda = 1538$ nm of the RTR ($R = 5.8\,\mu$m, $L = 2.5\,\mu$m) at room temperature (298 K) (scale bar=10μm)(b) Same as (a) except for the temperature of 373 K.

vacuum $\lambda = 1538$ nm (see Fig. 3.7(a)). Heating the resonator and keeping the incident wavelength at 1538 nm causes the transmission level to increase as shown in Fig. 3.7(b). Since the PMMA thermo-optical coefficient is negative ($\frac{\partial n}{\partial T} = -1.05 \times 10^{-4}\,K^{-1}$), if the temperature of the polymer is increased, the effective index of the DLSPPW mode decreases and leads to the observed resonance blue-shift. At room temperature, the resonance at the free space wavelength $\lambda = 1538$ nm corresponds to the mode order m=33 of Eq. 3.3 ($n_{eff} = 1.238$). Assuming that the temperature of the thermo-couple corresponds to the average temperature of the polymer waveguide, we find that the *effective* thermo-optical coefficient $\frac{\partial n_{eff}}{\partial T}$ is around 47 % of the thermo-optical coefficient of the polymer itself. This result is in fair agreement with the effective thermo-optical coefficient of $\frac{\partial n_{eff}}{\partial T} = 0.95\frac{\partial n}{\partial T}$ expected theoretically in Ref. [81] for a temperature rise of 100 K when taking into account the experimental uncertainty on the polymer temperature. For a temperature rise of about 110 K, we observe a blue-shift of the experimental spectra of about 6 nm, however we note that by cooling down the sample we could not retrieve the initial cold state spectrum. This observation indicates that for such a heating temperature, the structural parameters of the resonator have been degraded, in particular a narrowing of the separation gap has been noticed indicating

that PMMA resonators should not be operated at temperatures larger than 408 K.

RTR thermo-optic filter summary

In summary, experiments assessing the performances of plasmonic racetrack resonators made of a PMMA bus waveguide coupled to a PMMA racetrack shaped resonator deposited onto a thin gold film have been reported. By recording the radiation leakage images over the telecom frequency range, the transmission spectra of resonators featuring different radius and interaction length has been measured. RTR featuring a radius around 6 µm has been found to achieve the best trade-off between bend and propagation losses. For a separation gap around $G = 250$ nm, the critical coupling for resonators with such a radius is obtained for an interaction length around $L = 2.5$ µm. This particular size of gap is of great interest since it corresponds to the limit of resolution provided by common UV lithography, meaning that the results could be used further for industrial applications. With these structural parameters, the typical loaded quality factor is $Q = 110$ and extinction ratios between -20 and -30 dB are achievable. By connecting electrically the gold thin film and heating the resonators, we have demonstrated a thermo-optically controlled blue shift of the RTR resonance around 4.5 nm for a temperature rise of about 75 K. Such a shift leads to a 9 dB change of the transmitted power. These performances are not sufficient to qualify the PMMA as the appropriate loading material for DLSPPW resonators when targeting applications such as thermo-optically controlled plasmonic routers. However, the results reported in this work clearly indicate that changing the loading material of DLSPPW components to a polymer with a refractive index close to the refractive index of PMMA but featuring an approximately three times larger thermo-optical coefficient than PMMA would provide a relevant application potential. The study of thermo-optical 2×2 routers using a high TOC polymer is presented in the following with first the X-Add-Drop configuration that takes benefit of the geometrical optimization of RTRs [101].

3.2 Thermo-optical control of X-Add-Drop 2×2 DLSPPW routers

In order to reach the best performance possible for thermo-optical routing applications, the standard PMMA used so far as loading material is now replaced by a cycloaliphatic acrylate polymer, also known as Cyclomer. Prior to the lithography steps, this polymer exhibits a high TOC of $\partial n/\partial T \sim -3 \times 10^{-4} K^{-1}$ (extracted from ellipsometry measurements) and a refractive index of 1.53 at telecom wavelengths (1500-1600nm).

3.2.1 High TOC polymer processing

The Cyclomer is originally made to be processed by UV lithography and not known as an EBL resin. Thus for the purpose of this work, we have developed a fully new fabrication process. The first EBL attempts indicated that this polymer is much more sensitive than PMMA. Typical dose for EBL of Cyclomer are 2.8 µC/cm^2 at 15 kV. Taking in account the high sensitivity of Cyclomer imposes to adjust several hardware parameters during fabrication process.

In order to test the quality of our process, we first reproduce the performances of a single mode DLSPPW and RTR configuration that will be then used as a building block for the 2×2 X-Add-Drop routing system shown in the following.

DSLPPW made of Cyclomer

A good compromise between resolution, adherence and overall ridges quality has been reached by decreasing largely the dose during the lithography (from $172\,\mu C/cm^2$ for PMMA at 20kV to $2.8\,\mu C/cm^2$ at 15 kV). The dose being proportional to the ratio between electron beam current and dwell time, both values have been decreased to a level close to the limit of our equipment to reach such a low dose. A LRM characterization of a single mode DLSPPW has been realized to confirm the efficiency of the process of Cyclomer DLSPPW fabrication (Fig. 3.8).

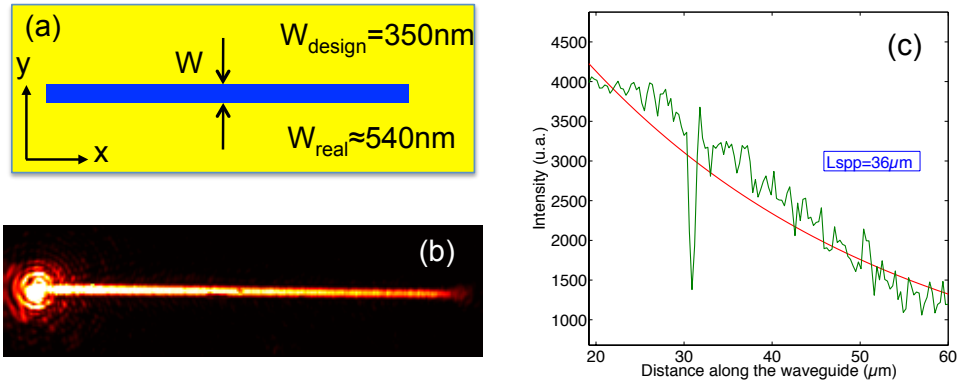

Figure 3.8: (a) Schematic view of a DLSPPW, (b) LRM image of a DLSPPW made of Cyclomer, (c) Exponential decay measurement along the Cyclomer waveguide axis.

The resulting waveguide reproduces the performances obtained for a similar PMMA DLSPPW with a propagation length close to 40 µm (Fig. 3.8(c)), for a 540 nm width (Fig. 3.8(a-b)). One can note that even with the diminution of the dose during the electron beam exposure, high proximity effects are still present (350 nm width programmed gives 540 nm waveguide width). However, these proximity effects being known, it's possible to anticipate over-exposure to obtain well resolved gaps, essential for evanescent coupling-based structures.

RTR made of Cyclomer

To confirm that DLSPPWs made of cyclomer are suitable for thermo-optic devices, a last test is performed on RTRs that requires a precise manufacturing. An optical image of RTRs made of Cyclomer is shown Figure 3.9(b), displaying well resolved waveguide and resonators.

The LRM images displayed in Fig. 3.9 (c) and (d) reveal that the high extinction ratios obtained previously by the geometrical optimization of RTRs with PMMA are reproducible with Cyclomer (over 30 dB extinction ratio between the resonant and off-

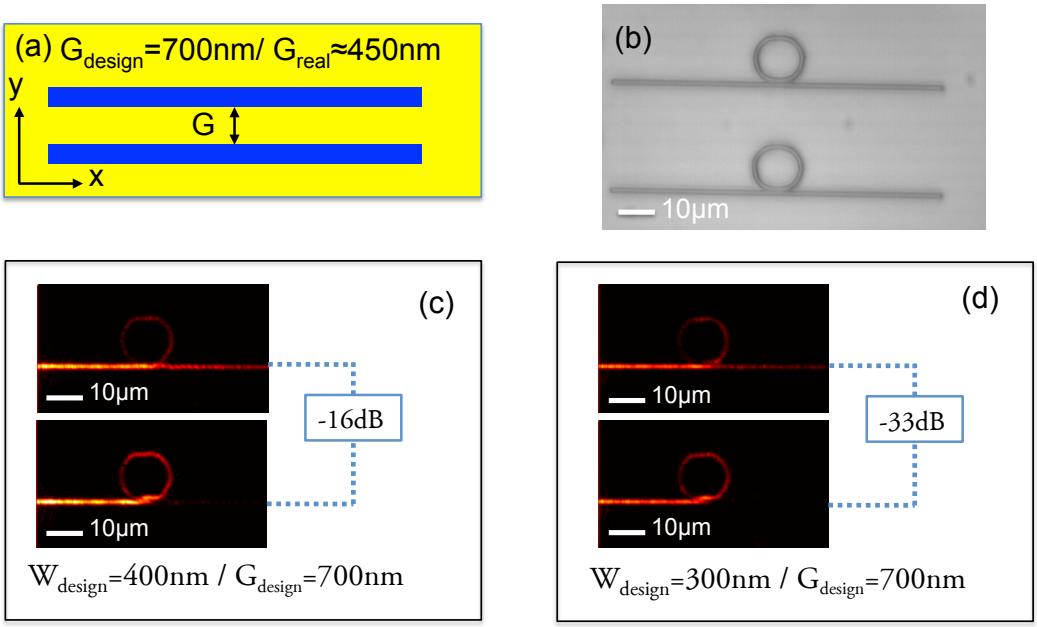

Figure 3.9: (a) Schematic view of a gap between two DLSPPW, (b) Optical images of RTR made of Cyclomer, (c-d) LRM images of resonant/non-resonant RTR for different lithography parameters.

resonant states). The proximity effects (Fig. 3.9 (a)) are thus sufficiently well controlled to obtain reproducible DLSPPW structures made of Cyclomer even width small gaps (G<400 nm).

3.2.2 X-Add-Drop Experimental images

The X-Add-Drop routing design [101, 106, 107], is shown Fig. 3.10. Two RTRs (resonators and bus) are placed at 90° in such a way that each resonator is in close proximity of both bus waveguides (Fig. 3.10(a)). Thus both RTRs interact with the two bus waveguides over a respective distance L_1 and L_2 that can be adjusted separately. Figure 3.10(b) shows an SEM image of a typical X-Add-Drop made of Cyclomer, with in insert zooms on the four small gaps of each interaction length areas. This configuration possesses two Input ports and two Output ports (Fig. 3.10(a)). The Output ports are labeled Through ports if the light is coming from the same Input bus waveguide, and they are labeled Drop ports if the light is coming from a perpendicular Input port. Similarly to the case of a simple RTR, it is a sum of constructive or destructive interferences that directs or redirects the incident signal between the two output ports. For the Through ports, the transmission spectra (Fig. Figure 3.10(c)) is similar to the single RTR configuration shown in the previous section. For the perpendicular Output ports, the transmission spectra shows several resonances related to the interference of three out-coming light: the light dropped by the first resonator, the light dropped by the second resonator

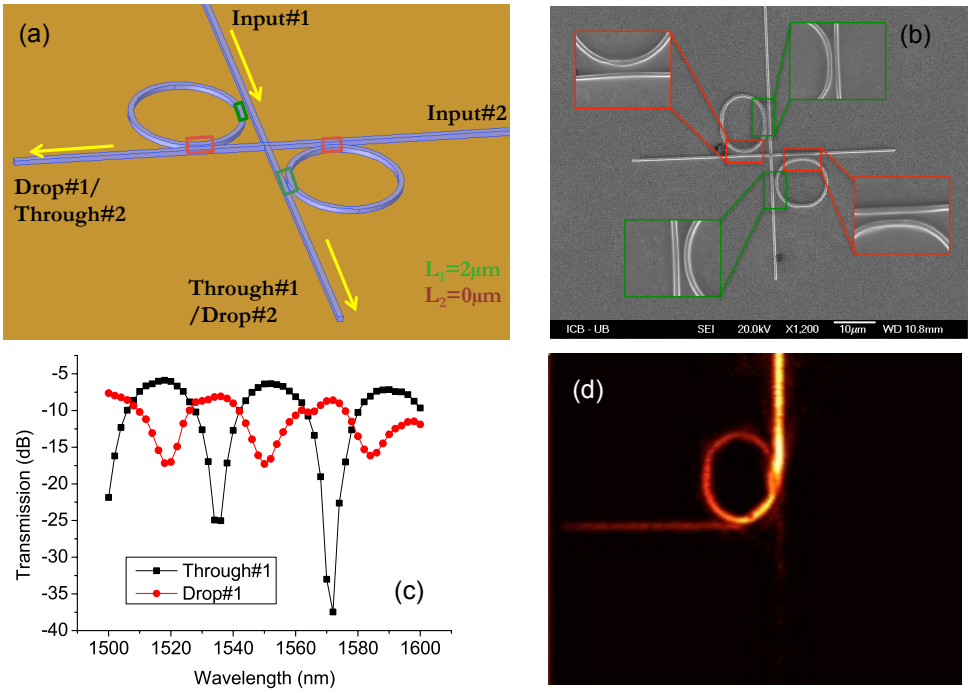

Figure 3.10: (a) Schematic view of the 2×2 X-Add-Drop design, (b) SEM view of an X-Add-Drop made of Cyclomer (inserts: zoom on Gaps), (c) Typical transmission spectra for the two output ports, (d) LRM image corresponding to (c) at $\lambda = 1500$.

(also known as "Q-route"), and the light directly scattered by the central waveguide crossing [101]. An example of LRM image is shown in Figure 3.10(d), corresponding to the transmission spectra at $\lambda = 1500$ where the intensity is maximum for the Drop port and minimum for the Through port.

By changing the overall temperature of the system, the resonance of each RTRs is changed allowing symmetric 2×2 routing operations. This system is relevant in term of the footprint since such a component can be enclosed in a typical surface of ~100 μm^2.

3.2.3 X-Add-Drop Thermo-optical routing

To evaluate the thermo-optical performances of the 2×2 X-Add-Drop routers, the LRM procedure described in the previous section is again applied (see Fig. 3.2). Considering the symmetry of our X-Add-Drop, configuration, the transmission spectra of the Drop and Throught ports are expected to be equivalent, whatever the input port. In this respect, only three regions of interest at the Input/Through/Drop ports #1 are used to measure the output over input power on both output directions.

The Figure 3.11 depicts the X-add-drop device at two temperature states, unheated (Fig. 3.11 (a)) and heated (Fig. 3.11 (b)). The heating has been provided by a 500 mA

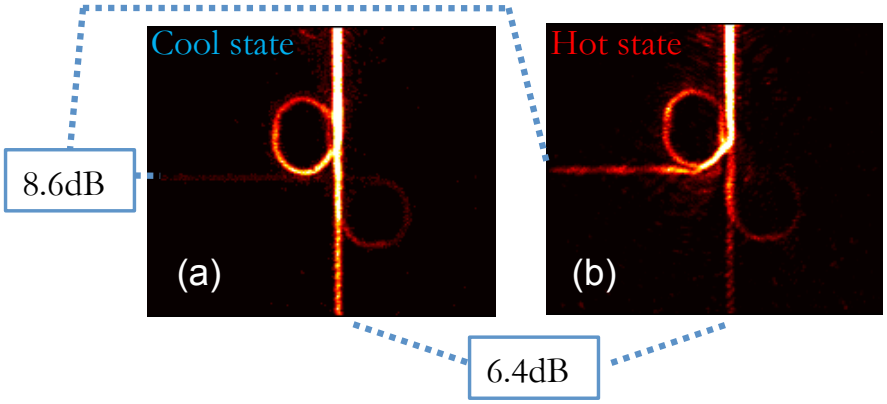

Figure 3.11: (a) LRM image (1520nm) of the device at the cold state. (b) Same as (a) in the hot state.

DC current flowing through the 3mm-wide underlying gold film, as performed for the study RTRs made of PMMA ($\Delta T \leqslant 75$ K). At the cool state (room temperature), the input signal goes to the Through port #1 whereas for the hot state, the signal is routed to the Drop port #1.

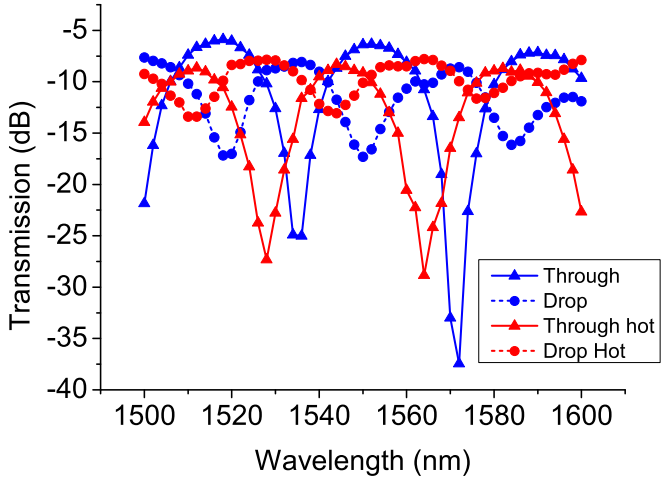

Figure 3.12: Transmission spectra for the unheated (blue) and heated (red) states for both Through (Straight, triangles) and Drop (Dashed, circles) ports.

By sweeping the incident wavelength, we extract the transmission spectra on both output ports for both temperature states, as shown Fig.3.12.

As expected, by using a high TOC polymer a large shift in the blue is observed for both output ports ($6 \sim 8$ nm, to be compared to the 4.5 nm obtained with standard

PMMA RTR). From this transmission spectra, we can select the optimum wavelength for which the extinction ratio between the heated and unheated states is maximum for both outputs at the same time. We found that the best performances for this structures is obtained for $\lambda = 1520$ nm, in good agreement with LRM images of the Figs 3.11 (a) and (b) with 8.6 dB and 6.4 dB of extinction ratio for the Drop and Through ports respectively.

3.2.4 Comparison with FEM

As exemplified for RTRs, the performances of evanescent coupling structures depend critically on the quality of the gaps separating the interacting structures. Owing to fabrication imperfections, a quantitative comparison of our experimental results with numerical computations is highly challenging. Hence we restrict our analysis to a qualitative comparison with numerical modeling. In this context, a good figure of merit characterizing the performances of the X-Add-Drop filter is given by the extinction ratio ER defined for each output ports as:

$$ER(dB) = |T_{cool}(dB) - T_{hot}(dB)| \tag{3.10}$$

Where T_{cool} and T_{hot} refers to the transmission levels in dB for the cool and hot states. Experimental and computed ERs are plotted in Fig. 3.13 (a) and (b) respectively.

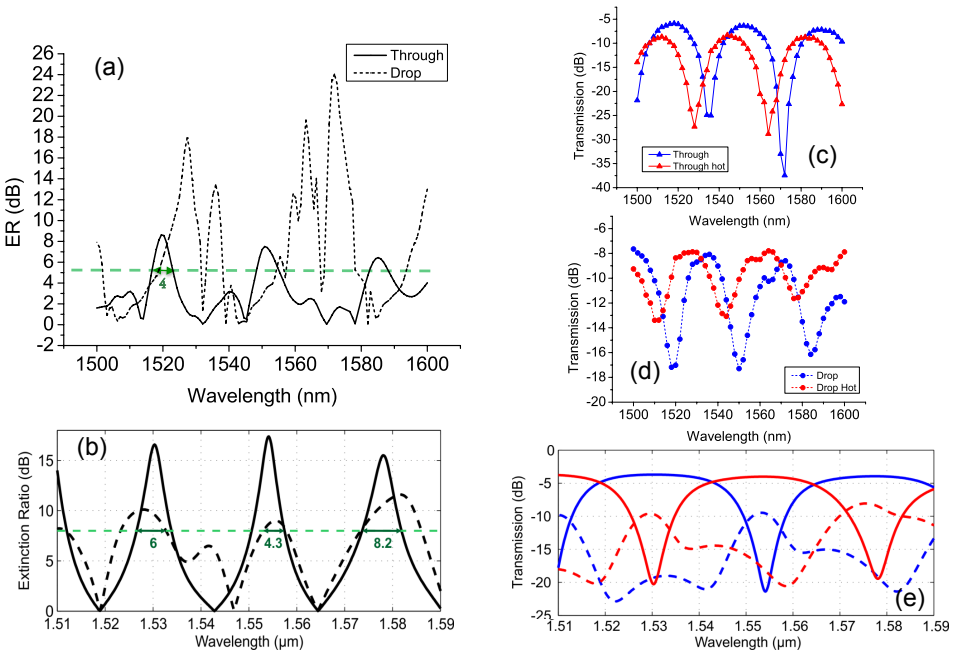

Figure 3.13: (a) and (b) Experimental and Numerical ERs of X-Add-Drops. (c-d) and (e) Corresponding transmission spectra cool and hot states used to calculate the ERs.

The numerical spectra, (FEM calculations provided by one of the Platon partner from *Tsilipakos et al.*, AUTH, Greece), informs us about the performances expected for perfect structures with the equivalent TOC ($\partial n/\partial T \sim -3 \times 10^{-4} K^{-1}$) and estimated heating ($\Delta T \sim 100$ K).

When comparing the figure of merit, the experimental performances (5.2 dB over 4 nm) are close to the calculated one (7.5 dB over $4 \sim 8$ nm). The difference can be explained by two factors. First the electrical heating is not perfectly controlled and thus the measured hot temperature could be over estimated. Second, TOC of the electron-beam processed Cyclomer could be lower than the unprocessed one.

The experimental transmission spectra, Figs. 3.13 (c) and (d), cannot be directly compared to the numerical one (Fig. 3.13 (e)). Any change on the geometry would modify the position of the peaks, and the extinction ratio efficiency. However, the simple peak shape Fig. 3.13 (c) of the Through port spectra and double peak shape Fig. 3.13 (d) of the Drop port spectra, reproduces well the numerical expected shapes.

X-Add-Drop routers summary

Using a new loading material (cycloaliphatic acrylate polymer), exhibiting a high Thermo-Optical Coefficient of $-3 \times 10^{-4} K^{-1}$, a dramatic enhancement of the device performances has been obtained, compared to other commonly used thermo-optic materials, such as the PMMA. The previous geometrical optimization of RTRs made of PMMA established a range of interaction lengths useful to obtain a first efficient 2×2 DLSPPW routing device. The performances have been quantitatively compared to FEM calculations, highlighting some uncertainty of temperature measurement and/or TOC changes after electron-beam processing. Extinction ratios of $6 \sim 8$ dB have been reached for a $\sim 100 \mu m^2$ router.

3.3 Thermo-optical control of plasmo-photonic mode DLSPPW routers

The routing designs we have considered so far rely all on evanescent coupling. Although appealing for their compactness, these structures suffer from low tolerance to fabrication imperfections. It is then of practical interest to investigate structures that do not rely on evanescent coupling. We focus now on the so-called Dual-Mode Interferometer. Single mode DLSPPWs support a quasi-TM fundamental mode (Figure 3.14(a) and (c)). However, sufficiently wide DLSPPWs are known to support a second-order mode with a large field component in the transverse-electric (TE) direction and an intensity peak (Figure 3.14 (b)), not situated at the metal/dielectric interface, but rather towards the center of the dielectric loading [55, 67, 108]. Owing to these properties, the second order mode suffers smaller propagation losses than the quasi-TM fundamental mode and can be labeled as a photonic mode or quasi-TM mode since the energy in the TM direction is non-zero (Figure 3.14 (d)). Although identified by many authors [48, 55] for quite some time, this modes have not been yet used in practical devices. We found numerically typical effective index of $n_{eff}^{(1)} = 1.347$ and $n_{eff}^{(2)} = 1.054$ ($\Delta n_{eff}^{FEM} = 0.293$) for

the plasmonic and photonic modes respectively.

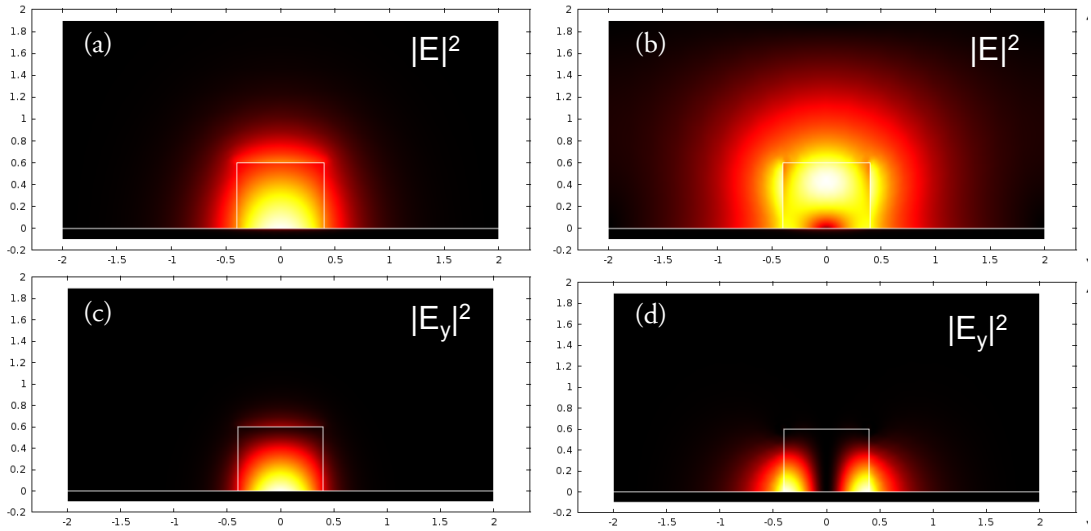

Figure 3.14: (a) Electric field map norm of the quasi-TM mode. (b) Electric field map norm of the quasi-TE mode. (c) and (d) Square norm of the Electric field map in the direction perpendicular to the surface for the quasi-TM and quasi-TE mode respectively.

In this section, we report on a efficient and compact 2×2 plasmo-photonic router relying on the interference of the fundamental plasmonic mode and a second-order identified as the photonic mode of the DLSPPW. Unlike previous plasmonic router designs [82], in our Dual-Mode configuration, the low-damping photonic mode contributes to the reduction of the insertion losses of the device.

3.3.1 DMI Experimental images

The samples we consider were fabricated by EBL applied on a Cyclomer (thickness ~ 540nm) spin-coated onto a gold strip (surface $3 \times 15\text{mm}^2$, thickness of 60nm) deposited onto a clean glass slide. Figs. 3.15(a) and (b) shows SEM images of the two input and output junctions respectively of a typical fabricated sample. The two Y-junctions are connected to a 119 µm-long Dual Mode Interference (DMI) waveguide. By injecting a current through the gold film, the polymer is heated, and the effective indices $n_{\text{eff}}^{(1)}$ and $n_{\text{eff}}^{(2)}$ of the two modes traveling along the DMI region are changed. This change modifies the beating length of the two interfering modes and eventually routing is achieved provided that the DMI waveguide is of sufficient length [108]. The optimum DMI length L is given by $2L = \lambda / \mid \Delta n_{\text{eff}}^{(1)} - \Delta n_{\text{eff}}^{(2)} \mid$ where λ is the free-space wavelength at the frequency of interest and where $\Delta n_{\text{eff}}^{(1,2)}$ denotes the effective index change for each mode when routing from the unheated (cool) to the heated (hot) state. If the DMI waveguide length is an even (or odd) multiple of the beating length, then the router will operate in the BAR (or CROSS) state. Figure 3.15(c) shows a LRM image of the beating

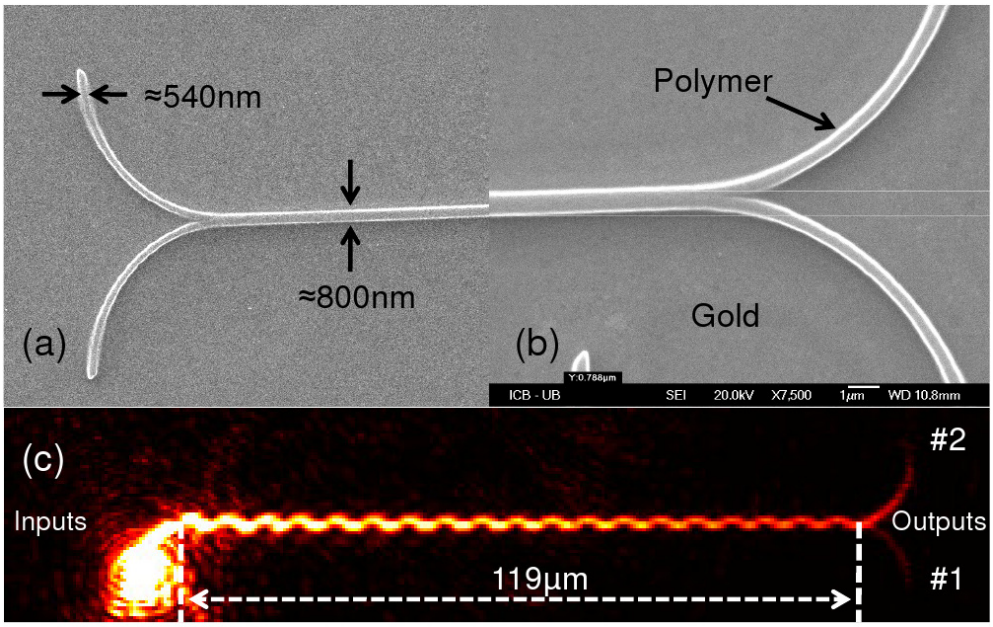

Figure 3.15: (a)(b) SEM images of a typical DLSPPW DMI router input and output made of cycloaliphatic acrylate polymer lying on a thin gold film. (c) LRM image of the DMI router we consider room at temperature for a free-space wavelength of 1566nm.

pattern in the cool (room temperature) state for $\lambda_0 = 1566$ nm. The Half-Beating length given by $L_{HB} = \lambda/2\Delta n_{eff}^{1,2}$, is measured experimentally: $L_{HB}^{exp} \simeq 3\mu m$, in good agreement with the numerical mode analysis giving $L_{HB}^{FEM} = 1.55/2\Delta n_{eff}^{FEM} = 2.65\mu m$. The input beam is focused on the bottom-left input port and exits through the upper-right output port, i.e. the router operates in the CROSS state. The two input/output ports of the Y-junctions are made of arced (10μm-radius) single-mode DLSPPW with a 540nm-wide polymer ridge whereas the DMI region is a polymer ridge with a width of $w \simeq 800$nm carefully designed in order to ensure that only two guided modes are supported in both hot and cool states [108]. The two modes supported by the DMI region are the fundamental DLSPPW mode and the second order mode respectively labeled TM_{00} and TE_{00} hereafter. The TM_{00} mode is naturally the fundamental plasmonic mode, whereas the second-order TE_{00}, as discussed earlier, resembles more the photonic mode. Moreover, for the particular dimensions considered here, the TM_{00} and TE_{00} have cross-sectional electric field distributions of opposite symmetry (symmetric and anti-symmetric respectively) for the component normal to the metal. Note that unlike a pure photonic mode, the TE_{00} mode we consider here has a significant electric field component in the direction perpendicular to the metal film [108]. Consequently, provided that the input waveguide is laterally shifted compared to the DMI axis, the incident TM_{00} mode can excite equally well the two DMI waveguide modes thus giving raise to the mode-beating employed for the routing [108].

3.3.2 DMI Thermo-optical routing

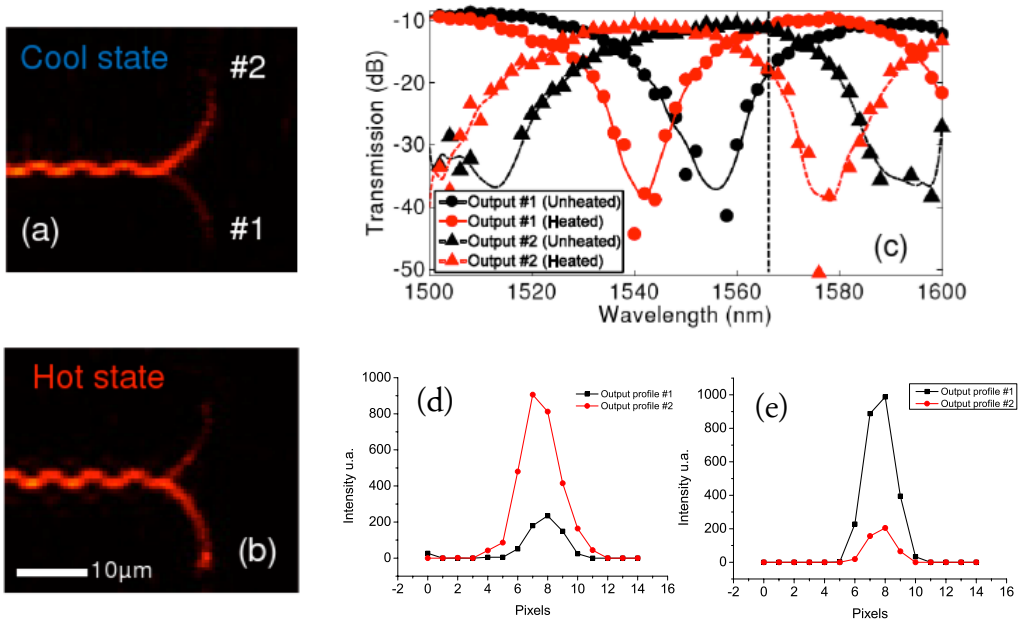

Figure 3.16: (a) LRM image (1566nm) of the device output at the cold state. (b) Same as (a) in the hot state (c) Experimentally measured transmission spectra at the two DMI router output ports, for the cold and hot states. (d) and (e) Intensity profiles of the outputs of the cool and hot states respectively.

The LRM images of the output ports of the device are displayed in Figs. 3.16(a) and (b), for the cool and hot state respectively. In this experiment, the hot state is obtained by injecting a 400 mA DC current through the gold film (cross-section 3000×0.06 µm^2). According to a reading of a shielded micro thermocouple placed in contact with the metal film at a distance of a few millimeters from the waveguides, the heating current induces a temperature raise in the polymer in the order of $\Delta T \simeq 60$K. At a given wavelength, the input and output levels are obtained by integrating the intensity of the corresponding LRM image over areas of interest located respectively at the input and the output ports as performed previously for RTRs and X-Add-Drop routers.

By sweeping the incident wavelength from 1500 to 1600nm and by normalizing the output signal to the input, the transmission spectra plotted on Fig. 3.16(c) has been obtained. For both temperature states, differences between the highest and the lowest transmission levels larger than −20dB are achievable. Note that for both temperature states, the insertions losses are lower than −10dB for a device with a total length up to 150 µm. Compared to a straight single-mode waveguide of equal length, where an attenuation of at least −15dB is expected, the damping along the DMI region is rather moderate. This is due to the fact that in the DMI waveguide the guided power is

splitted between the two supported modes, and the second-order mode of the DMI (TE_{00}) has lower propagation-losses compared to the fundamental DLSPPW mode (TM_{00}) [108]. Indeed, for the DMI we consider here, the TE_{00} mode has a $1/e$ damping distance at 1550nm (L_{spp}=100µm) more than two times larger than for the TM_{00} modes (L_{spp}=45µm).However, for DMI waveguides of moderate length (around 100µm), this difference does not impact sufficiently the amplitude of the mode beating to inhibit the routing effect. For symmetric 2×2 routing operation, the router Extinction Ratio (ER) (*i.e.* the ratio between the transmission levels when routing from the cool to the hot state) of each output port should be of equal magnitude and of opposite sign. These conditions apply for the wavelength of 1566nm leading to an ER around 7dB (see vertical line in Figure 3.16(c)). The Figs. 3.16(d) and (e) show the intensity profile at both output ports for both temperature states at the optimum thermo-optic wavelength, proving the symmetric routing operation. Note that for a given length of the DMI waveguide, the wavelength leading to a symmetric routing effect could be slightly adjusted by offsetting the temperature of the cool state.

3.3.3 Comparison with FEM

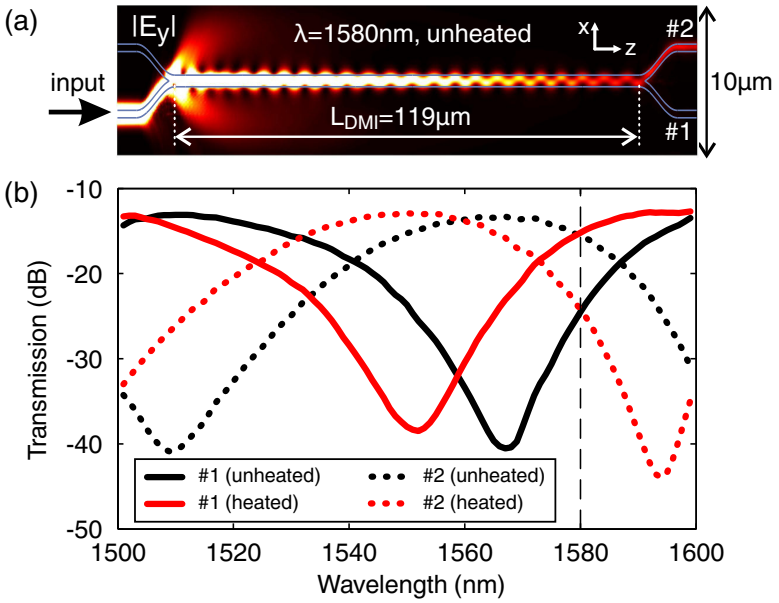

Figure 3.17: (a) Computed intensity beating pattern of the electric field component perpendicular to the metal film (axes not to scale). The DMI length is 119µm, the polymer layer is in the cool state and $\lambda = 1580$nm. Light is launched on the lower input port and is directed toward the opposite output-port # 2. (b) Transmission Spectra for the cold and hot states, at the two output-ports for a temperature increase of $\Delta T = 15$K.

The beating patterns and the measured transmission spectra acquired from the experimental setup have been compared to the ones produced by a finite-element beam propagation method (FE-BPM) from one of the Platon partner [109]. The FE-

BPM is a numerical tool very well adapted to the modeling of long axially arranged components such as the DMI router. Employing the same structural and thermo-optical parameters as the ones of the fabricated samples, the numerical investigations to field distributions and transmission spectra in qualitative agreement with our experimental results. Figure 3.17(a), depicts the numerically calculated beating pattern of the electric-field intensity, for a DMI length of 119μm, at the cool state and for a wavelength of 1580nm. The FE-BPM transmission spectra of Fig. 3.17(b), reveals an optimum routing ER of 9dB at 1580nm for a temperature increase of $\Delta T = 15K$, a Free Spectral Range (FSR) of 90-100nm and insertion losses of ~ 10dB. Noting that the red-shift of about 15nm observed in the simulated spectra originates from acceptable deviations in the fabricated sample dimensions, these spectral features, are in good agreement with the experimental ones. We note however that the theoretical temperature difference ΔT necessary to achieve the routing is clearly underestimated compared to the experimental value. This difference is attributed to a poor estimate of the waveguides temperature with the remotely located micro thermocouple.

3.3.4 Low frequency dynamic heating

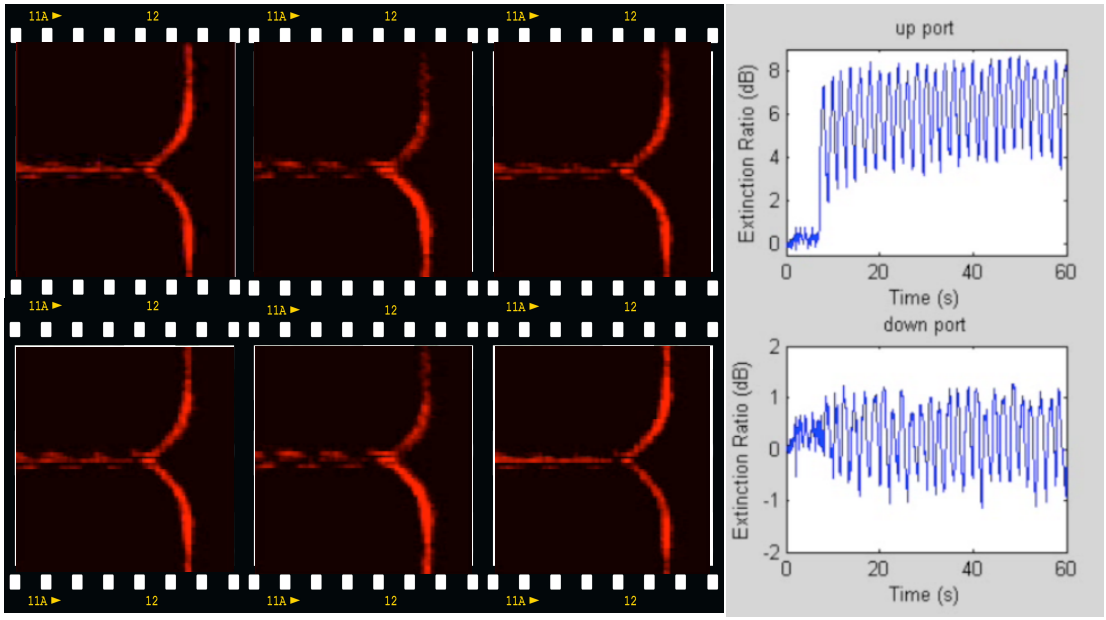

Figure 3.18: 0.5Hz dynamic heating partial sequence and extinction ratio in function of the time.

Beyond the performances extracted from the static cool and hot states of such a routing device, the dynamic heating of a standalone DMI router is of great interest since it could inform us on the maximum operating speed possible if the connection to the outer circuitry was perfect. Consequently, a low frequency AC current is now delivered to address dynamically the same structure, and the routing recorded by LRM images as

displayed Figure 3.18.

This sequence of images shows the fluctuations in time of the output intensity generated by a 0.5Hz AC square current (350 mA in the on state) and the extinction ratios of both output ports. Even if the dynamic heating is operated at low frequency, the LRM investigations have been limited by several factors. First, the quite large underlying electrode (cross-section 3000×0.06 μm^2) request a large amount of power to be heated. Unfortunately the dynamic electrical sources available in the lab were not sufficient to reach the 0.5 A necessary to get a symmetric routing. Furthermore, the frequency of routing has been limited by our detection technique. In fact, each LRM image needs from hundreds to thousand microseconds of integration time to be recorded. Thus the measurement of the time response of a standalone DLSPPW device cannot be obtained directly by LRM yet. This example shows clearly the need for a new characterization set-up for time resolved measurements. The development of a faster detection method coupled and to an efficient DLSPPW excitation using dielectric loaded grating has been recently demonstrated [110]. This approach will be operated on the next chapter dedicated to optically driven DLSPPW routers.

DMI routers summary

To summarize, we have reported on the fabrication and experimental demonstration of a thermo-optic 2×2 router based on dual-mode DLSPPWs supporting both the fundamental (or plasmonic) and the second-order (photonic) mode. The routing configuration studied is based on a Dual Mode Interference (DMI) design where the thermal tuning of the beating-length created by the interference of the plasmonic and the photonic mode in the dual mode waveguide is employed for the routing. Output-port extinction ratios of ~ 7dB have been measured in a 119µm-long DMI symmetric router, while insertions losses below -10dB are obtained owing to the contribution of the moderate damping of the photonic mode. The overall device experimental performances are found in good agreement with numerical simulation predictions. The thermal modeling of the device [81] indicates a routing time of $\simeq 1\mu s$ with this configuration, when using finite width electrodes instead of a macroscopic gold strip. The limitations of LRM for the evaluation of the response times on such a standalone structure have been highlighted, stressing the need for a characterization method not just relying on LRM imaging.

3.4 Conclusion

In summary, the fabrication and characterization tools presented in chapter 2 have been used to investigate the thermo-optical performances of various DLSPPW-based components. For instance, thermo-optic effects have been first measured through the use of RaceTrack Resonators. The geometrical parameters of this configuration have been optimized, to increase the quality factor of such a filter as compared to a ring resonator. Next, the thermo-optical performances of RTRs have been investigated by mean of LRM imaging. Through an electrical DC heating of the underlying gold film, an efficient

thermo-optical filtering of 9 dB has been measured for a temperature rise of about 75 K. Then, a high TOC polymer has been used to fabricate two kind of 2×2 routing elements. The first one, known as X-Add-Drop filter, is made of a double RTRs system crossed at 90° following the geometrically optimized design developed earlier. Reproducing the same electrical heating procedure as for RTRs, LRM images revealed high extinction ratio (6 ~ 8 dB), quantitatively comparable to numerical calculations. However, one evident drawback about this configuration is related to the low tolerance of fabrication deviation of efficient filters. in order to circumvent this limitation, we have considered next a 2×2 routing element relying on the interaction of two co-propagating modes traveling along a wide enough DLSPPW and denoted Dual-Mode Interferometer. The thermal tuning of this system modifies the beating length of the two modes, causing a symmetric 1×2 thermo-optical routing (~7 dB). This configuration is also appealing for its low propagation losses. Finally, the periodic electrical heating at very low frequency of the same device highlighted some limitations of the LRM method for the investigation of standalone DLSPPW components. In fact, the acquisition time required by the infrared camera being several order of magnitude higher than the expected time response of the devices, the dynamic measurement has been limited to few Hz instead of the MHz needed. A new Fiber-to-Fiber method will be described on the next chapter to overcome these limitations and provide response time measurements as well as true data transmission demonstration.

CHAPTER 4

Photo-thermal control of DLSPPW components

This chapter is dedicated to photo-thermal control of DLSPPW devices. So far, the thermal excitation of the components has been achieved by flowing a current through the metal film supporting the plasmon mode. In this approach, electrical and optical properties of the metal structure comprising the plasmonic waveguide are exploited. However, one can also imagine to exploit the strong dispersion of the metal optical properties in order to operate photo-thermal activation of the components [111]. Indeed, in the spectral region where inter-band transitions exist for the metal of interest, the metal exhibits a quite large absorption and hence operates a rather efficient light-heat conversion. Photo-thermal activation does not only open a route towards an "all-optical" control of plasmonic devices, but also offers the possibility to investigate situations such as short pulses excitation that has no equivalent when electrical activation is operated.

In the first section of this chapter, we discuss the properties of DLSPPW routers fabricated by using a polymer doped with metal nano-particles. We will demonstrate with this example the practical interest of photo-thermal activation of devices whose optical properties have been engineered in order to minimize their activation power.

In the second section, we discuss the results of all-plasmonic control of DLSPPW devices. In this case, the heating of the structures is produced by the absorption of SPP thin film modes launched either by total internal reflexion or by grating couplers. We also address specifically in this section the question of the response-time of the DLSPPW devices. In this respect, a set-up that does not rely on LRM is needed. We describe in the first paragraph of this second section a fiber-to-fiber set-up using efficient in and out grating couplers that can be operated for investigating the dynamic of DLSPPW devices or high-bit rate traffic along DLSPPWs.

4.1 Localised SPP for efficient light-heat conversion

In this first section, we consider the use of polymers doped with gold nanoparticles (NPs) to minimize the photo-activation power of DLSPPW thermo-optical components. Photo-thermal properties of NPs [112–114] have attracted much interest in the recent years for applications in fields ranging from nano-medicine (for a review see for exam-

ple [115]), biological applications [116], material processing [117, 118], micro-fluidic [119], nanophotonics [120, 121] but NP-doped materials have been only investigated a little in the context of dynamically controlled integrated optics devices. The DLSPPW devices we consider here are standalone 1×2 routers relying on Dual-Mode Interferometers, investigated numerically and experimentally in the section 3.3, and theoretically in Refs [108]. Unlike the previous chapter, the activation of the DMI routers is performed by using a pump beam with a frequency within the absorption band of the embedded NPs. On the basis of the LRM method used so far in this work, the photo-activated thermo-optical routers are characterized over the telecom frequency range. We show that the power necessary to photo-activate the NP-doped routers with a gold/polymer volume ratio in the range 0.5% is reduced by a factor 2.5 compared to un-doped routers. This factor is attributed to the enhanced absorption of the pump beam within the NP-doped polymer and not to a change of the thermo-optical properties of the polymer in the presence of the gold nanoparticles. Our experimental results indicate that significant further minimization of the activation power is still possible.

4.1.1 Samples fabrication

The samples were fabricated by electron-beam lithography applied to NP-doped or un-doped PMMA layer spin-coated onto a 80 nm-thick gold layer thermally evaporated onto a glass substrate. The NP-doped PMMA was obtained by dissolving solid PMMA (molecular weight 120K) into toluene and by subsequently mixing the resulting solution with commercially available (Aldrich, Ref. 660434) gold nano-particles (diameter ranging from 3 to 5nm) dispersed into toluene as well. When spin-coated onto a gold layer, the NP-doped PMMA layers feature pronounced colors ranging from light green to dark pink depending on layer thickness. Prior to the exposure, the PMMA layers were baked on a hot plate. For the NP-doped PMMA solution used for the fabrication of the samples investigated in the following, the volume occupied by the gold NP into the baked doped PMMA layers was estimated to be 0.52% of the solid polymer volume. This volume ratio has been computed from the density (0.9308) and gold concentration (2 % w/v) of the NP solution and from the known density of the 120K PMMA (1.118) and the experimentally measured concentration (0.22g/mL) of solid PMMA into the prepared PMMA-toluene solution. The volume ratio of 0.52% corresponds to a doping level of 2×10^{17} NP per cm^3 of solid polymer and a side-to-side average distance between the NPs in the range of 10 to 15nm. PMMA being a positive electron-beam resin, the routers were fabricated by exposing and eventually dissolving areas surrounding the plasmonic waveguides. In spite of the presence of the NPs, the optimum exposure doses ($165\mu C/cm^2$) were found to be similar for the doped and un-doped PMMA layers.

Scanning Electron Microscope (SEM) images of the routers fabricated following this process with the NP-doped PMMA resin are shown in Fig. 4.1. The DMI routers we considered are equipped with an input grating coupler (period= $2.45\mu m$) (see Fig. 4.1(a)) allowing a very efficient excitation of the device by means of a moderately focused beam (spot size = $30\mu m$) impinging at an angle of incidence of 30° for free-space

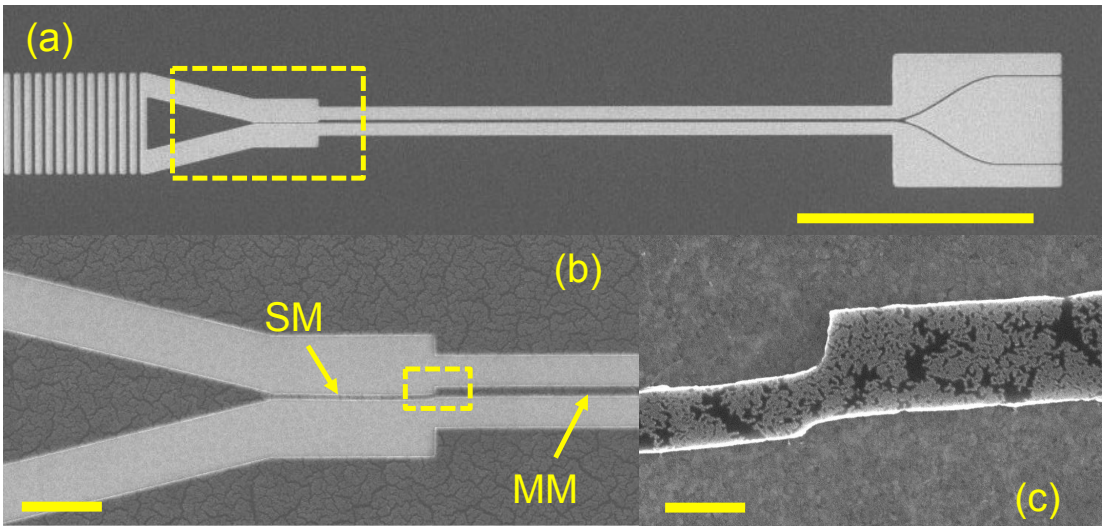

Figure 4.1: (a) SEM image of a NP-doped plasmonic DMI router (scale bar=50μm). The dark regions are coated with polymer, light-gray regions correspond to bare gold film. (b) Zoom onto the region corresponding to the dashed perimeter shown in (a) showing the single-mode (SM) and multi-mode (MM) waveguides (Scale bar=10μm). (c) Detail of the transition between the single-mode and multi-mode regions (Scale bar= 1 μm). The nano-particles are clearly visible on the DLSPPWs.

wavelengths ranging from 1500nm to 1600nm (this efficient excitation method will be widely discussed in the next section). Owing to the sensitivity of the InGaAs camera used in the following for the characterization of the routers, the efficiency of the grating couplers implemented at the input of the DMIs is not an issue at that stage. Thus we postpone the discussion of the design of the grating couplers to the second section of this chapter where the question of Fiber-to-Fiber characterization of the devices will be addressed specifically. The router we consider is comprised of the single-mode DLSPPW (labeled as SM in Fig. 4.1(b)) and a multi-mode waveguide with a typical length of 140μm and finally a Y-junction at the output end of the device. For a router relying on a dual-mode interference, the optimum length L of the multi-mode waveguide is given by $2L = \lambda_o/|\Delta n_e^{(1)} - \Delta n_e^{(2)}|$ where λ_o is the free space wavelength and where $\Delta n_e^{(i)}$ $(i = 1,2)$ denotes the change of effective index of each mode involved in the rout,ing process for a given change in temperature.

The excitation of the DMI waveguide is achieved by a straight single-mode DLSPPW laterally shifted with respect to the multi-mode waveguide as shown on the SEM image displayed in Fig. 4.1(c). This lateral shift is used to control the relative amplitude of the modes excited in the DMI region. The presence of the NP is clearly visible in Fig. 4.1(b) and 4.1(c). In particular, we note in Fig. 4.1(c) that the NPs have coagulated during the fabrication process. The NP distribution observed at the top surface of the polymer was also visible on the SEM images of the vertical side walls of the waveguides

indicating that the NPs are distributed in the volume of the doped PMMA layer. We note, however, that from the SEM images of the waveguide side-walls, we could only hardly estimate the NP density in the polymer as a function of the distance to the gold film. Finally, an atomic force microscope imaging of the waveguides reveals a roughness at the top surface of the doped waveguides with an average peak-to-peak height of 12nm significantly degraded compared to un-doped structures (average peak-to-peak roughness around 4nm).

4.1.2 Radiation leakage characterizations of the DMI routers.

Experimental set-up and DMI imaging

The impact of the presence of the NP onto the waveguiding properties of the doped DLSPPWs is evaluated by using the LRM set-up shown in Fig. 4.2(a). The near-infrared excitation of the routers was achieved using a fiber-focuser illuminating the grating coupler described in the previous section. The optimum coupling was obtained for a position of the polarization loops corresponding to a transverse magnetic (TM) orientation of the incident field. For the photo-thermal activation of the routers, a

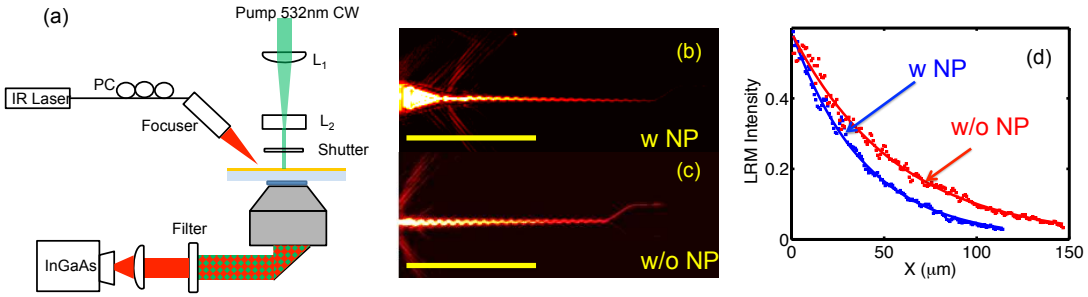

Figure 4.2: (a) Leakage radiation microscope set-up used for the observation and the photo-thermal activation of the routers. (b) (resp. (c)) Typical LRM images at λ_o =1580nm of a doped (resp. un-doped) DMI waveguide (scale bar=100μm). (c) Single-exponential fits (solid lines) of the experimental LRM intensity (dots) along the doped and un-doped DMI waveguide axis.

pump beam (CW free-space wavelength 532nm) was focused by two perpendicularly oriented cylindrical lenses onto the plasmonic devices. By adjusting carefully the distance between the two cylindrical lenses, an elliptically shaped pump beam with a typical size of $100\times30\mu m^2$ was obtained. This elliptical beam was implemented in this work in order to match the elongated shape of DMI routers.

The near-infrared signal and the visible pump beam transmitted through the gold film were collected by a high-numerical aperture objective (NA=1.49) forming the image of the surface onto the detector of an InGaAs camera as performed earlier in this work (see subsection 2.2.2). A long-pass filter with a cut-on wavelength of 900nm was used to remove the contribution of the visible light from the LRM images. LRM images of a NP-doped and un-doped DMI routers are shown in Fig. 4.2(b) and 4.2(c) respectively for an incident free-space wavelength of λ_o=1580nm. The DMI DLSPPWs we consider

are expected to support a fundamental symmetric DLSPPW mode with an effective index n_e^s and an higher-order anti-symmetric mode (effective index n_e^a) [108] where the symmetric and anti-symmetric natures of the modes refer to the electric field component perpendicular to the thin metal film on which the polymer ridge is deposited. On the LRM images, we observe a two modes beating pattern with a period of $p = 6.5\mu m$ and $p = 6.3\mu m$ for the doped and un-doped waveguides respectively. The beating period being given by:

$$p = \frac{\lambda_o}{(n_e^s - n_e^a)} \tag{4.1}$$

we conclude that the effective index difference $(n_e^s - n_e^a)$ for the two DLSPPW modes is only slightly changed by the NP doping. On the contrary the damping distance along the DMI waveguide is clearly affected by the presence of the NPs. By integrating the LRM image intensity over the width of the waveguide for each observation point along the waveguide axis, we find that the intensity profile is well fitted by a single-exponential function corresponding to a $1/e$ damping distance (at 1580nm) of respectively $L_{SPP} = 40 \pm 2\mu m$ and $L_{SPP} = 56 \pm 2\mu m$ for the NP-doped and un-doped DMI (see Fig. 4.2(d)).

Finite-element analysis of the DMIs

In order to correlate our experimental results to the properties of the DMI waveguides, we perform a finite-element eigenmode analysis. The modeled DMI we consider is made of un-doped PMMA and has a width w and height h of respectively 900nm and 400nm extracted from the SEM and AFM characterizations of the fabricated waveguides. As said before, the experimental waveguides are obtained by exposing and dissolving the (doped or un-doped) PMMA resin on each side of the waveguides leaving the waveguide itself unexposed. The PMMA, once exposed and developed, is known to create undercut sidewalls. In our situation, these undercuts result in trapezoidal cross-section waveguides. For a reasonable 15°-tilt of the waveguide side walls with respect to the normal, we found an effective index for the symmetric and anti-symmetric mode of respectively n_e^s=1.251

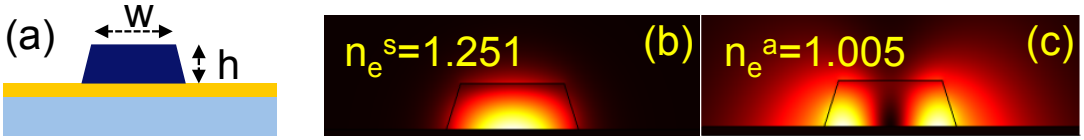

Figure 4.3: (a) Opto-geometrical parameters for the finite-element analysis of an un-doped DMI waveguides, W =900nm, h =400nm (see Fig. 4.3(a)), $n_{PMMA} = 1.489$, $n_{Au} = 0.57+i11.7$ for a wavelength of λ_o=1580nm. The trapezoidal shaped cross-cut of the DLSPPW accounts for the undercut of the vertical side-walls produced by PMMA processing. (b) (resp. (c)) Spatial distribution of the guided power for the fundamental symmetric (resp. higher-order anti-symmetric) DLSPPW mode.

and n_e^q=1.005 leading to a beating length (at 1580nm) with a period of $p = 6.4\mu m$ in fair agreement with the experimental value ($p = 6.3\mu m$).

The damping distance of each mode can also be extracted from the finite-element analysis and compared to the experimental values. The distribution of the guided power for symmetric and anti-symmetric modes are shown in Fig. 4.3(b) and 4.3(c) respectively. For the symmetric mode, the large field amplitude at the surface of the metal leads to a damping distance of $L_{SPP} = 37\mu m$ significantly smaller than for the anti-symmetric mode ($L_{SPP} = 60\mu m$) as already recognized on the previous chapter and ref. [108]. With such different decay lengths, the damping distance of the field intensity along the DMI waveguide depends upon the relative amplitude of each mode, a parameter which is controlled experimentally in our situation by the lateral shift of the single-mode DLSPPW exciting the DMI region. For the un-doped waveguide shown in Fig. 4.2(c), the experimental decay ($56\mu m$) is close to the decay of the anti-symmetric mode ($60\mu m$) suggesting a dominant excitation of the high-order mode at 1580nm. The same conclusion applies for the doped DMI of Fig. 4.2(b) since the lateral shift of the exciting single-mode DLSPPW was the same for both NP-doped and un-doped waveguides considered in Fig. 4.2. Thus, it is very unlikely that a dominant excitation of the symmetric mode is at the origin of the extra-damping (compared to un-doped PMMA) observed for the NP-doped DMI waveguide. Similarly, the absorption of the gold NP at telecom frequencies is not expected to be the dominant channel for this extra-damping. Relying on Maxwell-Garnett's approach (which is expected to be reliable far away from the surface plasmon resonance frequency of the NPs [122]), we find that the decay length of the symmetric and anti-symmetric modes decreases by less than 10% when taking into account the absorption of the composite medium with a gold volume fraction of 0.52%. In this respect, the reduced propagation length for the NP-doped waveguides is more probably related to the roughness of waveguides, leading in particular to the decoupling of the DLSPPW modes into the gold/air SPP supported by the bare thin film surrounding the polymer waveguides. This conclusion is supported by the fact that the excitation of gold/air interface SPP modes can be clearly observed on highly saturated LRM images of NP-doped waveguides.

4.1.3 Photo-thermal activation of DMI plasmonic routers

A quantitative comparison of the photo-thermal activation power for doped and un-doped DMI routers is only possible provided that devices operating an optimized light-heat conversion are used. The waveguides we consider being obtained by processing a positive resin, the reference system (in absence of waveguide) is a polymer thin film deposited onto a gold thin film. Characterizing this reference configuration for the doped and un-doped polymer is then necessary for an optimization of the photo-thermal behavior of the DMI routers.

Optical properties of the NP-doped PMMA layers

With the aim of extracting the optical properties of the NP-doped polymer, we first characterize the optical response of the NP in solution into toluene diluted PMMA. A dual beam spectrophotometer has been used to record the normal incidence absorbance spectra displayed in Fig. 4.4(a). These spectra have been recorded by comparing

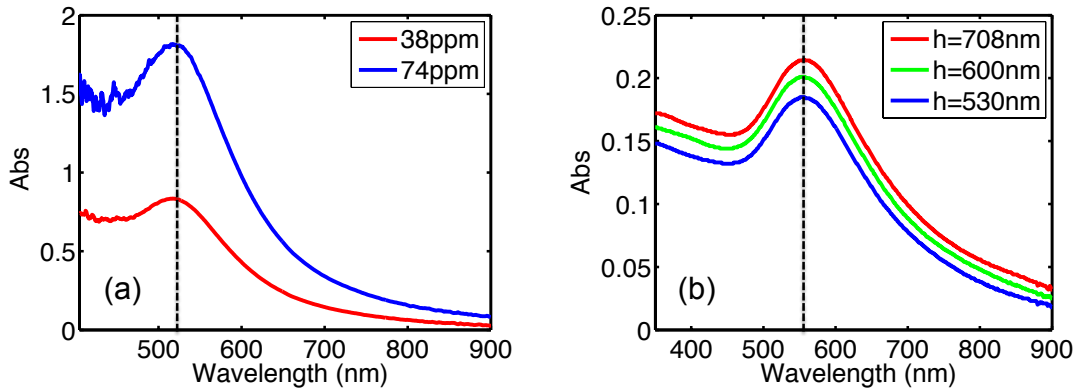

Figure 4.4: (a) Absorbance spectra of NP-PMMA solutions with gold volume fractions of 38 part per million (ppm) and 74 ppm. (b) Absorbance spectra for NP-doped PMMA layers of different thicknesses deposited on a glass substrate. The gold volume fraction of solid PMMA is 5200ppm (0.52%).

the transmission through 1 mm-thick calibrated cells filled with NP-doped PMMA solutions with NP concentration corresponding to gold volume fraction of 0.0038% and 0.0074%. For these measurements, a cell filled with un-doped PMMA was placed on the path of the reference beam of the spectrophotometer. As expected for gold NP embedded into a liquid matrix with a refractive index close to 1.5, the NP-doped solution exhibits a maximum absorbance at a free-space wavelength around 520nm. Starting from a NP-doped polymer solution diluted into toluene with a gold volume ratio of 0.04%, NP-doped PMMA films have been prepared by spin-coating at different speeds onto bare (without gold film) glass substrates. After spin-coating, and prior to absorbance measurements, the PMMA films were baked according to the process used for electron-beam lithography leading to a gold volume fraction of 0.52% in the solid PMMA layers.

The absorbance spectra shown in Fig. 4.4(b) have been obtained for baked NP-doped PMMA films deposited on the glass substrate with a bare glass slide placed on the reference arm of the spectrophotometer. On these spectra, we note a red-shift of the maximum absorbance of about 40nm compared to the NP-doped PMMA solutions. This red-shift results from the combined effect of the refractive index increase of the polymer host matrix when the solvent is evaporated and from the fact that the NP particles are closely-packed in the solid PMMA layer as previously noticed on the waveguide SEM images (see Fig. 4.1). Despite the red-shift of the absorbance peak, we note that the

532nm pump beam is still within the absorbance peak of the NP-doped solid PMMA layers. The radius of the NP we use in this study being very small compared to visible wavelengths, their scattering efficiency is more than three orders of magnitude smaller than their absorption efficiency over the whole visible range [123]. Thus, the spectra of the NP-doped PMMA layers are characteristic of the absorption of the composite medium. The absorbance Abs measured with the dual-beam of the spectro-photometer is defined as $Abs = -\log_{10}\frac{I}{I_{ref}}$ where I and I_{ref} are the powers transmitted through the coated and the bare substrate respectively. Neglecting the scattering of the NPs and the change of reflectivity due to the presence of the PMMA layer (compared to the bare substrate), the power I can be expressed as $I = I_{ref}\exp(-2\kappa_p k_o h)$ where k_o is the incident wavevector, h is the thickness of the doped layer and where κ_c is the extinction coefficient of the doped polymer defined as $\hat{n_p} = n_p + i\kappa_p$ with $\hat{n_p}$ the complex effective index of the composite medium. Knowing the thickness h of the NP-doped PMMA layers from AFM measurements, the effective extinction coefficient κ_p can be evaluated from:

$$\kappa_p = \frac{\lambda_o \times Abs \times \ln 10}{4\pi h} \tag{4.2}$$

By averaging the extinction coefficients extracted from the spectra displayed in Fig. 4.4(b), we find that the effective extinction coefficient for the NP-doped PMMA is equal to $\kappa_p = 0.031$ at $\lambda_o = 532$nm.

We have considered so far NP-doped PMMA layers deposited on a glass substrate whereas the DMI routers are implemented onto optically thick gold films. The quantity of interest for the photo-activation of the DMI routers is obviously the amount of incident pump light which is absorbed by the system. This quantity is difficult to extract from absorbance spectra in the presence of metal due to the high gold film reflectivity. However, by recording the transmittance T and the near-normal incidence reflectance R spectra of PMMA layers deposited onto gold coated glass substrates, the absorption can be extracted according to $A = 1 - (R + T)$ (assuming once again that the scattering of NPs is negligible). This measurement procedure is illustrated in Fig. 4.5(a) showing the experimental transmittance and reflectance spectra along with the experimental absorption spectrum in the case of a bare gold film (thickness=80nm) evaporated onto a glass substrate. These experimental spectra are compared to the theoretical ones (dashed-lines) computed with the dielectric function of gold extracted from ref. [95]. For this configuration, we note that only 23% of the incident light is converted into heat at 532nm making light-heat conversion rather inefficient at this wavelength for this configuration. The same measurements have been performed for un-doped and NP-doped PMMA layers with different thickness. For each PMMA layer, the absorption at 532nm has been computed and plotted in Fig. 4.5(b). For the un-doped PMMA, the experimental values are in good agreement with the computed absorption when the refractive index of PMMA at 532nm is 1.502 in agreement with PMMA specifications. Note that for the un-doped PMMA layer thicknesses leading to an anti-reflecting effect

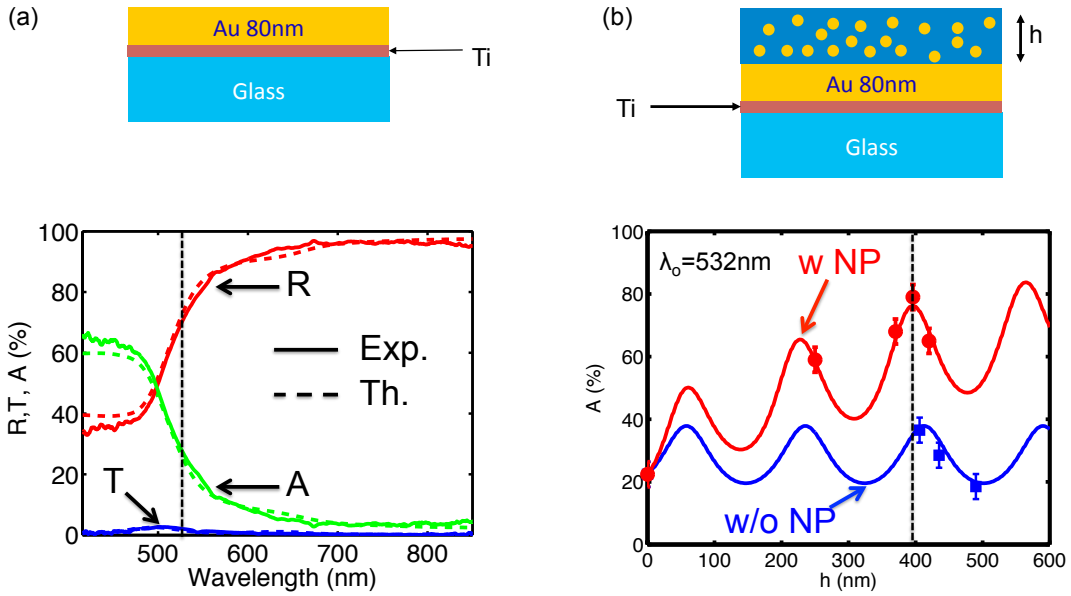

Figure 4.5: (a) Solid lines: Experimental normal incidence transmittance (T) and near-normal incidence reflectance (R) spectra of a 80nm-thick gold film deposited onto a glass substrate using a titanium adhesion layer with a thickness of 3nm . The Absorption spectra (A) is computed from T and R. Dashed lines: comparison of the experimental spectra with computed spectra using the gold dielectric function tabulated in Ref. [95] and neglecting the effect of the adhesion layer. (b) Dots: Experimental absorption values at 532nm for doped and un-doped PMMA layers deposited on a gold film. Solid lines: computed absorption at 532nm for PMMA layers deposited on a gold film. For un-doped PMMA, the best fit is obtained for n_{PMMA}=1.502, for doped PMMA, $n_{NP-PMMA}$=1.57+i0.031.

(for example $h = 403$nm), the maximum absorption level is about 38±2%. For NP-doped PMMA layers, a fairly good agreement between computed and experimental values is obtained when the complex refractive index at 532nm is $1.57 + i0.031$. In agreement with Maxwell-Garnett effective medium approach, the real refractive index of NP-doped PMMA layers is larger than for un-doped layers. However, the refractive index of 1.57 is about 0.02 larger compared to the refractive index returned by the Maxwell-Garnett theory. In spite of the rather low gold volume ratio, Maxwell-Garnett approach fails to provide an accurate value for the real effective index of the composite medium likely due to the coagulation of the NPs [122]. Finally, we note that for a NP-doped PMMA layer with a thickness of $h = 396$nm, the absorption is about 79±2.5%, two-fold larger than for an un-doped layer of same thickness. Hence, light-heat conversion for optimized layers is improved by a factor 2 for doped polymer.

Doped and un-doped DMI routers

Based on the results of the previous section, doped and un-doped DMIs have been fabricated using the optimized polymer layers. By using these optimized routers, we

demonstrate in this last paragraph the minimization of the photo-activation power provided by the NP doping. A direct comparison of the routing performances of different DMIs for a given activation power is difficult since the properties of each device depend critically on its opto-geometrical parameters [108]. Instead, we assess the performances of the DMI routers when photo-activated by comparison with their spectral response in the cold state. In other words, the spectral response in the cold state is used as calibration to characterize the photo-activation of the routers.

We consider first a DMI fabricated in an un-doped PMMA layer with a thickness of 406nm. Figure 4.6(a) shows the intensities I_{CROSS} and I_{BAR} at the outputs of

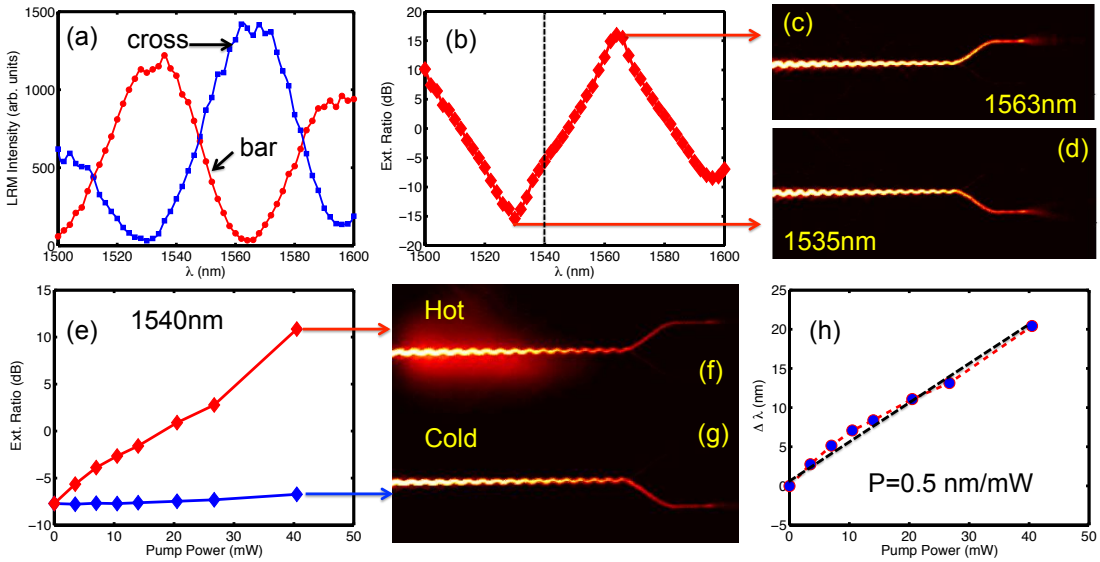

Figure 4.6: (a) LRM intensity integrated over the CROSS and the BAR output port of an un-doped DMI router for a signal sweeping the telecom frequency range. (b) CROSS-BAR Extinction ratio spectrum computed using the results of (a). (c) (resp.(d)) LRM image of the CROSS (resp. BAR) state. (e) For a fixed wavelength of 1540nm, change of extinction ratio at the output port as a function of the pump power. (f) (resp.(g)) LRM image taken at λ_o=1540nm in the hot (resp. cold) state. The elliptically shaped pump (532nm) beam with a power of 40mW is visible in (f). (h) Activation power efficiency obtained by correlating the extinction ratio change in (e) to a wavelength shift in the cold state given in (b).

the Y-junction obtained by integrating the LRM images over the two ports when sweeping the incident wavelength. The BAR (resp. CROSS) port is located on the same (resp. opposite) side of the DMI waveguide than the laterally shifted single-mode input waveguide. The cold spectrum displayed in Fig. 4.6(b) is obtained by computing the extinction ratio ER given by:

$$ER(dB) = 10\log_{10}\frac{I_{BAR}}{I_{CROSS}} \tag{4.3}$$

Symmetric ERs of +15 and −15 dB are measured at respectively λ_B=1563nm and λ_C=1535nm. The corresponding LRM images are displayed on Fig. 4.6(c) and 4.6(d) respectively. For the photo-activation, the incident wavelength is adjusted at 1540nm and the pump beam with an increasing power is focused onto the DMI region of the router. For each pump power, the ER is computed in the cold (pump OFF) and hot state (pump ON) and plotted in Fig. 4.6(e). When the pump power is increased, we observe an increase of the ER for the DMI we consider. This trend results from the negative thermo-optic coefficient of PMMA ($\frac{dn}{dT} = -1.05e10^{-4}$) causing a blue-shift of the ER spectrum when the temperature is increased, as observed on the previous chapter, and hence an increase of the ER in the case of the DMI we consider at $\lambda_o = 1540$nm. For a pump power of 40mW, the ER jumps from -8 to +12dB in the cold and hot state respectively as shown on the corresponding LRM images displayed in Fig. 4.6(f) and 4.6(g). Note that for recording the image of Fig. 4.6(f), the long-pass filter has been intentionally removed in order to show the elongated pump beam produced by the arrangement of two cylindrical lenses. Finally, the change of ER resulting from the DMI photo-activation is correlated to a change of wavelength by using the cold spectrum (see Fig. 4.6(b)). The result of this procedure is the curve plotted in Fig. 4.6(h) showing that the wavelength shift $\Delta\lambda$ depends almost linearly on the pump power with a slope $P = 0.5$nm/mW. Note that the value of P is not an intrinsic property of the DMI device but depends also on the pump illumination conditions. For the purpose of comparison of the un-doped and NP-doped DMIs, it is then critical to keep the pump illumination conditions unchanged when routing from a sample to another.

The same experiment has been conducted for a NP-doped DMI router fabricated in a doped PMMA layer with a thickness of 396nm. The extinction ratio observed for this NP-doped DMI is plotted in Fig. 4.7(a). The DMI router is in the BAR state at λ_B=1522nm (ER=+20dB) and in the CROSS state (ER=-18 dB) at λ_C=1558nm. The incident wavelength being fixed to 1536nm, the photo-thermal activation of the DMI leads to a decrease of the extinction ratio as shown in Fig. 4.7(b). This time, the ER drops from +6dB in the cold state to -4.5 dB for a pump power of only 8mW. The image displayed in Fig. 4.7(c) shows the difference of the LRM image in the hot and cold state for such a pump power. On this image, the build-up process along the DMI region leading to the routing at the Y-junction is clearly visible. Using once again the cold ER spectrum as a calibration curve, the drop of the ER is correlated to the wavelength shift plotted in Fig. 4.7(d) with a slope of $P = 1.37$ nm/mW. Similar characterizations have been repeated for several un-doped and NP-doped routers fabricated respectively on the same substrate as the devices considered above. The values of the slope P obtained in each case are summarized in Table 4.1. Based on the values of the slope P, we conclude that the pump power needed for the photo-thermal activation of the NP-doped DMIs is about 2.5 times smaller than for un-doped ones, a factor that is even larger than the absorption enhancement obtained for the doped and un-doped PMMA unstructured layers. This activation power ratio can, in principle, originate from the enhanced absorption of the NP-doped polymer and/or an increase of the

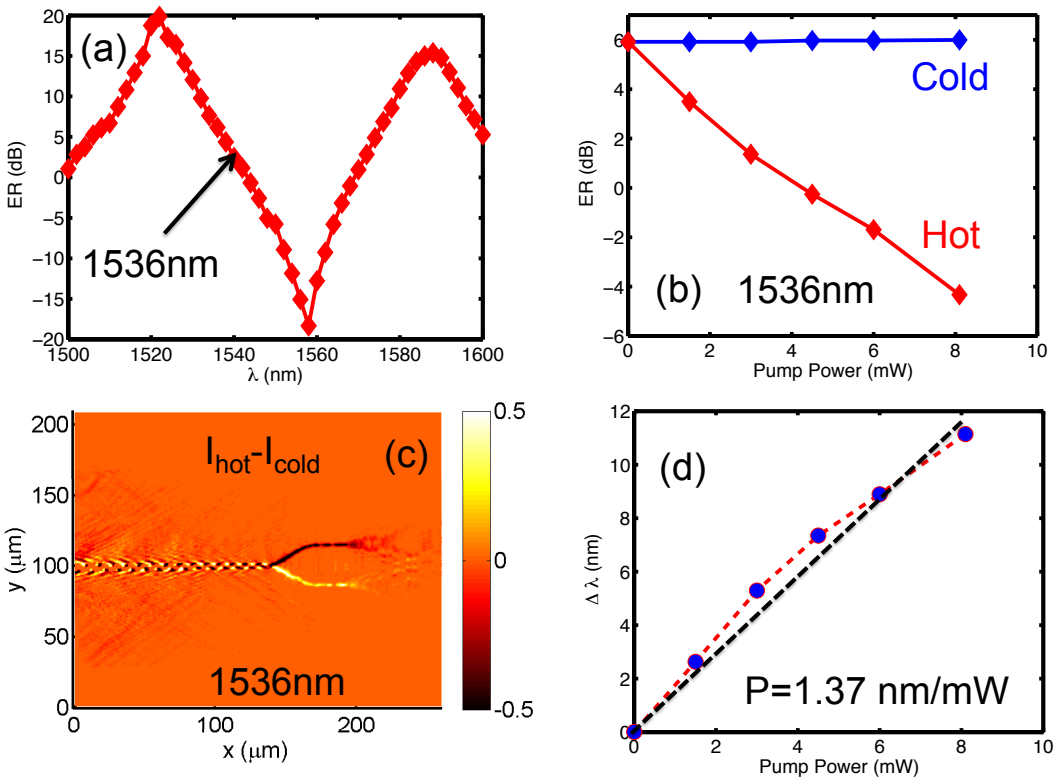

Figure 4.7: (a) CROSS-BAR extinction ratio for a doped DMI router. (b) For a fixed wavelength of 1536nm, change of extinction ratio at the output port as a function of the pump power. (c) Differences of the LRM images recorded in the hot and cold state for a pumping power of 8mW. (d) Activation power efficiency obtained from (b) and (a).

Table 4.1: Activation efficiency obtained for three different NP-doped and un-doped DMI routers

DMI router	Un-doped P (nm/mW)	NP-doped P (nm/mW)
A	0.50	1.37
B	0.48	1.19
C	0.52	1.17
Average	0.50	1.24

thermo-optic coefficient of the composite medium. In our situation, the contribution of the thermo-optic coefficient of the NP-doped polymer can be safely neglected. Indeed, the infrared signal being far from the plasmon resonance of NPs, the thermo-optic coefficient of the composite medium can be approximated as the volume fraction average of the TOCs of each compound of the composite medium [124]. Using the data of bulk gold [124], we find that the TOC of the doped polymer at 1550nm for a gold volume ratio of 0.52% is changed by less than 2% compared to the un-doped one. Thus, the decrease of the photo-thermal activation power is due to the enhanced light-heat conversion for the doped routers.

In fact, not only the total amount of absorbed light is changed when doping the polymer but also the spatial distribution of the heat source density. The volume density of heat sources is given by:

$$h(\vec{r}) = \frac{1}{2}\omega\varepsilon_o \mathrm{Im}(\varepsilon(\vec{r}))|E(\vec{r})|^2 \tag{4.4}$$

where $\mathrm{Im}(\varepsilon(\vec{r}))$ and $E(\vec{r})$ denote respectively the imaginary part of the relative dielectric function of the material and the electric field of the pump beam at the observation point $\vec{r}$. We have computed this density by using the differential method [88] for a DLSPPW ($h = 400$nm, $W = 900$nm, see Fig. 4.8(a)) illuminated at normal incidence by a cylindrical Gaussian beam with a waist of 10µm. The heat source density calculated along the vertical axis of the waveguide (see Fig. 4.8(b)) shows that for un-doped waveguides (n_p =1.502), the heating power is localized at the metal film surface as a consequence of the skin depth effect whereas for doped polymer ($\hat{n_p} = 1.57 + i0.031$), heat is generated also in the volume of the DLSPPWs. By integrating the heat density over the volume

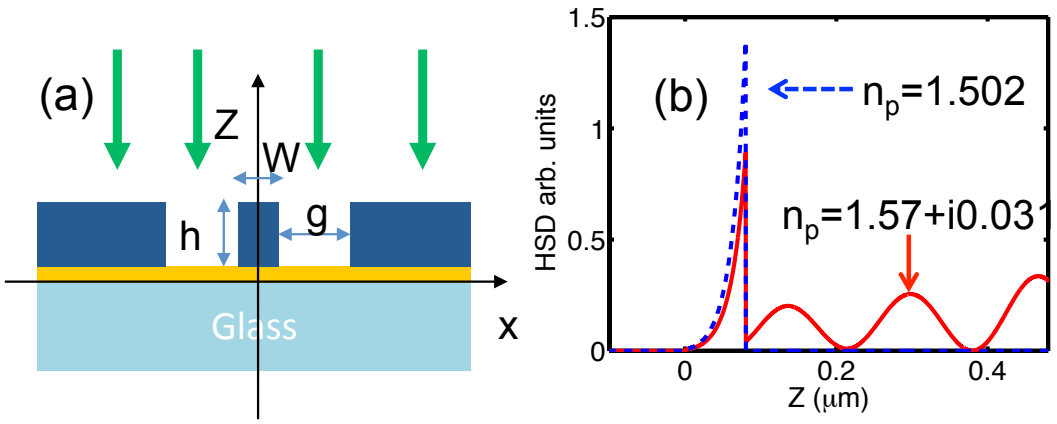

Figure 4.8: (a) Configuration for the heat source density computation. The parameters are W =900nm, h =400nm and g =2.5µm. The thickness of the gold film is 80nm. (b) Heat source density at 532nm computed for along the vertical (z-axis) of the waveguide for the doped and un-doped polymer.

of the active area, we find that for the doped DMI DLSPPWs, about 50% of the heat is generated within the polymer leading to a temperature distribution in the core of the waveguides that could enhance the thermo-optical response of the routers. We note also that, for the configuration we consider, the polarization of the pump beam (parallel or perpendicular to the waveguide axis) plays only a minor role since the topographic steps at the surface of the gold film achieve a very poor excitation of surface plasmon modes at a wavelength of 532nm. Finally, we emphasize that the spatial distribution of heat sources in the presence of the NPs could impact the response time of the routers.

Summary NP-doped "all optical" DMI routers

In summary, we have investigated the photo-thermal activation of 1×2 dielectric loaded plasmonic routers. The routers which rely on a DMI design were fabricated by electron beam lithography using a NP-doped positive resin. For a doping level corresponding to a gold volume ratio of 0.52%, the radiation leakage microscope images of the doped DMI waveguides reveal an decrease by about 30% of the plasmon modes propagation distance attributed to waveguide walls scattering losses. By inspecting the spectral response at room temperature of 140µm-long DMI waveguides, we note a routing between the CROSS and the BAR state with typical extinction ratios around 20dB over a wavelength range of 30±5nm for both doped and un-doped devices. For the purpose of comparing the power needed to thermally activate doped and un-doped routers, the thickness of polymer leading to an optimum light-heat conversion when illuminated at 532nm has been determined by analyzing absorbance spectra of homogeneous layers. For an optimized thickness of 400nm, light-heat conversion efficiency at 532nm is enhanced by a factor 2 by the presence of the NPs.

Next we have developed a procedure to compare the photo-activation power of doped and un-doped routers. This procedure is based on the conversion of the extinction routing ratios obtained for different heating powers into wavelength shifts by using the room temperature spectrum of the router under test. With this approach, which accounts for the routing performances of each device, we show that the power necessary to photo-activate a NP-doped router is about 2.5 times smaller than for the un-doped devices, demonstrating the interest of the NPs in this context of power consumption minimization. The decrease of the activation power is not due to a change of the doped polymer TOC but rather to the enhanced absorption of the pump light for the NP-doped devices and the large power generation into the polymer as shown by the computation of the heat source volume density.

In this study, the polymer material has been engineered to enhance light-heat conversion. Following this approach, many improvements can be suggested such as for example the use of silver NPs which are known to generate about ten times more heat when illuminated at their resonance frequency compared to gold NPs [113]. Finally, and beyond polymer doping, the metal film supporting the plasmon mode of interest can also be patterned to become fully absorbing at the pump frequency leading to an optimum light-heat conversion.

4.2 All plasmonic DLSPPW devices

Photons have been used for photo-thermal activation of doped polymer DMIs described in the previous section. In this section, we test the use of thin film SPP for the activation of our components. The interest of this approach is double. First, SPP modes can be significantly absorbed by the metal in spectral regions where photons are mostly reflected, and second the propagation of thin film SPP modes at the pump wavelength can be used to shape the pump beam in a educated way, with no need of sophisticated optical apparatus, but just by structuring the thin film on which the plasmonic signal propagates.

We also address in this section the question of response time of the DLSPPW structures. As said before, this question cannot be addressed with a characterization set-up relying on LRM. Thus, we have developed a fiber-to-fiber set-up relying on in and out grating couplers allowing us to investigate the dynamic of our DLSPPW structures. At this stage a careful design of the gratings is mandatory and deserves the detailed discussion of the next paragraph.

4.2.1 Dielectric Loaded Gratings for fiber-to-fiber characterizations

In this paragraph, we demonstrate an efficient fiber-to-fiber in and out coupling of DLSPPW components by using polymer gratings engraved on top of a metal film, denoted hereafter as Dielectric Loaded Gratings (DLGs) and excited by moderately focused spots. Unlike grating couplers engraved into the metal film [125], our approach can be used for fast prototyping of DLSPPW components since it requires a single step micro-fabrication process. Typical losses in the range of 10dB per coupler are obtained, making possible standard fiber-to-fiber telecom characterizations of standalone DLSPPW devices. First we discuss the properties of the DLG plasmonic Bloch modes, and in particular, we establish the dispersion of these Bloch modes as a function of the filling factor of the gratings. The role of the filling factor is analyzed on the basis of approximate analytical results providing a starting point for experimental optimizations of the couplers. Beyond fiber-to-fiber insertion loss measurements the efficient excitation of the DLSPPWs is directly observed on radiation leakage microscopy images. Finally, the practical interest of DLGs is illustrated by 10 Gbit/s transmission along standalone DLSPPW structures.

Period and filling factor Bloch mode dispersions

Metallic grating couplers for the excitation of different surface plasmon modes have been extensively investigated during the last decade. For surface plasmons traveling at a dielectric/metal flat interface, finite size gratings of protrusions [126, 127] or grooves [128] have been investigated and coupling efficiencies as large as 45% have been reported [129, 130]. In the case of long-range surface plasmon modes, typical efficiencies in the range of 15% for in-coupling and 60% for out-coupling have been obtained using once again

metallic gratings of bumps [131]. For gratings comprised of point-like scatterers or having a vanishing depth of modulation, the plane-wave excitation condition of the plasmon Bloch modes supported by a grating of period d is approximately given by:

$$k_{SPP} = k_{||}^{inc} + mG \tag{4.5}$$

where m is an integer, $G = \frac{2\pi}{d}$, $k_{||}^{inc}$ is the incident wave-vector component parallel to the average surface of the grating and where k_{SPP} is the phase constant of the surface plasmon mode traveling along the unperturbed surface (without the periodic modulation). However, when the grating can no longer be considered as a weak perturbation of a flat surface, the phase constant of the Bloch mode can deviate significantly from that of the unperturbed situation as already recognized by several authors [127, 132]. In this situation, Eq. 4.5 is no longer sufficient for an optimum Bloch mode excitation and numerical optimizations are usually necessary. When considering DLGs, the numerical optimizations can highly benefit from basic analytical considerations leading to the approximate dispersion of the surface wave Bloch modes as a function of the filling factor and/or the period of the gratings. From a practical point of view, the filling factor and the period of the DLGs are the only two parameters that can be easily changed on a sample with a fixed polymer thickness. In this respect, the dispersion of the plasmonic Bloch modes of the DLGs as a function of these two parameters deserves a careful examination as it determines the efficiency of the gratings when used as couplers.

The situation we consider here is shown in Fig. 4.9(a). The DLGs are made of periodically arranged (period d) rectangular cross-section lines of a dielectric material, deposited on top of a gold film lying on a glass substrate. Two adjacent lines are separated by a side-to-side air gap W_a. Assuming an $\exp(-i\omega t)$ time dependence, the electric field of a plasmonic Bloch mode propagating along the x-axis perpendicular to the lines of the grating can be written as:

$$\vec{E}(x,z) = \sum_{m} \vec{E}_{k_{||}^B}(m,z) \exp(imGx) \exp(ik_{||}^B x) \tag{4.6}$$

where $k_{||}^B$ denotes the x-component of the Bloch mode wave-vector, m is an integer and $G = \frac{2\pi}{d}$. Following the approach described in reference [133] for volume waves, the amplitude of each plane wave of expansion (4.6) can be obtained from the wave equation as:

$$\vec{E}_{k_{||}^B}(m,z) = \frac{k_o^2}{(k_{||}^B + mG)^2 - k_o^2 \varepsilon_g(0)} \sum_{n \neq 0} \varepsilon_g(n) \vec{E}_{k_{||}^B}(m-n,z) \tag{4.7}$$

with $k_o = \frac{2\pi}{\lambda_o}$ where λ_o is the free-space wavelength of the light , n an integer and $\varepsilon_g(n)$ the n^{th} Fourier coefficient of the grating profile. An incident plane wave traveling into the air superstrate and impinging at an angle θ with respect to the normal of the sample

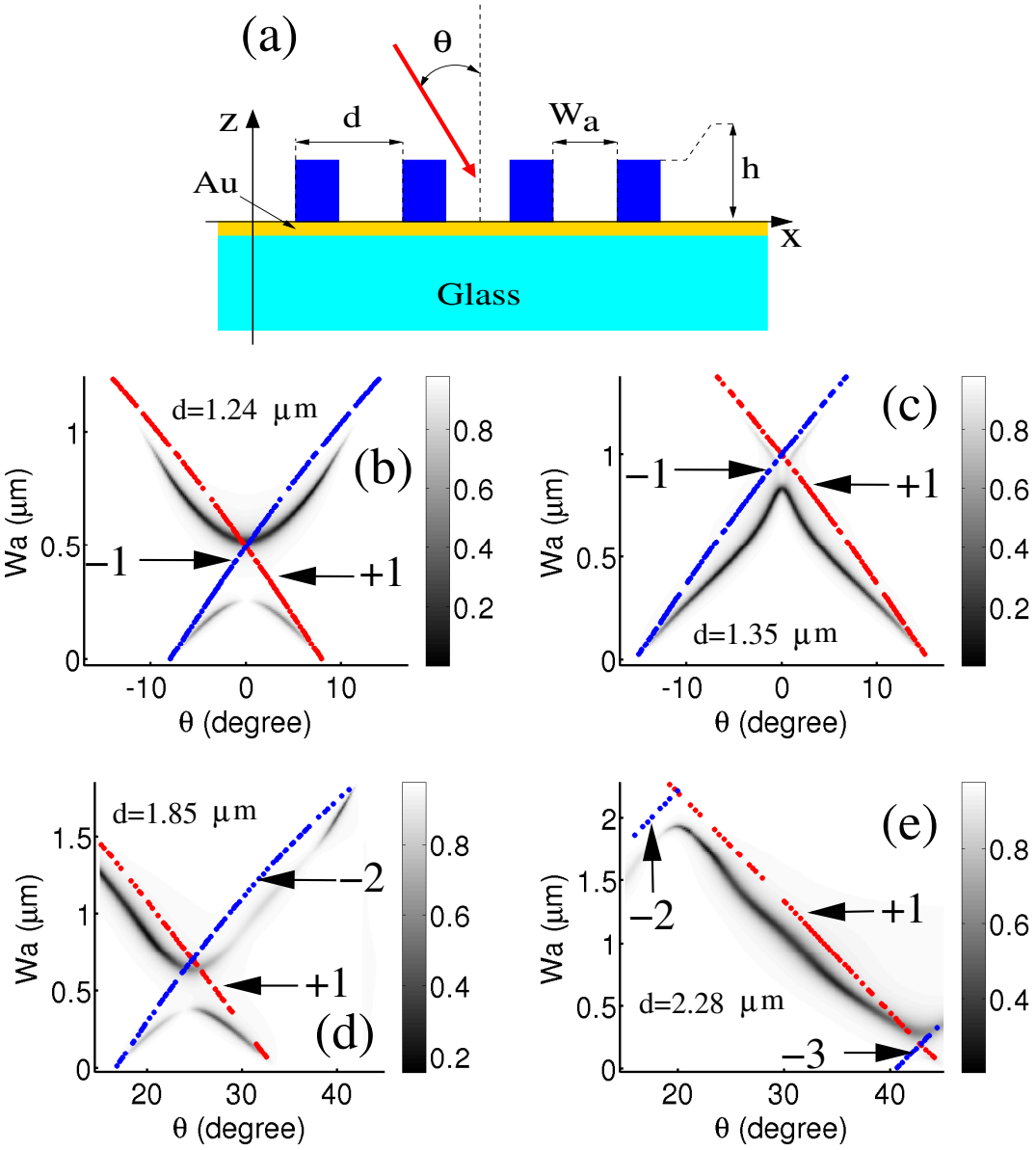

Figure 4.9: (a) Schematic view of a the Dielectric Loaded Gratings considered in this work. (b)(resp.(c)) Reflectivity of a DLG with a period d = 1.24µm (resp. d = 1.38µm) (h=530nm, polymer refractive index=1.45 at λ_o = 1.55µm) for angles of incidence around the normal incidence and varying air gaps W_a. (d) (resp (e)) Same as (b) except for the period d = 1.85µm (resp. d = 2.28µm), the angles of incidence are distributed around θ = 30°. In (b)-(e), the dotted lines are obtained from the excitation condition (4.10), the corresponding values of integers $m^{\pm}$ are displayed for each line.

surface is expected to excite resonantly the plane wave m of expansion (4.7) provided that:

$$(k_{||}^{inc} + mG)^2 - k_o^2 \varepsilon_g(0) = 0 \tag{4.8}$$

where $k_{||}^{inc} = k_o \sin\theta$. This last equation can be viewed as an approximate dispersion relation of the Bloch mode as a function of the frequency of the incident wave if k_o is changed or as a function of the period of the grating if G is changed or, finally, as a function of the filling factor of the grating if $\varepsilon_g(0)$ is varied. Indeed, as long as moderately damped SPP modes are involved, the Fourier coefficient $\varepsilon_g(0)$ can be approximated in our situation by:

$$\varepsilon_g(0) = n_p^2 + \frac{W_a}{d}(n_a^2 - n_p^2) \tag{4.9}$$

where n_a and n_p refer to the real part of the effective indices of the SPPs at the metal/superstrate and the metal/polymer flat interfaces respectively and where the filling factor $\frac{W_a}{d}$ appears explicitly. In essence, Eq. 4.8 is a generalization of condition (4.5) to gratings with non-vanishing filling factors. According to Eq. 4.8, the incident plane-wave can potentially excite two Fourier components in the Bloch mode expansion if:

$$m^{\pm} = \frac{d}{\lambda_o}(-\sin\theta \pm \sqrt{\varepsilon_g(0)}) \tag{4.10}$$

are integers. In this last equation, the coefficient $\sqrt{\varepsilon_g(0)}$ can be interpreted as an average effective index for the plasmon mode traveling along the metal surface textured by the dielectric grating [131]. The dotted lines displayed in Figs. 4.9 (b)-(e) have been obtained from Eq. 4.10 with the effective indices $n_a = 1.005$ and $n_p = 1.389$ returned by the reflection pole method [134] for the SPP modes at the gold/air interface and gold/polymer layer interface when $\lambda_o = 1.55\mu m$, $h = 530nm$ and for a polymer refractive index of 1.45. The reflectivity, computed with the differential method [88], for DLGs illuminated by a plane wave polarized perpendicularly to the grating lines for angles of incidence around $\theta = 0°$ and $\theta = 30°$ are also displayed in Figs. 4.9(b)-(c) and 4.9(d)-(e) respectively. In each figure, the loci of the points of minimum reflectivity reveals the plane wave excitation efficiency of the Bloch modes as a function of the air gap W_a. In Fig. 4.9(b) corresponding to a period of $d = 1.24\mu m$, we observe two distinct branches separated by a well-opened gap at the crossing of the two dotted lines at $\theta = 0°$. It is well-known from the frequency dispersion of surface wave Bloch modes [132] or volume Bloch modes [133] that such an anti-crossing occurs when two plane waves in expansion (4.6) are simultaneously resonantly excited. In this case, the orders m^+ and m^- given by (4.10) are both integers at the same value of θ. In this case, we conclude that no Bloch mode with a field distribution corresponding to the energy of the fixed frequency we consider and W_a within the filling factor gap can be found. In analogy with volume

waves, it is expected that the width of the filling factor gap depends upon the modulus of the grating Fourier coefficient $\varepsilon_g(m^+ - m^-)$ [133]. We also note in Fig. 4.9(b) that the Bloch mode corresponding to the lower branch cannot be excited by a normally incident plane wave. This behavior results from a vanishing overlap of the incident polarized plane wave and the longitudinal (along x) electric field component of the Bloch mode caused by specific values of the relative phase of the Fourier components $\varepsilon_g(m^+)$(or $\varepsilon_g(m^-)$) and $\varepsilon_g(m^+ - m^-)$ [132]. For incidence angles far enough from the anti-crossing, the approximate dispersion curves coincide quite well with the numerically computed ones. We note that for filling factor close to 0 or 1 (W_a=0 or $W_a = d$) the plane wave coupling efficiency decreases dramatically. This can be understood from the fact that the plane wave excitation of the Bloch modes is mediated by the fundamental harmonic $\vec{E}_{k_{||}^B}(0,z)$ in expansion (4.6) since this plane wave is the only one which is phase-matched with the incident plane wave when $k_{||}^{inc} = k_{||}^B$. By considering Eq. 4.7, it is clear that the Fourier component $\vec{E}_{k_{||}^B}(m,z)$ is resonantly excited by the incident plane wave, not only if condition (4.8) is verified, but also if the grating has a non-vanishing Fourier coefficient $\varepsilon_g(m)$. For DLGs, the grating coefficients can be approximated by $\varepsilon_g(m) \propto \frac{1}{m\pi}(n_p^2 - n_a^2)\sin(\frac{m\pi W_a}{d})$ causing the inefficient Bloch mode excitation for $m = \pm 1$ when W_a is approaching zero or d. The amplitude of $\varepsilon_g(m)$ is also decreasing with increasing values of $|m|$. Poor Bloch mode excitation observed in Figs. 4.9(d) and (e) for the branches corresponding to $m = -2$ or $m = -3$ arises from this decrease. On the basis of this first analysis, we conclude that, for given illumination conditions (angle of incidence and frequency), as usual for most of grating couplers, the DLG should allow the Bloch mode excitation with a minimum momentum transfer ($m = \pm 1$). Next, in the range of all possible periods, the period leading to the Bloch mode excitation for a filling factor around 0.5 ($W_a = \frac{d}{2}$) is expected to be the most efficient in the case of plane wave excitation. Note that this conclusion can only be used as a starting point for further optimizations since it does not account for the degeneracy lift of the Bloch mode dispersion curves.

Experimental characterizations of DLG couplers

With the criteria for efficient DLSPPW excitation by means of DLGs established in the previous paragraph, we consider now an experimental approach for minimizing DLSPPW insertion losses using fiber-to-fiber DLSPPW characterization. The setup we consider now differs from the LRM set-up described earlier subsection 2.2.2 by the fiber excitation/detection scheme situated above the sample plane (Fig. 4.10(a)). An incident radiation from a laser source ($\lambda = 1.55\mu m$) is focused by a lensed-fiber (NA=0.25, full-opening angle in air of 30°) onto the input grating coupler, whereas the resulting scattered light at the output grating coupler is collected with an identical fiber focuser (Fig. 4.10(a)). The focusers are aligned to the grating couplers by three dimensional translation stages and by fine positioning of the sample using a piezo-controlled translation stage. Radiation leaking in the substrate is collected by an oil

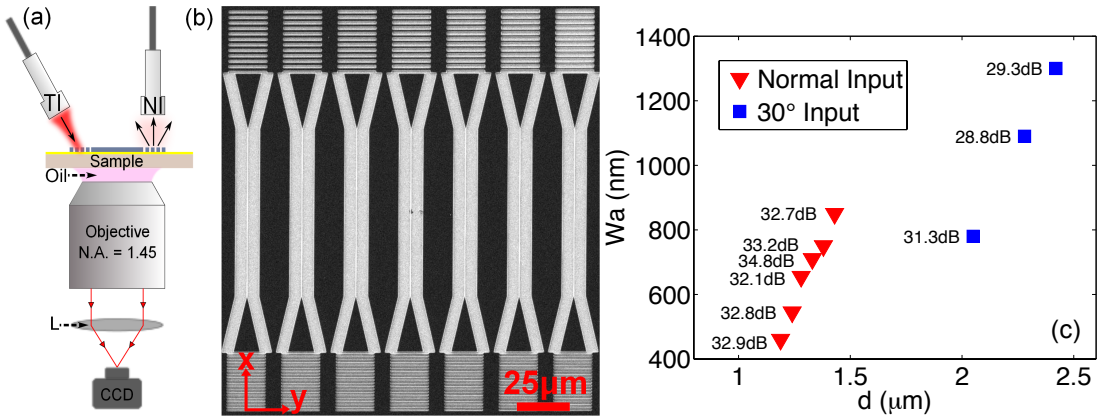

Figure 4.10: (a) Schematic representation of the characterization setup. The DLSPPW-mode is excited by focusing fiber-guided laser light onto the input grating whilst the scattered light at the output grating is collected by an identical focuser at normal incidence (NI) or tilted incidence (TI). The DLSPPW leakage radiation is collected by an oil-immersion objective (NA = 1.45) and focused onto an infrared CCD camera by a lens L. (b) SEM-image of a typical EBL writing-field comprising seven DLSPPWs.

immersion objective and focused by a lens onto an infrared (IR) camera. This gives the possibility to obtain both the LRM-image and the DLSPPW insertion loss in a single experiment. One focuser is oriented orthogonally to the sample plane while the other is tilted 30° with respect to the sample normal, enabling excitation/detection at normal incidence and tilted incidence, respectively. Note that with the chosen focuser orientations the risk of collecting stray light from a complementary focuser is eliminated.

In order to find experimentally the most efficient filling factor, we incorporate tapers and grating couplers at the input and output on several DLSPPWs, fabricated by electron-beam lithography (EBL) on a glass substrate ($n_{glass} = 1.5$) covered with 68nm of gold and 530nm of PMMA (Fig. 4.10(b)). The fabricated DLSPPWs have constant widths of 400nm and the taper base width and half-angle are fixed to 12µm and 15°, respectively. The main objective is to minimize the insertion loss below 30dB simply by varying the grating coupler filling factor for several periods. The insertion loss is determined by illuminating the input grating coupler at normal incidence with the polarization oriented along the x-axis (Fig. 4.10(b)), thereby launching the DLSPPW-mode via resonant excitation of the grating coupler Bloch modes, and detecting the scattered light at the corresponding output grating coupler with the second tilted focuser. The detected scattered light is guided to a power-meter by a single-mode fiber and finally normalized with the measured incident power, thereby yielding the insertion loss.

Repeating the characterization procedure for six different grating periods results in a map of optimized air gaps W_a for each period (triangular markers in Fig. 4.10(c)). Next a similar procedure is conducted for grating couplers excited at tilted incidence (square markers Fig. 4.10(c)). In this case, the excitation and detection scheme is

therefore reversed such that the input grating coupler is illuminated at 30° incidence while scattered light at the output is collected at normal incidence. For both normal and tilted incidence we conclude that a filling factor close to 0.5 is needed in order to ensure efficient excitation of the DLSPPW-mode, as predicted by the analytical approximate.

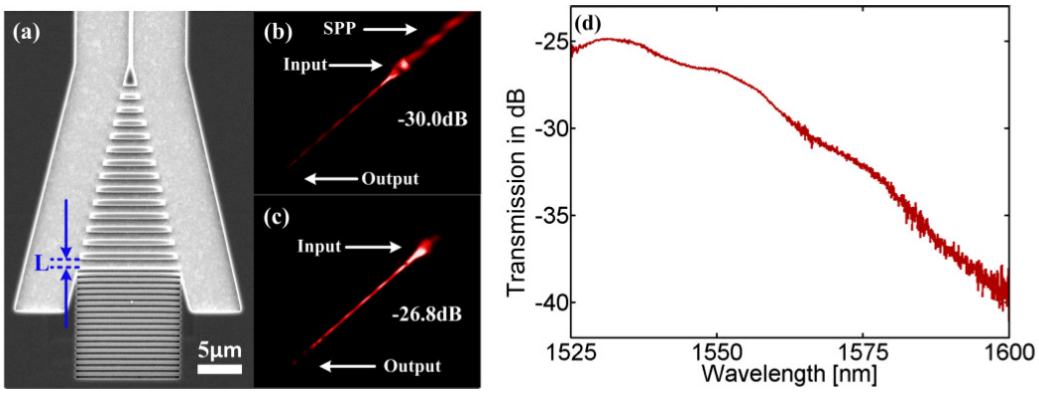

Figure 4.11: (a) SEM-image of a grating coupler with the grating incorporated into the taper and with implemented Bragg mirror. (b) LRM-image showing propagation of a guided DLSPPW-mode and a gold/PMMA SPP propagating in the opposite direction of the waveguide due to improper design of the Bragg mirror (50μs integration time). (c) Similar as (b), but with proper design of the Bragg-mirror functioning as a back-reflector for the gold/PMMA SPP. (d) Transmission as a function of wavelength.

Two extra improvements are finally added to obtain insertion losses well below 30dB. First by incorporating the grating couplers into the taper, which also has the interest of increasing the degree of integration, and second by inserting Bragg mirrors for the grating couplers excited at normal incidence (Fig. 4.11(a)), in order to reflect back the SPP mode excited in the opposite direction (see Fig. 4.11(b)). In order to ensure high Bragg mirror efficiency, the Bragg mirror period d_B and air gap w_{ab} must be chosen in a way that the SPP mode incident on the mirror is reflected. In addition, the air cavity length L, which is the distance between the grating coupler and the Bragg mirror (Fig. 4.11(a)), must be chosen such that the reflected SPPs are in phase with the Bloch modes in the grating coupler. The optimum values for the Bragg mirror period d_B, air gap w_{ab} and air cavity length L are calculated by using the Differential method and it is found that proper dimensioning of the Bragg mirror has a strong influence on the insertion loss (Fig. 4.11(b, c)). For example, when the Bragg mirror is designed with a period $d_B = 650nm$, air gap $w_{ab} = 250nm$ and air cavity length $L = 600nm$ the insertion loss is 30dB and the gold/PMMA SPP propagating away from the DLSPP is still visible in the LRM-image (Fig. 4.11(b)), whereas when the Bragg mirror period is $d_B = 600nm$, air gap $w_{ab} = 150nm$ and air cavity length $L = 600nm$ the insertion loss is 26.8dB and the leakage radiation from the gold/PMMA SPP is suppressed (Fig. 4.11(c)). In this last case, the power loss per coupler drops below 10dB disregarding DLSPPW propagation losses ($L_{SPP} = 43 \pm 2\mu m$, i. e. ~ 7.5dB for a 75 μm long DLSPPW).

Regarding suitability of the dielectric grating couplers for DLSPPW excitation in telecommunication applications, the wavelength dispersion is, along with a low insertion loss, a crucial parameter. Therefore the transmission as a function of wavelength is measured by exciting an optimized grating coupler at normal incidence with a broadband amplified spontaneous emission source (1520-1610nm) and transmitting the detected light to an optical spectrum analyzer. The transmission spectrum (Fig. 4.11(d)) is obtained by normalizing the light spectrum transmitted along the DLSPPW with the spectrum of the source. We note that the insertion loss is less than 35dB in a wavelength range 1525-1575nm and is only 25 dB at 1530nm, thereby indicating suitable conditions for telecom characterizations.

Telecom fiber-to-fiber DLSPPW characterization

The purpose of this section is to show that DLG couplers are of practical interest for fiber-to-fiber telecom characterizations of standalone DLSPPW components. For this purpose, we perform the measurement of the bit-error-rate (BER) for the propagation of a NZR 10 Gbits/s signal along a 75µm long DLSPPW equipped with optimized input and output DLG couplers. The set-up we have used is schematically shown in Figure 4.12. An optical NZR 10-Gbits/s pseudo-random bit sequence is generated by means of a pulse pattern generator associated to an intensity modulator acting on a continuous wave laser source tunable from 1500nm to 1610nm. The TM-polarized incoming non-return to zero signal can be transmitted directly to the EDFA through

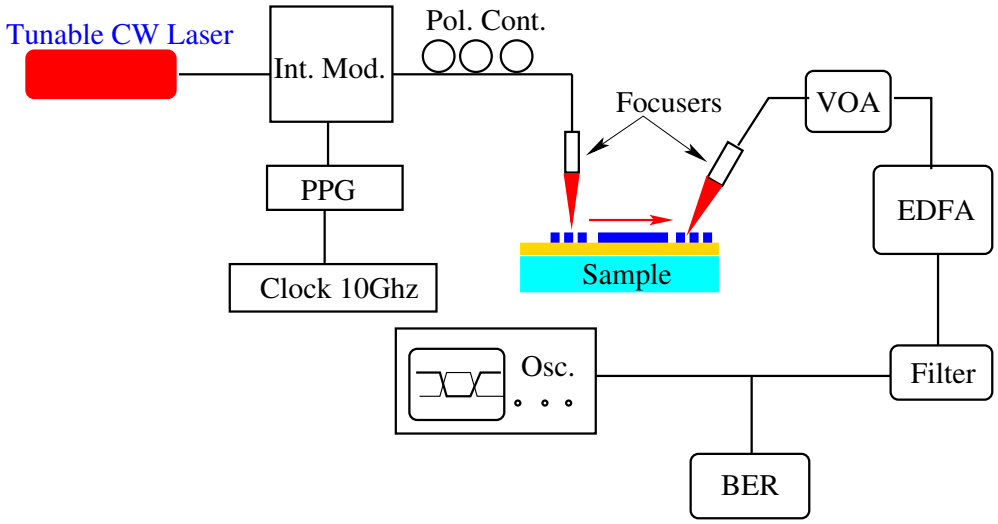

Figure 4.12: 10 Gbit/s telecom BER measurement set-up. CW laser tunable from 1500-1610nm. PPG: Pulse pattern Generator. Pol. Cont.: Single-mode fiber polarization controller loops . IM: Intensity modulator. VOA: Variable optical attenuator, EDFA: Erbium-doped fiber amplifier, gain 40dB. PD: Fast Photo-diode. BER: Bit-error rate measurement.

the variable optical attenuator (VOA) (Back-to-Back transmission) or transmitted first through the DLSPPW waveguide and next through the VOA (DLSPPW transmission). For the purpose of evaluating the impact of the DLSPPW transmission on the quality of a 10 Gbits/s signal, we first observed the eye-diagrams in the case of Back-to-Back (BtB) and DLSPPW transmissions. The eye-diagrams obtained for the two types of transmissions are shown in Figs. 4.13(a) and (b). In both cases, the eye-diagrams were recorded for an incident wavelength of $\lambda_o = 1545nm$ and an average received power of -24dBm. For both transmission schemes, the received power was adjusted by changing the VOA attenuation level while keeping constant the EDFA gain. We note that the transmission along the DLSPPW does not alter the opening of the eye-diagram suggesting that a DLSPPW can safely be used for transmission of 10 Gbits/s signal over short distances. This qualitative result is further confirmed by the BER measurement at 10Gbits/s as a function of the transmitted power for the BtB and DLSPPW transmission ($\lambda_o = 1545nm$) which is displayed in Fig.4.14(a). For this wavelength, we note that an error-free traffic at 10 Gbits/s along the DLSPPW is achievable for transmitted power larger than -36dBm. Next, we note that a weak BER power penalty of only 0.3±0.1 dB is obtained in agreement with measurements performed at 40Gbits/s along hybrid silicon-DLSPP waveguides [135]. The power penalty measurement has been repeated for incident free-space wavelengths extending from 1525nm to 1570nm at a BER of 10^{-7} (Fig. 4.14(b)). Apart from a slight increase to 0.5dB in the blue part of the wavelength range considered, the power penalty remains quite small confirming the suitability of DLSPPWs for WDM 10Gbits/s transmission over the whole C-band. Beyond the demonstration of high-bit rate traffic along DLSPPWs, these results show that DLG couplers are convenient for fiber-to-fiber telecom characterizations of standalone DLSPPW components.

We have shown in this last paragraph that a fiber-to-fiber characterization of standalone DLSPPW devices is possible provided that the in and out dielectric grating couplers are carefully designed (insertion losses below 30dB). Beyond the telecom characterizations performed with success, the efficiency of this coupling scheme allows us to investigate

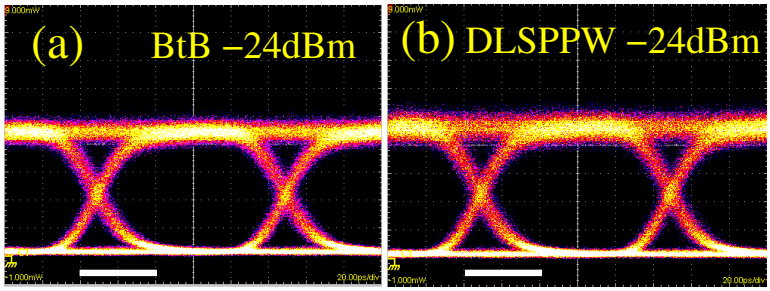

Figure 4.13: Eye-diagrams of the Back-to-Back (a) and transmitted 10 Gbits/S signal (b) for a received average power of -24dBm at $\lambda_o = 1545$nm.Scale bar= 40 ps.

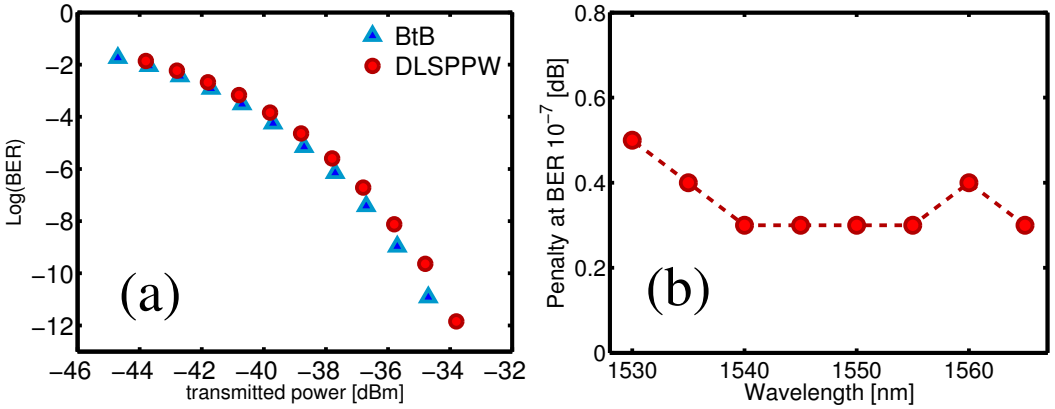

Figure 4.14: (a) Comparison of the BER for the back-to-back and DLSPPW transmission as a function of the transmitted power for a free-space wavelength of $\lambda_o = 1545$nm. (b) Power penalty as a function of the incident free-space wavelength at a BER of 10^{-7}.

the thermo-optical properties of DLSPPW-based devices by using a quite sensitive photo-diode without any additional amplification module. We operate now that kind of characterization in the two next paragraphs dedicated to plasmo-thermal activation of DLSPPW structures.

4.2.2 Plasmo-thermal activation by Kretschmann-Raether excitation

We investigate in this paragraph the possibility of using surface plasmon rather than photon to operate the activation of DLSPPW structures. The main motivation for this approach is to investigate the possibility of shaping the plasmonic pump beam for optimized interaction with the DLSPPW device. Next, SPP modes whose losses are mostly ohmic in nature (small contribution of radiation losses) convert the energy they carry in-plane into heat. In this respect, the use of SPP modes for thermo-optical applications is meaningful. The performances will be measured through the fiber-to-fiber procedure described in the previous paragraph and using the well-known Kretschmann-Raether (K-R) prism configuration [3], a focused beam being used to heat RTRs from the underneath glass substrate. It is known from ellipsometry that the absorption of a TM polarized beam on a metal is always higher than for a TE beam due to the so-called "pseudo-Brewster effect" [136–140]. In the case of a thin metallic layer, we found that SPP waves are more efficient heating sources as compared to a TE Gaussian beam, even though a fraction of the absorbed power for TM polarized beams is delocalized by the SPP propagation.

Kretschmann-Reather excitation for RTRs pumping

The Attenuated Total Reflection (ATR) method, also known as the Kretschmann-Reather configuration, is by far the most common way for the excitation of thin film SPP modes [141]. The transparent lower face of the substrate supporting the thin film is

placed onto a glass prism with an index-matching oil. When a plane wave is used for the SPP excitation, the reflected beam is analyzed as a function of the incident beam angle to determine the SPP excitation, revealed by a minimum in the reflected power. Such a configuration has been employed on numerous SPP related works, from the Surface Plasmon Resonance (SPR) method used for the detection of biological entities when the metal layer is functionalized [142], to the generation of guided waves when the metal layer is shaped to route the SPPs [39]. The optical modulation of light by SPPs [143, 144] or SPPs by light [145, 146], associated with thermal effects, has been also reported earlier in the case of ATR excitation.

We report here on the photo-thermal control of DLSPPW RTRs induced by SPP waves excited by ATR method. The Fiber-to-Fiber technique developed above is used to evaluate the efficiency of the light-heat conversion as a function of the polarization and power of excitation.

The experimental setup is depicted in Fig. 4.15, showing the Kretschmann-Reather prism configuration with a first SPP excitation focuser at the bottom. The incident angle θ can be adjusted with respect to the normal to the gold film. By adjusting the incident linear polarization of the Titanium-Sapphire laser ($\lambda_{pump} \simeq 795$ nm) with an half plate wave and polarization loops, it is possible to excite SPP waves at the top gold-air interface. The reflected beam power can be measured to control the stability of the pump power during the experiment. One can note that the pump beam wavelength is far away from the maximum of absorption of gold (typically $\sim 5\%$ at normal incidence, see Fig. 4.5(a)), however this wavelength is still relevant since the efficient generation of SPP waves could lead to a naturally shaped heating source, i. e. a ten microns long here, which is comparable with the size of the resonant racetracks we consider. Above the prism, the fiber-to-fiber excitation-detection setup is implemented. In order to add a visualization microscope on the top, both focusers are tilted at 30°. An Amplified Spontaneous Emission source (ASE) at the input provides an extended telecom source ranging from 1530 nm to 1600 nm. The output signal is then analyzed by an Optical Spectrum Analyzer (OSA Anritsu MS9740A). This tool can be operated from 600 to 1700nm and thus is well suited for the characterization of telecom components. Two pictures displayed in Fig. 4.15(a) and (b) show the entire experimental setup with the fine positioning system used for the focusers.

The picture in Fig. 4.15(a) shows the optical lens system used to form the images of the sample on two different cameras. The first camera is the same InGaAs infrared camera as the one used previously for the LRM experiments. In this case the camera is dedicated to the fine positioning of the telecom focused spots in order to improve the coupling efficiency on the dielectric gratings. A second Near-Infrared camera is added to visualize the near-infrared tilted pump beam and eventually the propagation of SPP waves. This second camera was also used to observe the dark arc circle that is visible in the reflected pump beam which is characteristic of the excitation of a thin film SPP by a focused spot [39, 147]. In all the following, the angle of incidence has been

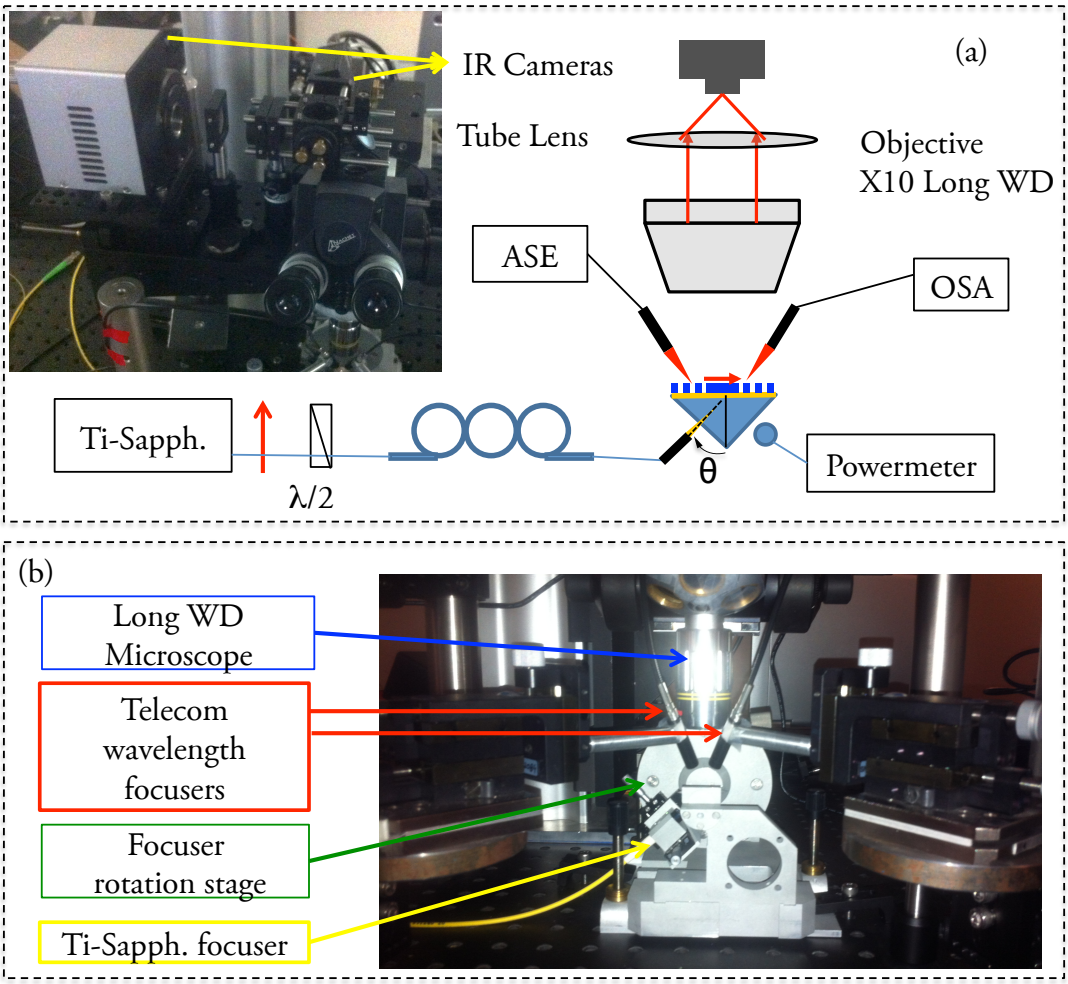

Figure 4.15: (a) Schematic view of the Fiber-to-Fiber Kretschmann-Reather setup. Titanium-Sapphire laser (λ=795 nm) with a polarization control. ASE: C+L band Amplified Spontaneous Emission source (1530-1610 nm). OSA: Optical Spectrum Analyzer. Plus a picture of the Infrared cameras. (b) Picture of the Fiber-to-Fiber Kretschmann-Reather set-up.

adjusted at 40° close to the expected theoretical values (43°). Note that in the case of a SPP excitation by a focused beam, the angle of incidence does not need to be adjusted accurately due to the broad wave-vector spectrum of the beam.

A typical optical image recorded with the setup described above is shown Figure 4.16(a). Compared to the initial RTR devices (see section 3.1), some structural modifications need to be detailed. First, the polymer used is now the high TOC Cyclomer, same as for the study of electrically controlled 2×2 routers performed chapter 3. Next, the resonators are implemented onto electrodes with a surface of 150×80 μm^2 and a thickness around

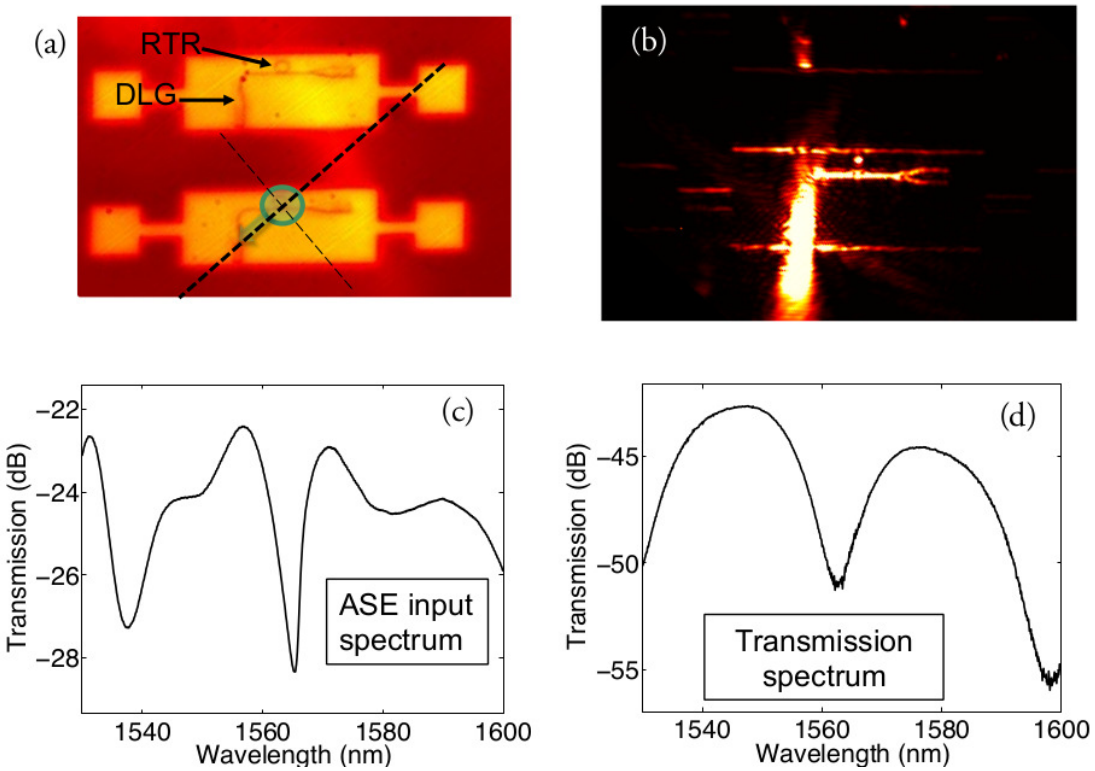

Figure 4.16: (a) Optical image provided by the hanging microscope. (b) Infrared images showing the coupling with a RTR. (c) ASE spectrum (d) Typical RTR spectrum measured with an OSA.

60 nm. Finally the input and output dielectric grating couplers are oriented at 90° with respect to each other in order to avoid any direct coupling between the input and output fibers. This modification is necessary since the two lensed fibers are placed symmetrically with respect to the normal at an angle incidence of 30° imposed by the visualization microscope (see Fig. 4.15(b)). The dielectric loaded gratings made of Cyclomer have been optimized experimentally following the procedure used for PMMA gratings discussed on the previous paragraph. The excitation of the DLSPPW mode can be observed from the very intense incident beam to the propagation scattering along the waveguiding structures and at the edges of the output dielectric grating (see Figure 4.16(b)). Additional scattering is visible at the edges of the gold electrodes. The ASE source spectrum has been analyzed directly on the OSA (Figure 4.16(c)) in order to normalize the measured signal and thus extract the RTRs spectral response (Figure 4.16(d)). Note that these spectra account also for the spectral response of the grating couplers, explaining why the RTR's spectra we observe here differs from those discussed in chapter 3.

Using an elliptical polarized beam with a power of 9 mW moderately focused ($\lambda_{pump} =$

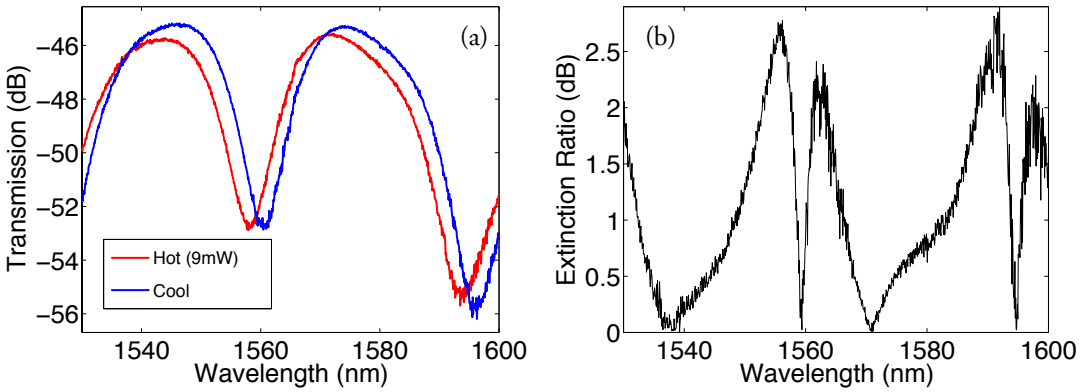

Figure 4.17: (a) Typical thermo-optical spectrum measured by Fiber-to-Fiber. (b) Corresponding Extinction Ratio spectrum (Eq. refeq:ER).

795nm, beam waist~ 10µm), a shift of 3 nm in the spectral response is measured (Fig. 4.17(a)), leading to a maximum extinction ratio (Eq. 3.10) of ~ 2dB (Fig. 4.17(b)), resulting from the combined low quality factor and poor evanescent coupling efficiency of this structure.

Polarization dependence

When considering an interface between two dielectric media with a refractive index n_i, $i = 1,2$, the power reflected of depends on the incident polarization (s for (TE) and p for (TM)) as defined by the Fresnel equations for plane waves:

$$R_{s,p} = r_{s,p} r^{\star}_{s,p}, \tag{4.11}$$

$$r_s = \frac{n_1 \cos\theta_1 - n_2 \cos\theta_2}{n_1 \cos\theta_1 + n_2 \cos\theta_2}, \tag{4.12}$$

$$r_p = \frac{n_2 \cos\theta_1 - n_1 \cos\theta_2}{n_2 \cos\theta_1 + n_1 \cos\theta_2}, \tag{4.13}$$

$$T_{s,p} = 1 - R_{s,p}. \tag{4.14}$$

If the angle between the reflected and transmitted light is 90°, the light is totally transmitted (see Fig. 4.18(a)), coinciding with a special angle of incidence known as Brewster, that can be found with the Snell's law as

$$\theta_{Brewster} = \arctan\frac{n_2}{n_1} \tag{4.15}$$

If the second medium is replaced by an absorbing medium, this special angle subsists, and is known as pseudo-Brewster angle since the dip is not anymore a zero [136–139]. The general relation used to determine the absorption, that generate the heats, is again

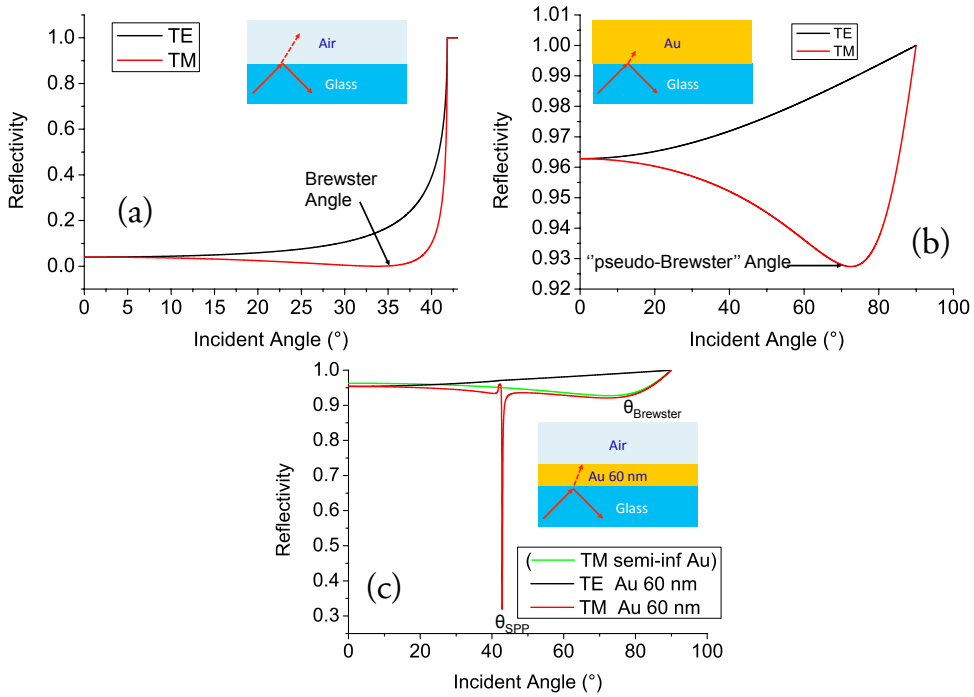

Figure 4.18: (a) Glass-Air reflectivity curve below the total reflection. (b) Glass-Gold reflectivity spectrum. (c) Thin gold layer reflectivity spectrum. A TM polarized light shows both SPP absorption and pseudo-brewster effect.

$A_{s,p} = 1 - (R_{s,p} + T_{s,p})$. In the case of a semi-infinite absorbing medium, the reflectivity spectrum is depicted in Figure 4.18(b). As the light cannot be transmitted through the thick gold layer, the absorption is directly given by the reflectivity as $A_{s,p} = 1 - R_{s,p}$, all the absorbed power generates heat [140]. For a TM polarized incident light, the absorption is always greater than for a TE polarization, and the maximum absorption is placed at $\theta_{brewster} = 78°$ with around 7% of the incident light converted to heat. Finally, in the case of a thin metallic layer corresponding to the DLSPPW devices we consider (Figure 4.18(c)), the largest dip in the reflectivity is obtained at the SPP resonance (θ_{SPP}) where only 30% of the incident power is reflected. However, although the transmitted power can be neglected, this calculation dos not inform us about the total power converted to heat since a fraction of the absorbed power is transfered to SPP (that also acts as a delocalized heating source). To that aim, we now calculate the power coupled to a thin film SPP mode excited by a focused beam.

The calculation of the power absorbed in the thin film illuminated by a focused beam can be obtained knowing the characteristic of the lens used for the focalisation and by expanding the beam into a sum of plane waves. Knowing the wave spectrum of the beam generated by a lens with a known clear aperture and numerical aperture [148], the amount of power carried by the beam and absorbed by the thin film can be readily

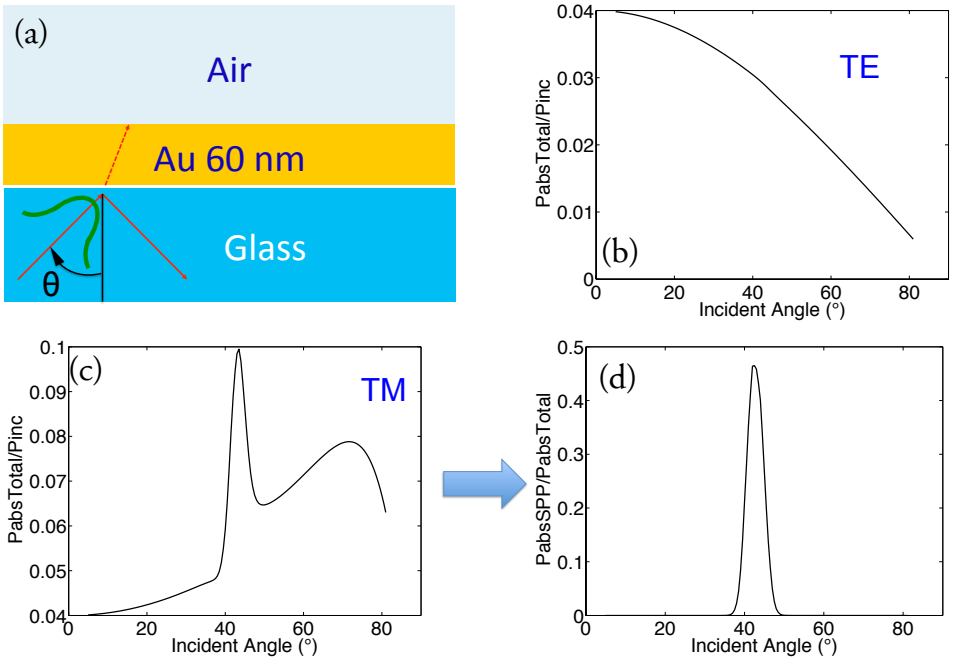

Figure 4.19: (a) Schematic view of the 2D Gaussian beam absorption calculation. (b) Total power absorbed by a TE Gaussian beam (waist~ 3µm). (c) Total power absorbed by a TM Gaussian beam (waist~ 3µm). (d) Corresponding fraction of power of (c) converted into SPPs.

evaluated by summing the absorbed power of each weighted plane-wave in the beam expansion (Fig. 4.19). For example, for a beam with a waist around 3µm [147], falling at an angle of incidence of 40° onto a 60 nm thick gold film at a wavelength of $\lambda = 800$nm, the absorbed power is only 3% of the incident power (Fig. 4.19(b)). In the case of a TM polarized beam, this amount rises to 10% of the incident power (Fig. 4.19(c)). Note that among these 10%, it is possible to evaluate the amount of absorbed power related to the excitation of SPP by summing the contribution of the incident plane waves falling onto the thin film at an angle within the SPP resonance. With this approach we evaluate that only 50% of the absorbed power in TM polarization results from the excitation of the SPP (Fig.4.19(d)). It is clear that this ratio as well as the total amount of absorbed power depend on the wave-vector spectrum of the incident beam. However, the values we give here are relevant to the experimental situations we discuss.

From these computations, we conclude that the best light-heat conversion is obtained for a TM polarized incident beam but it is however worth to note that the amount of absorbed power is only twice as large as in the case of a TE beam in spite of the excitation of the SPP.

The effect of the polarization is investigated experimentally in the Figure 4.20.

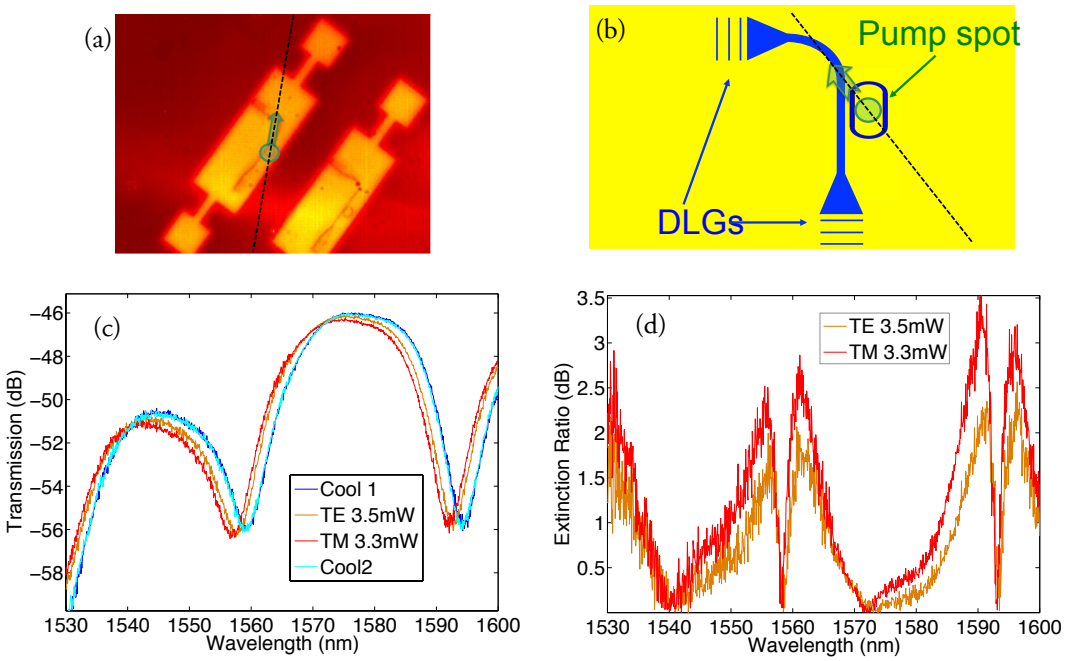

Figure 4.20: (a) Picture of a RTR and schematic near-infrared pump ($\lambda_{pump} = 795nm$). (b) Schematic view of the pump position (green circle), axis (dashed line), and SPP direction (transparent green arrow). (c) Transmission spectra hot and cool states measured chronologically. (d) Extinction Ratio corresponding to (c) TE and TM polarized incident beam for the same spot position.

Figure 4.20(a) shows the RTR considered here with a schematic representation of the pump spot (scattering not sufficiently intense to be visible with the InGaAs camera). The green arrow indicates the direction of propagation of the SPP. This direction was quite challenging to change due to the overall constraints of the Fiber-to-Fiber prism set-up. The cool and hot states transmission spectra for a fixed incident angle and power have been measured for two polarization states TE and TM. The quite low pump power used ($\sim 3.4mW$) prevents a possible thermal degrading. In the Figure 4.20(b), we observe the thermo-optical blue shift generated by the near-infrared pump, with $\Delta\lambda_{TM} = 2.2nm$ and $\Delta\lambda_{TE} = 1.6nm$. The corresponding effect on the extinction ratios is shown in Figure 4.20(c). The extra heat generated by the TM polarized pump leads to a maximum extinction ratio of 3.5dB compared to the 2.5dB for the TE case. For the same illumination parameters, the TM beam is ~0.3 times more efficient than a TE beam in terms of spectrum shift. This effect is lower than what was expected from the calculations (Figure 4.19).

On the basis of our experimental results, we note that the blue shift obtained with the TE polarized pumping is only little different from the case where a SPP is excited. More precisely, this blue shift is much smaller than expected when comparing the absorbed

power in TE and TM polarization. A quantitative analysis of this observation would require a sophisticated modeling . However, one can suggest a rather straightforward argument to explain, at least qualitatively, this result. In fact, the relevant parameter for photo-thermal excitation is not the absorbed power itself but more the volume density of absorbed power which plays the role of source term in heat diffusion equations. When a SPP is excited by an incident focused spot, the fraction of absorbed power related to the excitation of the SPP is delocalized over the propagation distance of the SPP jet, leading to a rather small heat source power density. In other words, although the power absorbed in the case of SPP excitation is about three times larger than for a TE incident beam, the temperature rises at the location of the RTR is only slightly larger for TM polarization owning to SPP delocalized absorption. These results suggest that "All-plasmonic" excitation using a propagating SPP mode should be restricted to longitudinal invariant structures where an elongated distribution of temperature is needed to accumulate phase effect along the propagation direction.

Aging measurements

For the purpose of optical interconnects, the aging and maximum pumping power limit of active components is of great interest. The electrical heating of DLSPPW RTRs performed in chapter 3 has been limited to approximately to a temperature 410 K for PMMA. The aging on DLSPPW RTRs made of Cyclomer driven by light is obtained by increasing progressively the pump power and controlling successively the cool state transmission spectra after each heating, as depicted in Figure 4.21(a).

After various heating cycles, the room temperature state does not come back to its initial position. This aging becomes slightly visible after the 5mW cycles, and then more and more pronounced with the increasing of power. Nevertheless, the thermo-optical properties of the RTR filter subsist, as shown in Figure 4.21(b) where the "cool 1" on the caption refers to the cool states after the $7mW$ cycles. Compared to an electrical heating, the power density is distributed locally on the devices. Thus an overheating would not destroy completely the devices but only impact locally the polymer. An example of overheating is illustrated in Figure 4.21(c) occurred after $17mW$. The narrowing of the gap between racetrack and bus waveguide could explain such a modification of transmission spectrum since the device keep its filtering functionality.

We have considered in this paragraph the excitation of RTRs by using SPP mode launched in the K-R configuration. From a practical point of view K-R configuration can only be hardly implemented at a chip scale as it requires an ATR set-up. In addition, ATR configuration cannot be used if the sample is implemented onto a substrate which is opaque at the pump wavelength. For example, this approach does not hold for a visible pump wavelength and an opaque SOI substrate. In this context, it is worth to consider the situation where SPPs are excited by metallic gratings.

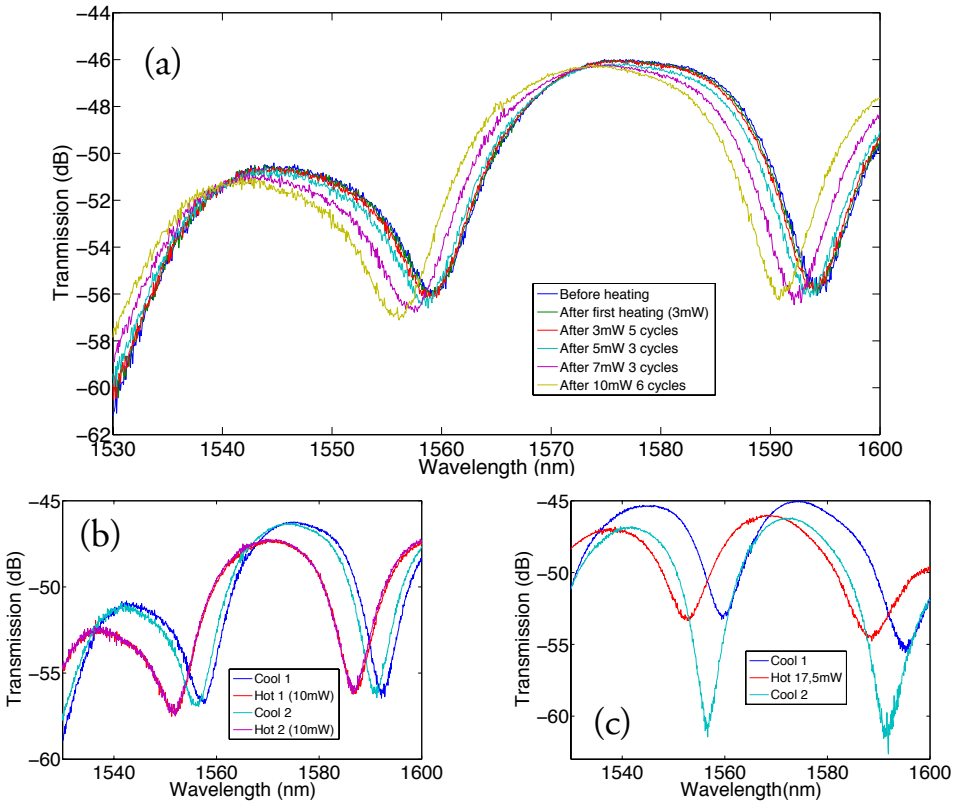

Figure 4.21: (a) Transmission spectra at the cool states after various heating cycles. (b) Thermo-optical effect shifting at moderated power. (c) Example of overheating illustrated by before/after transmission spectra.

4.2.3 Plasmo-thermal activation by Metallic Gratings excitation

With the aim of testing a fully integrated configuration for all-plasmonic pumping of DLSPPW structures, we investigate now the use of metallic gratings for the excitation of pump SPP in the near infrared. Metallic gratings for efficient SPPs coupling have been studied since more than ten years [126, 127, 149], and optimized geometric parameters at near-infrared wavelength have already been established [129, 130]. Many practical applications for passive and active plasmonic devices using metallic gratings have been proposed, with for example the coupling to Long-Range SPPs [131], or the use for ultrafast routing elements [150]. We report here on the photo-thermal control of DLSPPW RTRs, similar to the paragraph, the photo-thermal pumping being performed by a near-infrared Gaussian beam. The enhancement of the light-heat conversion provided by SPPs generated by metallic grating is demonstrated. Then, the evaluation of the thermal dynamic of such a filter in a standalone configuration is discussed [151–153]. In particular we extract the response time of standalone DLSPPW RTRs driven

optically by means of fiber-to-fiber measurements.

Experimental background

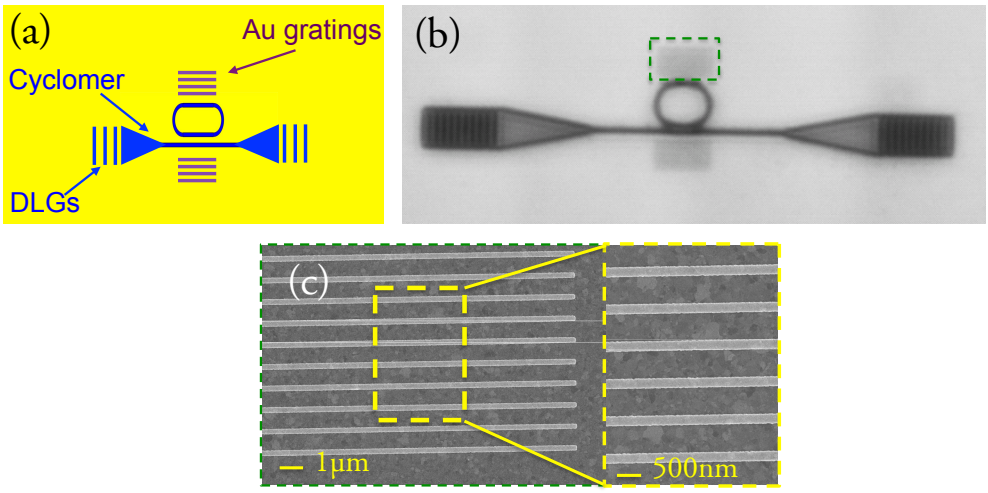

Figure 4.22: (a) Schematic of the DLSPPW RTR surrounded by two adjacent metallic gratings. (b) SEM view of the corresponding structures (a). (c) SEM view of the metallic gratings with a period of ~ 800nm and additional zoom in insert.

Metallic gratings with a period of 800 nm have been placed on each side of DLSPPW RTRs (Figure 4.22(a)). The fabrication of such a structure, in addition to the DLSPPW devices, requires a double step EBL for an accurate positioning with respect to the resonators of the metallic gratings. In this case, a bare gold film (thickness 60nm) is coated with a first layer of PMMA to define longitudinal holes where a second metallic layer of again 60nm is evaporated to form the metallic gratings (Figure 4.22(c)). The remaining PMMA is dissolved to permit the EBL of DLSPPW RTRs made of Cyclomer in between two sets of gold gratings (Figure 4.22(b)). Following the work of *Radko et al.* [129], the most efficient metallic gratings design for an height close to 60nm at $\lambda_{pump} \simeq 800\,\text{nm}$, is 11 ridges of ~ 280nm width, with a period of ~ λ_{pump}. Such a combination is expected to couple ~ 18% of the incident light power into SPP. By sweeping the EBL parameters around these values, we obtained various set of gratings more or less efficient.

The LRM-Fiber-to-Fiber setup we use for these experiments combines LRM and fiber-to-fiber set-up as shown in Figure 4.23. The long working distance diascopic illumination positioned above the LRM setup, originally used to excite the DLSPPW modes (subsection 2.2.2), can be used in addition to a 30°-tilted focusers of the fiber-to-fiber couplers. The LRM setup provides high resolution images of the incident focused spots, therefore the ±30° focusers can be placed face to face without direct reflection as the focusing can be instantaneously and precisely controlled by the Infrared camera. Note that this set-up can only be used at the expense of the use of a transparent thin

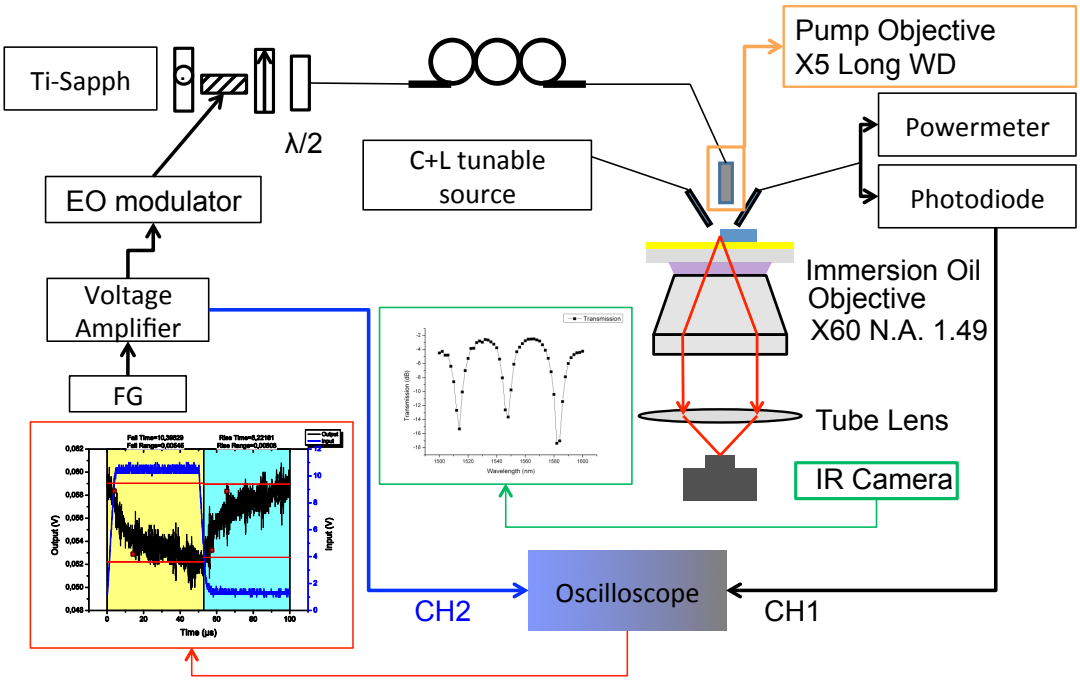

Figure 4.23: LRM-Fiber-to-Fiber setup. The LRM setup is complemented by a Fiber-to-Fiber excitation detection. FG: Function Generator. EO: Electro-Optical Modulator. Ti-Sapph: CW Titanium-Sapphire laser.

substrate (glass slides with a thickness of 170 µm). As the telecom excitation of the RTRs is already performed by the focusers, the top diascopic system made of a $\times 5$ long WD objective, is used to focus a $\lambda = 795$nm pump beam. This near-infrared pump is dynamically controlled by an Electro-Optical Modulator (EOM) placed between the CW Titanium-Sapphire pump laser and the polarization control circuit. The overall setup allows us to, first, control the positioning of the telecom in-and-out beam, second, place the beam pump through the LRM InGaAs camera, and finally verify in real time the thermal dynamic response of the system captured by a fast sensitive InGaAs photo-diode.

Steady states observations

In order to calibrate the entire setup, the cool and hot steady states are examined. This preliminary observation is also an opportunity to investigate the efficiency as an heating source of the SPPs excited by the metal gratings. To that aim, we define three illuminating positions of the near-infrared pump, as depicted in Figure 4.24(a).

By aligning the pump polarization with the y-axes and placing the well focused beam on the metallic gratings (positions #1 and #2), SPPs can be readily excited (Figure 4.24(b)-(c)). Note that SPPs are not unidirectionally launched, as the LRM

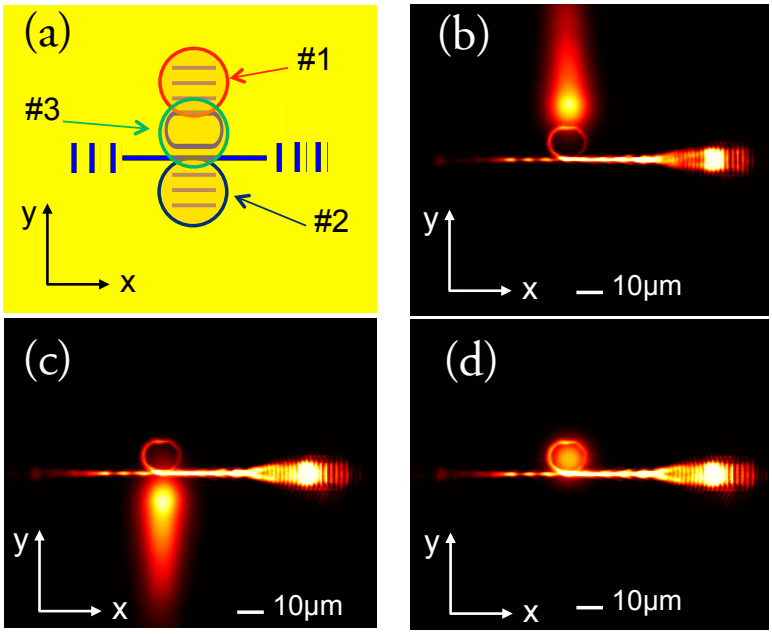

Figure 4.24: (a) Schematic of the different heating positions considered. (b), (c), (c) Corresponding LRM images of the positions #1, #2, and #3 respectively of the near-infrared pump.

images could be wrongly interpreted. In reality, the DLSPPW structures are stopping the propagation of the SPP waves. Thus, the propagation is only visible in the $+Y$ direction for the position #1 and $-Y$ in the position #2. The third illuminating position is centered with respect to the resonator (Figure 4.24(d)). The pump beam focus obtained with the $\times 5$ long WD objective is three times larger (beam waist $\sim 10\mu m$) than what has been obtained with the Kretschmann-Raether focuser, we found that a pump power without irreversible damage around $40mW$ can be used.

The telecom input wavelength is tuned from 1500 to 1600 nm in order to record the transmission spectra for different heating conditions, as shown in Figure 4.25. For a fixed pump power of $23mW$, the most efficient heating position for a TE polarization is obtained when the beam is centered with the RTR (#3), causing a blue shift of around $\sim 4nm$. By switching to the TM polarization at the same position #3, no additional shift in wavelength is measured. When the TM polarized beam is moved to the center of the metallic gratings placed at each side of the structures (positions #1 and #2), an enhancement of the thermo-optic effect is detected, with a total shift of around $\sim 6nm$, 0.5 times more than for the position #3. This enhancement can be directly attributed to the contribution of SPPs since, for a normal incidence, the absorption of light is supposed to be equal for both polarization states. From this assumption,

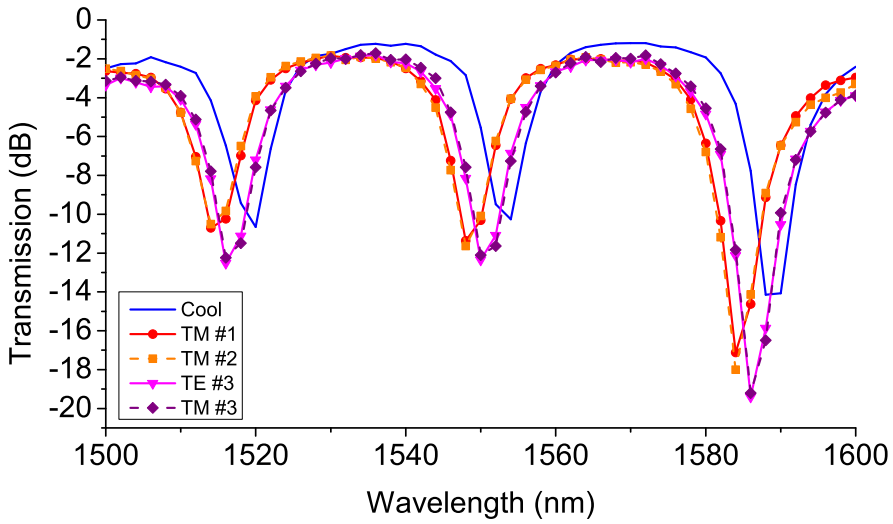

Figure 4.25: Transmission spectra for different illuminating positions and polarizations. Blue: Cool state. Red circles: TM pump at position #1. Orange squares: TM pump at position #2. Pink triangles: TE pump at position #3. Violet diamonds: TM pump at position #3.

we conclude that a significant amount of the power transferred to SPPs brings an additional heat generation to the system, leading to an increase of the thermo-optical shift up to +50% compared to a direct light absorption. To compare this result with the photo-thermal tuning of NP-doped DMIs performed at the beginning of this chapter (Table 4.1), we have here an activation efficiency of $P^{TE}_{gratings} = 0.17nm/mW$ and $P^{TM}_{gratings} = 0.26nm/mW$. Both results are clearly lower than in the case of 532 nm excitation, a result which can be understood from the poor absorption of the 795 nm pump wavelength we used here. Moreover, the metallic gratings were not unidirectional, meaning that half of the SPP coupled power is lost. Adding Bragg mirrors on one side of the metallic gratings could solve this issue and could increase light-heat conversion.

Response time and modulation depth

With the aim of measuring the response time of our DLSPPW, an EOM is implemented to control the near-infrared pump. The dynamic of the plasmo-thermal control of DLSPPW RTRs made of Cyclomer is then recorded using a fast (250MHz bandwidth) and sensitive InGaAs photo-diode. Before the dynamic heating, the operating telecom wavelength is chosen by steady state observations with the LRM set-up, and using the previous best SPP-heat position #1 (Figure 4.26(a)). We found three possible optimum positions centered at the cool states resonances and then fixed the wavelength at $\lambda = 1546nm$ in the following. At this wavelength, we obtained the steady states

extinction ratios given by Eq. 3.10, $ER_{max} \simeq 7.8dB$. Next, the pump signal ($P = 30mW$)

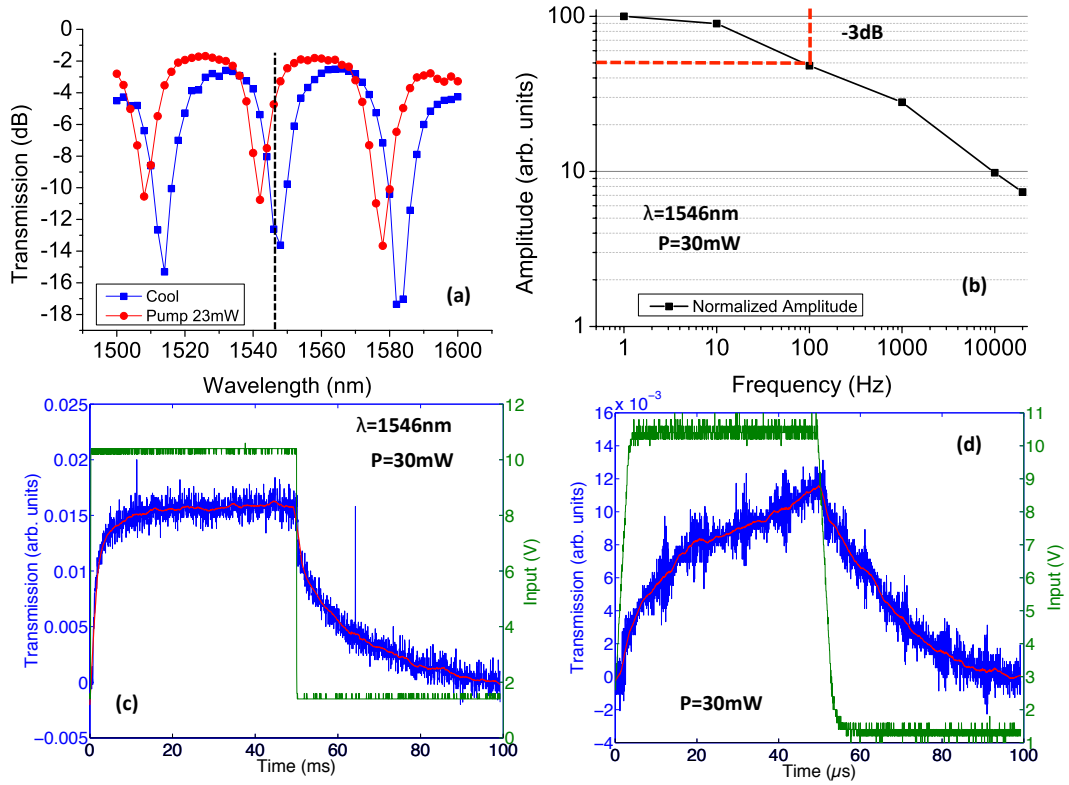

Figure 4.26: (a) Steady state transmission spectra for an illumination of P=23mW at the position #1. (b) Modulation amplitude normalized with a 3dB cutoff close to 100Hz. (c) Thermo-optical time response of a DLSPPW RTRs driven by SPPs modulated at 10Hz (P=30mW). (d) Thermo-optical time response of a the most efficient RTR fabricated driven by SPPs modulated at 10kHz (P=30mW). (c) and (d) Green curve: Square function input signal (V). Blue Curve: Transient response measured by the photo-diode. Red curve: Experimental data fitted for a noise reduction.

is modulated progressively from 1 Hz to 20 kHz. The modulation depth as a function of the pump frequency is plotted in Figure 4.26(b). By extracting the maximum and minimum transmission voltages for each frequency (not shown), respectively T_{max} and T_{min} given by the photo-detector, the extinction ratio is given by $ER_{photo-diode} = 20Log(T_{max}/T_{min})$ [154]. At the two slowest pump frequencies, we found $ER_{1Hz} = 5.3dB$ and $ER_{10Hz} = 4.8dB$ with a 3dB cutoff frequency close to 100Hz. The signal measured through the photo-diode at 10Hz is depicted in Figure 4.26(c). The rise time and the fall time, estimated by the time between 10% and 90% of the maximum, are found to be 8.3 ms and 28.2 ms for a 10Hz modulation pumping. It is still possible to increase the operation speed beyond the cutoff frequency and measure the plasmo-thermal response of

the RTR (see Figure 4.26(d)). We found a rise/fall time around 40µs at 10kHz, however such a result is not relevant for practical applications due to the low filtering efficiency (ER < 3dB). One can note that at high frequencies, the input signal is visibly not perfect and has a rise/fall time of ~3 µs. The response time obtained is a bit higher than recent demonstrations where microseconds regimes have been reported for DLSPPW-based devices controlled electrically on SOI substrate with similar modulation frequencies of 15-20kHz [152, 154].

The underlying reasons explaining the limited performances shown here are numerous. First our device is based on an evanescent coupling between bus and resonator, consequently, such a structure suffers more from the fabrication imperfections than other devices, as explained in chapter 3. To illustrate that fact, the ER at the steady state is below 8dB whereas the polymer used is the high TOC Cyclomer and a comfortable spectral shift of 6nm has been measured. One would expect that with a higher ER at the steady state, the ER at 10kHz could be greater than 3dB and thus relevant for a practical use. Next, the photo-thermal heating performed here is very different from a Joule heating since the light source is not distributed on the same way. Finally, the impact of the substrate materials on both modulation depth and response time of DLSPPW devices is now well established [82, 154, 155]. In this respect the use of a glass substrate with a low value of heat diffusivity is clearly not optimum to operate high frequency thermo-optical modulations.

In any case, we learn from these experiments that an educated design for the structure is necessary to decrease characteristic heating and cooling times. In particular the ratio between heat diffusivity of the active material (the polymer) and the substrate needs to be considered. This point has been investigated in a very recent publication by *Gosciniak et al.* [156]. In our case, the use of a glass substrate is clearly far from being an optimum choice if the dynamic properties of the DLSPPW routers are to be addressed. This very important issue for practical applications is only raised here and is still the subject of active research at the moment of the production of this manuscript.

Summary All-plasmonic DLSPPW devices

The characterization of standalone DLSPPW components has been improved by the creation of a Fiber-to-Fiber method. To that aim, dielectric loaded gratings, that can be fabricated in the same lithography step than the devices, have been optimized and tested in a real data traffic condition of 10Gbit/s. This new tool opens the possibility to characterize standalone DLSPPW structure without LRM imaging. Combining an ATR method using a prism to pump optically RTRs from below and Fiber-to-Fiber coupling, photo-thermal activation has been measured directly by monitoring the output telecom signal to an OSA, making the acquisition of telecom spectra instantaneous. Such an experiment requires far-field views of the telecom and pump spots provided by a classical microscope. The improvement of this method is particularly relevant for the characterization of standalone components designed on opaque substrates such as silicon

wafers. Then, metallic gratings have been implemented to integrate a SPP heating source close to our devices. The study has been conducted by extending the characterization tools of standalone DLSPPW components to the simultaneous use of LRM and fiber-to-fiber measurements. Starting from steady states observations of plasmo-thermal RTRs filtering driven by a near-infrared pump, the LRM images highlighted an enhancement of the light-heat conversion provided by metallic gratings placed in close proximity to the resonant structure. Indeed, the coupling to SPPs increases by 0.5 times the shift of the transmission spectra compared to an absorption of a gaussian beam in absence of SPPs. Improvement of the metallic gratings efficiency could clearly increase this enhancement, by using unidirectional gratings or Bragg mirrors for example. Finally, the recording of the fiber coupled signal indicates a response time of 40µs at 10kHz for our devices implemented onto a glass substrate, the performances being limited by the poor efficiency of the RTR evanescent coupling and the inappropriate substrate for thermally tuned devices.

4.3 Conclusion

To conclude, we have considered several new topics around DLSPPW components by addressing photo-thermal activation rather than electrical activation. In particular, we have demonstrated the possibility to engineer the optical properties of the loading material to minimize the power needed to activate the routers. This example is only one among many others to improve optical pumping efficiency. One can imagine for example that nano-resonators leading to a full absorption at the pump wavelength could be implemented directly onto metal films. This could make photo-thermal activation very power effective in comparison with electrical activation in particular if highly focused illuminations can be used for small footprint routers. Next we have investigated the added-value of using surface plasmon modes rather than photon for the photo-activation process. We have shown that, when propagating SPP are used in this context, the power absorbed by SPP excitation leads to a moderate heating due to the delocalization of the SPP jet. Nevertheless, this option is still of practical interest for elongated structures as it minimizes the power density along the structure and thus increases the damage threshold compared to a standard focused illumination. From the measurement of the characteristic response time of Racetrack Ring Resonators, we conclude that thermal considerations are necessary to reach the targeted bandwidth of the routers around megahertz. These thermal considerations must be conducted from the substrate level for an optimized passive cooling to the structure the DLSPPW itself. This last topic is investigated in details in the last chapter with the introduction of an original configuration denoted dihedron polariton.

CHAPTER 5

Dihedron Surface Plasmon Polaritons

Among all the progress made on the specific topic of DLSPPW devices in the last three years, only few improvements in term of design have been proposed [157–161], the most important one being the mixing between Long-Range SPPs and DLSPPW giving a promising solution for the main drawback of the DLSPPW devices presented so far, the intrinsic losses [157, 162, 163]. Very recently, the first passive component made of Long-Range DLSPPW has been reported [164]. However, the reduction of losses in the context of active integrated optic components is not the unique interesting improvement possible and we propose in this last chapter an original design of DLSPPWs, featuring a metallic dihedron which supports a specific kind of surface plasmon modes.

In the first section of this chapter, we will describe the properties of passive DLSPP dihedron Waveguides formed by adding a metal wall along one vertical side of the polymer ridge. In particular we will show that when the dihedron configuration is made symmetric, the hybridization of the DLSPPW modes leads to surface plasmon modes which can be excited as well in TM as in TE polarization.

In the second section we will address the thermal properties of electrically driven dihedron geometries by means of FEM computations. The role of the vertical metal wall onto heat diffusion during heating and cooling cycles will be considered in details.

5.1 Passive properties of symmetric and asymmetric Dihedrons

In this penultimate section, we demonstrate the polarization degeneracy of the plasmon modes sustained by a metallic Dihedron "loaded" with a polymer strip. Starting from a standard DLSPPW, we investigate first the influence of the presence of a metallic wall adjacent to the polymer strip. We show in particular that this metallic wall leads to a considerable improvement of the propagation length of the DLSPPW mode when the underneath metal strip is of reduced width [66]. Second, by making the system symmetric with respect to semi-angle of the Dihedron, we demonstrate the hybridization of the "horizontal" and "vertical" DLSPPW mode leading to an anti-crossing of the dispersion curves of the DLSPPW modes. Finally, we show that the Dihedron geometry acts as a compact polarization converter.

5.1.1 Impact of a single metallic shield

Geometry

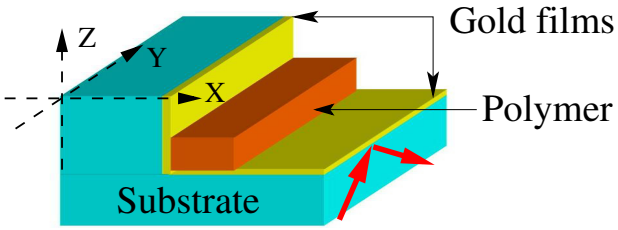

Figure 5.1: Schematic view of the Dihedron DLSPPW.

A schematic view of the Dihedral DLSPPW is shown in Fig. 5.1. A metallic Dihedron is formed by coating with gold films the vertical and horizontal sides of a dielectric step. A polymer strip is then formed at the inner corner of the Dihedron. From a practical point of view, such a structure could be obtained by deep etching process followed by a metal evaporation under a tilted angle and a subsequent polymer strip formation by UV lithography or EBL, as described subsection 2.2.1. The Dihedral waveguide differs from a standard DLSPPW by the presence of the vertical metal wall. It is then first necessary to analyze the influence of this vertical metal wall on the DLSPPW mode properties.

The initial situation we consider is shown in Fig. 5.2(a). A polymer strip having typical dimensions close to an optimized DLSPPW at telecom wavelength ($w_g = 600\,\text{nm}$, $h_g = 800\,\text{nm}$), and a refractive index of $n = 1.5$ is loaded onto a gold film of finite width $w_s = 2\,\mu\text{m}$ deposited on a glass substrate ($n = 1.5$). We use the Differential Method to characterize the properties of standard and shielded DLSPPW modes [55, 88].

Differential method analysis

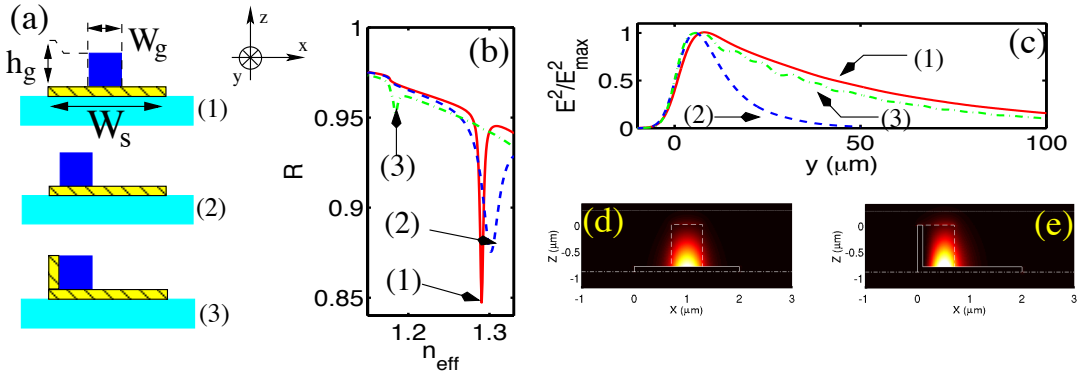

Figure 5.2: (a) Schematic view of the DLSPPW on metal strip without shield (1), off-centered (2), off-centered with metal shield (3), (b) Reflectivity curves for the situations (1-3) (c), Intensity profile along the y-axis for each situations, (d) and (e) cross-cut field map distributions for the situation (1) and (3) respectively.

For all the results presented in the following, we have necessarily made the problem

periodic (see section 2.1), with a period of 5 µm. With such a period, a number of 151 plane waves in the Fourier expansion of the electromagnetic field is found to be sufficient to obtain stable results. The leaky DLSPPW modes are characterized by their complex effective index values. Practically, we determine the real effective index of the DLSPPW by monitoring the reflectivity of the system when the DLSPPW are excited by a plane wave in the Kretschmann-Raether configuration with the plane of incidence being parallel to the longitudinal axis of the waveguide. Similarly to an ATR experiment (see subsection 4.2.2), the DLSPPW mode manifests itself as pronounced dip in the reflectivity curve. When the polymer strip is located at the center of the 2 micrometers wide gold film, the DLSPPW is single-mode at the telecom frequency ($\lambda_o = 1550$ nm) and the fundamental mode has a real effective index of $n_{eff} = 1.29$ as shown by the solid curve displayed in Fig. 5.2(b). If the polymer strip is moved to the edge of the gold film (dashed line in Fig. 5.2(b)), the real part of the mode effective index is rather unchanged whereas it drops to $n_{eff} = 1.183$ if the polymer strip is coated on one side with a gold film (thickness 100 nm). The attenuation constant of the mode can be conveniently obtained by computing the electric filed distribution along the waveguide when the mode is locally excited by a Gaussian beam. Taking the cross-cut along the longitudinal waveguide axis of the electric intensity distribution in an observed plane located 50nm over the waveguide leads to the profile displayed in Fig. 5.2(c). By mean of an exponential fit of the mode intensity tail we find a $1/e$ damping distance of DLSPPW mode is $L_{SPP} = 49$ µm for the centered polymer strip (situation 1), $L_{SPP} = 9.7$ µm for the shifted polymer strip (situation 2) and $L_{SPP} = 41$ µm for the side-coated polymer strip (situation 3). When the polymer strip is shifted to the edge of the metal strip, the DLSPPW mode is in direct contact with the substrate leading to very strong radiation leakages and thus small propagation length, a situation that also occurs when the metal strip is not large enough [66]. On the basis of this first result, we conclude that the vertical metal wall of the side-coated polymer strip shields the DLSPPW mode from the substrate and then prevents strong radiation leakages. It is worth to note that, adding a metal layer on one of the vertical side of the polymer is not detrimental to the DLSPPW mode propagation distance. This result which sounds rather counter-intuitive is in fact readily explained from the electromagnetic field distribution near a good conductor. Indeed, the DLSPPW mode being essentially TM polarized with a large E_z and H_x components, the electromagnetic field near the vertical metallic wall must vanish since outside the surface of a good conductor the electric and magnetic fields can only have a significant normal and tangential components respectively. As shown in Fig. 5.2(e), the field intensity drops in such a way that the electric field just inside the vertical metal film is necessary small, a situation that leads to reduce ohmic losses of the SPP mode. Compared to the DLSPPW mode of the centered polymer strip, the presence of a lateral metal wall for the side-coated polymer repels the field outside of the dielectric, causing the decrease of the real effective index of the DLSPPW mode previously in Fig 5.2(b). The effects of the metal shield could be of great interest for the reduction of the footprint of DLSPPWs modes supported by finite width metal stripes [66] since on

side of the waveguide could be placed very close to another component, the limit being $\simeq 100\,\mathrm{nm}$, below what the wall becomes leaky.

5.1.2 Symmetric Dihedron modes

Effective Index Method

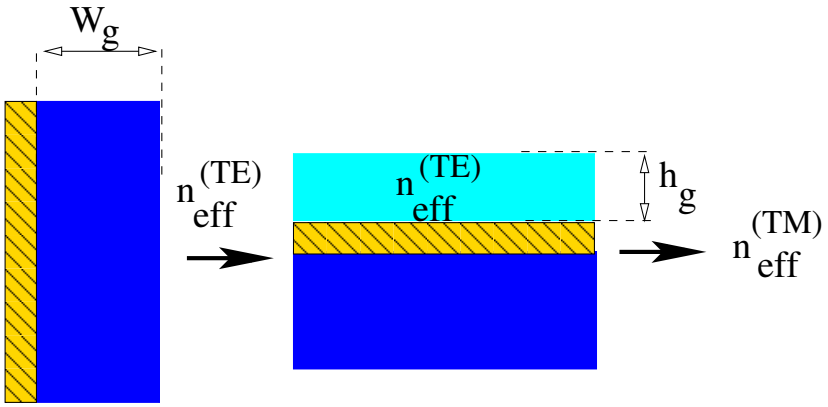

Figure 5.3: Effective Index Method applied to the Dihedron configuration

It has been shown that for standard DLSPPW, the real effective index of the mode can be conveniently obtained from the Effective Index Method [58]. It is then worth to check if this method is still reliable when a metal wall is added on one side of the polymer strip. As shown in Fig. 5.3, we first determine $n_{eff}^{(TE)}$ the complex effective index for a TE polarized mode of a dielectric slab coated on one side with a metal film and having the width w_g of the DLSPPW. Then, the DLSPPW mode index is obtained by placing a slab with an index $n_{eff}^{(TE)}$ and a thickness h_g on top of a metal film and by computing the effective index of the TM-polarized mode of the multi-layers. This approach (denoted as Effective Index Method 2 in Ref. [58]) is found to be efficient for DLSPPW sustaining modes far from their cut-off. From the simple DLSPPW case, one can anticipate that a vertical wall with a height in the range of a few micrometers will support a new DLSPPW mode attached to the vertical metal/polymer interface. In order to check this hypothesis, we consider now the situation depicted in Fig. 5.4(a).

Symmetric modes hybridization

The DLSPPW is now comprised of a polymer strip with a fixed width of $w_g = 800\,\mathrm{nm}$ lying on an horizontal thin film flanked by a metallic wall with a height of $2\,\mu\mathrm{m}$. In order to minimize the number of geometric parameters involved in the configuration we consider, the polymer is no more deposited on a gold strip as before but on a infinite horizontal thin film. Note however that the choice of an infinite horizontal thin film does not affect the generality of the results discussed below. Unlike the configuration described in Fig. 5.1, the metallic wall in our computational situation is not built against a dielectric step. The choice of a "stand-alone" metallic wall is convenient in

our situation because it prevents from the existence of leaky modes supported by the dielectric step alone. Note that a SPP mode at the vertical metal/polymer interface is almost unaffected by the presence of a dielectric step provided that the vertical metallic film is of sufficient thickness. In all the following we use a metallic wall with a thickness of 100 nm, roughly ten times the skin depth of gold ($n_{Au} = 0.55 + i11.5$ [95]) at $\lambda_o = 1.55\,\mu m$. With such a thickness, the results obtained for the DSPPW mode with the "stand-alone" metallic film are still relevant in the presence of the dielectric step.

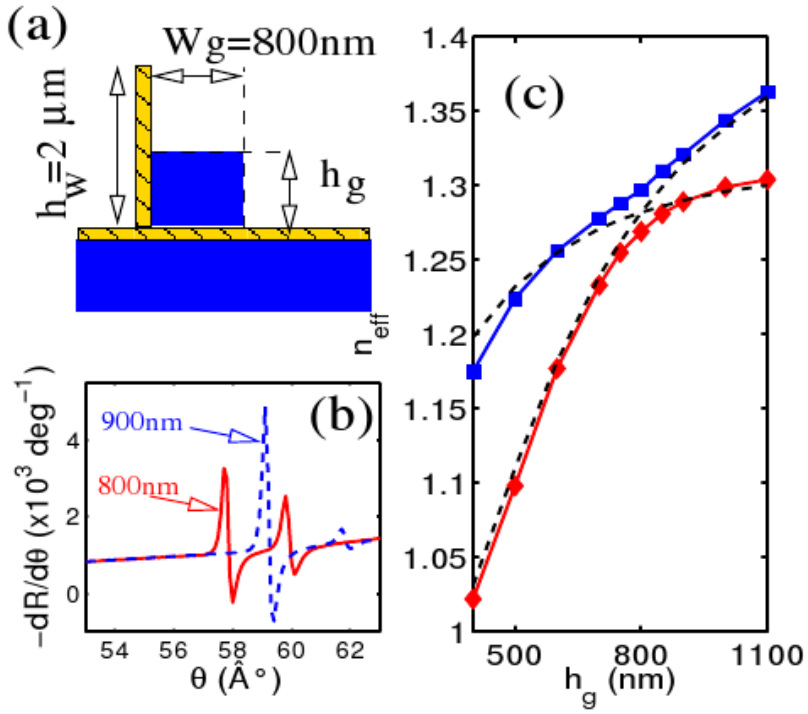

Figure 5.4: (a) Schematic view of a Dihedron, (b) Derivative curve of the reflectivity of the Dihedron illuminated by a TM polarized plane wave, (c) Dispersion curve: Real part of the effective index in function of h_g

We characterize the different modes of the Dihedron DLSPPW by computing the reflectivity of the system when illuminated by a TM polarized plane wave under different angle of incidence θ. In order to make the detection of the reflectivity dips in the reflectivity curves easier, we compute the numerical derivative $\frac{dR}{d\theta}$. Typical results of this computation are shown in Fig. 5.4(b) for a polymer strip height of $h_g = 800\,nm$ and $h_g = 900\,nm$. For both values of h_g we observe two peaks whose angular position can be converted in real effective index according to $n_{eff} = n_{sub} \times \sin\theta$ where $n_{sub} = 1.5$ is the refractive index of the glass substrate. The dispersion curves shown in Fig. 5.4(c) have been obtained by plotting the position of the two modes detected for h_g ranging from 400 nm to 1100 nm. When the dielectric strip is non-symmetric *i.e.* the width w_g

is significantly different from h_g the two modes can be, as expected, attributed to the vertical and horizontal DLSPPW mode. This conclusion is supported by the fact that the real effective index obtained for these two modes are in good agreement with the results of the effective index method (dashed lines in Fig. 5.4(c)) described previously and applied to dielectric strips having either a fixed width w_g and a height h_g or a width w_g and a fixed height h_g, and when the dielectric strip is symmetric (i. e. $h_g = w_g$) the dispersion curves exhibit an anti-crossing which can be attributed to the hybridization of the two DLSPPW modes supported respectively by the horizontal and the vertical interface. The refractive index difference between the low and high index mode is found to be $\Delta n_{eff} = 1.297 - 1.269 = 0.028$.

On the Fig. 5.5 is shown the Electric field distribution of the symmetric and non-symmetric case (e, f, g, h and a, b, c, d respectively). Those results are extracted from COMSOL by Mode Analysis (a, b, e, f) and Differential method (c, d, g, h). The effective index values the Electric field maps coming from the Differential method are in perfect agreement with the ones extracted by the commercial mode solver. On the asymmetric case ($h_g = 900\,\text{nm}$) we can see that the main field components of the two DLSPPW modes are orthogonal, while the longitudinal components are collinear. This provokes an hybridization in two normal modes when the system become symmetric, one mode being polarized at 45° from the horizontal when the modes are in-phase, and a second mode polarized at 135° from the horizontal when the modes are π phase shifted. The good agreement of the two methods for this Dihedral configuration give us the opportunity to study the propagation inside the Dihedron by exciting on such a system by either TE or TM polarised beam with the differential method.

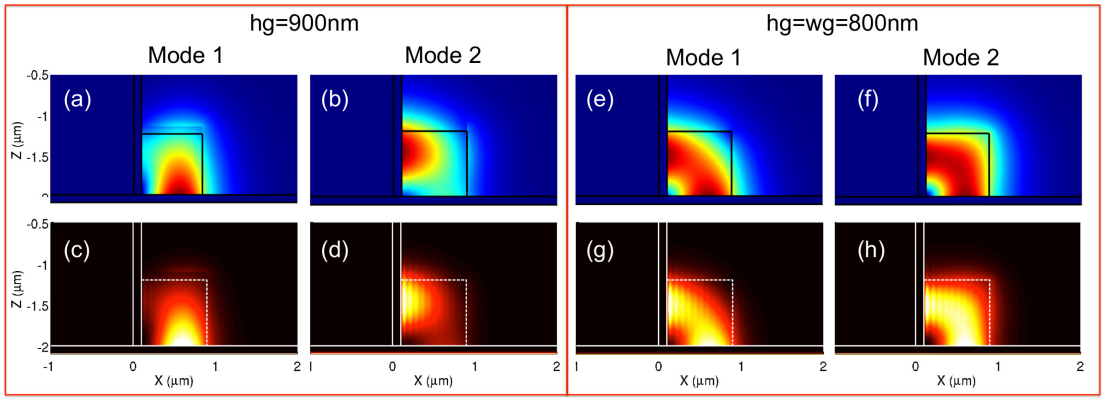

Figure 5.5: (a,b) Electric field distribution resulting from COMSOL Mode Analysis with $h_g = 900\,\text{nm}$, (c,d) Electric field distribution resulting from the Differential method calculation with $h_g = 900\text{nm}$, (e,f) Electric field distribution resulting from COMSOL Mode Analysis with $h_g = w_g = 800\,\text{nm}$, (g,h) Electric field distribution resulting from the Differential method calculation with $h_g = w_g = 800\,\text{nm}$

5.1.3 DLSPPW Polarization converter

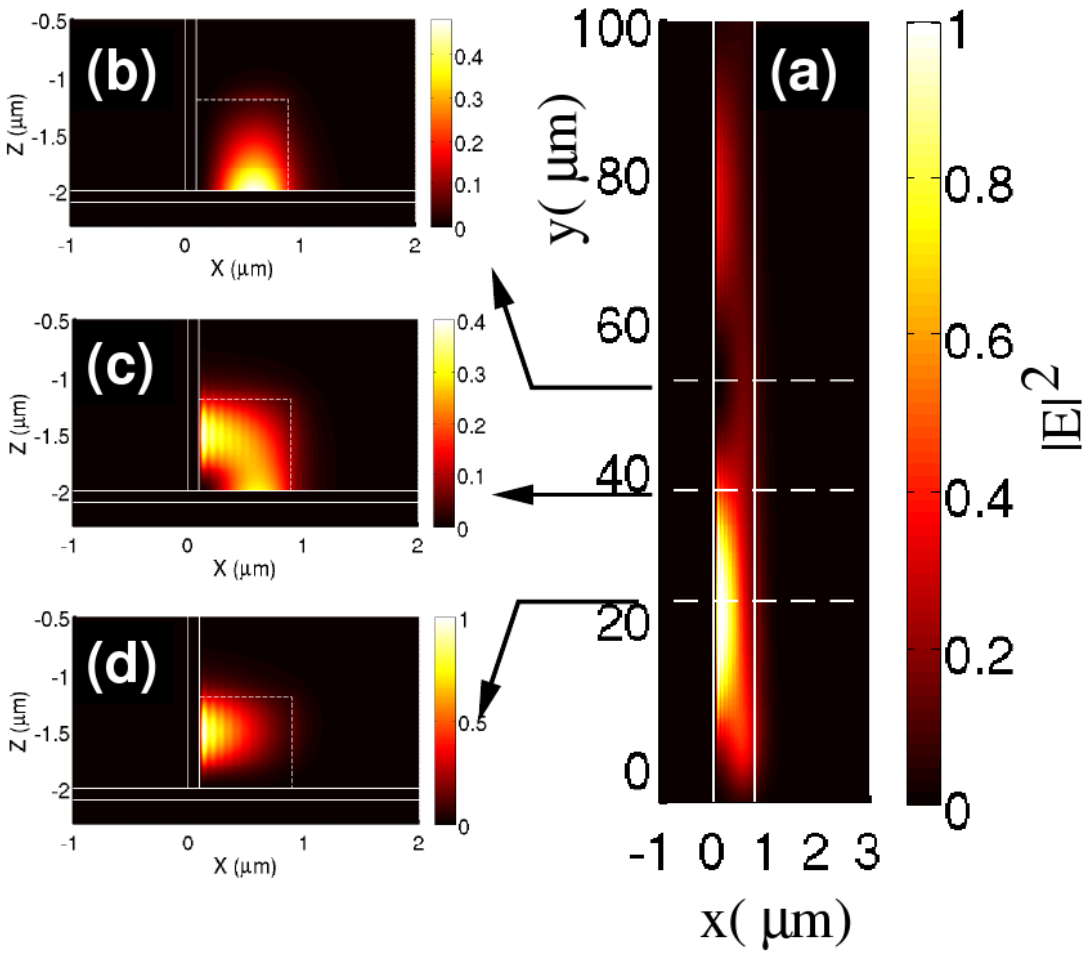

Figure 5.6: (a) Propagated intensity calculated for a symmetric Dihedron, (b,c,d) Electric field norm inside the Dihedron for three different propagation length

Fig. 5.6 depicts the propagation in a Dihedron excited by a TM polarized beam. We observe a beating resulting from the interference of the two normal modes, with a half-beat length of $L_{HB} = 28\,\mu m$, which is coherent with the difference of effective index of the two modes ($L_{HB} = \lambda_o/2\Delta n_{eff} = 28\,\mu m$). We can see that, during the propagation, a complete conversion of the polarization is achieved after one beating (Fig. 5.6(b,d)).

In order to finally compare the performances of this new passive component with the existing integrated optics polarization converters, the Polarization Conversion Efficiency (PCE) and Extinction Ratio (ER), reference quantities to evaluate the performances of such a device [165], are extracted from a full 3D-FEM computation (Figure 5.7).

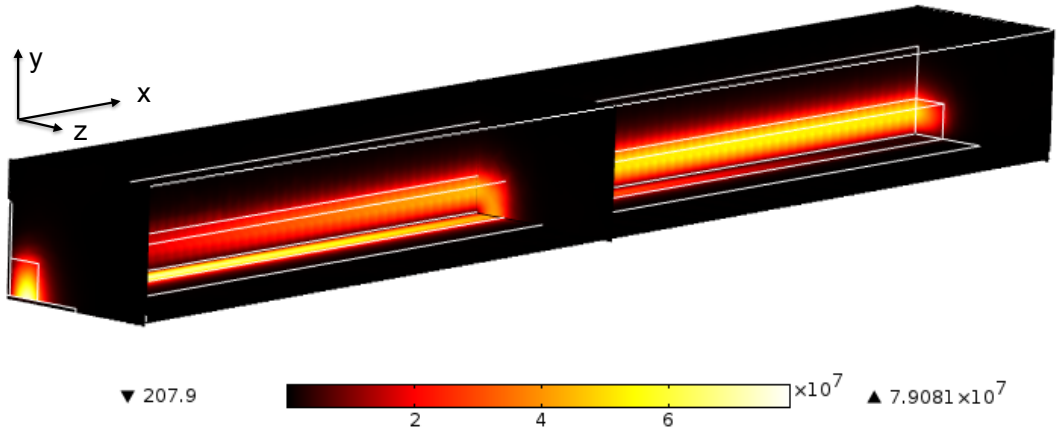

Figure 5.7: Electric field norm slices of a 30µm long Dihedron representing the input, output and intermediate intensity during the polarization conversion.

For a single TE to TM or TM to TE polarization rotation, the device need an approximate length of 30 µm, depending on the dielectric index and operating wavelength. Here we choose a typical refractive index for the dielectric of $n = 1.535$, corresponding to PMMA and keep $\lambda_o = 1550\,\text{nm}$. We perform mode analysis to find the two hybrid modes effective index, giving a half beat length of $L_{HB} = \lambda_o/2(1.328 - 1.302) = 29.84\,\mu\text{m}$ in this case, prior to the calculation of propagation. The 3D-FEM electric field map reproduce well the results obtained by Differential method (second polarization rotation of Fig. 5.6). The performances can now be extracting the Polarization Conversion Efficiency given by [165]

$$PCE_{TM\to TE} = \frac{P_{TE}^{out}}{P_{TE}^{out} + P_{TM}^{out}}, \tag{5.1}$$

where P_{TE}^{out} and P_{TM}^{out} correspond to the Poynting vector time average at the output of the device for the two polarization states given by

$$\begin{aligned} P_x &= \frac{1}{2}\text{Re}\iint (E \wedge H^*)dS.\vec{e_x}, && (5.2)\\ &= \frac{1}{2}\text{Re}\iint (E_y H_z - E_z H_y)dS.\vec{e_x}, && (5.3)\\ P_{TM} &= \frac{1}{2}\text{Re}\iint (E_y H_z)dS.\vec{e_x}, && (5.4)\\ P_{TE} &= \frac{1}{2}\text{Re}\iint (-E_z H_y)dS.\vec{e_x}. && (5.5) \end{aligned}$$

Finally the Extinction Ratio correspond to the ratio of intensity exiting the output port with the desired polarization:

$$ER_{TM\rightarrow TE} = 10\log\left(\frac{P_{TM}^{out}}{P_{TE}^{out}}\right). \tag{5.6}$$

The performances and comparisons are reported on the following Table 5.1.

Table 5.1: Polarization converter performances and comparisons to the literature.

	Dihedron	Ref. [166]	Ref. [167]	Ref. [168]	Ref. [169]
Material	Au/Polymer	InP	InP	Si	SOI
Length (µm)	30	784	48	22.1	44
PCE (%)	99.67	-	-	99.95	>92
ER (dB)	25	40	> 15	-	-
IL (dB)	~ 3.3	0.04	1	-	<1.6

Summary

The addition of a metallic shield on one side of a DLSPPW has been investigated numerically, by combining Differential method, Effective Index Method and Finite Element Method. The impact of the presence of a single metal wall on the standard DLSPPW mode supported by a finite width metal strip is double. First the effective index of the Dihedron modes are lower than the corresponding DLSPPW, and in addition the propagation length of the Dihedron mode is greater than for a DLSPPW mode implemented onto a finite width metal film. These two effects result from the fact that the electromagnetic field of the Dihedron mode is repealed by the vertical metal film. As each side of the dielectric in contact with the metal can support a high effective index mode propagating on the same direction, the hybridization of the two normal modes have been highlighted, leading to a polarization conversion when the system is exited by a TE or TM beam. The Differential Method results have been compared to the Effective Index Method and to a commercial FEM mode solver. The compactness of this polarization converter ($\simeq 30\,\mu m$) leads to relatively low loss for a plasmonic component and the polarization conversion performances are clearly competitive compared to classical integrated optic converters. The on-chip implementation of these Dihedron waveguides is in progress at the moment of this manuscript writing. On the next section, we present other promising properties of the Dihedral structures by performing 3D-FEM thermal analysis.

5.2 Electrical heating of Dihedrons

In this final section, we propose to investigate plasmonic Dihedrons by means of full 3D FEM multi-physics calculations featuring thermal and electromagnetic models eventually coupled. The same kind of calculations have been previously presented by *Tsilipakos et al.* for the evaluation of standard thermally tuned DLSPPW WRRs [81]. We first briefly describe the numerical method provided by the commercial FEM sofware Comsol, then we discuss the impact of the adjacent metallic wall of the Dihedron on the thermo-optical response time compared to a standard DLSPPW. Finally, the case of symmetric Dihedon geometry that introduces a new compact polarization converter is tested on a thermally variable environment in order to verify that such a device could support an electrical current without ruining the polarization conversion functionality.

5.2.1 Impact on the time response

To investigate the thermo-optical dynamic properties of the Dihedrons, we start by reproducing the previous results obtain in the literature for DLSPPW [81]. Since this work have been also performed by 3D-FEM method, we except to approach their results, providing a good starting point for further investigations on Dihedrons.

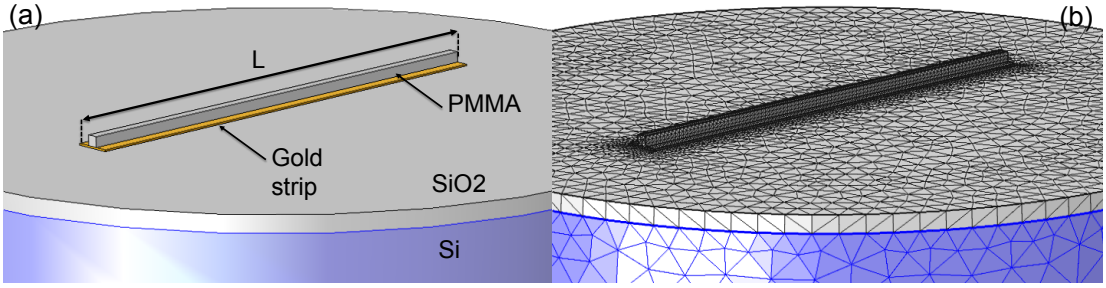

Figure 5.8: (a) Schematic view of the 3D DLSPPW reference structure used in Comsol. (b) Corresponding mesh.

The geometry investigated is shown in Figure 5.8(a). A DLSPPW consisting of a gold metallic gold strip with a cross-section of $0.1 \times 2\,\mu m^2$ and a dielectric ridge with a cross-section of $600 \times 600\,nm^2$ and $L = 30\,\mu m$ long, is placed on a silicon substrate ($4\,\mu m$ thick) with an additional $1\,\mu m$ thick silica layer on the top. The underlying gold strip that supports the DLSPPW mode has been intentionally made sufficiently thick ($100\,nm$) in order to shield optically the DLSPPW mode from the substrate. The current density of $J = 142.8\,GA/m^2$ used on the Ref. [81] is taken as reference, corresponding to a driving current of $28.5\,mA$ in our case. This current density is then fixed as input for the heat source Q given by

$$Q = \rho C_p \frac{\partial T}{\partial t} + \nabla.(-K\nabla T) = \frac{J^2}{\sigma} \tag{5.7}$$

Where $\sigma = 10^7\,S/m$ is the gold stripe conductivity, ρ the material density, C_p the

Specific heat, and K the thermal conductivity. We approach a realistic situation by thermalizing the bottom of the silicon substrate at $T0 = 293.15\,K$ and applying a heat flux of $10\,W/(m^2\,K)$, a typical value for passive convection in air. A partial view of the mesh used in this finite-element calculation is displayed in Figure 5.8(b). The mesh has been particularly increased on the DLSPPW region, with elements smaller than $\lambda/6$, for a total of around 100000 elements.

The material properties are also given by the Ref. [81], and reported on the following Table 5.2.

Table 5.2: Material properties defined on the thermal model from [81].

Material	Thermal conductivity K [W/(m K)]	Density ρ (kg/m^3)	Specific heat capacity C_p [J/(kg K)]
Si	145	2330	700
SiO_2	1.1	2200	703
Au	120	19300	129.1
Polymer	0.2	1200	1000

At this stage, it is worth to note that the heat conductivity for gold used in the calculation is about three times smaller than for bulk ($317\,W/(m\,K)$). This results from the so called classical size effect that leads to a decrease of K for the system with a characteristic size (here the thickness) close to the mean free path of heat carrier in the material (electrons in metals).

By applying a current to the gold strip, the temperature increases progressively in time. It is then possible to plot the temperature distribution along the structure (Fig. 5.9(a)). A slice of the temperature gradient is extracted at the center of the structure and reported in Figure 5.9(b). The temperature map reproduce well the results shown in the Ref. [81], and we found an average difference of temperature inside the polymer of $\sim 120°$. Then the average temperature inside the polymer is probed during the heating (Figure 5.9(c)), and fitted with an exponential function, to obtain the rise time constant of the device, given by

$$\Delta T(t) = \Delta T_{max}(1 - \exp(-t/\tau)) \tag{5.8}$$

The fitting returns a value for the DLSPPW of $\tau_{DLSPPW} = 1.42\,\mu s$, in good agreement with the time constant reported in the literature for a similar situation ($1.35\,\mu s$).

We investigate now the impact of a metallic side wall on the response time of a Dihedron DLSPPW. In order to compare the response time of DLSPPW to a Dihedron, the polymer ridge and underneath gold strip sizes are similar in both configurations. For such dimensions, the properties discussed at the beginning of this chapter are

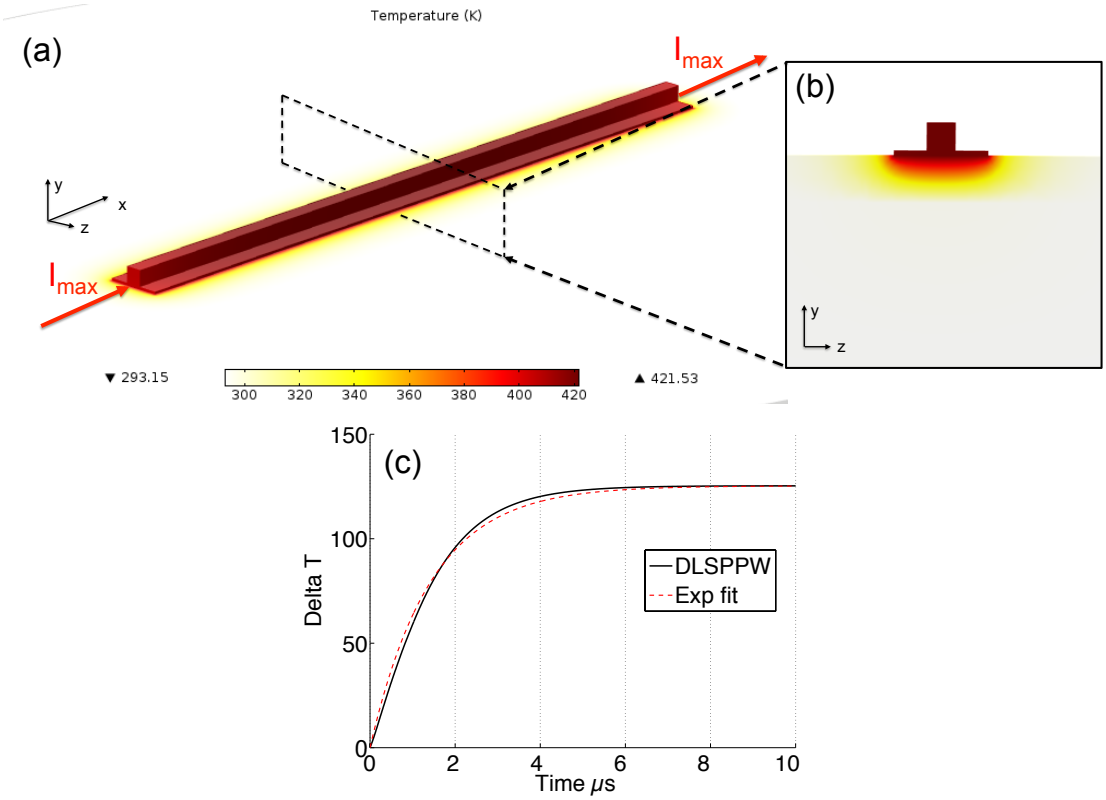

Figure 5.9: (a) Temperature distribution of the 3D DLSPPW heated by injecting a 28mA current into the metal stripe. (b) Slice of the temperature distribution inside the DLSPPW and the substrate. (c) Average temperature inside the polymer as a function of the time. The red dashed line correspond to an exponential fitting.

valid, except for the polarization conversion that request a larger polymer ridge of $800 \times 800\,\text{nm}$. The electrical heating of this larger structure will be proposed right after this comparison.

The Dihedral structure considered here is shown in Figure 5.10(a). A possible way to fabricate such a structure has been proposed in the previous section. To remain consistent with this statement, the metallic side wall need a support, chosen here to be a silica step. Then, the numerical procedure performed for DLSPPWs is repeated, with the same input current ($28.5\,\text{mA}$). A cross-cut of the temperature distribution is reported in the Figure 5.10(b). Compared to the DLSPPW (Fig. 5.9(b)), the temperature is distributed along the metallic step, increasing the total surface interaction of the polymer waveguide with the metal. Consequently, the time necessary to transfer the heat from the gold electrode to the dielectric ridge is decreased, as shown in Figure 5.10(c).

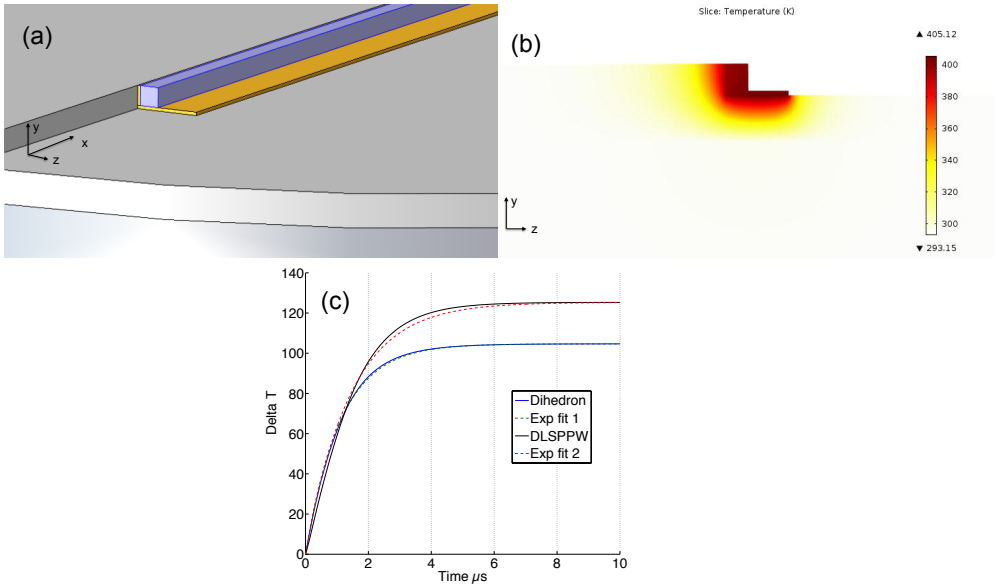

Figure 5.10: (a) Schematic view of the 3D Dihedron DLSPPW used in the heating calculations showing the silica step and substrate over what the Dihedron DLSPPW is placed. (b) Slice of the temperature distribution inside the Dihedron DLSPPW and the substrate. (c) Average temperature inside the polymer as a function of the time for both DLSPPW and Dihedron DLSPPW with the red and green dashed line respectively corresponding to exponential fitting of the response times.

For a Dihedron, the time constant estimated numerically is $\tau_{Dihedron}$ =1.1 µs, almost 25% faster than for a DLSPPW. But one can also note that, for an equivalent current source, the maximum temperature decreased in the same way due to the extra volume heated. However, one could find very attractive such gain of speed if the active polymer used features a high TOC, leading to high index changes for moderate temperatures changes. Such an improvement could be of interest for different DLSPPW components, such as DMIs shown chapter 3 or MZIs [152].

5.2.2 Thermo-optic behavior of plasmonic Dihedron based polarization converter

In the previous section, the particular case of the symmetric Dihedral structure has been introduced, showing that a Dihedron with a dielectric cross-section of $w_g = h_g = 800$ nm supports two hybrid normal modes that can be used to implement a compact polarization converter. However, the entire work presented so far report on the performances of thermo-optical structures, meaning that the optical chips using active DLSPPW devices for the optical interconnect purpose will obviously expose any other component to a thermally variable environment and eventually electrical current. In this context, it is worth to investigate the thermal behavior of these new structures when an electrical current flows through the metal stripes. In particular, we investigate the impact of a

temperature rise onto the polarization conversion properties of a symmetric Dihedron. The 3D-FEM model developed on the previous section for the calculation of the Dihedron polarization conversion performances is now coupled to the thermal model used in this section.

Using a typical TOC of $1.05 \times 10^{-4}\,\mathrm{K}^{-1}$ and $n = 1.535$ for the polymer, the two modes supported by the symmetric Dihedral structure are only slightly changed when a typical current of 28.5 mA is used to heat the system (Fig. 5.11(c)). Indeed, the field distribution of the two normal modes supported by a symmetric Dihedron being very similar (see Fig. 5.5), the temperature induced change of refractive index is expected to be of same amplitude for both modes. This is confirmed by the mode effective index calculations which returns for the cool state $n_{eff}^{cool_1} = 1.328$, $n_{eff}^{cool_2} = 1.302$ and for the hot state $n_{eff}^{hot_1} = 1.317$, $n_{eff}^{hot_2} = 1.291$. The corresponding two half-beating lengths are then $L_{HB}^{cool} = 29.84\,\mu m$ and $L_{HB}^{hot} = 29.77\,\mu m$. The half-beating lengths for the two temperature states are so close that the polarization conversion efficiency is unchanged. The difference between the electric field norm along the Dihedron DLSPPWs for the cool state (Fig. 5.7) and hot state (Fig. 5.11(a)) is indistinguishable. In addition, we found an average propagation length for the two modes at the two temperature states that is also unchanged ($L_{SPP}^{hot_{avg}} = 39.6\,\mu m$ and $L_{SPP}^{cool_{avg}} = 39.1\,\mu m$).

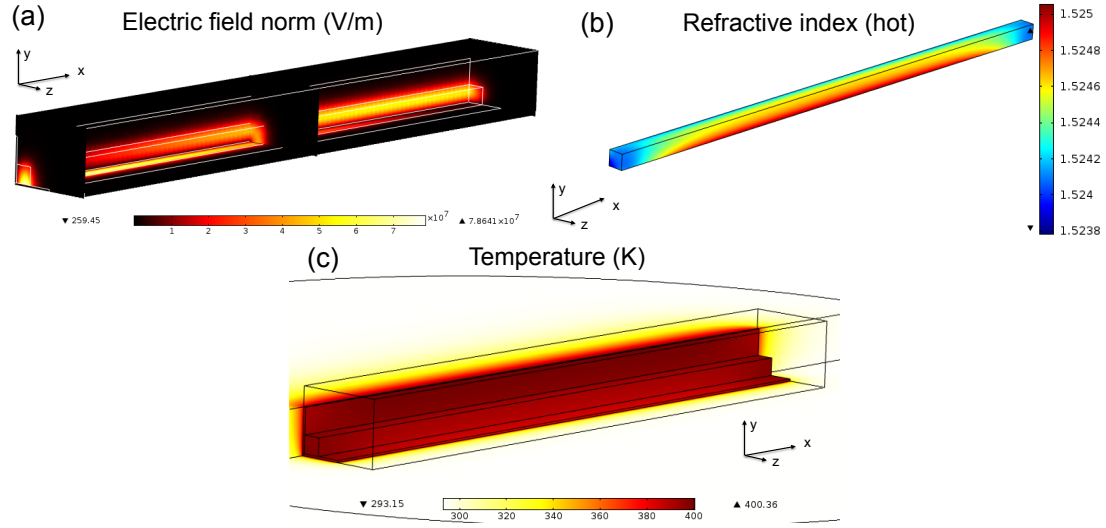

Figure 5.11: (a) Electric field map norm at the hot electrically heated. (b) Refractive index distribution induced by the electrical heating. (c) Temperature distribution for an electrical current of 28.5 mA.

One can note that the fully coupled model (electromagnetic and thermal calculations) takes into account the gradient of refractive index inside the polymer (Fig. 5.11(b)), induced by the electrical heating (Fig. 5.11(c)), making the propagation calculation of the Dihedron modes in the hot state more realistic (Fig. 5.11(a)).

As expected, the performances extracted are extremely close to the cool state, with a $\mathsf{PCE}_{\mathtt{hot}} = \mathsf{PCE}_{\mathtt{cool}} = 99.67\,\%$ and $\mathsf{ER}_{\mathtt{hot}} = 25.1\,\mathrm{dB}$ ($\mathsf{ER}_{\mathtt{cool}}$ =24.8 dB), confirming the thermal stability of this new passive component.

Summary Thermo-optical study of Dihedron DLSPPWs

A 3D-FEM model have been developed to investigate the thermal and thermo-optical properties of DLSPPWs and the new Dihedron DLSPPW introduced in this chapter. By exploring the response time of both structures placed on a Silica-Silicon substrate, we found that the thermal dynamic of a DLSPPW can be enhanced by 25% by adding a metallic wall one side of the polymer ridge. This calculation take into account a possible fabrication process relying on a deep etching of the top Silica layer that would produce a vertical wall necessary for the deposition of the vertical metallic shield. Finally, the symmetric Dihedral structure presented on the previous section have been analyzed by coupling thermal and optical models, which confirm the potential of this compact polarization converter for optical interconnect since it is unaffected by a thermally unstable environment.

5.3 Conclusion

In conclusion, we have presented an improvement of the basic DLSPPW using a metallic shield placed on one side of the polymer ridge called Dihedron. Two new properties offered by this configuration have been described. First we have shown that a DLSPPW featuring a metal wall on one side can be implemented on a metal strip with a reduced width compare to the situation where no wall is used. This property can be understood from the fact that the metal wall prevent the DLSPPW mode from leaking into the substrate. Second, when the Dihedron becomes symmetric, the system works as a compact polarization converter that can convert either TE to TM or TM to TE modes without any structural changes. The performances have been estimated by a full 3D-FEM calculations, proving that such a structure can be competitive with the existing one. Moreover, the metallic wall could play a role on the dynamic performances of the DLSPPW devices presented so far since the addition of a metallic wall reduces the minimum response time by 25%. Finally, the new polarization conversion have been analyzed in a thermally variable SOI chip. The results confirm that the polarization conversion functionality of a symmetric Dihedron DLSPPW is preserved in a changing temperature environment, making realistic the implementation of such a component into a thermally driven devices.

Conclusion and prospectives

We report in this work on the fabrication and characterization of thermo-plasmonic routing devices for a Tb/s architecture at telecom wavelengths. The devices are relying on particular electromagnetic modes existing at a metal-dielectric interface known as Surface Plasmon Polaritions. By confining these modes into three dimensional dielectric ridges made of polymers lying onto thin gold films or stripes, Dielectric Surface Plasmon Polariton Waveguides (DLSPPWs) have been combined to create passive and thermally controlled active devices. The physical nature of the plasmon modes propagating inside the DLSPPW-based devices has been analyzed numerically and experimentally on standalone configurations by means of far field Leakage Radiation Microscopy (LRM) imaging. By using momentum-space microscopy, we have shown the added values of Fourier plane imaging of leaky waveguiding structures as compared to direct image plane imaging. However, the limitations of LRM have been also exemplified in the case of bent waveguiding structures with small radius of curvature.

Next we have demonstrate thermal control of different plasmonic racetrack shaped resonators with improved performances. With these resonators, quality factors in the range of 130 have been achieved, and 4.5 nm spectral shift of their transmission spectra have been demonstrated in the case of high thermo-optical coefficient polymer waveguides. Resonators can be viewed as elementary building blocks for more sophisticated devices such as routers. However, the evanescently coupled devices impose low fabrication tolerance that are difficult to control with organic materials such as polymers. To circumvent this limitation, we have operated a longitudinal geometry based on dual mode interferometer thermally activated either by Joule or photo-thermal heating.

With photo-thermal heating, we open the way towards a specific kind of "all-optical" plasmonic devices with improved performances in particular if the optical properties of the active material are optimum at the pump wavelength. Beyond photo-thermal, we propose also "plasmo-thermal" devices for which heating is produced by the absorption of surface plasmon modes rather than photons. For pump wavelength leading to a significant plasmon propagation, the extension of the pump plasmon jet can be conveniently used to heat elongated-shape devices. By operating a new fiber-to-fiber characterization set-up relying on optimized dielectric grating couples, we have investigated the thermo-optical response time of standalone devices. The moderate response time in order of several

microseconds for the devices we have considered indicate that design improvements are necessary to reach the targeted bandwidth of ~ 1 MHz. Among several possibilities, we have proposed a new design for improved thermal performances by adding a vertical metallic wall to standard DLSPPW geometries. These new waveguides denoted as Dihedron plasmon polariton waveguides also feature very interesting properties when they are made symmetric. In this case the hybridization of the DLSPPW mode supported by the vertical and horizontal metal interface leads to the generation of normal modes that can be both excited in TE as well as in TM polarization. The beating of these normal modes is at the origin of the working principle of what we believe to be the first plasmonic polarization converter.

Finally, we would like to mention that actions in the continuity of this work and inspired by the results discussed in this work are currently in progress. In particular, one can cite the use of nanosecond pulses for the photo-thermal heating of DLSPPW devices. With DLSPPWs no more comprised of polymers but with solid state materials, unprecedented performances in terms of footprint and response time are expected for this thermo-plasmonic devices.

Bibliography

[1] D. Miller and H. Ozaktas. 'Limit to the Bit-Rate Capacity of Electrical Interconnects from the Aspect Ratio of the System Architecture'. *Journal of Parallel and Distributed Computing* (Feb. 1997) **41**(1), pp. 42–52.

[2] R. G. Hunsperger. 'Integrated Optics: Theory and Technology'. *Topics in Applied Physics, Berlin: Springer, 1979, 2nd Edition* (1987) **50**(11).

[3] H. Raether. *Surface plasmons on smooth and rough surfaces and on gratings.* (Springer-Verlag Berlin, 1988)

[4] R. Zia, J. Schuller, A. Chandran, and M. Brongersma. 'Plasmonics : the next chip-scale technology'. *Materials today* (2006) **9**(7), pp. 20–27.

[5] H. A. Atwater. 'The promise of plasmonics.' *Scientific American* (Apr. 2007) **296**(4), pp. 56–63.

[6] A. Snyder and J Love. *Optical waveguide theory.* (1983)

[7] G. T. Reed and A. P. Knights. *Silicon photonics an introduction.* Ed. by John Wiley and Sons. (2004)

[8] D. Miller. 'Optical Interconnects - OSA Technical Digest (CD)'. In *Optical Fiber Communication Conference.* (Optical Society of America, Mar. 2010) OThX1.

[9] E. Frachtenberg. 'Design Principles in the Open Compute Project - OSA Technical Digest'. In *Optical Fiber Communication Conference.* (Optical Society of America, Mar. 2012) OTu1B.4.

[10] J. Schmidtchen, A. Splett, B. Schuppert, K. Petermann, and G. Burbach. 'Low loss singlemode optical waveguides with large cross-section in silicon-on-insulator'. English. *Electronics Letters* (Aug. 1991) **27**(16), p. 1486.

[11] A. G. Rickman, G. T. Reed, and F Namavar. *Silicon-on-insulator optical rib waveguide loss and mode characteristics.* 1994.

[12] A. Sakai, G. Hara, and T. Baba. 'Propagation characteristics of ultrahigh-Q optical waveguide on silicon-on-insulator substrate'. *Jpn. J. Appl. Phys* (2001) **40**(4), pp. 383–385.

[13] W. Bogaerts, R. Baets, and P. Dumon. 'Nanophotonic Waveguides in Silicon-on-Insulator Fabricated With CMOS Technology'. *Journal of Lightwave Technology* (2005) **23**(1), pp. 401–412.

[14] B. Jalali. 'Teaching silicon new tricks'. *Optical Fiber Communication and the National Fiber* (2007) **1,** pp. 193–195.

[15] T. Tamir. 'Integrated optics'. *Topics in Applied Physics, Berlin: Springer, 1979, 2nd Edition* (1979).

[16] W. Barnes, A. Dereux, and T. W. Ebbesen. 'Surface plasmon subwavelength optics.' *Nature* (2003) **424**(6950), pp. 824–830.

[17] E. Burstein and F. De Martini. 'Polaritons'. In *Taormina, october 2-6.* (1972)

[18] D. K. Gramotnev and S. I. Bozhevolnyi. 'Plasmonics beyond the diffraction limit'. *Nature Photonics* (Jan. 2010) **4**(2), pp. 83–91.

[19] S. Maier. *Plasmonics: fundamentals and applications.* (Springer Verlag, 2007)

[20] S. Lal, S. Link, and N. J. Halas. 'Nano-optics from sensing to waveguiding'. *Nature Photonics* (Nov. 2007) **1**(11), pp. 641–648.

[21] A. Hohenau, J. R. Krenn, A. L. Stepanov, A. Drezet, H. Ditlbacher, B. Steinberger, A. Leitner, and F. R. Aussenegg. 'Dielectric optical elements for surface plasmons'. *Optics Letters* (Apr. 2005) **30**(8), p. 893.

[22] Z. Han and S. I. Bozhevolnyi. 'Radiation guiding with surface plasmon polaritons'. *Reports on Progress in Physics* (Jan. 2013) **76**(1), p. 016402.

[23] C. Manolatou, S. Johnson, S. Fan, P. Villeneuve, H. Haus, and J. Joannopoulos. 'High-density integrated optics'. *Journal of Lightwave Technology* (1999) **17**(9), pp. 1682–1692.

[24] E. Economou. 'Surface plasmons in thin films'. *Physical review* (1969) **2.**

[25] J. Burke, G. Stegeman, and T Tamir. 'Surface-polariton-like waves guided by thin, lossy metal films'. *Physical Review B* (1986) **33**(8).

[26] B. Prade, J. Y. Vinet, and A. Mysyrowicz. 'Guided optical waves in planar heterostructures with negative dielectric constant'. *Phys. Rev. B* (1991) **44**(24).

[27] R. Zia, M. D. Selker, P. B. Catrysse, and M. L. Brongersma. 'Geometries and materials for subwavelength surface plasmon modes.' *Journal of the Optical Society of America. A, Optics, image science, and vision* (Dec. 2004) **21**(12), pp. 2442–6.

[28] T. Nikolajsen, K. Leosson, I. Salakhutdinov, and S. I. Bozhevolnyi. 'Polymer-based surface-plasmon-polariton stripe waveguides at telecommunication wavelengths'. *Applied Physics Letters* (2003) **82**(5), p. 668.

[29] D. Sarid. 'Long-range surface-plasma waves on very thin metal films'. *Physical Review Letters* (1981) **47**(26), pp. 1927–1930.

[30] J. Dionne, L. Sweatlock, H. A. Atwater, and A. Polman. 'Plasmon slot waveguides: Towards chip-scale propagation with subwavelength-scale localization'. *Physical Review B* (Jan. 2006) **73**(3), pp. 1–9.

[31] S. I. Bozhevolnyi. 'Effective-index modeling of channel plasmon polaritons'. *Optics express* (2006) **14**(20), pp. 9467–9476.

[32] J. Takahara, S. Yamagishi, and H. Taki. 'Guiding of a one-dimensional optical beam with nanometer diameter'. *Optics express* (1997) **22**(7), pp. 475–477.

[33] J.-C. Weeber, A. Dereux, C. Girard, J. R. Krenn, and J.-P. Goudonnet. 'Plasmon polaritons of metallic nanowires for controlling submicron propagation of light'. *Physical Review B* (Sept. 1999) **60**(12), pp. 9061–9068.

[34] I. Novikov and a. Maradudin. 'Channel polaritons'. *Physical Review B* (June 2002) **66**(3), p. 035403.

[35] J.-C. Weeber, Y. Lacroute, and A. Dereux. 'Optical near-field distributions of surface plasmon waveguide modes'. *Physical Review B* (2003) **68**(11), pp. 1–10.

[36] P. Berini. 'Plasmon-polariton waves guided by thin lossy metal films of finite width: Bound modes of symmetric structures'. *Physical Review B* (Apr. 2000) **61**(15), pp. 10484–10503.

[37] P. Berini. 'Plasmon-polariton waves guided by thin lossy metal films of finite width: Bound modes of asymmetric structures'. *Physical Review B* (Mar. 2001) **63**(12), p. 125417.

[38] B. Lamprecht, J. R. Krenn, G. Schider, H. Ditlbacher, M. Salerno, N. Felidj, A. Leitner, F. R. Aussenegg, and J.-C. Weeber. 'Surface plasmon propagation in microscale metal stripes'. *Applied Physics Letters* (2001) **79**(1), p. 51.

[39] J.-C. Weeber, J. R. Krenn, and A. Dereux. 'Near-field observation of surface plasmon polariton propagation on thin metal stripes'. *Physical review B* (2001) **64,** pp. 1–9.

[40] J.-C. Weeber, M. U. Gonzalez, A.-L. Baudrion, and A. Dereux. 'Surface plasmon routing along right angle bent metal strips'. *Applied Physics Letters* (2005) **87**(22), p. 221101.

[41] S. I. Bozhevolnyi, V. S. Volkov, and E. Devaux. 'Channel plasmon subwavelength waveguide components including interferometers and ring resonators'. *Nature* (2006) **440**(March), pp. 2–5.

[42] W. Cai, W. Shin, S. Fan, and M. L. Brongersma. 'Elements for plasmonic nanocircuits with three-dimensional slot waveguides.' *Advanced materials (Deerfield Beach, Fla.)* (Dec. 2010) **22**(45), pp. 5120–4.

[43] G. Veronis and S. Fan. 'Bends and splitters in metal-dielectric-metal subwavelength plasmonic waveguides'. *Applied Physics Letters* (2005) **87**(13), p. 131102.

[44] L. Liu, Z. Han, and S. He. 'Novel surface plasmon waveguide for high integration'. *Optics Express* (2005) **13**(17), pp. 1976–1980.

[45] C. Delacour, S. Blaize, P. Grosse, J. M. Fedeli, A. Bruyant, R. Salas-Montiel, G. Lerondel, and A. Chelnokov. 'Efficient directional coupling between silicon and copper plasmonic nanoslot waveguides: toward metal-oxide-silicon nanophotonics.' *Nano letters* (Aug. 2010) **10**(8), pp. 2922–6.

[46] B. Steinberger, A. Hohenau, H. Ditlbacher, A. L. Stepanov, A. Drezet, F. R. Aussenegg, A. Leitner, and J. R. Krenn. 'Dielectric stripes on gold as surface plasmon waveguides'. *Applied Physics Letters* (2006) **88**(9), p. 094104.

[47] A. V. Krasavin and A. V. Zayats. 'Passive photonic elements based on dielectric-loaded surface plasmon polariton waveguides'. *Applied Physics Letters* (2007) **90**(21), p. 211101.

[48] T. Holmgaard and S. I. Bozhevolnyi. 'Theoretical analysis of dielectric-loaded surface plasmon-polariton waveguides'. *Physical Review B* (June 2007) **75**(24), pp. 1–12.

[49] M. Brongersma, J. Hartman, and H. A. Atwater. 'Electromagnetic energy transfer and switching in nanoparticle chain arrays below the diffraction limit'. *Physical Review B* (2000) **62**(24), pp. 356–359.

[50] M. Février, P. Gogol, A. Aassime, R. Mégy, C. Delacour, A. Chelnokov, A. Apuzzo, S. Blaize, J.-M. Lourtioz, and B. Dagens. 'Giant coupling effect between metal nanoparticle chain and optical waveguide.' *Nano letters* (Feb. 2012) **12**(2), pp. 1032–7.

[51] A. Boltasseva, V. S. Volkov, R. B. Nielsen, E. Moreno, S. G. Rodrigo, and S. I. Bozhevolnyi. 'Triangular metal wedges for subwavelength plasmon-polariton guiding at telecom wavelengths.' *Optics express* (Apr. 2008) **16**(8), pp. 5252–60.

[52] Y. Vlasov and S. McNab. 'Losses in single-mode silicon-on-insulator strip waveguides and bends.' *Optics express* (Apr. 2004) **12**(8), pp. 1622–31.

[53] C. Reinhardt, S. Passinger, B. N. Chichkov, C. Marquart, I. P. Radko, and S. I. Bozhevolnyi. 'Laser-fabricated dielectric optical components for surface plasmon polaritons.' *Optics letters* (May 2006) **31**(9), pp. 1307–9.

[54] B. Steinberger, A. Hohenau, H. Ditlbacher, F. R. Aussenegg, A. Leitner, and J. R. Krenn. 'Dielectric stripes on gold as surface plasmon waveguides: Bends and directional couplers'. en. *Applied Physics Letters* (2007) **91**(8), p. 081111.

[55] S. Massenot, J. Grandidier, A. Bouhelier, G. Colas des Francs, L. Markey, J.-C. Weeber, A. Dereux, J. Renger, M. U. Gonzalez, and R. Quidant. 'Polymer-metal waveguides characterization by Fourier plane leakage radiation microscopy'. *Applied Physics Letters* (2007) **91**(24), p. 243102.

[56] A. Drezet and A. Hohenau. 'How to erase surface plasmon fringes'. *Applied Physics Letters* (2006) **091117.**

[57] T. Holmgaard, S. I. Bozhevolnyi, L. Markey, and A. Dereux. 'Dielectric-loaded surface plasmon-polariton waveguides at telecommunication wavelengths: Excitation and characterization'. *Applied Physics Letters* (2008) **92**(1), p. 011124.

[58] T. Holmgaard, S. I. Bozhevolnyi, L. Markey, A. Dereux, A. V. Krasavin, P. Bolger, and A. V. Zayats. 'Efficient excitation of dielectric-loaded surface plasmon-polariton waveguide modes at telecommunication wavelengths'. *Physical Review B* (Oct. 2008) **78**(16), pp. 1–8.

[59] T. Holmgaard, Z. Chen, S. I. Bozhevolnyi, L. Markey, A. Dereux, A. V. Krasavin, and A. V. Zayats. 'Bend- and splitting loss of dielectric-loaded surface plasmon-polariton waveguides'. *Optics Express* (Aug. 2008) **16**(18), p. 13585.

[60] T. Holmgaard, Z. Chen, S. I. Bozhevolnyi, L. Markey, and A. Dereux. 'Dielectric-loaded plasmonic waveguide-ring resonators'. *Optics Express* (2009) **17**(4), pp. 2968–2975.

[61] Z. Han, C. Garcia-Ortiz, I. P. Radko, and S. I. Bozhevolnyi. 'Detuned-resonator induced transparency in dielectric-loaded plasmonic waveguides'. *Optics Letters* (2013) **38**(6), pp. 875–877.

[62] T. Holmgaard, Z. Chen, S. I. Bozhevolnyi, L. Markey, A. Dereux, A. V. Krasavin, and A. V. Zayats. 'Wavelength selection by dielectric-loaded plasmonic components'. *Applied Physics Letters* (2009) **94**(5), p. 051111.

[63] Z. Chen, T. Holmgaard, S. I. Bozhevolnyi, A. V. Krasavin, A. V. Zayats, L. Markey, and A. Dereux. 'Wavelength-selective directional coupling with dielectric-loaded plasmonic waveguides.' *Optics letters* (Feb. 2009) **34**(3), pp. 310–2.

[64] T. Holmgaard, S. I. Bozhevolnyi, L. Markey, and A. Dereux. 'Design and Characterization of Dielectric-Loaded Plasmonic Directional Couplers'. *Journal of Lightwave Technology* (Dec. 2009) **27**(24), pp. 5521–5528.

[65] O. Tsilipakos and E. E. Kriezis. 'Microdisk resonator filters made of dielectric-loaded plasmonic waveguides'. *Optics Communications* (Aug. 2010) **283**(15), pp. 3095–3098.

[66] J. Grandidier, G. Colas des Francs, L Markey, A. Bouhelier, S. Massenot, J.-C. Weeber, and A. Dereux. 'Dielectric-loaded surface plasmon polariton waveguides on a finite-width metal strip'. *Applied Physics Letters* (2010) **96**(6), p. 063105.

[67] R. M. Briggs, J. Grandidier, S. P. Burgos, E. Feigenbaum, and H. A. Atwater. 'Efficient Coupling between Dielectric-Loaded Plasmonic and Silicon Photonic Waveguides.' *Nano letters* (Oct. 2010).

[68] S. Massenot, J.-C. Weeber, A. Bouhelier, G. Colas des Francs, J. Grandidier, L. Markey, and A. Dereux. 'Differential method for modeling dielectric-loaded surface plasmon polariton waveguides'. *Optics Express* (Oct. 2008) **16**(22), p. 17599.

[69] G. Colas des Francs, J. Grandidier, S. Massenot, A. Bouhelier, J.-C. Weeber, and A. Dereux. 'Integrated plasmonic waveguides: A mode solver based on density of states formulation'. *Physical Review B* (Sept. 2009) **80**(11), pp. 1–7.

[70] Y. Song and L. Zhi. 'Bending Loss Calculation of a Dielectric-Loaded Surface Plasmon Polariton Waveguide Structure'. *Chinese Physics Letters* (Feb. 2010) **27**(2), p. 027303.

[71] J. Gosciniak, V. Volkov, S. I. Bozhevolnyi, L. Markey, S. Massenot, and A. Dereux. 'Fiber-coupled dielectric-loaded plasmonic waveguides'. *Optics Express* (2010) **18**(5), pp. 5314–5319.

[72] A. Kumar, J. Gosciniak, and T. Andersen. 'Power monitoring in dielectric-loaded surface plasmon-polariton waveguides'. *Optics express* (2011) **19**(4), pp. 2972–2978.

[73] J. Gosciniak, M. G. Nielsen, L. Markey, A. Dereux, and S. I. Bozhevolnyi. 'Power monitoring in dielectric-loaded plasmonic waveguides with internal Wheatstone bridges'. *Optics Express* (Feb. 2013) **21**(5), p. 5300.

[74] A. V. Krasavin and A. V. Zayats. 'Three-dimensional numerical modeling of photonic integration with dielectric-loaded SPP waveguides'. *Physical Review B* (2008) **78**(4), pp. 1–8.

[75] A. V. Krasavin, S. Randhawa, J.-S. Bouillard, J. Renger, R. Quidant, and A. V. Zayats. 'Optically-programmable nonlinear photonic component for dielectric-loaded plasmonic circuitry.' *Optics express* (Dec. 2011) **19**(25), pp. 25222–9.

[76] J. Grandidier. 'Guide plasmonique polymère-métal: composants passifs et actifs pour la photonique intégrée'. (2009).

[77] J. Grandidier, G. Colas des Francs, S. Massenot, A. Bouhelier, L. Markey, J.-C. Weeber, C. Finot, and A. Dereux. 'Gain-assisted propagation in a plasmonic waveguide at telecom wavelength'. *Nano Letters* (2009) **9**(8), pp. 2935–2939.

[78] J. Grandidier, G. Colas des Francs, S. Massenot, A. Bouhelier, L Markey, J.-C. Weeber, and A. Dereux. 'Leakage radiation microscopy of surface plasmon coupled emission: investigation of gain-assisted propagation in an integrated plasmonic waveguide.' *Journal of microscopy* (Aug. 2010) **239**(2), pp. 167–72.

[79] C. Garcia, V. Coello, and Z. Han. 'Partial loss compensation in dielectric-loaded plasmonic waveguides at near infra-red wavelengths'. *Optics express* (2012) **20**(7), pp. 7771–7776.

[80] F. Huang, H. Yuan, and X. Sun. 'Amplification of SPPs in a methyl orange doped dielectric loaded SPPs waveguide'. (Nov. 2012). Ed. by Z. Zhou and K. Wada, 85641F–85641F–8.

[81] O. Tsilipakos, T. V. Yioultsis, and E. E. Kriezis. 'Theoretical analysis of thermally tunable microring resonator filters made of dielectric-loaded plasmonic waveguides'. *Journal of Applied Physics* (2009) **106**(9), p. 093109.

[82] J. Gosciniak, S. I. Bozhevolnyi, T. B. Andersen, V. S. Volkov, J. Kjelstrup-Hansen, L. Markey, and A. Dereux. 'Thermo-optic control of dielectric-loaded plasmonic waveguide components.' *Optics express* (Jan. 2010) **18**(2), pp. 1207–16.

[83] J. Grandidier, S. Massenot, G. des Francs, A. Bouhelier, J.-C. Weeber, L. Markey, A. Dereux, J. Renger, M. U. Gonzalez, and R. Quidant. 'Dielectric-loaded surface plasmon polariton waveguides: Figures of merit and mode characterization by image and Fourier plane leakage microscopy'. *Physical Review B* (Dec. 2008) **78**(24), pp. 1–9.

[84] I. Stefanon, S. Blaize, A. Bruyant, S. Aubert, G. Lerondel, R. Bachelot, and P. Royer. 'Heterodyne detection of guided waves using a scattering-type Scanning Near-Field Optical Microscope.' *Optics express* (July 2005) **13**(14), pp. 5553–64.

[85] A. Krishnan, S. P. Frisbie, L. Grave de Peralta, and A. A. Bernussi. 'Plasmon stimulated emission in arrays of bimetallic structures coated with dye-doped dielectric'. *Applied Physics Letters* (2010) **96**(11), p. 111104.

[86] J. Berthelot, A. Bouhelier, G. Colas des Francs, J.-C. Weeber, and A. Dereux. 'Excitation of a one-dimensional evanescent wave by conical edge diffraction of surface plasmon.' *Optics express* (Mar. 2011) **19**(6), pp. 5303–12.

[87] C. J. Regan, O Thiabgoh, L. Grave de Peralta, and A. A. Bernussi. 'Probing photonic Bloch wavefunctions with plasmon-coupled leakage radiation.' *Optics express* (Apr. 2012) **20**(8), pp. 8658–66.

[88] M. Neviere and E. Popov. 'Light Propagation in Periodic Media: Diffraction Theory and Design'. (2003).

[89] A. B. Buckman. *Guided-Wave Photonics.* (Saunders College Pub., 1992)

[90] A. Drezet, A. Hohenau, D. Koller, A. L. Stepanov, H. Ditlbacher, B. Steinberger, F. R. Aussenegg, A. Leitner, and J. R. Krenn. 'Leakage radiation microscopy of surface plasmon polaritons'. *Materials Science and Engineering: B* (Apr. 2008) **149**(3), pp. 220–229.

[91] S. Frisbie, C. Regan, A. Krishnan, C. Chesnutt, J. Ajimo, A. A. Bernussi, and L. Grave de Peralta. 'Characterization of polarization states of surface plasmon polariton modes by Fourier-plane leakage microscopy'. *Optics Communications* (Dec. 2010) **283**(24), pp. 5255–5260.

[92] B. Hecht, H. Bielefeldt, L. Novotny, Y. Inouye, and D. Pohl. 'Local Excitation, Scattering, and Interference of Surface Plasmons.' *Physical Review Letters* (1996) **77**(9), pp. 1889–1892.

[93] A. Bouhelier, T. Huser, J. M. Freyland, H. J. Guntherodt, and D. W. Pohl. 'Plasmon transmissivity and reflectivity of narrow grooves in a silver film.' *Journal of microscopy* (1999) **194**(Pt 2-3), pp. 571–3.

[94] A. Yariv. 'Universal relations for coupling of optical power between microresonators and dielectric waveguides'. *Electronics Letters* (2000) **36**(4), pp. 1–2.

[95] E. Palik. *Handbook of Optical Constants of Solids lll.* (1998)

[96] E. Marcatili and S. Miller. 'Improved Relations Describing Directional control in electromagnetic wave guidance'. *Bell Syst. Tech. J* (1969).

[97] D. J. Dikken, M. Spasenovic, E. Verhagen, D. van Oosten, and L. K. Kuipers. 'Characterization of bending losses for curved plasmonic nanowire waveguides.' *Optics express* (July 2010) **18**(15), pp. 16112–9.

[98] C. Yang, E. J. Teo, T. Goh, S. L. Teo, J. H. Teng, and A. A. Bettiol. 'Metal-assisted photonic mode for ultrasmall bending with long propagation length at visible wavelengths'. *Optics Express* (Oct. 2012) **20**(21), p. 23898.

[99] M. Heiblum and J. Harris. 'Analysis of curved optical waveguides by conformal transformation'. *Quantum Electronics, IEEE Journal of* (1975).

[100] Z. Han, P. Zhang, and S. I. Bozhevolnyi. 'Calculation of bending losses for highly confined modes of optical waveguides with transformation optics'. *opticsinfobase.org* (2013) **38**(11), pp. 1778–1780.

[101] O. Tsilipakos. 'Thermo-optic microring resonator switching elements made of dielectric-loaded plasmonic waveguides'. *Journal of Applied Physics* (2011) **073111,** pp. 1–9.

[102] J. M. Choi, R. K. Lee, and A. Yariv. 'Control of critical coupling in a ring resonator-fiber configuration: application to wavelength-selective switching, modulation, amplification, and oscillation.' *Optics letters* (Aug. 2001) **26**(16), pp. 1236–8.

[103] T. Baehr-Jones, M. Hochberg, C. Walker, and A. Scherer. 'High-Q ring resonators in thin silicon-on-insulator'. *Applied Physics Letters* (2004) **85**(16), p. 3346.

[104] W. R. McKinnon, D. X. Xu, C. Storey, E. Post, A. Densmore, A. Delage, P. Waldron, J. H. Schmid, and S. Janz. 'Extracting coupling and loss coefficients from a ring resonator.' *Optics express* (Oct. 2009) **17**(21), pp. 18971–82.

[105] J. Niehusmann, A. Vorckel, P. H. Bolivar, T. Wahlbrink, W. Henschel, and H. Kurz. 'Ultrahigh-quality-factor silicon-on-insulator microring resonator.' *Optics Letters* (2004) **29**(24), pp. 2861–2863.

[106] B. Lee and A. Biberman. 'High-Speed 2 x 2 Switch for Multiwavelength Silicon-Photonic Networks–On-Chip'. *Journal of Lightwave Technology* (2009) **27**(14), pp. 2900–2907.

[107] A. Biberman and B. Lee. 'Broadband operation of nanophotonic router for silicon photonic networks-on-chip'. *Photonics Technology Letters,* (2010) **22**(12), pp. 926–928.

[108] A. Pitilakis and E. E. Kriezis. 'Longitudinal 2 x 2 Switching Configurations Based on Thermo-Optically Addressed Dielectric-Loaded Plasmonic Waveguides'. *Journal of Lightwave Technology* (2011) (99), pp. 1–1.

[109] O. Tsilipakos, A. Pitilakis, A. C. Tasolamprou, T. V. Yioultsis, and E. E. Kriezis. 'Computational techniques for the analysis and design of dielectric-loaded plasmonic circuitry'. *Optical and Quantum Electronics* (Jan. 2011) **42**(8), pp. 541–555.

[110] M. G. Nielsen, J.-C. Weeber, K. Hassan, J. Fatome, C. Finot, S. Kaya, L. Markey, O. Albrektsen, S. I. Bozhevolnyi, G. Millot, and A. Dereux. 'Grating Couplers for Fiber-to-Fiber Characterizations of Stand-Alone Dielectric Loaded Surface Plasmon Waveguide Components'. *Journal of Lightwave Technology* (Oct. 2012) **30**(19), pp. 3118–3125.

[111] D. Perron, M. Wu, C. Horvath, D. Bachman, and V. Van. 'All-plasmonic switching based on thermal nonlinearity in a polymer plasmonic microring resonator.' *Optics letters* (July 2011) **36**(14), pp. 2731–3.

[112] H. Richardson and Z. Hickman. 'Thermooptical properties of gold nanoparticles embedded in ice: characterization of heat generation and melting'. *Nano letters* (2006) **6**(4), pp. 783–788.

[113] A. Govorov and H. Richardson. 'Generating heat with metal nanoparticles'. *Nano Today* (2007) **2**(1), pp. 30–38.

[114] H. H. Richardson, M. T. Carlson, P. J. Tandler, P. Hernandez, and A. O. Govorov. 'Experimental and theoretical studies of light-to-heat conversion and collective heating effects in metal nanoparticle solutions.' *Nano letters* (Mar. 2009) **9**(3), pp. 1139–46.

[115] E. Boisselier and D. Astruc. 'Gold nanoparticles in nanomedicine: preparations, imaging, diagnostics, therapies and toxicity.' *Chemical Society reviews* (June 2009) **38**(6), pp. 1759–82.

[116] A. S. Urban, M. Fedoruk, M. R. Horton, J. O. Radler, F. D. Stefani, and J. Feldmann. 'Controlled nanometric phase transitions of phospholipid membranes by plasmonic heating of single gold nanoparticles.' *Nano letters* (Aug. 2009) **9**(8), pp. 2903–8.

[117] S. Maity, L. N. Downen, J. R. Bochinski, and L. I. Clarke. 'Embedded metal nanoparticles as localized heat sources: An alternative processing approach for complex polymeric materials'. *Polymer* (Mar. 2011) **52**(7), pp. 1674–1685.

[118] D. Huhn, A. Govorov, P. R. Gil, and W. J. Parak. 'Photostimulated Au Nanoheaters in Polymer and Biological Media: Characterization of Mechanical Destruction and Boiling'. *Advanced Functional Materials* (Jan. 2012) **22**(2), pp. 294–303.

[119] C. Fang, L. Shao, Y. Zhao, J. Wang, and H. Wu. 'A gold nanocrystal/poly(dimethylsiloxane) composite for plasmonic heating on microfluidic chips.' *Advanced materials (Deerfield Beach, Fla.)* (Jan. 2012) **24**(1), pp. 94–8.

[120] G. Baffou, C. Girard, and R. Quidant. 'Mapping Heat Origin in Plasmonic Structures'. *Physical Review Letters* (Apr. 2010) **104**(13), p. 136805.

[121] A. Sanchot, G. Baffou, R. Marty, A. Arbouet, R. Quidant, C. Girard, and E. Dujardin. 'Plasmonic nanoparticle networks for light and heat concentration.' *ACS nano* (Apr. 2012) **6**(4), pp. 3434–40.

[122] M. A. Garcia, J. Llopis, and S. E. Paje. 'A simple model for evaluating the optical absorption spectrum from small Au-colloids in sol–gel films'. *Chemical Physics Letters* (1999) (December), pp. 313–320.

[123] C. Bohren and D. Huffman. *Absorption and scattering of light by small particles.* (2008)

[124] M. Rashidi-Huyeh and B. Palpant. 'Counterintuitive thermo-optical response of metal-dielectric nanocomposite materials as a result of local electromagnetic field enhancement'. *Physical Review B* (Aug. 2006) **74**(7), p. 075405.

[125] X. Li, L. Huang, Q. Tan, B. Bai, and G. Jin. 'Integrated plasmonic semicircular launcher for dielectric-loaded surface plasmon-polariton waveguide'. *Optics Express* (2011) **19**(7), pp. 6541–6548.

[126] H. Ditlbacher, J. R. Krenn, A. Hohenau, A. Leitner, and F. R. Aussenegg. 'Efficiency of local light-plasmon coupling'. *Applied Physics Letters* (2003) **83**(18), p. 3665.

[127] G. Leveque and O. J. Martin. 'Optimization of finite diffraction gratings for the excitation of surface plasmons'. *Journal of Applied Physics* (2006) **100**(12), p. 124301.

[128] J. Renger, S. Grafström, and L. Eng. 'Direct excitation of surface plasmon polaritons in nanopatterned metal surfaces and thin films'. *Physical Review B* (2007) (December 2006), pp. 1–7.

[129] I. P. Radko, S. I. Bozhevolnyi, G. Brucoli, L. Martin-Moreno, and A. Boltasseva. 'Efficiency of local surface plasmon polariton excitation on ridges'. *Physical Review B* (Sept. 2008) **78**(11), pp. 1–7.

[130] I. P. Radko, S. I. Bozhevolnyi, G Brucoli, L Martin-Moreno, F. J. Garcia-Vidal, and A Boltasseva. 'Efficient unidirectional ridge excitation of surface plasmons.' *Optics express* (Apr. 2009) **17**(9), pp. 7228–32.

[131] C. Chen and P. Berini. 'Grating couplers for broadside input and output coupling of long-range surface plasmons.' *Optics express* (Apr. 2010) **18**(8), pp. 8006–18.

[132] W. Barnes, T. Preist, S. Kitson, and J. Sambles. 'Physical origin of photonic energy gaps in the propagation of surface plasmons on gratings.' *Physical review. B, Condensed matter* (Sept. 1996) **54**(9), pp. 6227–6244.

[133] A. Yariv and P. Yeh. *Optical waves in crystals.* (1984)

[134] E. Anemogiannis, E. N. Glytsis, and T. K. Gaylord. 'Determination of Guided and Leaky Modes in Lossless and Lossy Planar Multilayer Optical Waveguides: Reflection Pole Method and Wavevector Density Method'. *Journal of Lightwave Technology* (May 1999) **17**(5), pp. 929–.

[135] D. Kalavrouziotis et al. '10 Gb/s Transmission and Thermo-Optic Resonance Tuning in Silicon-Plasmonic Waveguide Platform - OSA Technical Digest (CD)'. In*37th European Conference and Exposition on Optical Communications.* (Optical Society of America, Sept. 2011) We.10.P1.27.

[136] M. Elshazly-Zaghloul and R. Azzam. 'Brewster and pseudo-Brewster angles of uniaxial crystal surfaces and their use for determination of optical properties'. *JOSA* (1982) **72**(5), pp. 657–661.

[137] R. Azzam and N. Bashara. 'Ellipsometry and polarized light'. (1987).

[138] M. AKIMOTO and Y. GEKKA. 'Brewster and pseudo-Brewster angle technique for determination of optical constants'. eng. *Japanese journal of applied physics* () **31**(1), pp. 120–122.

[139] T. Wakamatsu and K. Saito. 'Interpretation of attenuated-total-reflection dips observed in surface plasmon resonance'. *Journal of the Optical Society of America B* (2007) **24**(9), p. 2307.

[140] Y. F. Lu, T. E. Loh, B. S. Teo, and T. S. Low. 'Effect of polarization on laser-induced surface-temperature rise'. *Applied Physics A Solids and Surfaces* (Apr. 1994) **58**(4), pp. 423–429.

[141] E. Kretschmann. 'Die bestimmung optischer konstanten von metallen durch anregung von oberflächenplasmaschwingungen'. *Zeitschrift für Physik* (1971) **324,** pp. 313–324.

[142] B. Liedberg, C. Nylander, and I. Lunström. 'Surface plasmon resonance for gas detection and biosensing'. *Sensors And Actuators.* Sens. Actuators (Switzerland) (1983) **4**(2), pp. 299–304.

[143] K. Katayama, T. Sawada, Q. Shen, and A. Harata. 'Detection of photoinduced electronic, thermal, and acoustic dynamics of gold film using a transient reflecting grating method under three types of surface plasmon resonance conditions'. *Physical Review B* (Oct. 1998) **58**(13), pp. 8428–8436.

[144] a. L. Lereu, a. Passian, J.-P. Goudonnet, T. Thundat, and T. L. Ferrell. 'Optical modulation processes in thin films based on thermal effects of surface plasmons'. *Applied Physics Letters* (2005) **86**(15), p. 154101.

[145] D. Pan, Y. Chen, R. Wu, X. Chen, Q. Meng, and Z. Sun. 'All-optical light modulation in anthraquinone dye doped waveguides based on an improved prism coupling method'. *Synthetic Metals* (Mar. 2007) **157**(4-5), pp. 186–189.

[146] P. Shankar and N. K. Viswanathan. 'All-optical thermo-plasmonic device.' *Applied optics* (Nov. 2011) **50**(31), pp. 5966–9.

[147] J.-C. Weeber, K. Hassan, A. Bouhelier, G. Colas des Francs, J. Arocas, L. Markey, and A. Dereux. 'Thermo-electric detection of waveguided surface plasmon propagation'. en. *Applied Physics Letters* (2011) **99**(3), p. 031113.

[148] L. Novotny and B. Hecht. *Principles of Nano-Optics.* (2006)

[149] H. Ditlbacher, J. R. Krenn, G. Schider, A. Leitner, and F. R. Aussenegg. 'Two-dimensional optics with surface plasmon polaritons'. *Applied Physics Letters* (2002) **81**(10), p. 1762.

[150] K. MacDonald and Z. Samson. 'Ultrafast active plasmonics'. *Nature Photonics* (2008) **3**(December 2008), pp. 2–5.

[151] S Papaioannou, G. Giannoulis, D. Kalavrouziotis, K. Vyrsokinos, J.-C. Weeber, K. Hassan, L. Markey, A. Dereux, A. Kumar, S. I. Bozhevolnyi, D. Apostolopoulos, H. Avramopoulos, and N. Pleros. 'WDM Switching Employing a Hybrid Silicon-Plasmonic A-MZI'. In*ECEOC.* **1.** 4. (2012) pp. 1549–1551.

[152] S. Papaioannou, D. Kalavrouziotis, K. Vyrsokinos, J.-C. Weeber, K. Hassan, L. Markey, A. Dereux, A. Kumar, S. I. Bozhevolnyi, M. Baus, T. Tekin, D. Apostolopoulos, H. Avramopoulos, and N. Pleros. 'Active plasmonics in WDM traffic switching applications.' *Scientific reports* (Jan. 2012) **2,** p. 652.

[153] A. Kumar et al. 'Dielectric-loaded plasmonic waveguide components: Going practical'. *Laser & Photonics Reviews* (Feb. 2013), n/a–n/a.

[154] J. Gosciniak, L. Markey, A. Dereux, and S. I. Bozhevolnyi. 'Thermo-optic control of dielectric-loaded plasmonic Mach-Zehnder interferometers and directional coupler switches.' *Nanotechnology* (Nov. 2012) **23**(44), p. 444008.

[155] J. Gosciniak, L. Markey, A. Dereux, and S. I. Bozhevolnyi. 'Efficient thermo-optically controlled Mach-Zhender interferometers using dielectric-loaded plasmonic waveguides'. *Optics Express* (July 2012) **20**(15), p. 16300.

[156] J. Gosciniak and S. I. Bozhevolnyi. 'Performance of thermo-optic components based on dielectric-loaded surface plasmon polariton waveguides.' *Scientific reports* (May 2013) **3,** p. 1803.

[157] T. Holmgaard, J. Gosciniak, and S. I. Bozhevolnyi. 'Long-range dielectric-loaded surface plasmon-polariton waveguides'. *Optics express* (2010) **18**(22), pp. 1307–1309.

[158] Y. Bian, Z. Zheng, Y. Liu, J. Zhu, and T. Zhou. 'Dielectric-loaded surface plasmon polariton waveguide with a holey ridge for propagation-loss reduction and subwavelength mode confinement.' *Optics express* (Nov. 2010) **18**(23), pp. 23756–62.

[159] Y. Li, H. Zhao, A. Ma, and X. Zhang. 'Semi-elliptical dielectric-loaded surface plasmon-polariton waveguides'. *Optics Communications* (June 2011) **284**(12), pp. 2839–2842.

[160] H. Zhao, Y. Li, and G. Zhang. 'Study on the performance of bimetallic layer dielectric-loaded surface plasmon polariton waveguides'. *Journal of Optics* (Nov. 2011) **13**(11), p. 115501.

[161] H. Zhao, Y.-e. Li, and G.-m. Zhang. 'On the characteristics of commonly nonideal rectangular ridge dielectric-loaded surface plasmon polariton waveguides in practical fabrication processing'. *Optics Communications* (Mar. 2012) **285**(6), pp. 1091–1096.

[162] J. Gosciniak, T. Holmgaard, and S. I. Bozhevolnyi. 'Theoretical Analysis of Long-Range Dielectric-Loaded Surface Plasmon Polariton Waveguides'. *Journal of Lightwave Technology* (May 2011) **29**(10), pp. 1473–1481.

[163] V. S. Volkov, Z. Han, M. G. Nielsen, K. Leosson, H. Keshmiri, J. Gosciniak, O. Albrektsen, and S. I. Bozhevolnyi. 'Long-range dielectric-loaded surface plasmon polariton waveguides operating at telecommunication wavelengths.' *Optics letters* (Nov. 2011) **36**(21), pp. 4278–80.

[164] V. A. Zenin, Z. Han, V. S. Volkov, K. Leosson, I. P. Radko, and S. I. Bozhevolnyi. 'Directional coupling in long-range dielectric-loaded plasmonic waveguides'. *Optics Express* (Apr. 2013) **21**(7), p. 8799.

[165] H. Deng. 'Design and Characterization of Silicon-on-Insulator Passive Polarization Converter with Finite-Element Analysis'. Electrical and Computer Engineering. University of Waterloo, 2005.

[166] C. Alonso-Ramos, S. Romero-Garcia, A. Ortega-Monux, I. Molina-Fernández, R. Zhang, H. G. Bach, and M. Schell. 'Polarization rotator for InP rib waveguide.' *Optics letters* (Feb. 2012) **37**(3), pp. 335–7.

[167] D. M. Beggs, M. Midrio, and T. F. Krauss. 'Compact polarization rotators for integrated polarization diversity in InP-based waveguides.' *Optics letters* (Aug. 2007) **32**(15), pp. 2176–8.

[168] Z. Wang and D. Dai. 'Ultrasmall Si-nanowire-based polarization rotator'. *JOSA B* (2008) **25**(5), pp. 747–753.

[169] L. Liu, Y. Ding, K. Yvind, and J. Hvam. 'Efficient and compact TE–TM polarization converter built on silicon-on-insulator platform with a simple fabrication process'. *Optics letters* (2011) **36**(7), pp. 1059–1061.

Publications associated with this work

Refereed Journal Publications

1. **K. Hassan**, A. Bouhelier, T. Bernardin, G. Colas-des-Francs, J.-C. Weeber, R. Espiau de Lamaestre and A. Dereux. Momentum-space spectroscopy for advanced analysis of dielectric-loaded surface plasmon polariton coupled and bent waveguides. *Phys. Rev. B*, 87(19), 195428, 2013. **Chapter 2**
2. **K. Hassan**, J.-C. Weeber, L. Markey, A. Dereux, A. Pitilakis, O. Tsilipakos, and E. E. Kriezis. Thermo-optic plasmo-photonic mode interference switches based on dielectric loaded waveguides. *Applied Physics Letters*, 99(24):241110, 2011. **Chapter 3**
3. **K. Hassan**, J.-C. Weeber, L. Markey, and A. Dereux. Thermo-optical control of dielectric loaded plasmonic racetrack resonators. *Journal of Applied Physics*, 110(2):023106, 2011. **Chapter 3**
4. J-C Weeber, **K Hassan**, L Saviot, A Dereux, C Boissière, O Durupthy, C Chaneac, E Burov, and a Pastouret. Efficient photo-thermal activation of gold nanoparticle-doped polymer plasmonic switches. *Optics express*, 20(25):27636–49, December 2012. **Chapter 4**
5. J.-C. Weeber, **K. Hassan**, A. Bouhelier, G. Colas-des Francs, J. Arocas, L. Markey, and A. Dereux. Thermo-electric detection of waveguided surface plasmon propagation. *Applied Physics Letters*, 99(3):031113, 2011.
6. M. G. Nielsen, J.-C. Weeber, **K. Hassan**, J. Fatome, C. Finot, S. Kaya, L. Markey, O. Albrektsen, S. I. Bozhevolnyi, G. Millot, and A. Dereux. Grating Couplers for Fiber-to-Fiber Characterizations of Stand-Alone Dielectric Loaded Surface Plasmon Waveguide Components. *Journal of Lightwave Technology*, 30(19):3118–3125, October 2012. **Chapter 4**

Conference Publications

1. **K. Hassan**, J.-C. Weeber, L. Markey, A. Dereux, A. Pitilakis, O. Tsilipakos, and E.E. Kriezis. Characterization of thermo-optical 2x2 switch configurations made of Dielectric Loaded Surface Plasmon Polariton Waveguides for telecom routing

architecture - OSA Technical Digest. In *Optical Fiber Communication Conference*, page OW3E.5. Optical Society of America, March 2012. **Chapter 3**

2. J.-C. Weeber, **K. Hassan**, M. G. Nielsen, A. Pitilakis, O. Tsilipakos, E. E. Kriezis, J. Fatome, C. Finot, L. Markey, O. Albrektsen, S. I. Bozhevolnyi, and A. Dereux. Dielectric loaded surface plasmon waveguides for datacom applications. In *Proc. of SPIE*, volume 8424, pages 842407–842407–14, May 2012. **Chapter 3, 4**
3. A. Dereux, **K. Hassan**, J.-C. Weeber, N. Djellali, S.I. Bozhevolnyi, O. Tsilipakos, A. Pitilakis, E. Kriezis, S. Papaioannou, K. Vyrsokinos, N. Pleros, T. Tekin, M. Baus, D. Kalavrouziotis, G. Giannoulis, H. Avramopoulos. Parametric study of dielectric loaded surface plasmon polariton add-drop filters for hybrid silicon/plasmonic optical circuitry. In *Proceedings of SPIE*, volume 7945, page 794513, 2011. **Chapter 3**

Conference Talks

1. **K. Hassan**, J.-C. Weeber, L. Markey, A. Dereux. Composants Plasmonique pour le routage Tb/s Telecom. In *GDR ondes, RF Millimétrique et optique intégrée*, Grenobles, Jan. 17–18, 2013. **Chapter 3, 4**
2. **K. Hassan**, J.-C. Weeber, L. Markey, A. Dereux, A. Pitilakis, O. Tsilipakos, and E.E. Kriezis. Characterization of thermo-optical 2x2 switch configurations made of Dielectric Loaded Surface Plasmon Polariton Waveguides for telecom routing architecture. In *EMRS Spring Meeting, Symposium N*, Strasbourg, Mai 14–18, 2012. **Chapter 3**
3. **K. Hassan**, J.-C. Weeber, L. Markey, A. Dereux, A. Pitilakis, O. Tsilipakos, and E.E. Kriezis. Characterization of thermo-optical 2x2 switch configurations made of Dielectric Loaded Surface Plasmon Polariton Waveguides for telecom routing architecture - OSA Technical Digest. In *Optical Fiber Communication Conference*, page OW3E.5. Optical Society of America, Los Angeles, March 4–8, 2012. **Chapter 3**

Conference Posters

1. **K. Hassan**, J.-C. Weeber, L. Markey, A. Dereux. Fabrication et Caractérisation de résonateurs plasmoniques pour des systèmes de routage thermo-optique. During the: *PhD days, Carnot PhD School*, Dijon, Mai 5–6, 2011. **Chapter 2, 3**
2. **K. Hassan**, J.-C. Weeber, L. Markey, A. Dereux. Thermo-optic plasmonic components for Tb/s routing. During the: *The 6th International Conference on Surface Plasmon Photonics, SPP6*, Ottawa, Canada Mai 26–31, 2013. **Chapter 3, 5**

Fabrication and characterization of Thermo-Plasmonic routers for Telecom Applications

Abstract: The Dielectric Loaded Surface Plasmon Polariton Waveguides (DLSPPWs) have recently emerged as a possible solution to carry both optical and electrical signals on-chip. However, in the particular context of optical interconnects, advanced functionalities such as filtering, switching, and routing are required in order to replace in the future the equivalent electronic components which are too much power consumer and also to reduce their footprints. After presenting the interest and limitation of the leakage radiation microscopy method used all along this work, we show several active devices using thermo-sensitive polymers as the dielectric load driven electrically by Joule heating. Then we demonstrate the feasibility of all-optical systems by either doping the dielectric with metallic nanoparticles or by plasmo-thermal effect of a second plasmonic mode providing a localized heating of controlled shape. The dynamic activation of our thermo-optical devices is performed using a homemade fiber-to-fiber setup which allows us to investigate the response time of a plasmo-thermal heating as well as true datacom transmission. Some improvements of the original DLSPPWs performances are proposed by adding a metallic wall on one side of the polymer ridge. This system can act as a compact and athermal polarization converter.

Key words: Plasmonic waveguides; Thermo-optic; Integrated optics; Leakage radiation microscopy; All-optical systems.

Fabrication et Caractéristion de routeurs thermo-plasmoniques pour les applications télécom

Résumé: Les guides d'ondes plasmoniques à rubans dielectriques (DLSPPW) sont récemment apparus comme une des solutions possible pour le transport de signaux optiques et électriques sur puce. Néanmoins, dans le contexte particulier des interconnections optiques, des fonctionalitées avancées telles que filtrage, commutation, et routage sont nécessaires afin de remplacer dans le futur les composants electroniques équivalents trop gourmands en énergie et aussi réduire leur empreinte. Après une présentation des intérêts et limitations de la technique de microscopie à fuite radiative, nous montrons plusieurs composants actifs utilisant pour diélectrique des polymères thermo-sensibles controlés électriquement par effet Joule. Par la suite nous démontrons la faisabilité de systèmes tout optique que ce soit par dopage du polymère par des nanoparticules metalliques ou par effet thermo-plasmonique d'un second mode plasmon permettant un échauffement localisé de forme choisie. L'activation dynamique de nos composants thermo-optiques est réalisée grâce à un montage fibre-à-fibre créé spécialement nous permettant d'investiguer le temps de réponse d'un chauffage plasmonique ainsi que la transmission de signal télécom. Des améliorations de performances du concept DLSPPW original sont proposées par l'ajout d'un mur métallique sur le côté du ruban de polymère. Ce système peut alors fonctionner comme un convertisseur de polarisation compacte et athermique.

Mots clés: Guides d'ondes plasmoniques; Thermo-optique; Optique intégrée; Microscopie à fuites radiatives; Systèmes tout optique.